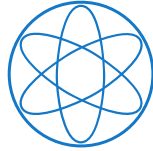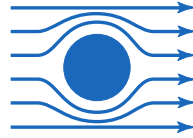Technische
Universität
München

School of
Natural Sciences

Walther-Meißner
Institut

Bayerische
Akademie
der Wissenschaften

Near- and far-field Raman spectroscopy as an experimental approach to correlated kagome metals

Dissertation

Leander Peis

April 2023

School of Natural Sciences

TECHNISCHE UNIVERSITÄT MÜNCHEN

Technische Universität München
TUM School of Natural Sciences

Near- and far-field Raman spectroscopy as an experimental approach to correlated kagome metals

Leander M. Peis

Vollständiger Abdruck der von der TUM School of Natural Sciences der Technischen Universität München zur Erlangung eines

Doktors der Naturwissenschaften (Dr. rer. nat.)

genehmigten Dissertation.

Vorsitz: Prof. Dr. Johannes Knolle

Prüfer*innen der Dissertation:

1.   apl. Prof. Dr. Rudolf Hackl

2.   Prof. Dr. Martin Knupfer

Die Dissertation wurde am 19.04.2023 bei der Technischen Universität München eingereicht und durch die TUM School of Natural Sciences am 07.06.2023 angenommen.

Abstract

This thesis comprises a Raman spectroscopy study of highly correlated metals having kagome lattices and the development of a low-temperature ultra-high-vacuum tip-enhanced Raman scattering (TERS) setup. Momentum-resolved Raman spectroscopy accesses excitations relevant to study lattice, electron, and spin dynamics. By combining light scattering data with thermodynamic measurements and theoretical calculations, the spin-reorientation in the ferromagnet Fe_3Sn_2 at approximately $100\,K$ could be related to strong spin-phonon coupling. In the kagome superconductor CsV_3Sb_5, several strong coupling signatures in the charge density wave phase were identified, contrasting the dominant weak-coupling scenario driven by Fermi surface nesting. TERS combines scanning tunneling microscopy with polarization-dependent Raman scattering beyond the diffraction limit. By enabling the in-situ preparation of metallic tips and samples, strongly enhanced Raman signals on single-wall carbon nanotubes were observed at low temperatures.

Kurzzusammenfassung

Diese Arbeit umfasst Untersuchungen an hoch-korrelierten Metallen mit Kagome-Gittern mithilfe von Raman-Streuung und die Entwicklung eines Tieftemperatur-Ultrahochvakuumaufbaus für spitzen-verstärkte Raman-Streuung (TERS). Impulsaufgelöste Raman-Spektroskopie ermöglicht den Zugriff auf Anregungen die für die Analyse der Gitter-, Elektronen- und Spin-Dynamik relevant sind. Durch die Kombination von inelastischen Lichtstreuungsdaten mit thermodynamischen Messungen und theoretischen Berechnungen wurde die Spin-Umorientierung im Ferromagneten Fe_3Sn_2 bei etwa $100\,K$ mit einer starken Spin-Phonon-Kopplung in Verbindung gebracht. In dem Kagome-Supraleiter CsV_3Sb_5 wurden mehrere Hinweise auf starke Kopplung als Ursache der Ladungsdichtewellenphase identifiziert, die gegen ein Szenario mit schwacher Kopplung induziert durch Fermiflächen-Nesting sprechen. Der neu entwickelte TERS-Aufbau kombiniert Rastertunnelmikroskopie mit polarisationsabhängiger Raman-Streuung jenseits der optischen Auflösungsgrenze. Durch die in-situ-Präparation von metallischen Spitzen und Proben wurden stark verstärkte Raman-Signale an einwandigen Kohlenstoff-Nanoröhren bei tiefen Temperaturen beobachtet.

Contents

1. Introduction

Archimedes of Syracuse discovered that the two-dimensional (2D) plane such as a floor can be tiled with regular polygons in not more than eleven different ways, if all shared edges are equally long and the nodes are topologically equivalent. For this reason and for the resulting high symmetry, Archimedian lattices play an important role in modern solid-state physics [1, 2, 3, 4]. A popular example is the triangular coordination of vortices of a superconductor in a magnetic field [5]. In graphene the carbon atoms occupy a honeycomb lattice sitting on two inequivalent sites. The resulting electronic band structure exhibits a linear dispersion at the K and K' points of the Brillouin zone [6]. The two doubly degenerate bands intersect at these high-symmetry points and form Dirac points, which are protected by inversion and time reversal symmetry.

The kagome lattice, that is another archimedean structure combining hexagons and triangles, was introduced to statistical physics in 1951 by Syozi [7]. If magnetic ions occupy the nodes and the interaction is antiferromagnetic, the order is frustrated as indicated in Fig. 1.0.1 (a). At low temperature spin-ice or spin-liquid states may emerge [8]. The band structure resembles that of graphene but, in addition, is expected to have a flat band as shown in Fig. 1.0.1 (b) as a result of destructive quantum interference of localized states on the triangles [9]. Mielke *et al.* suggested that the flat band is at the origin of ferromagnetism such as in Fe_3Sn_2 [10]. However, Pollmann and coworkers favor a mechanism based on kinetic energy arguments [11]. As is the case in graphene, Dirac points are expected at the K-points, where the dispersing bands cross [12]. If inversion or time reversal symmetry are broken, the degeneracy is lifted, separating the Dirac point into two Weyl points [13]. Prominent examples making use of this electronic band structure are ferromagnetic kagome systems with spin-orbit coupling (SOC), the latter inducing the formation of a gap at the band crossings. This configuration naturally realizes non-trivial topology and exhibits an intrinsic anomalous Hall effect due to a large Berry curvature [14, 15, 16]. The dispersing bands also display saddle points at the M-points entailing Van Hove singularities (VHs) in the electronic density of states (DOS). These divergences in the DOS were suspected to be at the origin of charge density wave (CDW) order [17] and superconductivity (SC) [18] in different kagome based materials. The interplay of these phenomena allow the investigation of strong interactions, frustrated geometry, correlations, and topology.

Fe_3Sn_2 and CsV_3Sb_5 were studied during this thesis. The metallic kagome ferromagnet Fe_3Sn_2 exhibits a large anomalous Hall effect [19], massive Dirac fermions [20] and a large topological Hall effect [21]. Here, the bilayer nature specific to this particular kagome system gives rise to interlayer hybridization of the Fe d-orbitals, consequently blurring the ideal band structure picture of Fig. 1.0.1 (b) [22]. For instance, Lin *et al.* [23] observed a clear flatband near the Fermi surface, which, however, does not extend over the entire
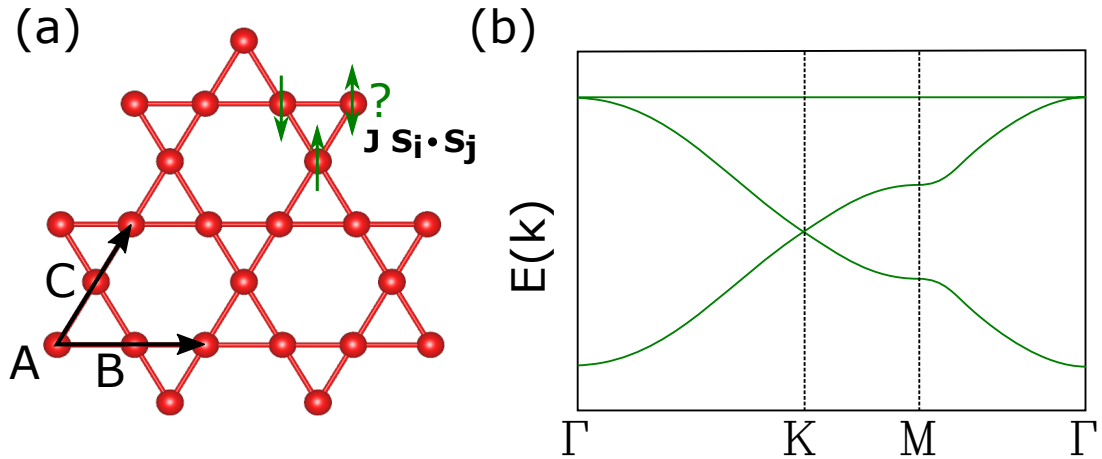
(a)

(b)

$J\ S_i \cdot S_j$

Figure 1.0.1.: Kagome lattice schematic and resulting band structure from a tight-binding model. The kagome lattice has three triagonally coordinated not necessarily equivalent sites entailing a geometrical frustration of the spins (green arrows). The band structure is mostly dominated by honeycomb-driven features in the form of two VHs and a Dirac point between dispersive bands. As a consequence of the triangles in the kagome structure, a band that is flat over the complete Brillouin zone can be observed. Band structure adopted from [9].

Brillouin zone as anticipated. Fe_3Sn_2 develops itinerant ferromagnetic order at high temperatures, the origin of which is still under debate [10, 11]. Interestingly, there is a slow spin-reorientation from out-of-plane to in-plane upon cooling with its transition peak at approximately $120\,K$ [24]. Similar to the ferromagnetism itself the origin of the reorientation is open [25]. Accordingly, the main objective revolves around any potential interactions of the spin system with the lattice, as a probable driving force for this reorientation.

Secondly, the family AV_3Sb_5 (A = K, Rb, Cs) was observed to be a quasi-2D kagome superconductor with non-trivial topology in addition to a commensurate CDW transition which, according to specific heat results, is presumably first order. [17]. The interplay of lattice geometry, electronic instabilities, and band topology stimulated extensive research [9, 26, 27, 28, 29, 30]. Density functional theory (DFT) [31], scanning tunneling microscopy (STM) [32], angle-resolved photoemission spectroscopy (ARPES) [33, 34], and X-ray scattering [35] laid important groundwork on understanding the electronic properties and ordering mechanism. Recently, a competition between the CDW and SC was observed as a function of applied pressure where T_{CDW} is suppressed, whereas T_c increases [36]. T_c displays a double dome and becomes maximal where T_{CDW} approaches zero. As opposed to the cuprates or the iron-based systems, SC competes here with charge order rather than magnetism. Thus, this kagome family seems to be a paradigm of a new type of coupling.

Raman scattering enables the investigation of the lattice, the electronic and magnetic system, as well as the interactions thereof and is thus a valuable tool for addressing some of the open questions here. The method was applied to bulk materials and quasi-2D stacked layered systems [37, 38], yet its large penetration depth and its diffraction-limited spatial resolution of more than $500\,nm$ hamper the study of thin films or local quantum objects. TERS, in principle, affords a window into local properties in the submicron range down to

a few nanometers by exploiting the excitation of localized surface plasmon resonances at a metallic tip apex upon irradiation of laser light. The field-enhancement effect was originally observed for pyridine on a rough silver surface [39] but is now realized exclusively by scanning a metal tip across a sample. The resulting increase in the electric field intensity at the tip-sample junction yields enhanced Raman signals by several orders of magnitude. As the plasmonic near-field enhancement is confined by the effective tip apex dimensions, objects in the nanometer and even sub-molecule range were successfully resolved using TERS [40, 41, 42, 43]. This already led to insights into the chemical composition of molecules and their interaction with surfaces [44, 45], but also opens the door for studying thin film and surface physics in the future. Yet, such an extension of TERS applications needs a contrast between the near- and far-field Raman signal at least on the order of 10^9, to compensate for the much larger volume illuminated in the far field [46, 47]. For the study of adsorbates and their interaction with the surface and of surface effects in solids ultra-high vacuum (UHV) and in many cases low temperatures (LT) are required. In the first case, catalytic reactions may be studied for instance. In the latter case, metallic surface states of topological insulators, surface superconductivity, phonons close to grain boundaries or static charge order could be accessed. Yet, combining a stable STM under these challenging environmental conditions with highly functional optics, while also maintaining access to clean polarizations in limited space remains a challenge. Thus, low temperature TERS is still in its infancy and only a few instruments were demonstrated to work in UHV conditions at either liquid nitrogen [48] or liquid helium temperature [47].

The thesis is organized as follows: In chapter 2, an introduction to the physical properties of the two kagome systems Fe_3Sn_2 and CsV_3Sb_5 is presented. Thereafter, in chapter 3 a brief introduction to the theory of inelastic light (Raman) scattering is described with the main focus placed on the application to this work. The results including analysis and discussion are presented in chapter 4. In the second part, in chapter 5, the LT-UHV-TERS system is described in detail. Section 5.1 introduces the basic ideas and reasoning. The augmentation of the system and its final realization are described in detail in section 5.2. The successful operation of the system is demonstrated and benchmarked against single-wall carbon nanotubes (SWNT) in section 5.3. The most important far- and near-field results are summarized in chapter 6.

2. Properties of kagome lattice materials

This chapter introduces two metallic compounds, whose physics are dominated by 3d orbital atoms ordered in a kagome lattice. These two crystals are for one the kagome ferromagnet Fe_3Sn_2 and secondly the kagome superconductor CsV_3Sb_5. Their general properties regarding lattice structure, electronic band structure, magnetism, and phase transitions are the main focus of the following.

2.1. Lattice structure
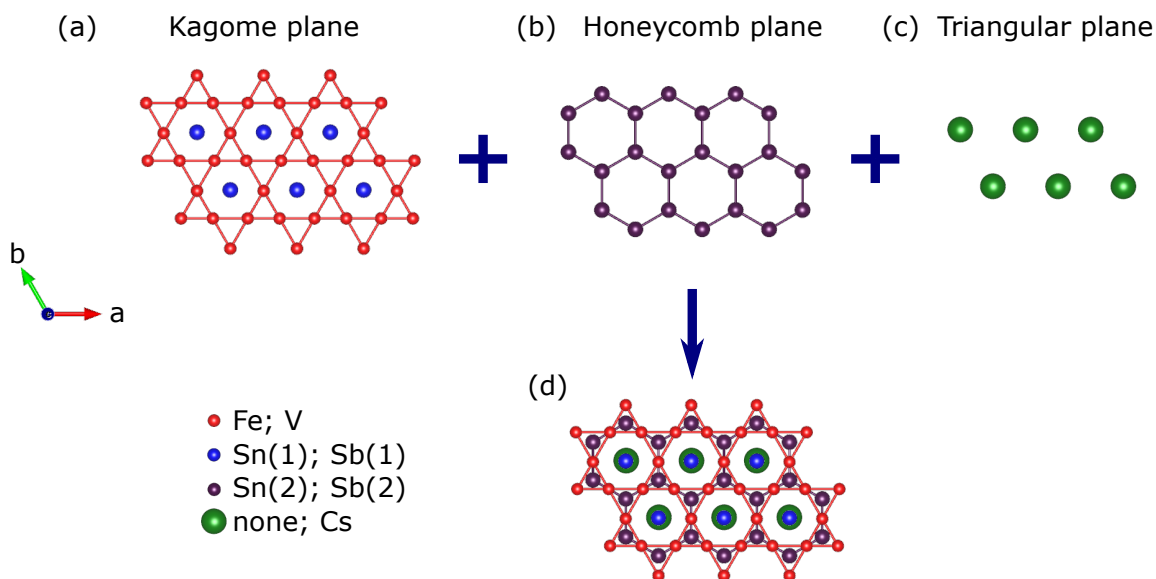
Figure 2.1.1.: Different 2D-planes of the investigated compounds Fe_3Sn_2 and CsV_3Sb_5, emphasizing their layered nature. (a) Kagome plane, consisting either of Fe or V atoms, located around a Sn or Sb atom at the center of the hexagon. (b) and (c) display the separation layers as a honeycomb structure made of either Sn or Sb and a triangular plane of Cs. The studied compounds are the result of a layered combination of these individual planes, leading to the structure in panel (d). Partially adopted from [17, 49].

The two compounds of interest, Fe_3Sn_2 and CsV_3Sb_5, share several similarities in their layered crystal structure as shown in Fig. 2.1.1. Both display a sixfold symmetry, consisting

of kagome planes (red balls) filled with an atom in the hexagon centers (blue), stacked on top of each other. The kagome planes are separated by additional layers in the form of a honeycomb lattice (violet) and in CsV_3Sb_5 also by a triangular plane (green).
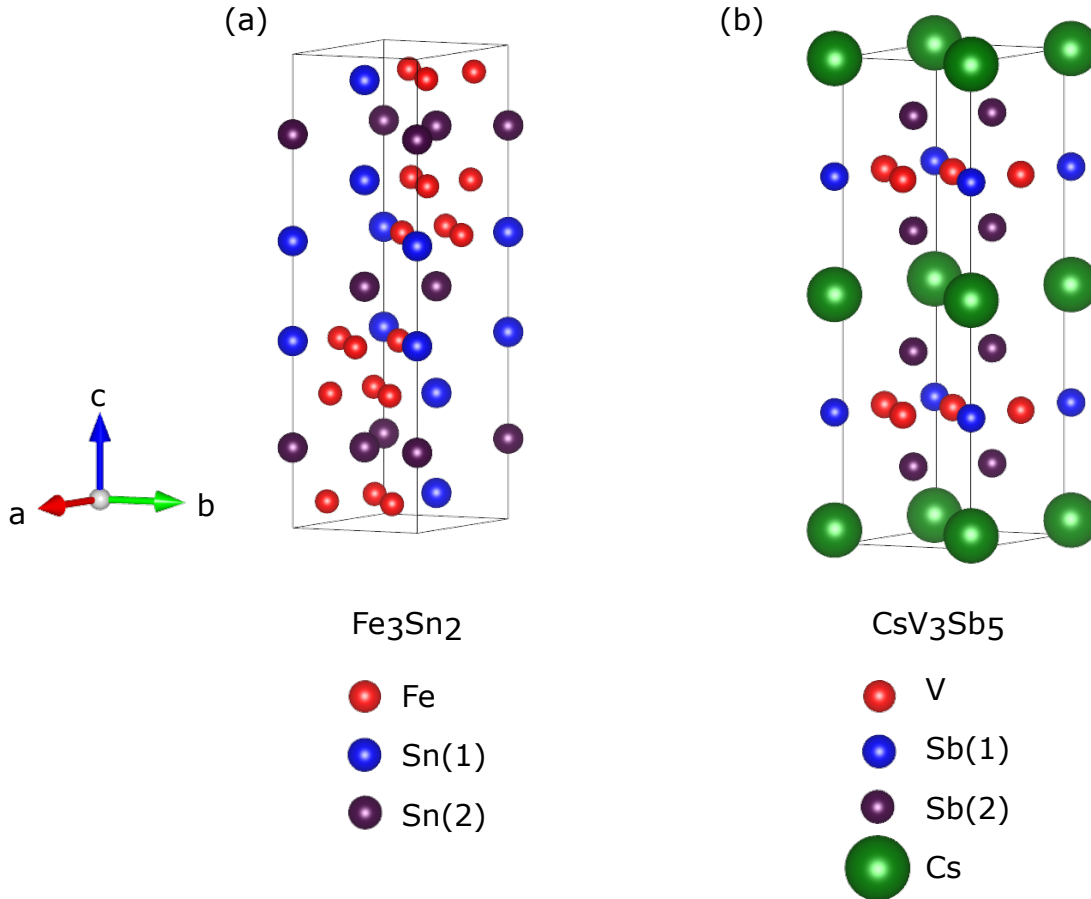
Figure 2.1.2.: Crystal structures of Fe_3Sn_2 and CsV_3Sb_5 in panels (a) and (b), respectively. The respective atoms are indicated with a color code and the same atoms on inequivalent sites are marked with different colors and numbered accordingly. The structure is visualized using VESTA [50].

Fe_3Sn_2

Fe_3Sn_2 has a layered rhombohedral crystal structure, belonging to the space group $R\bar{3}m$ (No. 166) and the D_{3d} ($\bar{3}m$) point group. The lattice constants are $a = 5.338\,\text{Å}$ and $c = 19.789\,\text{Å}$ due to the complex stacking nature. The unit cell is illustrated in Fig. 2.1.2 (a). Two adjacent Fe_3Sn-layer are stacked with a different lattice offset and are separated by a Sn-honeycomb plane. The Fe in the Fe_3Sn layer forms a ferromagnetic kagome lattice with Sn atoms positioned at the center of the hexagons.

CsV_3Sb_5

The recently discovered kagome family of AV_3Sb_5 with A = (K, Rb, Cs) [17] has generated great interest since all these compounds exhibit chiral charge order, a superconduct-

ing phase, and potential influences of a non-trivial topological band structure. Here, the CsV_3Sb_5 system was selected, as it is expected to yield the most dominant two-dimensional electronic structure and minimal disorder in the alkali sublattices. The system crystallizes in the hexagonal $P6/mmm$ space group, with a layered structure in the unit cell (Fig. 2.1.2 (b)). The kagome lattice is formed by the V atoms centered around an Sb atom. This plane is sandwiched by two honeycomb lattices of Sb and each of these stacked complexes is separated by a triangular Cs-layer.

2.2. Electronic structure

Expanding from the general picture drawn for a simple kagome structure in Fig. 1.0.1, we take a look at the calculated and confirmed band structures of Fe_3Sn_2 and CsV_3Sb_5, revealed mainly by DFT calculations and ARPES measurements.

Fe_3Sn_2

A simplistic approach and model band structure is sufficient for the following investigation of the ferromagnet Fe_3Sn_2. In a tight binding model, one only considers two kagome planes being stacked on top of each other with small adjustments of the triangle sizes and including an in-plane hopping of t and inter-plane hopping $0.3t$ according to Ye *et al.* [20]. The results are depicted in 2.2.1(a) with (red) and without (blue) spin-orbit coupling. The stacking leads to a doubling and shifting of the band features for a simple kagome plane and therefore to double Dirac cones at the K-point. The degeneracy at the intersection points is lifted if spin-orbit coupling is switched on. This is magnified in the inset. The splitting of the bands, leading to four crossing points is a natural consequence of the bilayer structure of Fe_3Sn_2, similar to the case of multi-layer graphene [51]. This rather simple approach very well describes the experimental band structure around the K-point observed by ARPES, resolving two Dirac points at 70 and 180 meV above and below a Dirac circle at 125 meV and four dispersive bands at the Fermi energy in the vicinity of the high symmetry point K. For clarity, the Fermi energy is tentatively indicated as a dotted line in panel (a). Ye *et al.* also discovered an energy gap of around 30 meV at the second Dirac point, and attributed it to the emergence of massive Dirac fermions as a consequence of the combination of spin-orbit coupling and ferromagnetic splitting from the 3d Fe-orbitals in the underlying kagome structure [20]. Furthermore, they argue that these massive Dirac bands lead to a non-trivial Berry curvature, qualitatively explaining the intrinsic anomalous Hall effect observed in transport measurements. This connects the quasi-2D massive Dirac fermions directly to the concentration of Berry curvature and indicates the topological character of the electronic properties. One can furthermore learn from the negligible k_z-dispersion experimentally substantiated in ARPES measurements, that the band structure is mostly dependent on the kagome planes and the quasi-2D nature of the Fe_3Sn_2 bands. The predicted flat bands have been partially observed in ARPES measurements by Lin *et al.*, having an energy of around -0.2 eV and being located in an extended region around Γ [23]. In these measurements, high DOS regions were also revealed at and slightly

below E_F, in the range between Γ and K, but closer to the latter.
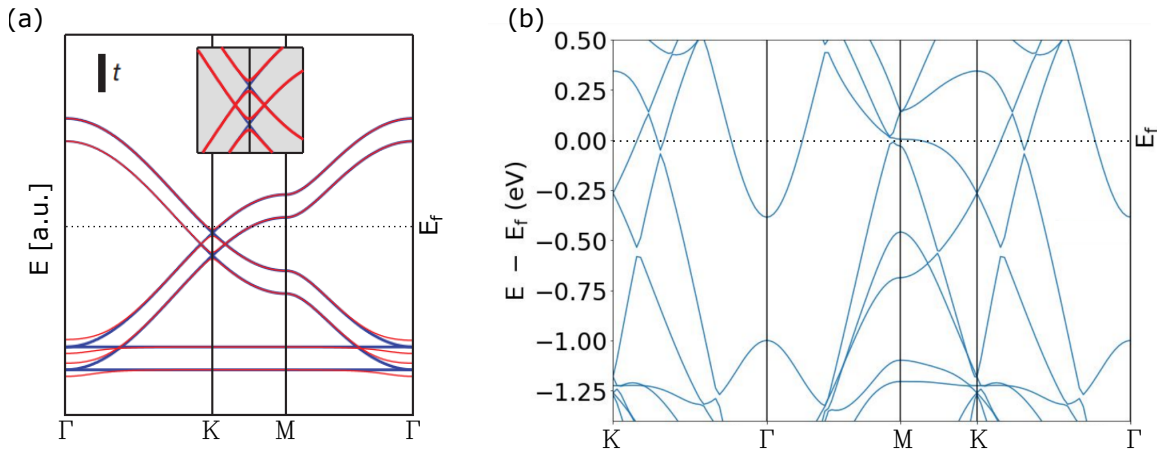
(a)

(b)

Figure 2.2.1.: Calculated band structure of Fe_3Sn_2 (a) and CsV_3Sb_5 (b) between high symmetry points. (a) Via a tight binding model of a bi-layer kagome lattice the bands predicted for a single layer are duplicated and shifted. This approach describes the physics in Fe_3Sn_2 already reasonably well, indicating four band crossings around the K-point. The inset zooms into this region with (red) and without (blue) spin-orbit coupling. The image was adopted from [20]. (b) DFT calculations for CsV_3Sb_5, kindly provided by Cuddy *et al.*, reveal the main contributions in the band structure to be stemming from the V-atoms of the kagome lattice. One observes two band crossings at the K-point and several bands intersecting at the M-point close to the Fermi energy.

CsV_3Sb_5

The electronic nature of CsV_3Sb_5 has been intensively studied in recent years. DFT calculations performed by Cuddy *et al.* are displayed in Fig. 2.2.1(b) with the Fermi energy indicated. Like for all AV_3Sb_5 compounds [17, 52] the structure consists of several bands crossing the Fermi energy, which indicates the metallic nature. Around the Γ-point, an electron-like parabolic band is observed. This shape is mainly a result of the p_z-orbital projections of the antimony atoms in the kagome plane (blue dots). Furthermore, two other main features resulting from the kagome structure are present. One is a Dirac point at the K-point. The other one consists of two VHs close to the Fermi energy at the M-point with one of them being directly connected to the Dirac point at K. These singularities were identified to play a major role in the physical properties of CsV_3Sb_5, especially for the formation of an unconventional charge density wave. The strong 2D nature of this compound can be seen in the dispersion of the bands along k_z, which reveals no strong changes in this momentum direction. This electronic behavior is supported by a large anisotropy in the electronic transport between in-plane and out-of-plane measurements. While the system is metallic for all directions, the resistivity along the c-axis is 600 times larger than in the kagome planes [28]. The transport measurements published by Ortiz *et al.* were completed by ARPES measurements and reproduce the qualitative behavior anticipated by DFT [28]. This agreement suggests that the electronic correlations are weak [27] and insufficient to explain putative unconventional superconductivity [53, 54, 36].

It is worth noting, that in contrast to other kagome metals, no magnetic ordering and no

local magnetic moments are present. Thus, ordered phases are more likely to be attributed to charge dynamics [28].

Partially responsible for the massive interest in this compound is the addition of non-trivial topology to the correlated states intrinsically originating from a 2D kagome structure. Due to the small but existing dispersion along k_z, the topological Dirac points are extended to 1D nodal lines of non-trivial band crossings in the complete BZ. This is a natural candidate for the origin of a large Berry curvature. Thus, a large anomalous Hall effect or helical Cooper pairing are in the realm of possibility. The described band structure features were assigned to have a $\mathcal{Z}_2$ topological index [28], which might stem from a band inversion away from the Fermi level. The potentially arising surface states cannot be observed directly due to the metallic nature of CsV_3Sb_5, yet the existence of these topological effects adds to the variety of phenomena in kagome metals. Hu *et al.* [55] claimed recently to have witnessed these non-trivial topological surface states slightly over the Fermi level via ARPES measurements, further confirmations would be desirable.

2.3. Magnetism in Fe$_3$Sn$_2$

The most dominant physical property of the kagome metal Fe_3Sn_2 is its frustrated itinerant ferromagnetism with a high $T_C = 670\,\mathrm{K}$ [56]. DFT Perdew-Burke-Ernzerhof calculations find all the spins to be located on the Fe atoms of the kagome layer with all spins being aligned in-plane for its ground state [57]. The saturation magnetization M_s shows only mild T-dependence and plateaus at approximately $1.9\mu_B$ per Fe atom at low temperatures [20]. The crystals display a high metallicity with a residual resistivity ratio of $\rho(300\,\mathrm{K})/\rho(2\,\mathrm{K}) = 29.3$, as observed by transport measurement presented in Fig. 3.2.4(a). Several interesting physical phenomena were investigated in magnetic field-dependent measurements. Prominent examples would be the formation of skyrmion bubbles [58], a high anomalous Hall effect connected to a non-trivial Berry curvature [59, 19], and topological band structure modulations in the form of Weyl points at E_F and their movement in reciprocal space by a rotation of the magnetization direction [60]. Yet, we are interested in the zero-field properties, where a spin-reorientation from in-plane to out-of-plane magnetization takes place upon warming up. This scenario has been observed very early by Mössbauer experiments [61, 62] and was also found later by X-ray [63] and transport studies [19]. As mentioned before, the contributing spins are located on the Fe atoms, a schematic of the described spin-reorientation above and below T_{SR} is drawn in Fig. 2.3.1. This magnetization change takes place over a broad temperature range from around 150 to below 100 K and its origin is not fully understood yet [25]. Transport and magnetization experiments performed on the here investigated samples and their respective plot in Fig. 3.2.4 confirm the crossover in this temperature range. Its actual origin, its contribution to the lattice, and any potential spin-phonon coupling are still under investigation and will be discussed later.
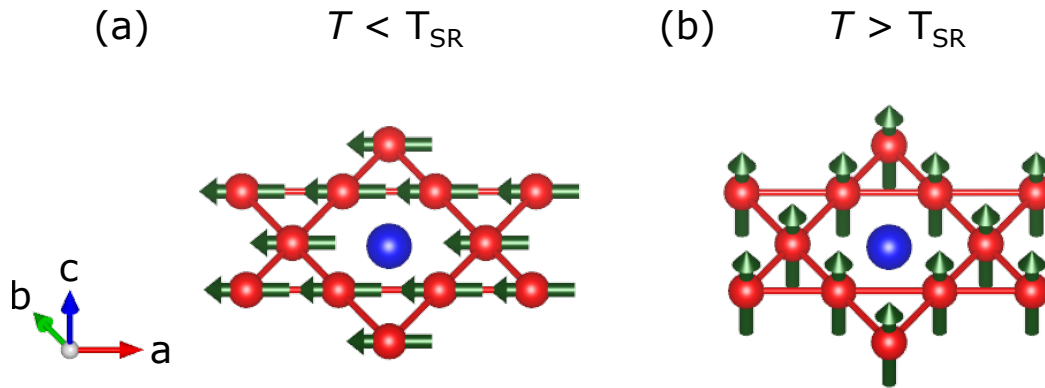
Figure 2.3.1.: Spin reorientation in the kagome ferromagnet Fe$_3$Sn$_2$ at $T_{SR} \approx 100$ K. Upon warming up the magnetization of the Fe atoms rotates from an in-plane configuration to a perpendicular alignment concerning its origin layer. The process takes place over a broad temperature region of arguably around $\Delta T = 80 - 150$ K.

2.4. Ordering phases in CsV$_3$Sb$_5$

Two dominant ordering phases are observed in CsV$_3$Sb$_5$, namely superconductivity and an unconventional CDW phase. In principle, these two phases can be either in coexistence or competition. Pressure experiments revealed a sharp increase of T_c under the application of hydrostatic pressure, which is accompanied by concomitant suppression of T_{CDW} until it vanishes [64, 65]. Hence, these experiments point rather toward competition between the two ordered phases. The simple manipulation of these two phases points towards their interdependence, a clear understanding of either one might allow a better explanation of the properties of both. The CDW phase is of greater importance for this work, nevertheless, for the sake of completeness a brief introduction to the scientific state regarding superconductivity is given.

2.4.1. Charge density wave order

One of the main ordering features in CsV$_3$Sb$_5$ regards an unconventional charge density wave below $T_{CDW} = 94$ K and its interaction with the observed superconductivity. While CDW ordering is a rather old phenomenon, its actual understanding is mostly comprised in 1D and lacks clear quantitative predictions in the 3D and even 2D cases. A general overview of the driving origins is given next, before introducing the special case of CsV$_3$Sb$_5$. For a more detailed description of CDWs, the reader is referred to the works of Georg Grüner "Density Waves in Solids" [66].

General picture

As a starting point, we consider the simplest case of an emerging CDW to explain its general shape, before presenting different microscopic origins. Thus we look at a linear chain of atoms in a 1D metal, regularly spaced by the lattice constant a, as depicted in Fig. 2.4.1(a).

The electron density is connected to the atom position, displaying uniform behavior, while the electron bands are half filled to ε_F. This situation is depicted in Fig. 2.4.1(a). In panel (b), we now introduce a sinusoidal modulation of the charge density, in the form of:

$$\rho(\mathbf{r}) = \rho_0(\mathbf{r}) \left[1 + \rho_1 \sin(\mathbf{q}_0 \mathbf{r} + \phi)\right], \tag{2.1}$$

with the starting electron density $\rho_0(\mathbf{r})$ in the unperturbed case, ρ_1 the amplitude, $\mathbf{q}_0$ the wavevector, and ϕ the phase of the electron density modulation. This wave-like pattern leads to each ion perceiving a different electric potential, consequently moving them to a new equilibrium position. This results in a periodic lattice modulation given by

$$p_i = p_0 cos(i|\mathbf{q}_0|a + \phi), \tag{2.2}$$

with p_i the position of the i-th ion and the amplitude of displacement p_0, which is usually small compared to the lattice constant a. This situation can also be reversed by using this modulation of the ion position as a starting point, which would result in the electron density trying to screen the new ionic potential, reproducing the density modulation as described in Eq. 2.1. We therefore can conclude that a CDW phase is always accompanied by a structural modulation and vice versa. The microscopic origin, stabilizing this formation against the Coulomb forces, is not clear from the beginning, since either the electronic system or ion interaction of the lattice can be responsible for the starting modulation.
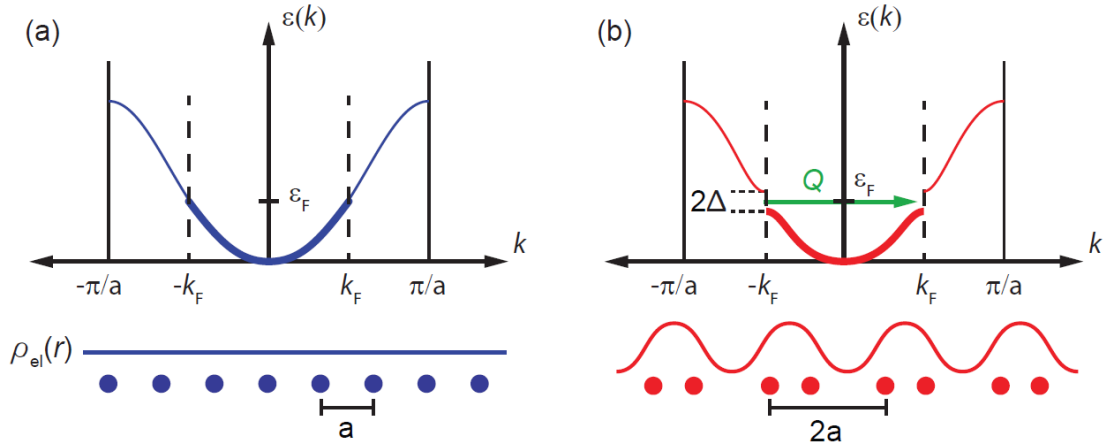
Figure 2.4.1.: Schematic drawing of a CDW and accompanying lattice distortion according to the Peierls theorem. (a) Linear chain of atoms in a 1D metal with half-filled bands. (b) Modulation of either the charge density or the periodic distortion of ion positions can become energetically favorable if the resulting backfolding leads to the emergence of an energy gap 2Δ being larger than the elastic strain on the charges. Taken from [67].

A well-known model describing qualitatively most characteristics of a CDW in a 1D metal was proposed by Peierl in 1930, revolving around a so-called Peierls transition [68]. The principle idea is that, if we consider electron-phonon coupling and introduce a modulation of electron density and lattice as described beforehand in a 1D metal, the unit cell is enlarged to $2a$ and hence, due to backfolding of the energy bands and accompanying anti-

crossing, a gap opens at the Fermi surface (upper part of Fig. 2.4.1(b)). This new structure is stable if the energy gain stemming from the gap in the electronic system is large enough to compensate for the energy costs of the Coulomb interaction. Therefore, the metallic chain of atoms is turned into an insulator. As visualized with a green arrow, the periodicity of the modulation is given by the ordering vector $Q = 2\mathbf{k}_F = \pi/a$ in the case of half-filled bands as a result of perfect nesting, thus the periodicity depends on the band filling and the shape of the Fermi surface. Usually, the charge modulation yields a non-matching periodicity with respect to the original lattice and is therefore incommensurate. This also points towards the importance of the effective nesting vector magnitude as a driving force of the transition.

A Peierls transition to a CDW can be described quantitatively by a mean-field approximation in the case of a 1D electron-lattice system in the weak coupling limit. We then can obtain the well-known BCS relation:

$$2\Delta(0) = 3.52 k_B T_0, \tag{2.3}$$

with the zero temperature gap size $\Delta(0)$ and the mean field transition temperature T_0. The understanding of the driving forces for such a phase transition is limited here by the dimensionality of the system, as well as the coupling strength. If we expand the dimensions of the electronic system, the probability to find a stable CDW phase decreases since one specifically needs large parallel regions on the Fermi surface to promote strong nesting. So in a 2D or 3D material in the weak coupling limit the shape of the Fermi surface is of exceptional importance, which can be probed by ARPES. If we move to the strong coupling limit, the Peierl model fails. In this scenario, one finds much larger energy gap sizes, larger distortion amplitudes, and smaller coherence lengths as compared to the weak coupling limit. The connection given by Eq. 2.3 is then not valid anymore, the ratio of energy gap and mean-field transition temperature yields much higher values. Even though the electronic system is still the origin of the phase transition, a strong coupling CDW tends to be more appropriately described within a local-chemical-bonding picture. Here, non-linear electron-lattice interactions lead to the distortion of the lattice by the formation of pairs and clusters, consequently resulting in much larger atomic displacements and higher electron density amplitudes. This scenario is much more likely to produce a commensurate CDW order, in contrast to the weak coupling limit in higher than 1D, which is intimately connected to the shape of the Fermi surface. This clear connection of the latter to the $\mathbf{k}$-space gives a simple explanation of the resulting long coherence length and incommensurate periodicity with respect to the original lattice. The energy gain then manifests itself mostly near the nested Fermi surface, whereas the strong coupling CDW displays its energy gain over a much larger portion of the BZ.

Charge order in CsV$_3$Sb$_5$

The most pronounced ordering phase in AV$_3$Sb$_5$ (A = K, Rb, Cs) is a symmetry-breaking, commensurate charge density wave, displayed in all compounds' unconventional behavior. The observed ordering temperature in CsV$_3$Sb$_5$ sits at approximately $94\,\mathrm{K}$ [64] and was

verified in several measurements using upon others STM [69, 70, 53], ARPES [34, 71, 72], and X-ray experiments [29, 73]. A 2×2 charge modulation in each kagome layer was resolved, unclear findings regard a c-axis modulation yielding either $2 \times 2 \times 2$ [70, 32] or $2 \times 2 \times 4$ [74, 29] superstructure, its true nature is still under debate to date. Two potential distortions in the kagome plane are probable as "breathing" modes (Fig. 2.4.2), either a Star of David (SOD) or an inverse Star of David (tri-hexagonal, iSOD), with the latter being resolved in STM [53, 32]. Interestingly, Xiao *et al.* were able to manipulate the CDW order from $2 \times 2 \times 2$ to $2 \times 2 \times 4$ during the cooling process, by slow- or fast-cooling, respectively [75]. This hints towards only small differences in the energy minima of the respective superstructure, with $2 \times 2 \times 2$ being slightly more energetically favorable. Convincing x-ray diffraction measurements were performed by Stahl *et al.* [76], observing the sharp order-disorder transition at $94\,\mathrm{K}$ from the pristine $1 \times 1 \times 1$ to a $2 \times 2 \times 4$ structure and a following second order-order transition to a $2 \times 2 \times 2$ below $\approx 60\,\mathrm{K}$. The most probable configurations are staggered, but shifted layers of iSOD or SOD patterns without mixing of the two types of distortions. The temperature of the second order-order transition is accompanied by anomalous behavior in the charge order at $60 - 70\,\mathrm{K}$ measured by muon-spin relaxation (μSr) [77], transport [78], and Raman measurements [79]. To date no consensus on the origin of the second transition has been reached.

(a)   Star of David (SoD)   (b)   inverse Star of David (iSoD)
                                                            (tri-hexagonal)

b

a   ● Sb   ● V
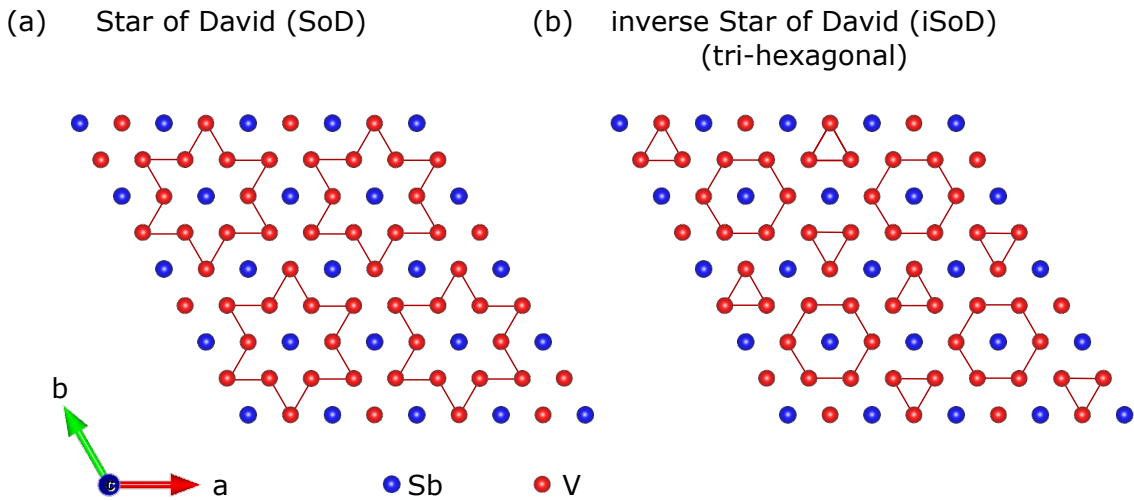
Figure 2.4.2.: Structural distortion of the kagome lattice in either a Star of David (a) or inverse Star of David (b) superlattice. The distortions of the V-atoms forming the kagome structure are small, its closest neighbors are marked with red bonds.

Extensive studies were conducted to reveal the driving force of the CDW order. Several of the published results point towards an electronically driven scenario related to the M-points and their VHs [71]. These divergences in the density of states yield a nesting instability via a vector connecting the Fermi surfaces between the M-points [9]. Clear signs of this scenario being relevant are given by the reduction of the density of states upon entering the CDW at the Fermi surface, with localized gaps opening at the M point [34, 80]. No gaps were observed around Γ [72]. The observed gap values are considered to be at approximately $20\,\mathrm{meV}$ according to ARPES [34] and STM measurements [32]. The momentum dependence of the energy gap and its highest value being localized at the nesting

points draw a clear picture of an electronic nature in the weak-coupling limit. In contrast to these observations, infrared spectroscopy observed clear fingerprints of an energy gap having a 4 times larger value [81, 82], leading to some controversy of the final gap structure and the coupling picture most appropriate for these materials.

As a last unconventional characteristic of the dominant ordering phase in CsV_3Sb_5, several fingerprints in experimental data are pointing to time-reversal symmetry breaking (TRSB) in the CDW phase. This is rather intriguing for a non-magnetic material. The putative chiral character of the charge ordering phase has been discussed in the literature rather extensively, after the first observation in STM dI/dV-mapping measurements under the influence of an external magnetic field [69]. There, the intensity of the three charge ordering nesting vectors in CsV_3Sb_5 was observed to differ in a non-trivial way, defining a chirality of the CDW order. Upon applying a magnetic field along the c-direction the chirality changes from clockwise to anti-clockwise depending on the sign of the field. This change in the response function breaks the Onsager reciprocal relation, which connects the two functions of a time-reversal preserving system under $+B$ and $-B$ via an operator. Its breaking indicates the TRSB in this kagome material without an intrinsic magnetic field. Additionally, strong evidence of TRSB was observed by two groups using muon spin relaxation (μSR) spectroscopy on either KV_3Sb_5 [83] or CsV_3Sb_5 [77]. In both cases, very small local magnetic fields emerged right below T_{CDW} strongly suggesting its origin to be stemming from the TRSB. The STM-findings could not be reproduced consistently by x-ray diffraction measurements under magnetic fields [76], pointing rather towards a result from twinning between layers than TRSB, but no definitive conclusions can be made from this point of view. As a last example towards TRSB, a giant anomalous Hall effect concurrent with the CDW order was observed with contributions of the intrinsic Berry curvature and extrinsic impurity scattering. This can also also be connected to putative TRSB in CsV_3Sb_5 [54].

2.4.2. Superconductivity

Superconductivity was observed in all compounds of AV_3Sb_5 with the highest T_c at $2.5\,K$ in CsV_3Sb_5 [17]. The corresponding pairing symmetry is crucial to explain the mechanism leading to superconductivity. Due to the various unconventional properties of the CDW like its complex gap structure or TRSB, and the simple connection between T_{CDW} and T_c during pressure, an unconventional nature of the superconducting phase is possible [9]. The pressure dependence shows a common behavior for all three compounds of AV_3Sb_5, as apart from the competition of charge order and Cooper pairing at low pressures, the T_c exhibits two distinct domes when investigating a broader pressure regime [84, 64]. Using X-ray scattering, these changes to the phase transition are identified to be a manifestation of pressure-induced changes to the band structure [85]. It is quite interesting that the peaks of T_c are connected to either an anomaly of T_{CDW} and the magnitude of the magnetoresistance at around $60\,K$ or the vanishing of T_{CDW} altogether. This increase in T_c displays a strong resemblance to the case of the doped Fe-based superconductor $Ba(Fe_{1-x}Co_x)_2As_2$, where quantum critical fluctuations potentially lead to an enhancement of the superconducting

transition temperature [86]. Experimental verification of the existence of quantum critical fluctuations is still needed, to clarify these observations.

The superconducting gap has the potential to allow some conclusions about the nature of the present superconducting state. In KV_3Sb_5 and CsV_3Sb_5, multiple similar superconducting gaps have been found, allowing the conclusion of the pairing interaction stemming from the intrinsic band structure of the AV_3Sb_5 compounds [53, 36, 87]. Yet, the question if it's fully gapped [74, 87] or hosts gap nodes [53, 88] cannot be answered at the moment. It is also still under debate whether the pairing wavefunction is of singlet [74] or triplet [78] nature. Therefore, several important aspects of the superconducting state are still not understood.

3. Methods and experiment

This chapter is a brief summary of the experimental methods with their physical concepts and the following application during the work of this thesis. First, an insight into the theoretical basis of polarization-resolved Raman scattering is given, covering mainly the basic interaction of light with the lattice and electronic system. Some examples of expected spectral shapes will be presented. Second, the conventional experimental setup used for the first part of this thesis will be described. Third, crucial fitting procedures and the preparation and characterization of the samples described in chapter 2 will be introduced. A separate chapter 5 will be devoted to the description of the setup for tip-enhanced Raman scattering. The overview given here is by no means a complete picture of Raman spectroscopy on correlated materials, a more thorough analysis was written by Devereaux and Hackl [89].

3.1. Inelastic light scattering

3.1.1. Theory of Raman scattering

Raman scattering describes the inelastic scattering of an incoming photon on a target material, producing a new outgoing photon with different energy. The starting point in understanding Raman spectroscopy is the Born-Oppenheimer approximation, where we assume the electronic and nuclear motion to be separated. This is reasonable as a consequence of the large mass ratio between electrons e and the nucleus N: $\frac{m_e}{m_N} < 1860$. Due to these differences in mass, the movements of electrons are much faster than those of heavy atomic nuclei. Thus, we can assume the electronic wavefunction to be dependent on the position of the nucleus, but not on their velocity, and also that the nuclear motion only feels a blurred potential of the fast-moving electrons. We can then write the wavefunction in the form

$$\Psi_{\text{total}} = \Psi_{\text{electronic}} \Psi_{\text{vibration}} \Psi_{\text{rotation}} \tag{3.1}$$

and following this the energies of each type of motion:

$$E_{\text{total}} = E_{\text{electronic}} + E_{\text{vibration}} + E_{\text{rotation}}. \tag{3.2}$$

This separation gives rise to electronic and vibrational quantum numbers. In the case of an incoming oscillating electric field, due to this mass difference and the following separation of electrons and nuclei, only the electronic cloud is driven to an oscillation. As a consequence of coupling between electrons and phonons, spins, and/or themselves, energy can be transferred from the initial excitation to these other systems. After such a partial trans-

fer of the electron cloud energy, the system can relax under the emission of an outgoing photon with the new cloud energy. Similar to the initial excitation of the electrons, only the oscillation of the electronic cloud can lead to the emission of new outgoing photons. Thus, in contrast to optical conductivity with only one dipole transition, the basic principle of Raman scattering revolves around two dipole transitions. For now, the most simplistic picture is sufficient: We begin with the electronic system in an initial state $|I\rangle$ with energy E_I as depicted in Fig. 3.1.1. The system is then excited by an incoming photon with energy ω_i, momentum $\mathbf{k}_i$, and polarization $\mathbf{e}_i$ to a new virtual state $|\nu\rangle$. Since this state is unstable, by the creation or destruction of a low energy excitation of the system, having energy Ω and momentum $\mathbf{q}$, it can decay quickly to a second intermediate state $|\nu'\rangle$. From there the system can relax to the final state with energy E_F under the emission of a scattered photon, described by ω_s, $\mathbf{k}_s$, and $\mathbf{e}_s$. Due to energy and momentum conservation, we can state:

$$\Omega = \omega_i - \omega_s \tag{3.3}$$

and

$$\mathbf{q} = \mathbf{e}_i - \mathbf{e}_s. \tag{3.4}$$

The incoming photon energy is usually in the visible wavelength region, having $\hbar\omega_i \geq 2\,\text{eV}$. The energy Ω is analyzed in an inelastic light scattering experiment as the Raman shift, giving the value of transferred energy to the system. Energy-wise, its scales are far smaller than incoming and scattered light energies ($\hbar\Omega \ll \hbar\omega$), giving insights into the low energy regime of only several meV up to approximately $1\,\text{eV}$. The transition rate of an inelastic scattering event taking place is usually very low with only a ratio of 1 to 10^7 incoming photons. By tuning the incoming light energy close to the transferred energy values, resonance effects come into play, increasing the transition probability by several orders of magnitude. This is called resonance Raman spectroscopy.
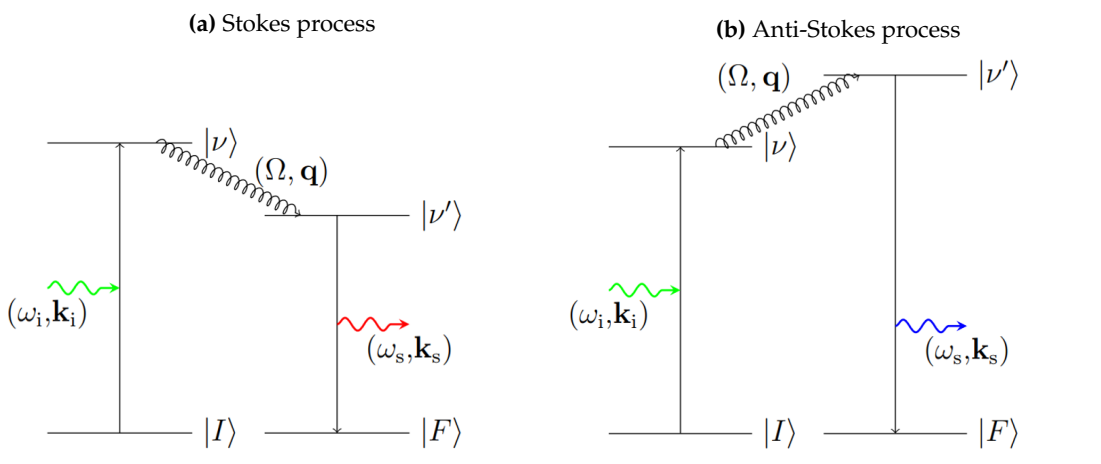

Figure 3.1.1.: Energy diagram of the Stokes and anti-Stokes processes relevant for inelastic light scattering. Scheme adopted from [90].

The relation of Ω to the initial photon energy ω_i gives the name Stokes process for $\omega_i > \omega_s$

or anti-Stokes for $\omega_i < \omega_s$. The latter needs the contribution of additional energy and has consequently a reduced excitation probability by a factor $\exp\{-\beta\Omega\}$. The ratio of Stokes and anti-Stokes intensity enables therefore the determination of the temperature on the investigated sample, which will be taken to advantage later. The excited Raman processes are confined to $|\mathbf{q}| \approx 0$, due to the dispersion of light [91]. The two dipole transitions over virtual and real energy states also lead to selection rules of the allowed transitions, dependent on incoming and outgoing polarization. These selection rules are going to be discussed further in the next section.

The transferred energy to the system allows various excitations like phonons, magnons, orbitons, and electrons. Here, we give a closer look at the electronic Raman effect, governing the measured cross-section of scattered photons on electrons in solids. Experimentally, one tracks the number of scattered photons per second $\dot{N}(\omega, T)$, described via the differential cross section:

$$\dot{N}(\omega, T) \propto \frac{\partial^2 \sigma}{\partial\Omega\partial\omega_s} = \frac{\hbar r_0^2 \omega_s}{\omega_i} \cdot \mathcal{R}, \tag{3.5}$$

where $r_0^2 = \mathrm{e}^2/4\pi\epsilon_0 mc^2$ is the Thompson radius and $\mathcal{R}$ the transition rate. In simple words, $\dot{N}(\omega, T)$ is given by the probability of an incident photon with ω_i being scattered into the solid angle Ω to $\Omega + d\Omega$ and the frequency ω_s to $\omega_s + d\omega_s$. The transition rate is determined by the Fermi golden rule, as:

$$\mathcal{R} = \frac{1}{\mathcal{Z}} \sum_{I,F} \mathrm{e}^{-\beta E_I} |M_{F,I}|^2 \delta(E_F - E_I - \hbar\omega). \tag{3.6}$$

$\mathcal{Z}$ denotes here the partition function, E_F and E_I are the energies of the final and initial state, and $\beta = 1/k_\mathrm{B}T$. $M_{F,I} = \langle F| M |I\rangle$ denotes the matrix element transitioning the initial state via the effective light scattering operator M to the final state and contains the information of all participating states, as well as the polarization and energy of incoming and scattered light. To continue, several simplifications and assumptions are necessary, the reader is for a closer discussion referred to [89]. One finally arrives at the Raman effective density-density correlation function or so-called Raman response $\tilde{S}(\mathbf{q}, i\Omega)$:

$$\tilde{S}(\mathbf{q}, i\Omega) = \sum_I \frac{\mathrm{e}^{-\beta E_I}}{\mathcal{Z}} \int d\tau \, \mathrm{e}^{i\Omega\tau} \langle I| T_\tau \tilde{\rho}(\mathbf{q}, \tau)\tilde{\rho}(-\mathbf{q}, 0) |I\rangle, \tag{3.7}$$

where τ is the complex time. This can be transitioned to real frequencies with the analytic continuation $i\Omega \to \Omega + i0$, which connects $\tilde{S}$ to the cross section by:

$$\frac{\partial^2 \sigma}{\partial\Omega\partial\omega_s} = \frac{\hbar r_0^2 \omega_s}{\omega_i} \cdot \tilde{S}(\mathbf{q}, i\Omega \to \Omega + i0). \tag{3.8}$$

From these expressions, one can draw the connection between the Raman response $\tilde{S}$ to the effective density susceptibility $\tilde{\chi}$:

$$\tilde{S}(\mathbf{q}, \Omega) = -\frac{1}{\pi}(1 + n(\Omega, T)) \, \mathrm{Im}[\tilde{\chi}''(\mathbf{q}, \Omega)]. \tag{3.9}$$

$n(\Omega, T)$ is the Bose-Einstein distribution and $\tilde{\chi}''(\mathbf{q}, \Omega) = \langle[\tilde{\rho}(\mathbf{q}), \tilde{\rho}(-\mathbf{q})]\rangle_\Omega$. Thus, the Ra-

man response is given for non-interacting electrons as a two-particle effective density cor-
relation function $\tilde{\chi}''$ and can be directly connected to the experimentally measured count
rate $\dot{N}$.

3.1.2. Selection rules

Raman scattering is characterized by certain selection rules, which result from the combi-
nation of two dipole transitions and can be generally classified using group theory argu-
ments. The charge density fluctuations emerging under light illumination are modulated
along directions oriented correspondingly to the electric field of incoming light, while also
obeying the symmetry rules of the underlying lattice in their scattering polarization. Every
scattering process involves two dipole transitions, as discussed before between the states
$|I\rangle \to |\nu\rangle$ and $|\nu'\rangle \to |F\rangle$, giving away information of different crystal symmetries by the
combination of incoming and scattered polarization. The polarization sets used in the ex-
periments during this work are displayed in Fig. 3.1.2, with the six combinations xx, $x'x'$,
RR, xy, $x'y'$, and RL. The laboratory axis x is here parallel to the a-axis of the sample. The
polarizations x' and y' are rotated by $45°$ to the respective x and y polarization directions,
yielding $x' = \sqrt{2}/2(\hat{x} + \hat{y})$ and $y' = \sqrt{2}/2(\hat{x} - \hat{y})$. Circular polarizations in right and left
direction are defined as $R, L = \sqrt{2}/2(\hat{x} \pm i\hat{y})$, respectively.
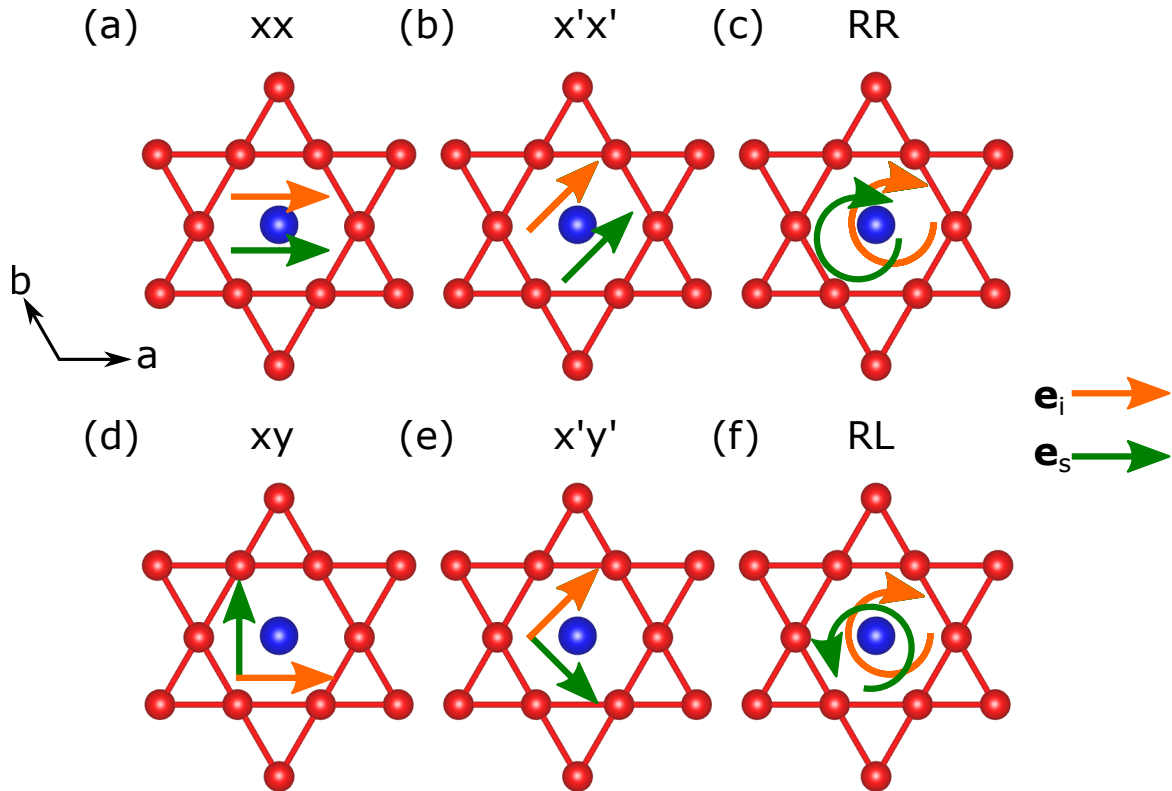

Figure 3.1.2.: Six different polarization combinations in a kagome structure. The a- and b-axes
are defined with respect to the kagome layer and the polarization vectors with
respect to these axes. Incoming polarization is displayed in orange and scattered
in green.

A convenient approach to discuss projected symmetries in the Brillouin zone (BZ) with

respect to the incoming and scattered polarization is via the 3×3 matrix called Raman tensor $\hat{\alpha}$. For a given Raman tensor one can estimate the resulting projected intensity of a set of polarization $(\mathbf{e}_i, \mathbf{e}_s)$ by:

$$I_{is} \propto |\mathbf{e}_s^* \cdot \hat{\alpha} \cdot \mathbf{e}_i|^2. \tag{3.10}$$

The D$_{3d}$ point group represents the main interest of this thesis, having the following Raman vertices:

$$A_{1g} = \begin{pmatrix} a & 0 & 0 \\ 0 & a & 0 \\ 0 & 0 & b \end{pmatrix}, \qquad A_{2g} = \begin{pmatrix} 0 & c & 0 \\ -c & 0 & d \\ 0 & d & 0 \end{pmatrix}, \tag{3.11}$$

$$E_g^{(1)} = \begin{pmatrix} c & 0 & 0 \\ 0 & -c & d \\ 0 & d & 0 \end{pmatrix}, \quad \text{and} \quad E_g^{(2)} = \begin{pmatrix} 0 & -c & -d \\ -c & 0 & 0 \\ -d & 0 & 0 \end{pmatrix}. \tag{3.12}$$

With Eq. 3.10, we can write down the according intensities of each polarization combination in Tab. 3.1.1, in addition to the projected symmetries.

Table 3.1.1.: Raman intensities and their projected symmetries for different sets of polarization.

	xx	$x'x'$	RR	xy	$x'y'$	RL
Intensity	$a^2 + d^2$	$a^2 + d^2$	$a^2 + c^2$	$c^2 + d^2$	$c^2 + d^2$	$2d^2$
Symmetry	$A_{1g} + E_g^1$	$A_{1g} + E_g^2$	$A_{1g} + A_{2g}$	$A_{2g} + E_g^2$	$A_{2g} + E_g^1$	$E_g^1 + E_g^2$

We quickly can see that each set of polarization yields the sum of two different symmetries. Thus, in order of extracting pure symmetries of the Raman response a linear combination of the established polarization configurations is necessary. We can calculate the pure symmetries as:

$$I_{\mathrm{A}_{1g}} = \frac{1}{3} \left[(xx + x'x' + RR) - \frac{1}{2}(xy + x'y' + RL) \right] \tag{3.13}$$

$$I_{\mathrm{A}_{2g}} = \frac{1}{3} \left[(xy + x'y' + RR) - \frac{1}{2}(xx + x'x' + RL) \right] \tag{3.14}$$

$$I_{\mathrm{E}_g^1} = \frac{1}{3} \left[(xx + x'y' + RL) - \frac{1}{2}(xy + x'x' + RR) \right] \tag{3.15}$$

$$I_{\mathrm{E}_g^2} = \frac{1}{3} \left[(xy + x'x' + RL) - \frac{1}{2}(xx + x'y' + RR) \right] \tag{3.16}$$

$$\tag{3.17}$$

Due to the connection between the polarization of the light and its **k**-dependent transition rate of the electronic system, we can effectively probe excitations at certain regions of the Brillouin zone with these polarization combinations. This makes polarization-controlled Raman spectroscopy a powerful approach to studying highly correlated electronic systems.

In order to evaluate these momentum dependencies, one can derive the Raman ver-

tices phenomenologically from the lattice symmetry and periodicity via a group theory approach. In accordance with the description by Djurdjic-Mijin *et al.* [92] for $1T$-TaS$_2$, one can utilize Brillouin zone harmonics as a set of functions reflecting the lattice structure [93]. $1T$-TaS$_2$ belongs to the same point group as Fe$_3$Sn$_2$ and CsV$_3$Sb$_5$, hence, similar calculations need to be performed. Here, trigonometric trial functions, e.g a sine function for odd parity representation and cosine for even parity is used. By combining trial functions, the periodicity of the Brillouin zone can be simulated. First, $F = \cos(k_x a)$ acts as a trial function with a being the in-plane lattice constant, leading to the basis functions of A_{1g} and E_g^1:

$$\Phi_{A_{1g}^{1st}}(\mathbf{k}) = \frac{1}{3}\left[\cos(k_x a) + 2\cos\left(\frac{1}{2}k_x a\right)\cos\left(\frac{\sqrt{3}}{2}k_y a\right)\right], \tag{3.18}$$

$$\Phi_{A_{1g}^{2nd}}(\mathbf{k}) = \frac{1}{3}\left[\cos(2k_x a) + 2\cos\left(k_x a\right)\cos\left(\sqrt{3}k_y a\right)\right], \tag{3.19}$$

$$\Phi_{E_g^1}(\mathbf{k}) = \frac{2}{3}\left[\cos(k_x a) - \cos\left(\frac{1}{2}k_x a\right)\cos\left(\frac{\sqrt{3}}{2}k_y a\right)\right]. \tag{3.20}$$

The second projection describes only one of two basis functions of the two-dimensional representation of E_g. The second basis function can be derived via symmetry arguments, yielding:

$$\Phi_{E_g^2}(\mathbf{k}) = 2\sin\left(\frac{1}{2}k_x a\right)\sin\left(\frac{\sqrt{3}}{2}k_y a\right). \tag{3.21}$$

The resulting squared Raman vertices are plotted in Fig. 3.1.3 with the high symmetry points marked as black dots.
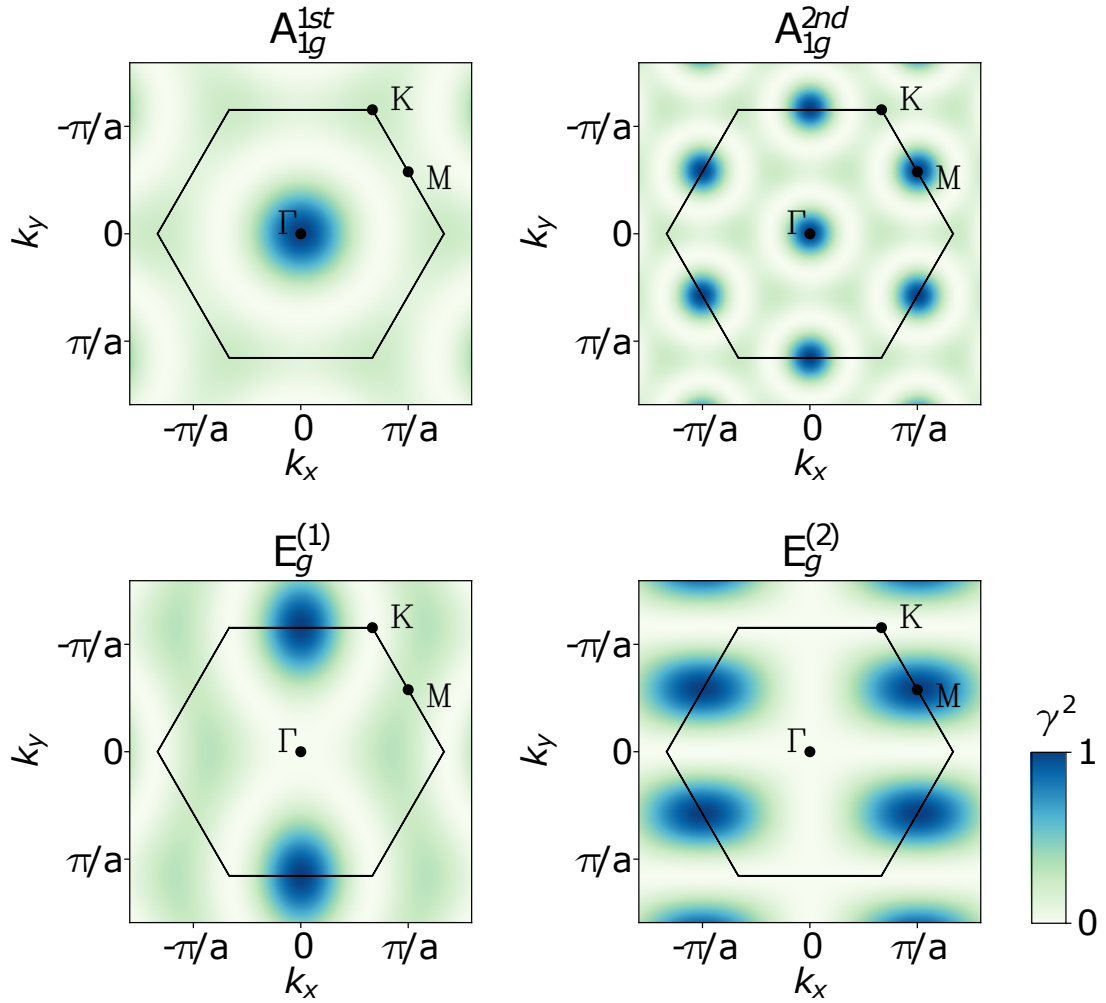
Figure 3.1.3.: Squared Raman vertices for the investigated symmetries. A_{1g} mainly projects the Γ-point but also shows contributions at the M-point, when doubling the unit cell in real space. E_g shows contributions mainly around the M-point for both sets of basis functions.

3.1.3. Characteristic signatures of Raman processes

Moving on from the selection rules, which allow the differentiation of certain regions in the Brillouin zone, some idealized examples of Raman features shall be described now, illustrated in Fig. 3.1.4. Through the knowledge of these response pictures, one can identify different physical properties and map them to their predominant **k**-values. One should keep in mind that the actual Raman measurements are a superposition of several distinct features at their corresponding energy and a careful evaluation of the temperature dependence is often necessary for clear identification.
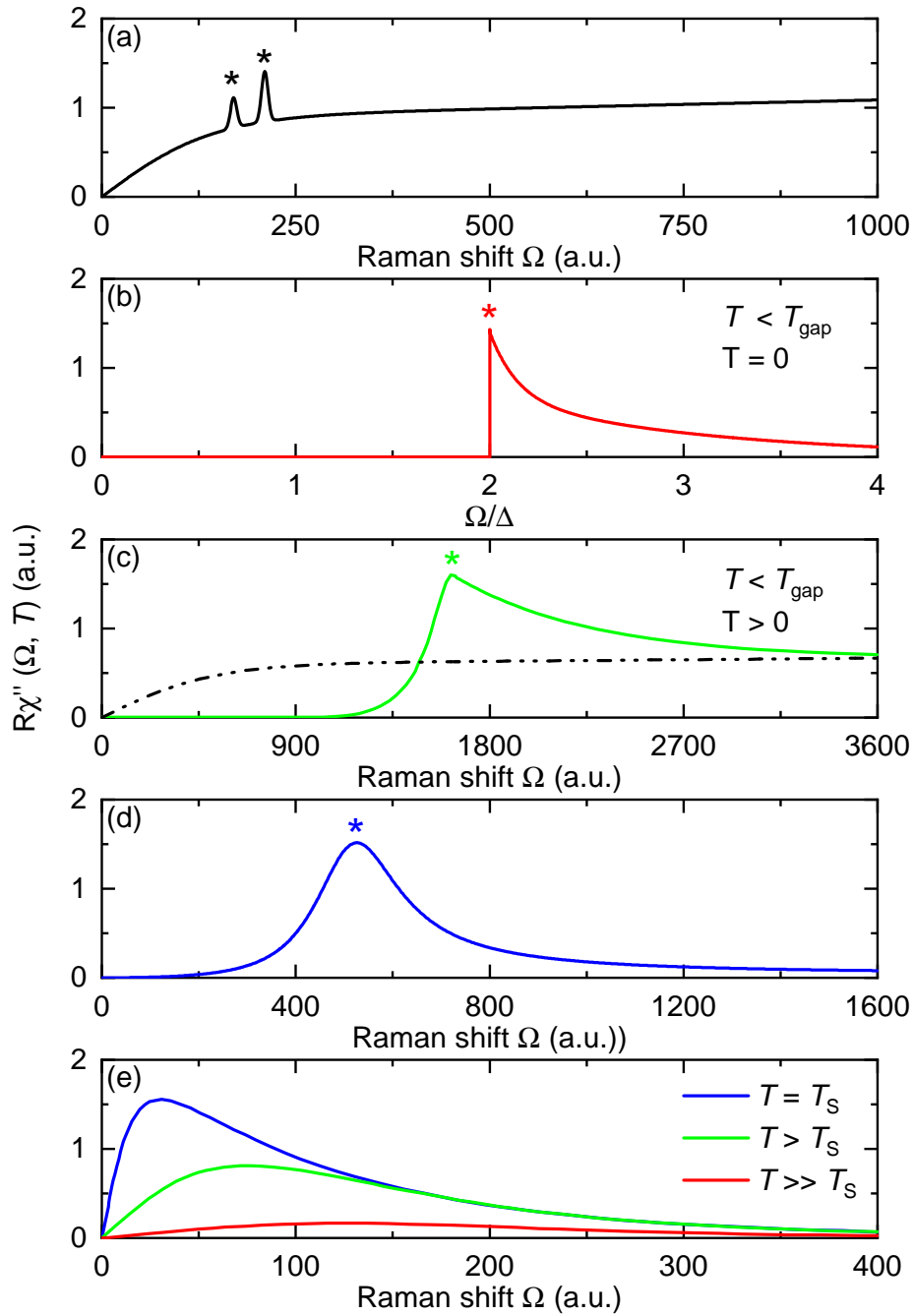
Figure 3.1.4.: Phenomenological idealized Raman spectra of different physical processes. (a) Electronic continuum as a manifestation of particle-hole excitations and two peaks marked with black asterisks stemming from phononic modes. (b) Opening of an energy gap at the zero temperature and in the collision-less limit yields a square-root-like singularity at 2Δ (red asterisk). (c) For temperatures higher than zero but below T_{gap}, the energy gap shape is thermally softened. Here, the distinct shape of the electronic continuum (dashed-dotted black line) is being redistributed, shifting spectral weight to higher energies, marked with a green asterisk. The spectra finally merge for high energies. (d) Two-magnon peak being excited for example in some antiferromagnetic materials, as described in [94]. (e) Fluctuations of incipient order above the transition temperature manifest themselves in an increasingly strong build-up of spectral weight in the low energy region [95].

The most commonly observed response behaviors by Raman scattering in condensed

matter are the particle-hole excitation continuum and phonons of the crystal, depicted in Fig. 3.1.4(a). Since all other Raman processes and their corresponding intensity are superimposed with the electronic continuum, a phenomenological description of the latter is necessary to differentiate the individual response functions. This can be done with:

$$\chi''(\Omega) = a \tanh |\frac{\Omega}{c}| + b\Omega, \tag{3.22}$$

where, a, b, and c are fit parameters. Such a mentioned superposition is here already visible in the form of two peaks, representing phononic modes. These modes are generally only a few wavenumbers wide and display a symmetric shape, which can be described via a Voigt function to account for the excitation response shape of a Lorentz distribution and the Gaussian distribution of the spectrometer resolution. This allows the extraction of changes to the peak energy and linewidth with respect to the temperature. Since these modes can couple to the electronic and magnetic system, they can be used as powerful probes thereof, while also giving insights into the dynamics of the lattice and its symmetry.

Upon cooling, the opening of an energy gap can lead to an energy minimization of electrons at the Fermi level and thus becomes more stable than the previous state. Panel (b) illustrates an energy gap in the collision-less limit for zero temperature, depicting no potential excitations below the gap energy. As an example, in a superconducting transition, this energy value would correspond to the binding energy 2Δ of Cooper pairs. When this energy is surpassed, the pairs can be broken and excitations become available, leading to the characteristic pair-breaking peak. If we switch on the temperature as well, one expects a behavior as illustrated in panel (c). The sharp increase in spectral weight is softened due to the additional thermal energy. The particle-hole continuum shape is then redistributed, with spectral weight being shifted to higher energies. As the smaller slope of the green curve compared to the red curve is a manifestation of the softening of the Fermi energy occupation in both energy directions, the crossing point of the electronic continuum and the gapped spectra is here defined as the energy gap. These gaps can originate from several different ordering mechanisms, like already mentioned superconductivity [96], but also for example spin-density waves [37] or charge density waves [97, 98]. Their existence, as well as their dependence on temperature, doping, and pressure, gives far-reaching insights into the ordering phenomena.

On a side note, potential excitations of localized spins in an antiferromagnetically ordered material shall be described. Magnetism is usually strongly connected to the exchange interaction J between localized electrons, which potentially can be excited by Raman scattering via a 2-magnon process. The resulting Raman response is then dominated upon cooling by a continuously hardening peak in the energy region of $3J$, schematically plotted in panel (d). The careful evaluation of the Raman response in La_2CuO_4 [99] and $BaFe_2As_2$ [100] enabled the differentiation between localized and itinerant electrons carrying spin via the existence of a 2-magnon peak or an energy gap opening from a spin density wave, respectively.

Fluctuations of the order parameter can be probed with Raman spectroscopy as well,

giving access to charge [101], orbital [102], and spin fluctuations [37]. The interested reader is referred to a more sophisticated description focusing on the iron-based superconductors (IBS) [103], some basics are presented here as well. The general shape of a fluctuation response is depicted in panel (e), with a hump-like build-up of spectral weight at low energies, which is increasingly rising upon cooling towards a phase transition. The depicted shape is displayed for an IBS, a system in which it was shown to only accommodate fluctuations in B_{1g}-symmetry [104]. As derived by Caprara and co-workers [95] the spectral shape in this symmetry of the contribution stemming from fluctuations coupled to the lattice is given by:

$$\Delta\chi''_{B_{1g}} = \Lambda^2_{B_{1g}} \int_0^\infty dz[b(z - \Omega/2) - b(z + \Omega/2)] \times \frac{z_+ z_-}{z_+^2 - z_-^2}[F(z_-) - F(z_+)] \qquad (3.23)$$

with the Bose function $b(z)$, $z_\pm \equiv (z \pm \Omega/2)(1 + {}^{(z\pm\Omega/2)^2}/\Omega_0^2)$, and

$$F(z) \equiv \frac{1}{z}\left[\arctan\left(\frac{\Omega_0}{z}\right) - \arctan\left(\frac{m}{z}\right)\right]. \qquad (3.24)$$

Ω_0 is a cut-off coming from the coupling of the fluctuations to the lattice and is typically a phonon frequency. $\Lambda_{B_{1g}}$ is the vertex strength in B_{1g}-symmetry, and $m(T)$ is the mass of the collectives modes. The investigation of fluctuations can lead to insights into the ordering mechanism below the phase transition. In a recent study, quantum critical fluctuations were used as probes to investigate the doping-dependent phase diagram of $Ba(Fe_{1-x}Co_x)_2As_2$, suggesting a contribution of quantum fluctuation to the enhancement or formation of superconductivity [86].

3.2. Experimental setup, data analysis, and sample preparation

In this section, the experimental setup facilitating the Raman measurements is described, followed by the procedure to analyze more general aspects of the spectra, including some fitting processes. This is concluded with the general preparation of the samples and the individual characterization of the investigated Fe_3Sn_2 and CsV_3Sb_5.

3.2.1. Optical path

The Raman setup, schematically drawn in Fig. 3.2.1, ensures the quality of the incident excitation beam, the possibility to select the desired polarizations, and a sufficient collection, as well as filtering of the inelastically scattered light. The Raman process starts with either a diode-pumped solid-state laser (Coherent-Genesis MXSLM), emitting light at $\lambda_i = 575\,\text{nm}$, or an Ar^+-Ion laser (Coherent Innova 304C) for five different laserlines in the range of 458 to 514 nm, enabling a resonance analysis. The beams from both laser systems are expanded to approximately 2.5 mm and directed towards a first pinhole system (PH1, 30 μm) for spatial filtering of off-axis beam contributions. This is followed by a prism monochromator

(PMC), which in combination with the following slit system acts as a single-stage spectrometer, removing laser lines stemming from plasma excitations. The beam is redirected with a mirror (M3) and the polarization of the incident beam is selected by making use of a polarizer (P1) and a Soleil-Babinet compensator (SB). This configuration allows the selection of any desired polarization, via the phase shift between the ordinary and extraordinary direction in the two-wedge-system compensator. By calibrating the optical constants, one can achieve clear linear and circular polarization in the sample surface, accounting for elliptical deformations of the spot. For a more detailed description, the reader is referred to [105]. The beam is spatially filtered one more time by a pinhole system (PH2) and subsequently focused and directed onto the sample, utilizing a lens (L1) and an adjustable mirror (M4). The laser power is selected with a $\lambda/2$-plate in front of the polarizer by rotating the beam in relation to the latter. The power is measured with a power meter (PM) after the focusing lens. The laser hits the sample with an approximate angle of incidence $\Theta_l = 66°$. The sample is mounted on a rotatable holder inside a continuous-flow ^{4}He cryostat on the coldfinger. A heater close to the sample in this configuration allows the temperatures to be set in the range from 2 to 350 K, with a vacuum of around 1×10^{-6} mbar. The c-axis of the sample is for all measurements along the z-axis of the laboratory, parallel to the spectrometer axis and perpendicular to the sample surface.

The scattered light is collected by the objective O2 and its polarization is selected using a $\lambda/4$-retardation plate and an analyzer A. The following $\lambda/2$ plate rotates the polarization into the direction of the highest sensitivity of the spectrometer. The light is focused onto the adjustable entrance slit of the spectrometer (Jarrell-Ash 25-100 double monochromator equipped with 2400 gr/mm gratings). The width of the intermediate slit sets the energy resolution of the spectrometer, the latter selects the transmitted wavelength via the rotation of the gratings.

The scattered and wavelength-filtered light is finally focused on the nitrogen-cooled CCD chip, where the number of photons is counted. The measurements were performed by driving through the desired transferred energy range with a selected resolution and step size. The complete spot on the CCD was then integrated for a certain time as a superpixel, yielding the desired count rate $\dot{N}$. This allowed a background correction by using the unilluminated part of the CCD chip. The resulting countrate is now dependent on the Raman shift and needs to be corrected further as described in the next section 3.2.2.
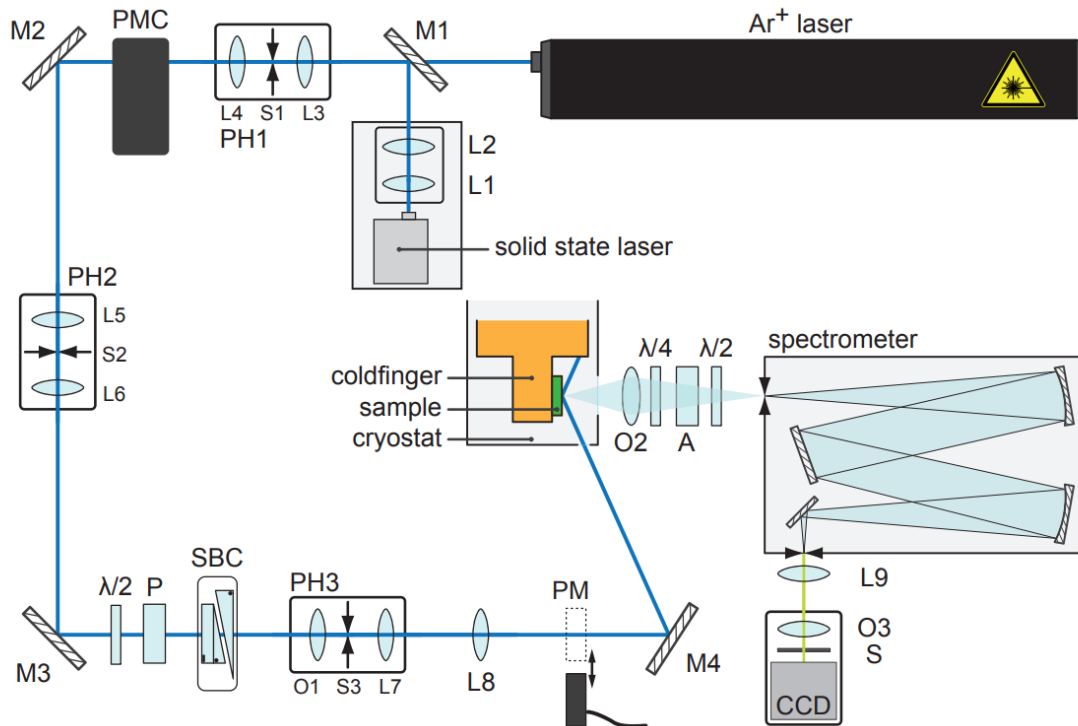
Figure 3.2.1.: Optical setup for polarization selected Raman spectroscopy. Two Laser setups allow the investigation with various laserlines by only minimally changing the optical path. The components for preparing the laser beam and selecting the polarizations are described in the text, as well as the cryogenic environment and the final wavenumber-dependent readout by a CCD camera. The diagram was taken from [106].

3.2.2. Intensity calibration and data analysis

The optical setup enables the counting of wavelength-selected photons, an intensity calibration of this bare number is needed to adjust for the properties of the used setup. This calibration is described next before here relevant peak fitting procedures, as well as the general determination of material-specific optical constants for clean polarizations are presented.

Intensity calibration

In previous sections 3.1.1, the quantity of interest χ'' was connected directly to the differential cross-section, which can be accessed experimentally in the form of the count rate $\dot{N}_{is}$. This count rate at a specific wavelength of the scattered light originates from the illuminated area dependent on the absorbed laser power $P_i = I_i \hbar \omega_i$. The inelastically scattered light is distributed isotropically in the complete room $\Omega = 4\pi$. Thus, the count rate is dependent on the angle of acceptance $\Delta\Omega$, the resolution width $\Delta\omega_s$, and the energy-dependent sensitivity $s(\omega_s)$ of the measurement instrument. With that and the equations regarding the differential cross section Eq. 3.8 and 3.9, we can connect the measured count rate to the Raman susceptibility:

$$R\chi''_{\mathrm{is}}(\Omega, T) = \frac{\dot{N}_{\mathrm{is}}}{P_i \cdot s(\omega_{\mathrm{s}})} \frac{\omega_{\mathrm{i}}^2}{\omega_{\mathrm{s}}\tilde{\omega}} \left[1 - \exp\left(-\frac{\hbar\Omega}{k_B T} \right) \right] \qquad (3.25)$$

The constant R includes temperature and energy-independent factors, such as the angle of acceptance, the resolution of the spectrometer, as well as the ratio of scattering events in the illuminated area. ω_{i} and ω_{s} are the energies of the incident and scattered photons, respectively. The count rate $\dot{N}_{\mathrm{is}}$ has to be divided by the relative sensitivity $s(\omega_{\mathrm{s}})$, which needs to be determined via calibration. Since the CCD detects photons, the laser power has to be divided by the photon energy to reach a numerical quantity. Finally, for arriving at a corrected count rate close to unity, we divide this rate by $\tilde{\omega} = 20000$, leaving the temperature-dependent link between the count rate and the Raman susceptibility.

Raman peak fitting procedure

As already featured in Fig. 3.1.4, Raman measurements give insights into the lattice dynamics via its vibrations and their temperature dependence. To investigate these fingerprints, their corresponding phonon energy and linewidth have to be extracted. Two schematics of commonly observed Raman peaks, generally a manifestation of phononic excitations, are displayed in Fig. 3.2.2. In panel (a), the peak exhibits a symmetric shape, whereas an asymmetry with respect to the electronic continuum is visible in panel (b).
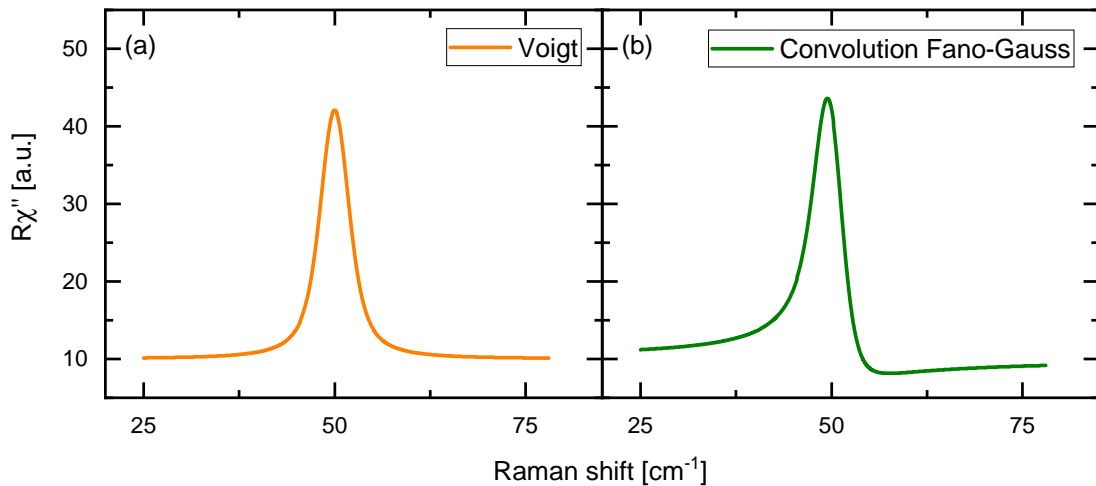
Figure 3.2.2.: Exemplary peak shapes, which are often observed for phononic modes with Raman spectroscopy. A Voigt function describes symmetric peaks well, whereas asymmetric shapes with respect to the electronic continuum are better described with a Fano-function. Similar to the Voigt function, the Fano has to be convoluted with a Gaussian to account for influences by the spectrometer.

The first, symmetric peak can be described by a Voigt function, which is a convolution of a Lorentzian peak shape, explaining the physical excitation process, and a Gaussian to account for the resolution of the spectrometer. This gives the general shape of the intensity

$I(\omega)$:

$$I(\omega) = I_0 + A \cdot \frac{2\ln(2) \cdot \omega_{\mathrm{L}}}{\pi^{3/2} \cdot \omega_{\mathrm{G}}^2} \int_{-\infty}^{\infty} \frac{\mathrm{e}^{-t^2}}{\left(\sqrt{\ln(2)} \cdot \frac{\omega_{\mathrm{L}}}{\omega_{\mathrm{G}}}\right)^2 + \left(2\sqrt{\ln(2)} \cdot \frac{\omega - \omega_c}{\omega_{\mathrm{G}}} - t\right)^2} dt. \qquad (3.26)$$

ω_c represents the peak center, whereas ω_L and ω_G are the linewidths of the Lorentzian and the Gaussian distribution, respectively. A is the peak area, I_0 is a quantity describing a linear background. As we have seen before, Raman spectra display a particle-hole excitation continuum, which is better described phenomenologically with Eq. 3.22. If the background is far from linear, this description of the background was taken.

If we look for example at high electron-phonon coupling materials, one often finds asymmetric shapes due to changes in the excitability of the phonons upon interaction with the electronic continuum. This behavior is then better described by a Fano function [107]:

$$I(\omega) = I_0 \frac{[1 + (\omega - \omega_c)/q\Gamma]^2}{1 + [(\omega - \omega_c)/\Gamma]^2}, \qquad (3.27)$$

with I_0 being a fit parameter, ω_c the peak center, Γ the linewidth, and q as the asymmetry factor. One usually plots $1/|q|$ against temperature, revealing the highest value for the strongest coupling to the electronic continuum. Similar to the symmetric case, the observed peak shape is also influenced by the resolution of the spectrometer, the Fano function has to be therefore convoluted with a Gaussian as well. This has been done already in [108]:

$$I(\omega) = I_0 \frac{2\sqrt{\ln(2)}}{\omega_G \pi^{3/2}} \left\{ B(\omega) - \frac{2q}{q^2 - 1} \cdot C(\omega) \right\} \qquad , \text{with}$$

$$B(\omega) = \int_{-\infty}^{\infty} \frac{\sqrt{\ln(2)} \cdot \frac{\omega_L}{\omega_G} \cdot \mathrm{e}^{-t^2}}{\left(\sqrt{\ln(2)} \cdot \frac{\omega_L}{\omega_G}\right)^2 + \left(2\sqrt{\ln(2)} \cdot \frac{\omega - \omega_c}{\omega_G} - t\right)^2} dt \qquad , \text{and} \qquad (3.28)$$

$$C(\omega) = -\int_{-\infty}^{\infty} \frac{\left(2\sqrt{\ln(2)} \cdot \frac{\omega - \omega_L c}{\omega_G} - t\right) \cdot \mathrm{e}^{-t^2}}{\left(\sqrt{\ln(2)} \cdot \frac{\omega_L}{\omega_G}\right)^2 + \left(2\sqrt{\ln(2)} \cdot \frac{\omega - \omega_c}{\omega_G} - t\right)^2} dt.$$

The fit parameters have the same meaning as in the case of the Voigt function. In the case of very small or no asymmetry, $1/|q|$ becomes very small and the last term of the convolution $C(\omega)$ vanishes, leaving only the Voigt function behind.

Determination of the optical constants

In the employed setup, the incoming light is not perpendicular to the surface for several reasons, mainly for the reduction of the elastic portion close to the laserline. This also leads to a distortion of the laser spot including a difference in the absorption rate and a phase shift at the metal interface of the two polarization components perpendicular or parallel

to the plane of incidence. This is especially important in the circular configurations, as it leads to an ellipsoid polarization in the sample instead of an actual circular shape, weakening the applicability of the selection rules. Since the sixfold symmetry of the here studied kagome materials allows a convenient investigation by utilizing circularly polarized light as well as the possibility of extracting clean symmetries, a brief description of the optical constant determination is presented here. To adjust for the absorption rates, knowledge of the complex index of refraction n_{m} of the metallic sample is essential. To ensure the minimization of anisotropy effects of the crystal, the measurement of the optical constants was performed at a matching geometrical configuration with respect to the following Raman measurements. n_{m} can be determined by the measurement of the interaction of light with a given polarization by the reflection on the sample surface. For convenience, we can define the ratio of reflection coefficients R and the difference in phase shift Δ as

$$P \equiv \tan(\psi) = \frac{\rho_\perp}{\rho_\parallel} \tag{3.29}$$

and

$$\Delta = \chi_\parallel - \chi_\perp \ . \tag{3.30}$$

From here, one can find an expression for these newly defined quantities to be connected to n_{m} with the angle of incidence θ:

$$\frac{\sqrt{n_{\mathrm{m}}^2 - \sin^2(\theta_1)}}{\sin\theta_1 \tan\theta_1} = -\frac{\cos 2\psi + i\sin 2\psi \sin\Delta}{1 + \sin(2\psi)\cos\Delta} \tag{3.31}$$

The angle of incidence is well known to be $66°$, thus one needs to determine R and Δ experimentally. The utilized setup is presented in Fig. 3.2.3(a), reproducing the geometric parameters of the experiment in angle and focus. By selecting a polarization of the incoming light, one can measure the change of intensity depending on the chosen polarization configuration of P2 for the elastically reflected light. An example of a CsV_3Sb_5 sample and its polarization angle dependence at $575\,\mathrm{nm}$ is plotted in panel (b). The resulting behavior is related to the ellipticity of the light and can be fitted using:

$$I(\Phi) = \frac{E_x^2}{2}\cos^2(\Phi) + \frac{E_y^2}{2}\sin^2(\Phi) + \frac{E_x E_y}{2}\sin^2(2\Phi)\cos(\delta) \tag{3.32}$$

This enables the extraction of the x- and y- components of the electrical field (E_x and E_y, respectively), as well as the phase difference between y- and x-components. Since in the utilized setup, the x-direction is parallel to the plane of incidence, we can write $P = \tan(\psi) = E_y/E_x$ and $\Delta = -\delta$. This reveals the optical constants to be $n_{\mathrm{m}} = 2.2504 + i2.0917$ for CsV_3Sb_5 at $575\,\mathrm{nm}$. From the optical constants, one can adjust the Soleil-Babinot compensator in its two degrees of freedom (angle and wedge distortion) to achieve a suitable ellipsoid shape of the polarization, which leads to a circular distribution in and on the sample. A detailed description regarding the calibration and setting of the compensator can be found in [105]. Note, that the absorption coefficients vary with the wavelength, thus a calibration of the compensator via the here described determination of n_{m} has to be performed for each laserline of interest.
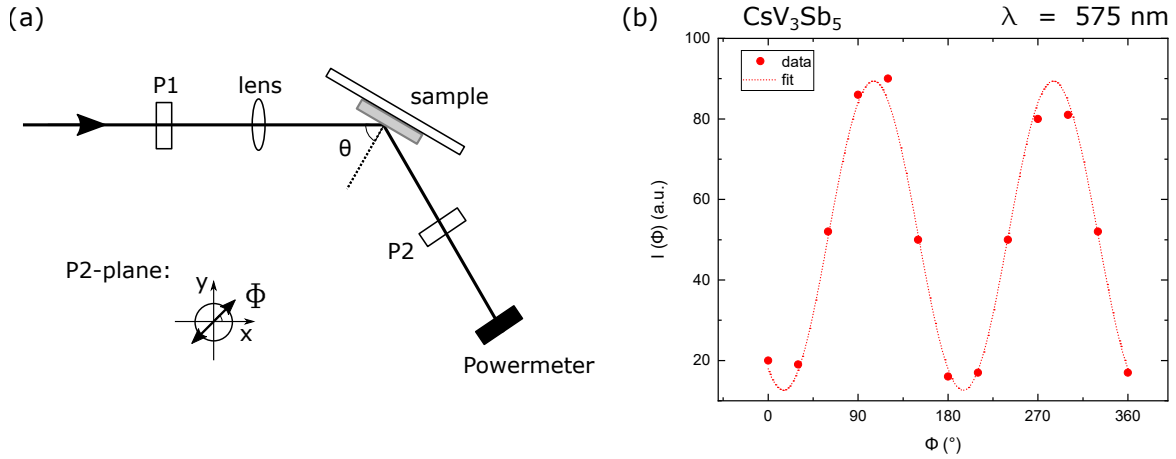
(a)

(b)

Figure 3.2.3.: Determination of the optical constants to ensure clean polarizations. (a) Schematic of the experimental setup extracting the polarization angle dependence via the elastically reflected light. (b) Intensity against angle Φ for CsV_3Sb_5 at 575 nm laser wavelength.

3.2.3. Preparation and characterization of samples

A short introduction to the manufacturing, as well as a characterization of the samples studied during this thesis, is given here. Their mounting and general final preparation before measuring polarization-dependent Raman spectra is described as well.

Fe_3Sn_2

Fe_3Sn_2 single crystals were grown from a pre-synthesized poly-crystalline powder of high purity Fe and Sn, using the chemical transport reaction method. Iodine was used as the transport agent. In two-zone furnaces, the growth process took place inside SiO_2 ampules at temperatures between 730 and 680 K. A resulting single crystal after $4 - 6$ weeks of transport can be inspected in the inset of Fig. 3.2.4 (a). The grown crystals have dimensions of $3 - 5$ mm in ab-plane and a thickness of $20 - 40\,\mu m$.

Electrical resistance, as well as magnetization measurements, were performed (Fig. 3.2.4). A residual resistance ratio of $\rho_{300K}/\rho_{2K} = 29.3$ was obtained, indicating high crystal quality. The green curve in panel (a) depicts the derivative of the resistivity $d\rho/dt$, which has a qualitative change in slope at around 100 K. The high-temperature end of this region is expected to have all spins pointing along the c-axis, the region itself is shaded for visibility. To confirm the spin-reorientation taking place, the temperature dependence of the magnetic susceptibility for in-plane and out-of-plane configurations was measured. This revealed strong anisotropies for the differently aligned magnetic fields. For high temperatures χ_{ab} is only around a third of the susceptibility along the c-axis. The difference vanishes at around 100 to 50 K, with χ_c starting to decrease and χ_{ab} saturating. Thus, the crystal becomes increasingly harder to magnetize along the c-axis, matching well with the presumable spin-reorientation. The resulting crossing point agrees well in its temperature localization with a kink in the resistivity, best seen in the derivative of the latter. We conclude that we can observe the spin-reorientation of these samples in transport and magnetic measurements.
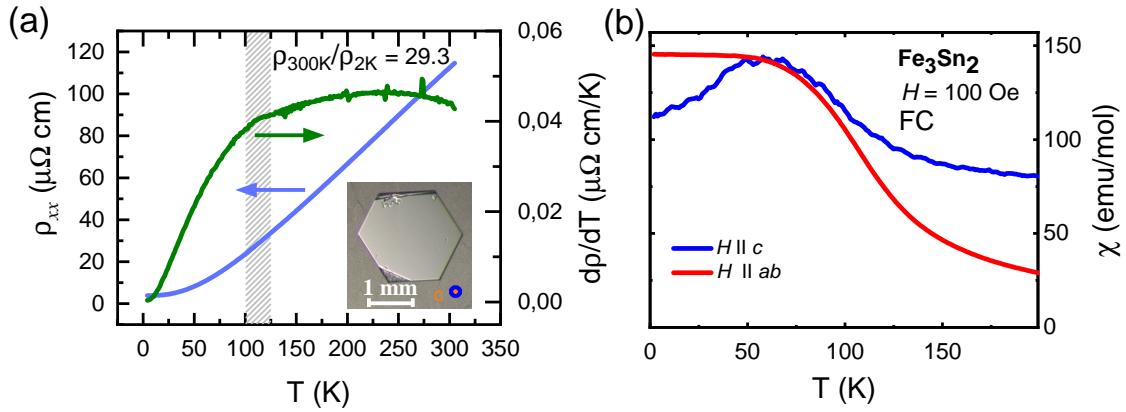
Figure 3.2.4.: Transport and magnetic susceptibility measurements on Fe_3Sn_2. The resistivity and its derivative are displayed in panel (a), including a picture of a single crystal. Panel (b) depicts the anisotropies of in-plane and out-of-plane magnetic susceptibility. Both measurements are able to resolve the signature of the spin-reorientation at around $100\,K$.

CsV_3Sb_5

Via a modified self-flux method, single crystals of CsV_3Sb_5 were grown from a Cs liquid, a V powder and an Sb shot. The mixture was put inside an alumina crucible and sealed under an Argon atmosphere in a quartz ampule. The mixture was further processed by heating at $600\,°C$ for $24\,h$ and soaked at $1000\,°C$ for $24\,h$, and subsequently cooled at $2\,°C/h$. As a final step, the crystal was extracted from the flux by an exfoliating technique. Since Cs is highly reactive, the treatments were performed in a glove box under an argon atmosphere to avoid the introduction of water, air, or other foreign particles. The only exceptions were the sealing and heating procedures. The obtained crystals have a typical hexagonal shape, similar to the Fe_3Sn_2 sample depicted above. Their size is over $2 \times 2 \times 1\,mm^3$ and they have been shown to be stable for several days in ambient conditions. Nevertheless, special care was taken to avoid influences of air exposure by keeping the time at ambient conditions small.

The crystallinity of the samples was checked with XRD measurements using a Rigaku SmartLab SE X-ray diffractometer with copper-K-α radiation ($\lambda = 0.15418\,nm$) at room temperature. The resulting XRD patterns can be found in Fig. 3.2.5 (a), exhibiting a single preferential orientation of $(00l)$ as marked in the figure. Magnetic susceptibility was determined by a SQUID magnetometer (Quantum Design MPMS XL-1), revealing no T-dependence for high temperatures and a sharp change at approximately $97\,K$ under an external magnetic field. This temperature was estimated to be a phase transition and since no magnetic ordering seems to take place, a charge order was identified consistent with the earlier described results in the literature. Transport measurements were performed on a Quantum Design Physical Properties Measurement System (PPMS), with their results for the resistivity and its derivative depicted in panels (c) and (d). The CDW phase transition can be clearly observed as a kink or a dip for R and dR/dT, respectively.
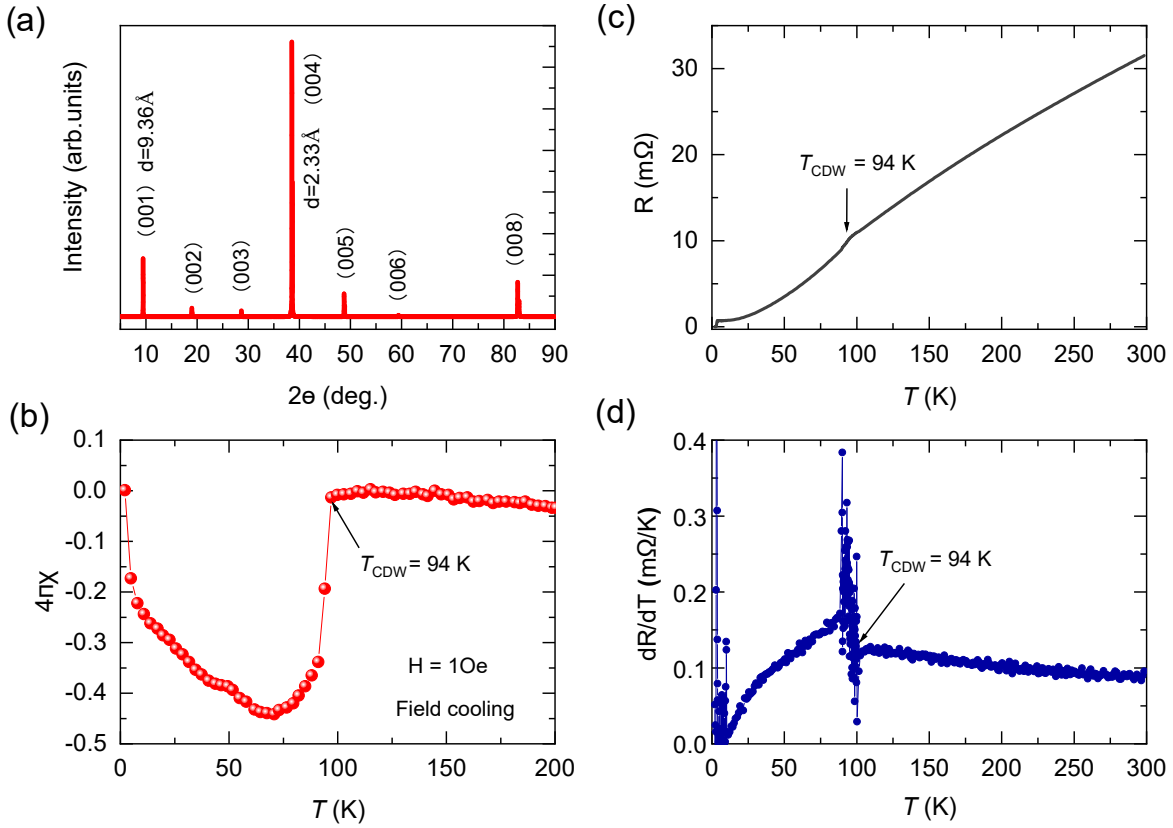
(a)

(b)

(c)

(d)

Figure 3.2.5.: Quality characterizations of the CsV$_3$Sb$_5$ single crystal. (a) The $\theta - 2\theta$ scan of the sample only obtains $(00l)$ peaks. (b) Temperature dependence of field-cooling normalized magnetization reveals no magnetic changes above $94\,\mathrm{K}$. Here, the field is perpendicular to the ab-plane of the sample. Due to no magnetic influence, a charge order was identified. The CDW transition occurs at approximately $97\,\mathrm{K}$. (c) and (d) In-plane electrical resistance and its first-order derivative as a function of temperature reveal similar transition temperatures for T_{CDW}.

Preparation of the samples

To ensure successful access to the selection rules discussed in earlier sections (3.1.2), the crystallographic axes of the investigated sample have to be aligned with the laboratory axes. A specific custom-built sample holder (Fig. 3.2.6 (a)) was utilized to allow the tilting of the crystal surface in two directions, in addition to a simple setting possibility for the subsequent in-plane rotation. Beforehand, the sample was glued onto a copper block, securing good thermal contact. The glue was chosen to be either GE low-temperature varnish or conducting silver paste, as both are suitable for low temperatures and high vacuums but either shows high luminescence or potentially increase the strain on the sample, which alters the T-dependence. Afterward, by using a polarization microscope, one can satisfyingly calibrate the sample surface with respect to the holder, followed by the crystal axes determination via X-ray diffraction. By iteratively rotating the sample inside the holder and measuring the axis, a good agreement of the a-b-crystal axis and laboratory system can be achieved. An example of good agreement on a CsV$_3$Sb$_5$ sample is displayed in Fig. 3.2.6 (b). The sixfold symmetry can be clearly distinguished, with one axis running from top to bottom corresponding to the y-direction in the laboratory system. The sample

holder was proceedingly mounted on the coldfinger of the cryostat. Before the cryostat was pumped, the alignment could be checked via Raman scattering, taking advantage of some already-known phonon selection rules. An example is the A_{1g} phonon line at 135 cm^{-1} of CsV_3Sb_5. By checking its intensity in yy and comparing it to yx one finds ideally no signal in the latter, if the laboratory system of the polarizations is in line with the crystal axes. Lastly, before beginning the actual measurements, the surface of the sample was checked for potential degradation. A clear sign is a strong visible reflection of the elastically scattered light. To remove this portion of light, the sample surface was cleaved using adhesive tape. Since the here used crystals show a clear 2D-layered structure, the exfoliating process resulted most of the time in a flat, clean surface.

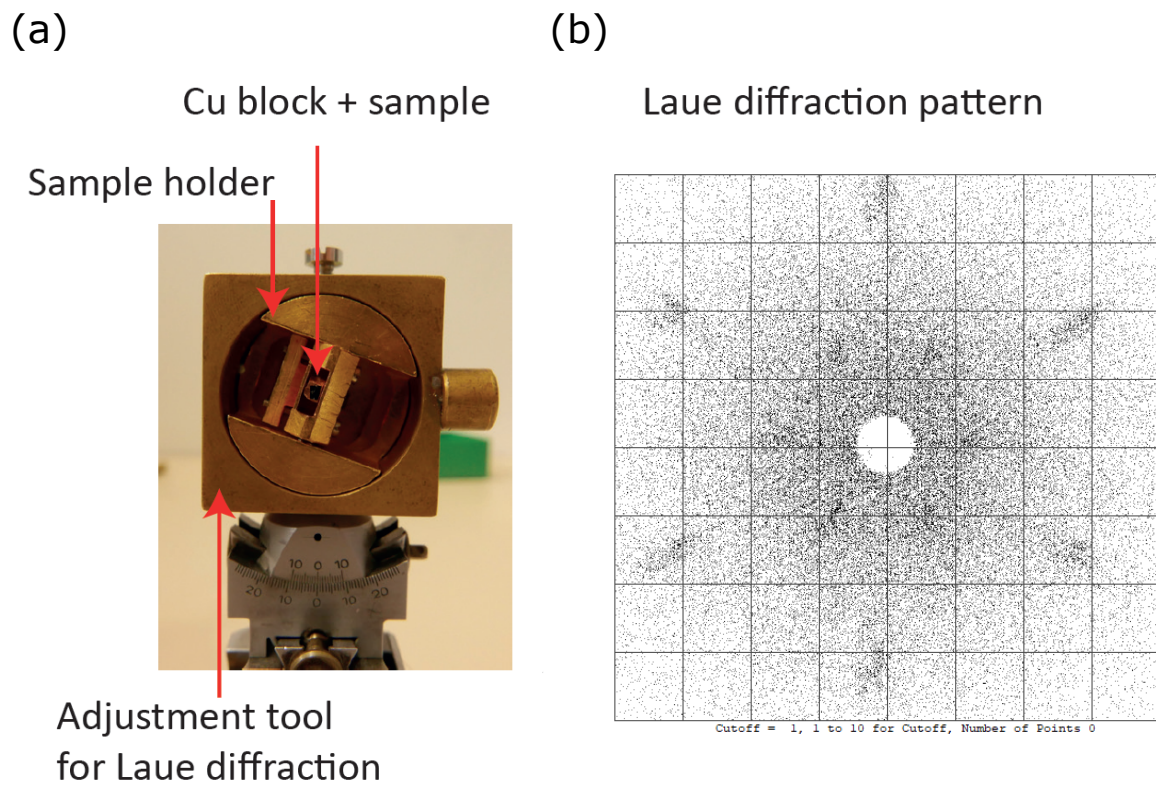**Figure 3.2.6.: Alignment of sample and laboratory system.** (a) Custom-built sample holder made of copper, allowing the tilting and controlled rotation of the sample. (b) Laue diffraction reveals the crystal pattern, here for a CsV_3Sb_5 sample. The six-fold symmetry can be clearly observed and its alignment of one axis is in good agreement with the y-axis of the laboratory. The picture was adapted from [103].

4. Kagome lattice materials

Strong electronic correlations combined with non-trivial topology can lead to various interesting and exciting physical many-body phenomena, like more robust topological superconductors [109]. Kagome lattice based systems have been excessively studied recently as their bandstructure features Dirac fermions, van Hove singularities, and flat bands, which can potentially lead to strongly correlated physics if these features are located close to the Fermi energy. Two interesting compounds with this specific lattice structure in 2D, namely Fe_3Sn_2 and CsV_3Sb_5, were investigated and studied for their electronic and lattice properties using polarization-dependent inelastic light scattering.

4.1. Fe_3Sn_2

In this section, Raman studies of the kagome ferromagnet Fe_3Sn_2 are first presented and then discussed in the subsection 4.1.2. All measurements were performed with an excitation wavelength of $575\,$nm with an absorbed laser power of $P_{abs} = 4.0\,$mW, leading to an increase in temperature in the spot region on the order of $1 - 2\,$K/mW. In the following section, the indicated temperatures are nevertheless those of the sample holder.

4.1.1. Results

The Raman susceptibility of Fe_3Sn_2 versus the Raman shift Ω is depicted in Fig. 4.1.1 with temperatures ranging from 320 down to $4.2\,$K as indicated. The experiments were performed in the energy range of 30 to $3600\,$cm^{-1} with a step size of $\Delta\Omega = 5\,$cm^{-1} below 100 cm^{-1}, $\Delta\Omega = 10\,$cm^{-1} up to 1000 cm^{-1}, and $\Delta\Omega = 50\,$cm^{-1} above. Circular polarization configurations were selected with RL and RR being displayed in panels (a) and (b), respectively. Two spectra were multiplied to fit with the intensities of the other high Raman shifts by less than $10\,\%$ to account for small misalignments of the spectrometer slits.
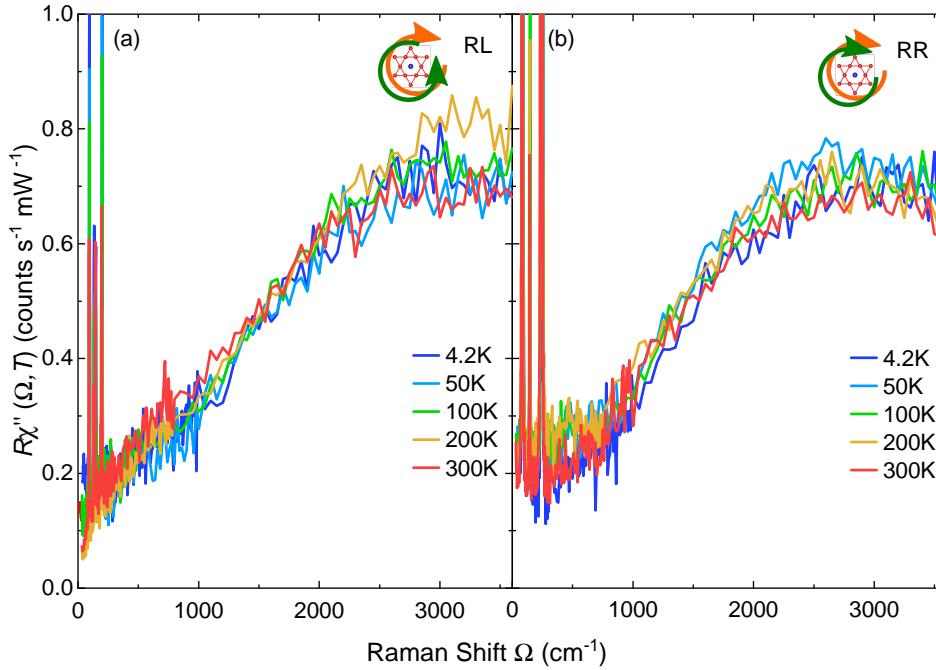
Figure 4.1.1.: Raman response in Fe_3Sn_2 for high Raman shifts at temperatures as indicated. In this energy range neither the spectra in RL-polarization in panel (a) nor those in RR in panel (b) reveal very little change if any upon cooling.

Fig. 4.1.2 zooms in on the data shown in Fig. 4.1.1 and displays spectra for small transferred energies in the range from 30 to $350\,cm^{-1}$. Spectra in RL and RR-polarization are again shown in panels (a) and b, respectively. Below 300 cm^{-1} the spectra were measured with a step increment of 2.5 cm^{-1}. In the energy range of the strong peaks, the step size was set at 1 cm^{-1}. The peaks are numbered from 1 to 4 in either polarization combinations and all peaks sharpen and harden, i.e., shift towards higher Raman shifts. With the Wyckoff positions of the Fe (18) and Sn $(6c)$ atoms in this compound, one finds several Raman-active phonons, 4 in A_{1g} and 5 in E_g symmetry. This allows a preliminary assignment of the four peaks in RR-configuration to A_{1g} phonons. On the other hand, the RL-polarization allows the investigation of the E_g-symmetry, so the four observed peaks can be explained by the Raman-active modes, even though the fifth peak escaped observation, presumably because of its low intensity.

The verification of this assignment, as well as a quantitative discussion of the phononic modes and their temperature dependence, is given in section 4.1.2. The latter gives insights into changes in the lattice due to its coupling to the electronic or spin system. As a spin reorientation takes place at around $100\,K$, two measurement runs with RR-polarization were performed, with a quasi-continuous cool-down from 320 to $4.2\,K$ and a warm-up from 50 to $150\,K$ in smaller temperature steps.
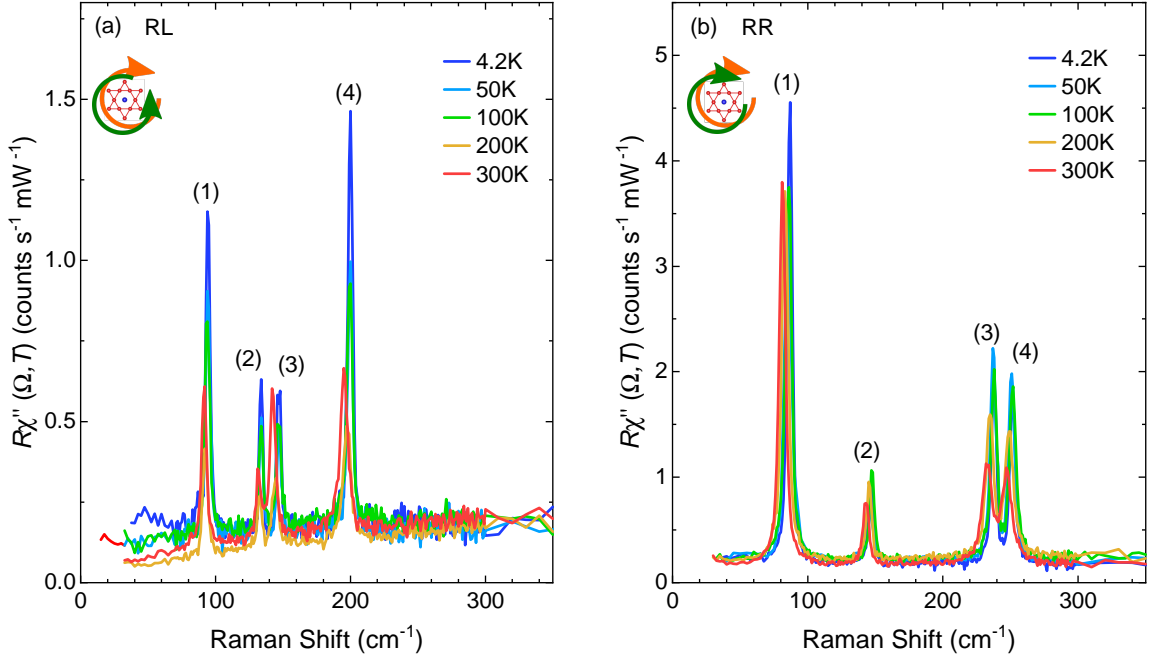
Figure 4.1.2.: Raman measurements of Fe_3Sn_2 focusing on small energy transfers. Panels (a) and (b) depict RL- and RR-polarization, respectively, with temperatures according to the color scale. Four peaks in the Raman susceptibility are clearly resolved in both polarization configurations.

In addition to the just described peaks, polarization-dependent changes in the low energy response are visible in Fig. 4.1.2. While no T-dependence can directly be observed in RR-configuration, RL shows an increase of spectral weight in the region of 30 to 70 cm^{-1} upon cooling. The pronounced rise at wavenumbers below 30 cm^{-1} is most likely a manifestation of elastically scattered light from the laser beam due to surface contamination, hampering the extraction of information closer to the laserline. To improve the statistical significance and check the reproducibility of the measurements, two runs with differently cleaved surfaces were performed.

4.1.2. Spin-phonon coupling in Fe_3Sn_2

In this section, the electronic continuum for low as well as high energies will be discussed first. This is followed by the main analysis of this section, regarding the individual phonons and their interaction with the spin-reorientation of the ferromagnet Fe_3Sn_2. From the Raman tensors and the selection rules presented in chapter 3.1.2, we can conclude that RR projects mainly A_{1g}, while RL corresponds to E_g symmetry.

Electronic continuum

The high energy spectra illustrated in Fig. 4.1.1 show no significant temperature dependence in both symmetries. As expected for the investigated metal and high T_C ferromagnet Fe_3Sn_2, no signs of an energy gap or 2-magnon processes (c. Fig. 3.1.4) similar to the

case of Fe(Se,Te) [100] were found in the studied temperature range. Since there were no changes at the high energies, it is unlikely that the spectral changes in the low energy region are related to magnetic excitations or gap formations. This lack of deviations makes correlations of changes in the low-energy realm to the background improbable. Flat bands in the band structure have been observed by ARPES for energies of approximately $0.2\,\text{eV}$ in a broad region around the Γ-point, which vanish upon approaching the BZ edge [23]. There might be some signatures of this broad region with increased DOS in the high energy Raman results presented here, as the shape of the spectra differs for the A_{1g} (RR) and E_g (RL) symmetry. While both reach a similar intensity at the highest energies, the increase from low wavenumbers is basically linear in E_g, whereas we observe first a constant area, followed by a sharper increase and a subsequent plateau in A_{1g}. The turning point of the slope is located at approximately 1500 cm^{-1}, similar to the flat band position. Thus, the k-dependent location of the flat bands might result in this polarization dependence of the high energy spectra. The temperature independence is in this scenario most likely again a consequence of the much higher phase transition temperature. Resonance measurements as well as theoretical calculations of the Raman vertices from the band structure would presumably be necessary to conclude the origin of this slope difference between the symmetries.

A closer inspection of the low energy region is given in Fig. 4.1.3 with a focus on wavenumbers below the pronounced first peaks for A_{1g} and E_g in panels (a) and (b), respectively. The data is reliable above 40 cm^{-1}. While the observed changes are especially subtle in A_{1g} symmetry, a pile-up of spectral weight in the region of interest in addition to the formation of a small peak in the E_g spectra at ≈ 47 cm^{-1} is detected. The latter may have its origin either in the form of particle-hole excitations reflecting the T-dependence of the resistivity (Fig. 3.2.4), interband transitions as proposed by optical conductivity [25], or fluctuations similar to FeSe$_{1-x}$S$_x$ [110]. Even though the seen decrease of intensity around this peak towards the lowest wavenumbers (≈ 40 cm^{-1}) is unusual for elastically scattered light, the actual existence, origin, and T-dependence of the discussed inelastic peak should be carefully verified by additional measurements of bigger and cleaner samples. Nevertheless, for a simple comparison, Fig. 4.1.3 (c) displays the normalized area of the shaded region in the two symmetries, giving to some extent a quantitative value for the general increase in the Raman susceptibility, allowing a clear differentiation between the two symmetries. Since the individual spectra for both polarization configurations at specific temperatures were measured shortly after each other and A_{1g} lacks growth upon cooling, the polarization dependence cannot be explained by diffuse scattering of the laser light due to more surface contamination at lower temperatures. Looking at the correspondence of low energy E_g spectra and transport measurements 3.2.4, the in-plane carrier relaxation observed in A_{1g} is probably T-independent. A clear explanation and conclusion for this interesting anisotropy and T-dependence in the E_g channel needs more studies in optimized samples.
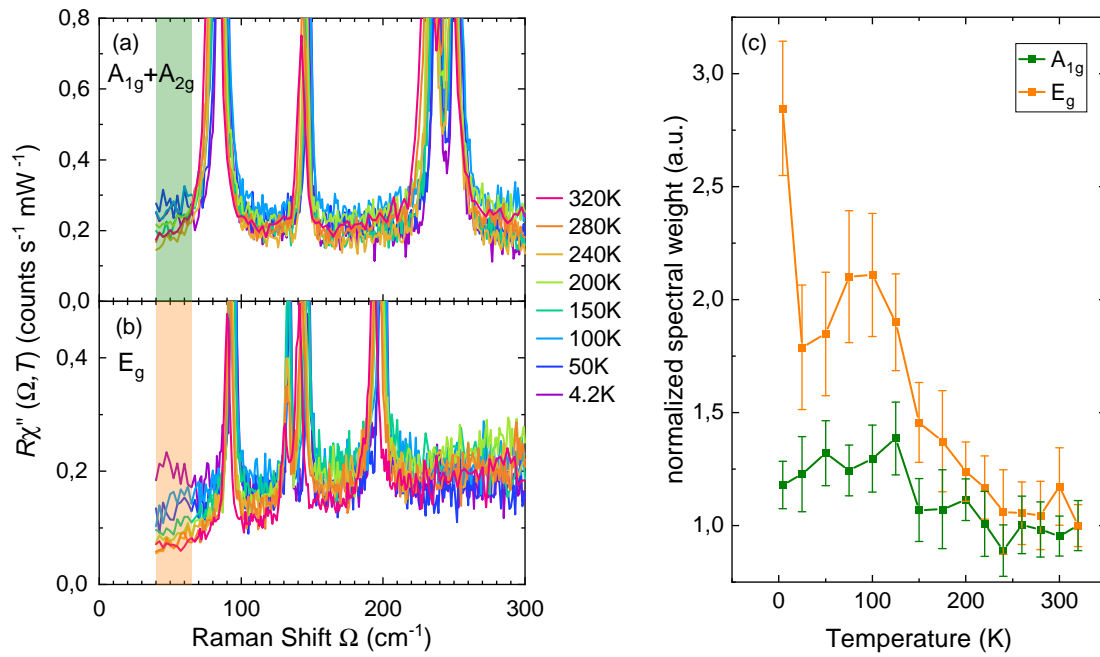
Figure 4.1.3.: Electronic continuum at low transferred energies. Panel (a) and (b) focus on the shaded regions of the A_{1g} and E_g symmetry, respectively. The T-dependent changes are rather subtle in A_{1g} symmetry, while a clear increase of spectral weight is observed in E_g. Panel (c) depicts the integrated areas of the shaded region, visualizing a quantitative distinction between the two symmetries. The areas were normalized to one for easier comparison.

Interrelation of lattice and spin system

The main focus of the investigation in Fe_3Sn_2 was put in the potential coupling between spin and lattice dynamics. For that matter, experimentally measured phonons were identified and quantitatively analyzed as powerful probes for the proposed interactions. Fig. 4.1.4 pictures the T-dependent changes of all eight observed and numbered phonons in a stacked fashion.

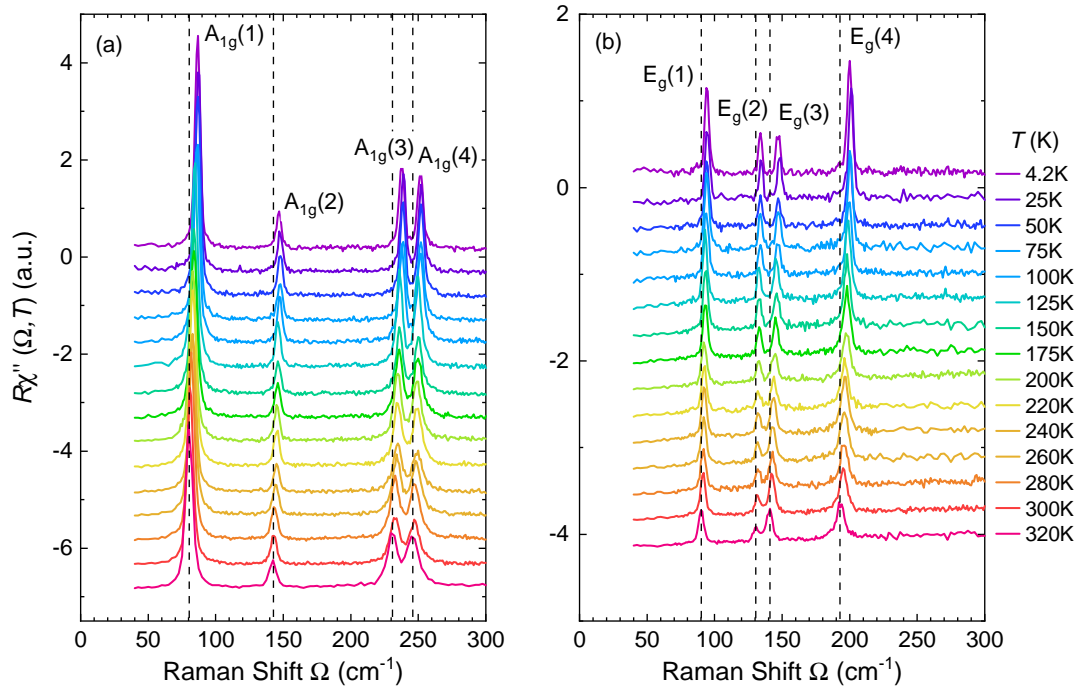**Figure 4.1.4.: Phonon excitations in A_{1g} (panel (a)) and E_g (panel (b)).** Peaks are numbered from 1-4 in both symmetries and vertical dashed lines emphasize the hardening of the phononic modes upon cooling. The spectra are consecutively shifted vertically by $0.5\,\text{cm}^{-1}$ for A_{1g} and $0.3\,\text{cm}^{-1}$ for E_g for clarity.

All phonons show a symmetric lineshape with small linewidth compared to their energies and were therefore fitted with a Voigt function as described in Sec. 3.2.2. An exemplary fit for both symmetries at $4.2\,\text{K}$ is shown in Fig. A.1.1, whose extracted phonon energies are written in Tab. 4.1.1.

Using density functional theory (DFT) and the projector augmented wave (PAW) method, electronic structure calculations were performed in VASP, in order to calculate the Raman-active phonon energies and eigenvectors at the Γ-point of the Brillouin zone. A symmetry analysis of all phonon modes with the Phonopy package allowed the assignment of experimentally observed energies to the vibration modes illustrated in Fig. 4.1.5. The fifth phonon in E_g was supposed to be at around $278\,\text{cm}^{-1}$, but even under closer inspection, no corresponding Raman signal could be detected in this energy region. A more detailed description of the used calculation approach is given in [111] and the results are displayed in Tab. 4.1.1.
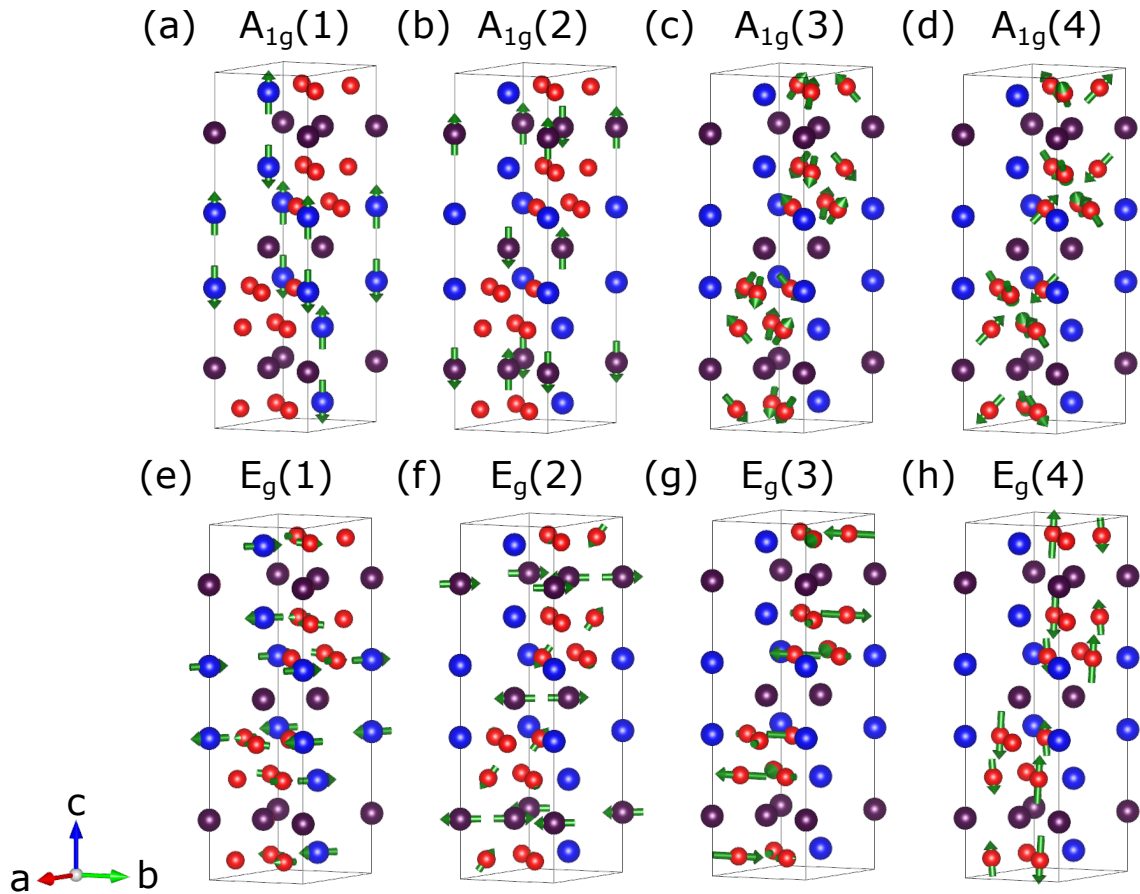
Figure 4.1.5.: Eigenvectors of the A_{1g} and E_g phonon modes, calculated by DFT. Panel (a)-(d) depicts the A_{1g}, (e)-(h) the E_g symmetry. Red balls describe the Fe-atoms building the kagome lattice, blue the Sn-atoms in the kagome plane, and violet the Sn-atoms out-of-plane. Green arrows on the participating atoms denote the vibrational direction of specific phononic modes, numbered according to increasing resonance energy.

The now identified phonon modes were investigated in more detail for their T-dependence, the extracted results of phonon energy and linewidth are presented in Fig. 4.1.6 for E_g and Fig. 4.1.7 for A_{1g} numbered from low to high energies in accordance to Fig. 4.1.4. On the right side, phonon energies are depicted as full black squares for the "quasi" cool-down measurements, with the addition of open black squares for the warm-up sequence in A_{1g}. A similar approach for the left side with the linewidth as full and open blue dots for "quasi" cool-down and warm-up, respectively. As expected for phononic modes, cooling leads to an energy increase and a sharpening of the widths as a result of the lattice contraction [112] and a decrease of anharmonic decay channels [113]. The distinction between these two driving mechanisms is going to be discussed later in this chapter.
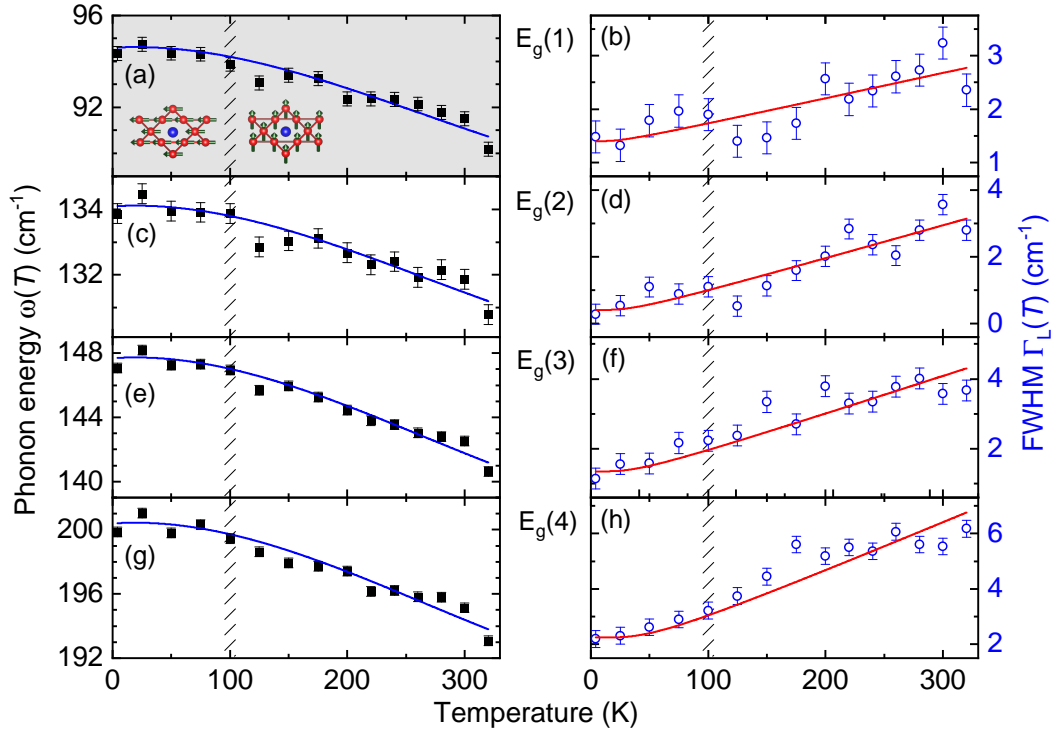
Figure 4.1.6.: Phonon energies ω **(left side, black closed squares) and linewidth** Γ_L **(right side, blue open circles) against temperature for the** E_g **phonons.** Raman peaks were fitted with a Voigt function and the resulting T-dependence is fitted with equations 4.4 (blue line) and 4.1 (red line) with the resulting parameters in Tab. 4.1.1 as described in the text. The spin-reorientation temperature is marked as a shaded region around $100\,\mathrm{K}$, while no clear anomalies to the expected hardening and sharpening towards low temperatures are observed.

The linewidth of a phononic excitation is dependent on the potential decay channels of the latter, which in general become increasingly harder to relax into upon cooling. This leads to a sharper peak, with a resulting T-dependence that can be described with [113]:

$$\Gamma_\mathrm{L}(T) = \Gamma_\mathrm{L}(0)\left(1 + \frac{2\lambda_\mathrm{ph\text{-}ph}}{\exp\left(\frac{\hbar\omega_0}{2k_B T}\right) - 1}\right). \tag{4.1}$$

Here, $\Gamma_\mathrm{L}(0)$ and ω_0 are being extracted as the mean value of the respective 4.2 and $25\,\mathrm{K}$ measurements, leaving only the phonon-phonon coupling $\lambda_\mathrm{ph\text{-}ph,i}$ as a free parameter. The corresponding fit curves can be seen as red lines on the left sides of the two now discussed figures.
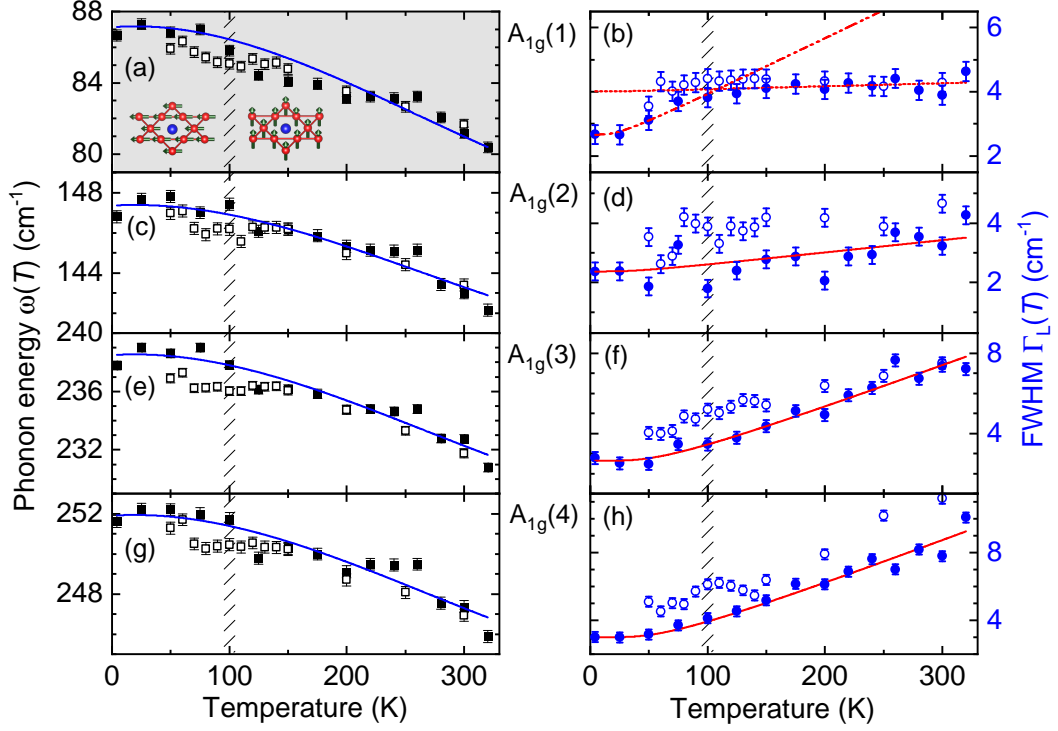
Figure 4.1.7.: Phonon energies ω (left side, black closed and open squares) and linewidth Γ_L (right side, blue open and closed circles) against temperature for the A_{1g} phonons. To investigate any existing hysteresis, two measurement runs were performed including a quasi-cool down (closed symbols) and a warm-up (open symbols) procedure. Similar to Fig. 4.1.6, peak characteristics were fitted by accounting solely for the anharmonic decay to understand Γ_L (red line), whereas a combination of anharmonic contributions and the thermal expansion of the lattice are needed to explain the energy shift of the phononic modes (blue line). The thermal expansion data was measured by Gegenwart *et al*. While the three high-energy phonons behave as expected, a clear anomaly can be observed in the linewidth of A_{1g} (1) around the spin-reorientation temperature marked as a shaded region. Additionally, a small deviation of the expected results for the phonon energy is observable in both warm-up and cool-down runs. This phenomenon is shown and described in Fig. 4.1.9.

The changes in phonon energy have been mainly described by two different approaches in the literature. For one, higher-order anharmonic effects have been argued to be responsible by Balkansky and coworkers [114]. In this model, an incoming photon is absorbed, creating an optical phonon while emitting a photon. The created phonon then decays into two or three phonons. These additional decay channels lead to a different description of the linewidth and energy of the created mode:

$$\Gamma(T) = A \left(1 + \frac{2}{e^x - 1} \right) + B \left(1 + \frac{3}{e^y - 1} + \frac{3}{(e^y - 1)^2} \right), \qquad (4.2)$$

$$\Omega(T) = \omega_0 + C \left(1 + \frac{2}{e^x - 1} \right) + D \left(1 + \frac{3}{e^y - 1} + \frac{3}{(e^y - 1)^2} \right). \qquad (4.3)$$

Here $x = \hbar\omega_0/2k_BT$, $y = \hbar\omega_0/3k_BT$, and ω_0, as well as A, B, C, D being fitting constants, allowing the attribution of three or four phonon processes to the seen changes. Notice, the first term of the linewidth attributed to two-phonon decays is very similar to the used

formula 4.1 while disregarding a potential coupling between the two phonons. Instead higher anharmonicity terms are included, thus the observed data can be described with good agreement in most cases. One could argue that this simple fitting procedure is responsible for the widespread use of this model, even though several physical issues arise within this approach. On the one hand, the resulting fitting constant pairs $A-C$ and $B-D$ should yield somewhat similar values, since the attribution of both three or four phonon processes needs to be similar for the linewidth and position of the exactly same excitations. Yet, this constraint cannot be fulfilled either for the discussed silicon phonon by Balkansky *et al.*, nor the here investigated phonons. On the other hand, the proposed model starts with the assumption of constant volume, which is experimentally tremendously challenging. Instead, the thermal expansion of the lattice needs to be taken into account, while the pressure is constant in accordance with the findings by Postmus *et al.* [112]:

$$\omega_{\mathrm{ph},i}(T) = \omega_i(0) + \Delta_i(T) = \omega_i(0) + \Delta_i^{(1)}(T) + \Delta_i^{(2)}(T)$$

$$= \omega_i(0) + \omega_i(0)\left\{\exp\left[-3\gamma_i\int_0^T\alpha(T')dT'\right]-1\right\} - \frac{\Gamma_i(0)^2}{2\omega_i(0)}\left[1+\frac{4\lambda_{\mathrm{ph\text{-}ph},i}}{\exp\left(\frac{\hbar\omega_0}{2k_BT}\right)-1}\right].$$

$$(4.4)$$

The energy shift is now dependent on the zero temperature value ω_0, which can be approximated from the experimental data, as well as the two terms $\Delta_i^{(1)}(T)$ and $\Delta_i^{(2)}(T)$, approximating the lattice contraction and the anharmonic decay, respectively. Here, we find a strong advantage of using the phonon-phonon coupling parameter. Since the anharmonic properties of the two extracted quantities, energy and linewidth of the same single phonon, should be equal, we are able to extract $\lambda_{\mathrm{ph\text{-}ph},i}$ of a specific phononic mode from the linewidth and use it for the phonon position as well. For $\Delta_i^{(1)}(T)$ one needs to find the Grüneisen parameter γ_i, connecting the change of the lattice volume to the behavior of the vibration energies of each individual mode. By measuring the thermal expansion coefficient $\alpha(T)$, only the Grüneisen parameter γ_i stays undefined in Eq. 4.4 and can now be extracted from our experimental data. The thermal expansion data was kindly provided by Dr. Christoph Meingast's group from the Karlsruhe Institute of Technology, displayed in Fig. 4.1.8(a). Resulting fits of the phonon energies are visualized as blue solid lines in the right columns of Fig. 4.1.6 and 4.1.7. The fitted parameters of γ_i and $\lambda_{\mathrm{ph\text{-}ph},i}$ can be found in Tab. 4.1.1.

The used description of the position and linewidth shows generally good agreement with the analyzed data, leading to fit values of $\lambda_{\mathrm{ph\text{-}ph}}$ between 0.14 and 1.11. The overall Grüneisen parameters are in the range of 0.22 to 0.51 with the exception of the A_{1g} (1) mode. This particular phonon undergoes the only anomaly of the crystal dynamics, especially pronounced in the linewidth. More subtle discrepancies in the phonon energy behavior of this mode can also be observed. To confirm that these small deviations are not stemming from unexpected changes in the lattice itself, one can look at the T-dependence of the macroscopic Grüneisen value $\gamma_{\mathrm{macro}}(T)$. This parameter combines the weighted av-

Table 4.1.1.: Key data of the lattice vibrations in Fe_3Sn_2. Calculated and measured energies ω_0 as well as corresponding linewidths (FWHM) Γ_L for the eight observed phonons in A_{1g} and E_g at lowest temperatures ($4.2\,K$). Additionally, the phonon-phonon coupling $\lambda_{\text{ph-ph}}$ as well as the overall Grüneisen parameter γ of each mode is displayed. The A_{1g} (1) mode has two values attached, in order to account for the anomaly in the linewidth around $100\,K$.

Phonon		A_{1g} (1)	A_{1g} (2)	A_{1g} (3)	A_{1g} (4)
Energy (cm^{-1})	Simulation	83.9	140.1	232.1	241.8
	Experiment	86.6	146.8	237.7	251.6
FWHM (cm^{-1})		4.5	4.1	4.7	4.9
$\lambda_{\text{ph-ph}}$		0.20 ± 0.02 0.015 ± 0.008	0.14 ± 0.05	0.68 ± 0.08	0.74 ± 0.08
γ		0.84 ± 0.05 0.88 ± 0.05	0.34 ± 0.02	0.32 ± 0.02	0.22 ± 0.01
Phonon		E_g (1)	E_g (2)	E_g (3)	E_g (4)
Energy (cm^{-1})	Simulation	92.7	138.2	147.1	196.7
	Experiment	94.3	133.8	147.0	199.8
FWHM (cm^{-1})		3.6	3.1	3.8	4.1
$\lambda_{\text{ph-ph}}$		0.11 ± 0.03	1.11 ± 0.59	0.29 ± 0.06	0.42 ± 0.07
γ		0.46 ± 0.02	0.25 ± 0.01	0.51 ± 0.02	0.37 ± 0.02

erages of all phononic contributions in a crystal, as well as all influences from charges or magnetism. It can be calculated from several different thermodynamic properties according to the following equation:

$$\gamma_{\text{macro}}(T) = \frac{3\alpha(T) \cdot K(T) \cdot V^{\text{mol}}(T)}{C_p^{\text{mol}}(T)} \tag{4.5}$$

The bulk modulus $K(T)$ can be found in [56], whereas the other coefficients, namely the molar volume and specific heat were kindly provided by our collaborates Gegenwart *et al.* and Tsurkan *et al.* The resulting macroscopic Grüneisen parameter is displayed in panel (b) of Fig. 4.1.8, with the inset zooming in on smaller temperatures well below the spin reorientation. At around $100\,K$, where one would expect to observe influences of the transition, no clear signs of deviations are observed. Thus, changes in the phonon energy from the expected lattice expansion-driven behavior are most likely a manifestation of some coupling specific to the vibrational mode. The residuals of the fitted energies are depicted in panel (c), with black squares for the quasi-cooldown and blue squares for the warm-up. All E_g, as well as the three higher energy phonons in A_{1g}, follow the lattice expansion reasonably well. For the A_{1g} (1) mode, a dip in the energy behavior around T_{SR} is observable in both measurement runs, with higher residual values for the cool-down procedure. This region is shaded in grey for clarity since this anomaly is small. Nevertheless, due to its continuous T-dependence over several measurements, this effect is considered significant.
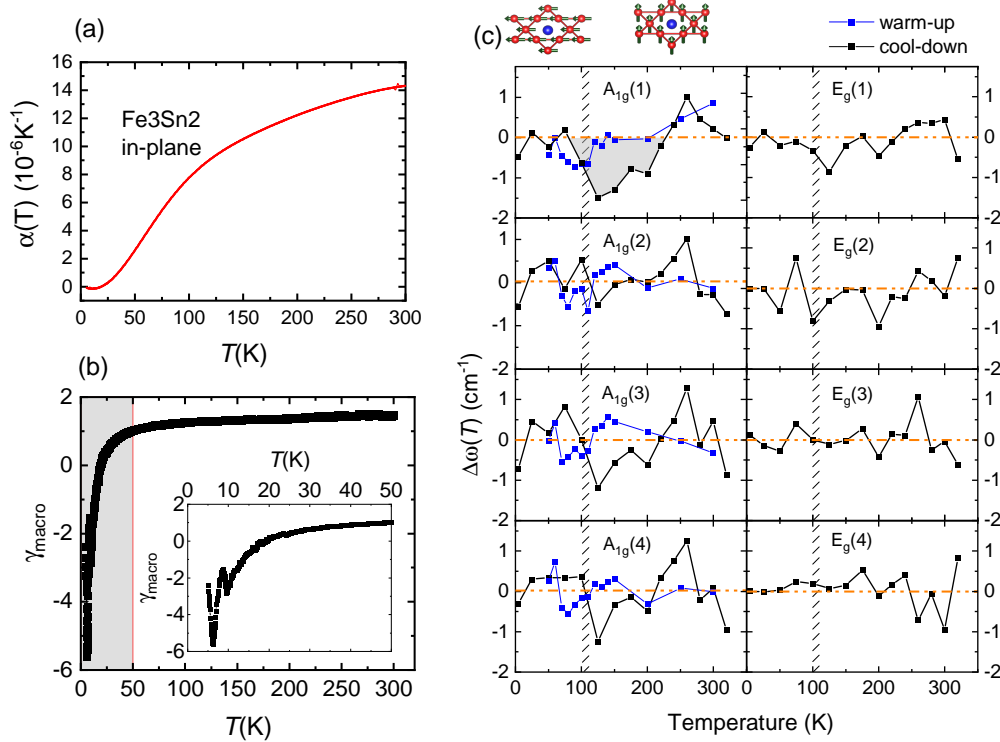
Figure 4.1.8.: Anomaly of the temperature-dependent behavior of the A_{1g} (1) mode around the spin-reorientation. (a) Thermal expansion coefficient data, (b) macroscopic Grüneisen parameter $\gamma_{\text{macro}}(T)$ with the inset zooming in on $T < 50$ K. No sharp changes in the spin-reorientation temperature region are observable. (c) Residuals of the phonon energies of all vibrational modes. Small but significant changes can be found for A_{1g} (1) around T_{SR}.

More pronounced, is a clear change in the linewidth behavior around 100 K, strongly overlapping with the spin-reorientation temperature of the iron atoms in the kagome layer. Coming from low temperatures, the linewidth increases rather sharply, as a lot of potential decay channels are reachable for a small increase in thermal energy. This leads to a higher phonon-phonon coupling value $\lambda_{\text{ph-ph}} = 0.20 \pm 0.02$. When breaching approximately 100 K, the linewidth becomes more or less temperature independent, quantitatively illustrated by a much smaller $\lambda_{\text{ph-ph}} = 0.015 \pm 0.008$. This is unusual, for increasing temperature more decay channels should become accessible, but while and after the spin reorientation takes place, additional decay possibilities seem to stay forbidden. The phonon energy displays a more subtle distinction to the expected dependence but is still arguably visible since for both measurement runs, the extracted phonon energy displays a dip around the reorientation temperature. Additionally, the fitted Grüneisen parameter with a value of either 0.84 or 0.88 ± 0.05 is at least around double the amount compared to all other phonons. The anomalous behaviors of A_{1g} (1) are observed for the "quasi" cool-down and warm-up with very little if any hysteresis.

The observed anomaly is most likely explained by a spin-phonon coupling, leading to visible changes in the linewidth and eigenfrequency only for the low-energy phonon in A_{1g}. The strong interaction of this particular phononic mode is best explained by the spatial

connection of its vibrating atoms to the tilting spins of the iron kagome layers. This is illustrated in Fig. 4.1.9 (c), where the red iron atoms carry a spin and the vibration of the in A_{1g} (1) participating tin atoms are visualized as green arrows, displaying the perpendicular distortion to the kagome layers. From this coupling strength, the spatial proximity of spins and vibrational eigenvectors, and the T-dependence, the A_{1g} (1) phonon is a solid candidate for driving the spin-reorientation in Fe_3Sn_2. Theoretical calculations for further clarifying the experimental observations are desirable.
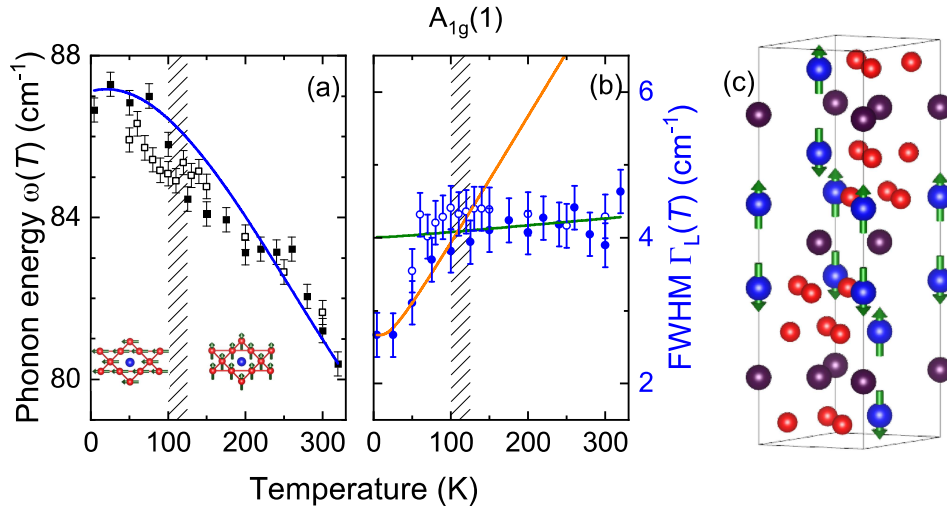

Figure 4.1.9.: Anomaly of the temperature dependent behavior of the A_{1g} (1) mode around the spin-reorientation. Peak position and linewidth exhibit unexpected changes, with a more pronounced deviation for the latter, visualized with two fits in orange and green for small and high temperatures, respectively. A potential explanation lies in the lowest energy and in the eigenvector of this vibrational mode in panel (c), where the Sn atoms in the Kagome plane oscillate perpendicular to the 2D layers. The spin-phonon coupling changes, when the Fe-spins rotate from in-plane to out-of-plane at higher temperatures.

Noticeably, the large differences of $\lambda_{\text{ph-ph}}$ for high and low temperatures are only weakly connected to the Grüneisen parameter, as the latter is varied by less than five percent. This fact is in accordance with the earlier discussed separate influences of anharmonic decay and lattice contraction on phonons, underpinning the latter as the driving force of the phonon hardening.

4.2. CsV_3Sb_5

The recently discovered kagome metal family around the ternary metal AV_3Sb_5 (A=K, Rb, Cs) exhibits unconventional ordering phenomena connected to a rich bandstructure. All compounds exhibit a presumably chiral charge density wave, breaking time-reversal symmetry without magnetism [69]. Adding to that, several experiments reveal superconductivity ($T_c = 0.9 - 2.5$ K) which was suggested to be in a strong coupling regime [36]. Competition between these two ordering phenomena was found under hydrostatic pressure experiments [64], the study of their interplay might lead to a better understanding of both. In this section, temperature-dependent and momentum-resolved Raman studies on the superconducting kagome metal CsV_3Sb_5 are first presented and then discussed, while focusing on the correlated electronic charge density wave phase with an ordering temperature $T_{CDW} = 94$ K and on temperatures slightly above T_c.

4.2.1. Results

Three different samples were measured in different experimental runs to investigate the lattice and electronic properties of CsV_3Sb_5, while accounting for different laser wavelengths, sample aging, and gluing procedures, as well as increasing the statistical significance by varying spot position and surface quality.

Spectra revealing the temperature dependence of high energy transitions were performed using Raman spectroscopy, depicted in Fig. 4.2.1. The measurements were conducted in a Raman shift range of $\Omega = 50$ to 3600 cm^{-1} with a resolution of $\Delta\Omega = 50$ cm^{-1}. The absorbed laser power was set at 4.0 mW and temperatures were driven from 4.2 to 300 K at the sample holder. Circular polarization was selected, as one can excite all symmetries with the two configurations RR (panel (a)) and RL (panel (b)), without any misalignment due to rotation of the sample with respect to the optical path. With the exception of the 300 K spectra, no multiplication to match the intensity took place.
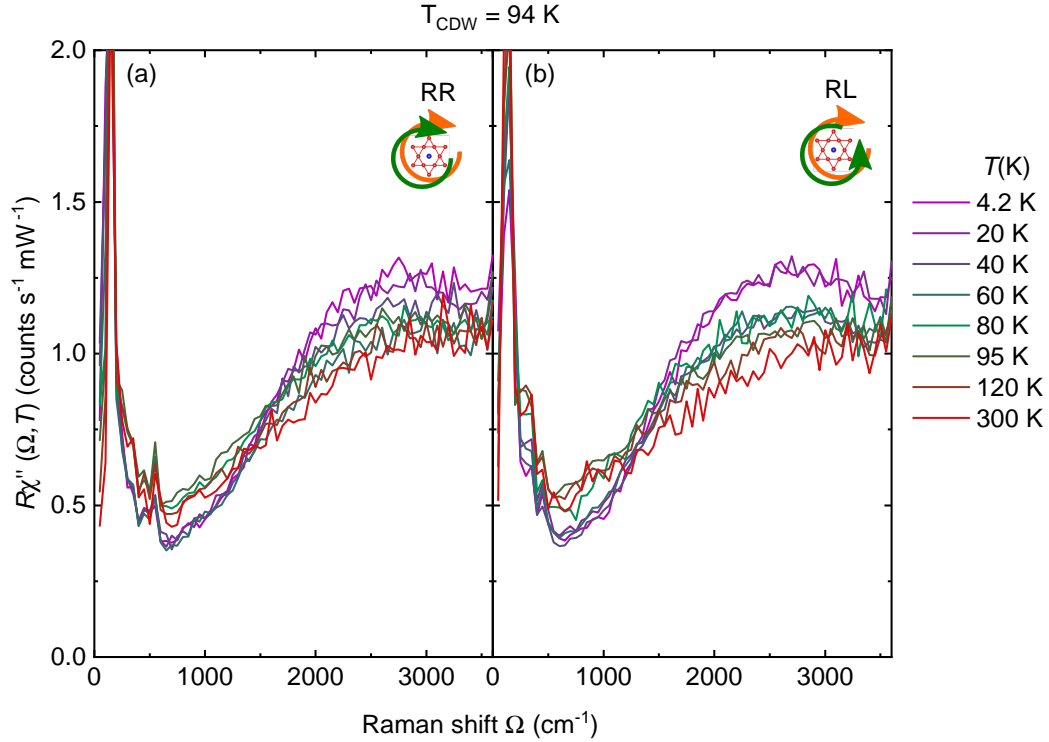
Figure 4.2.1.: Raman spectra of the high energy continuum in CsV_3Sb_5 with circularly polarized light. RR is illustrated in (a) and RL in (b), observing similar changes in the shape and intensity of the broad hump at high energies.

The spectra are dominated by two features, a sharp peak in the front of the curves and a broad hump at high energies for the electronic continuum. In both polarization configurations, we observe very few deviations in the overall intensity and shape of the electronic continuum for temperatures above T_{CDW}. Only upon cooling below this threshold, spectral weight begins to change significantly in both sets of spectra with a decrease of the Raman response at lower transferred energies and an increase at higher Raman shifts. The resulting crossing point of the low T spectra with high T is localized at approximately 1500 cm^{-1} or 180 eV and varies only slightly for the different polarization combinations. The sharp peaks at the lowest energies cannot be resolved properly with these experimental configurations. Thus, new spectra were taken with a higher resolution of $\Delta\Omega = 1, 2.5, 5,$ or 10 cm^{-1}, in a maximal range of 5 to 1500 cm^{-1}. Measurements at four temperatures between 4.2 and 300 are depicted in Fig. 4.2.2 from 25 to 300 cm^{-1}. The RR polarizations are found in the right column and RL in the left. High intensities are located in the upper row, whereas a zoomed-in version of smaller intensities is placed in the lower row. Each combination reveals one large peak with high intensity, marked as 1_{RR} at 137 cm^{-1} and 2_{RL} at 119 cm^{-1} for their respective polarizations in (a) and (b), respectively. While both modes sharpen and greatly increase in intensity upon cooling, only 1_{RR} visibly shifts to higher energies. For these high intensities, one can still observe some smaller peaks at the bottom. A closer look for a Raman susceptibility $R\chi''$ between 0 and 6 $\frac{counts}{s \cdot mW}$ reveals various changes in this region.
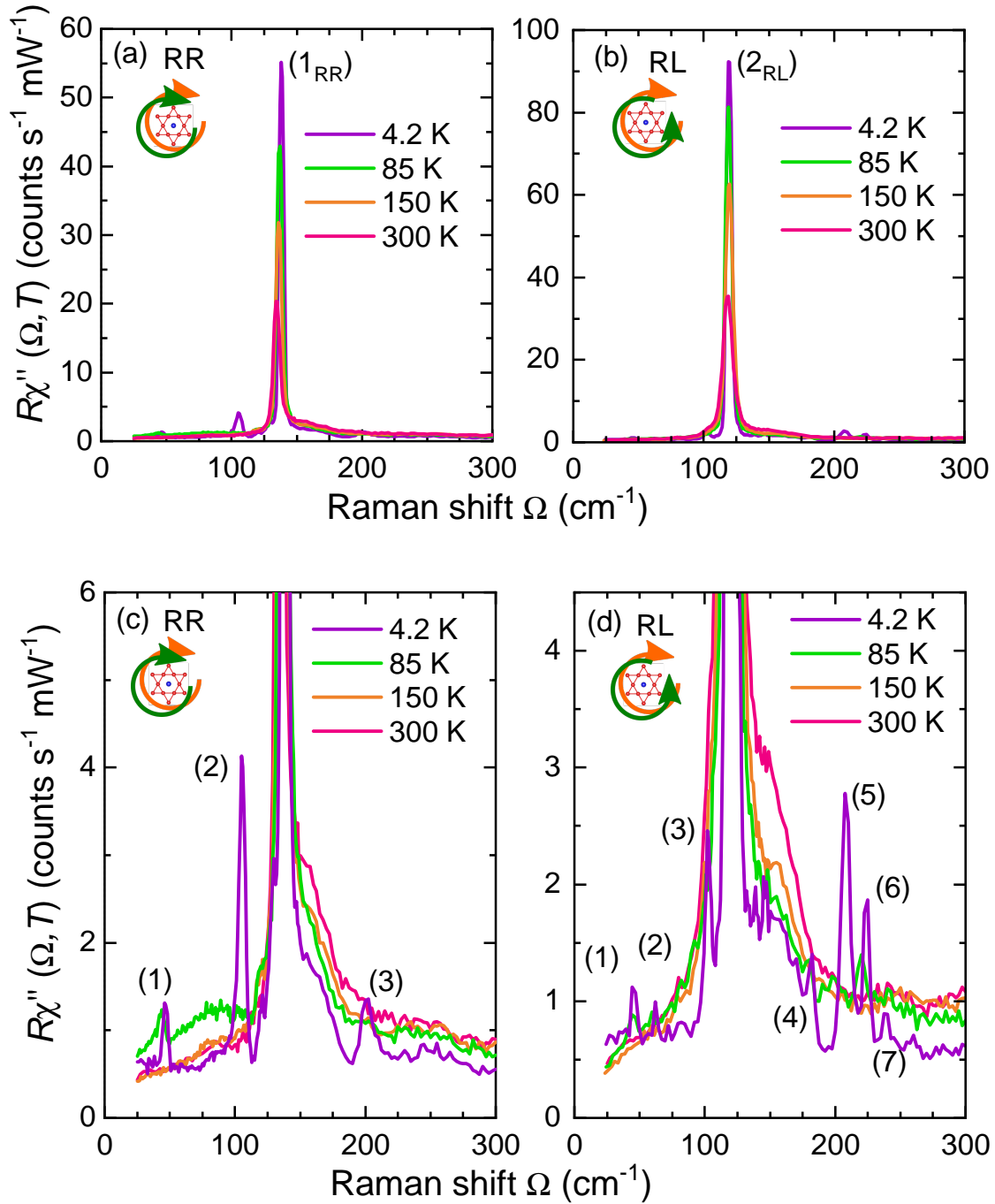
Figure 4.2.2.: Low Raman shift measurements focusing on high and low intensities. Four temperatures above and below T_{CDW} are depicted for RR polarization on the left side ((a) and (c)) and on the right for RL ((b) and (d)). Several peaks can be observed, with a strong peak for each polarization in the complete temperature range and several smaller peaks below T_{CDW}.

Most pronounced is the rise of several new peaks in both polarization combinations at the lowest temperatures. They are numbered from 1 to 3 for RR at 47, 105, and 201 cm^{-1}, whereas from 1 to 7 in RL at 48, 62, 102, 180, 208, 225, and 238 cm^{-1}. No clear changes can be observed for temperatures above T_{CDW}, while some peaks rise immediately after cross-

ing this phase transition and others cannot be distinguished until further cooling takes place. By looking at different wavelengths close below T_{CDW} as presented in B.1.1, one can distinguish all peaks immediately under one or the other excitation wavelength. Thus, while they all exist as soon as T drops below the charge ordering temperature, some of their intensities are too small to be resolved for the yellow laser. Peak 2 in RR shows an unconventional behavior in the form of a broad hump slightly below T_{CDW} sharpening and hardening tremendously towards $4\,\mathrm{K}$. Apart from these peaks, the big peaks both show some shoulder-like shape on their right side, changing for different temperatures in magnitude with what seems like a linear T-dependence. Finally, we can observe a lower overall intensity for the lowest temperatures, most likely a manifestation of the shift in spectral weight towards higher energies observed in Fig. 4.2.1 for both polarizations. In the shown measurements the sample surface was not sufficient to make clear observations of the Raman response down to $5\,\mathrm{cm}^{-1}$, a second run on a different sample with several cleaving attempts allowed a closer inspection of the transitions close to the laser line. A close-up of RR and RL measurements can be found in Fig. 4.2.3 for $\Omega = 5 - 400\ \mathrm{cm}^{-1}$.
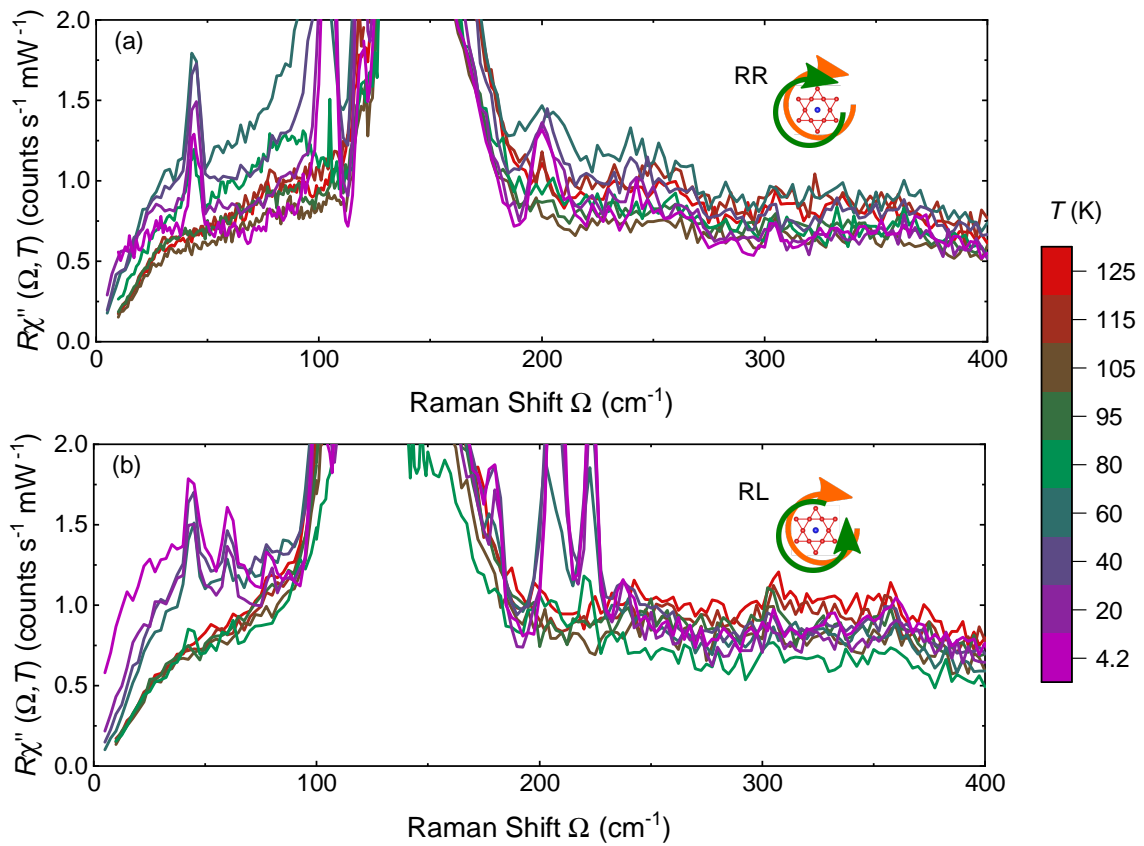
Figure 4.2.3.: Low energy response down to lowest wavenumbers in RR and RL. Above T_{CDW} no visible changes take place in the electronic background or the rise of different peaks, rather only below this transition new, distinct features arise. The RR spectrum is dominated in this temperature range by the progressively sharpening and hardening of one of the new peaks, whereas a strong, but broad accumulation of spectral weight takes place in RL with its maximum at around $50\,\mathrm{cm}^{-1}$.

No strong changes are visible for temperatures above T_{CDW}. The main feature we can ob-

serve is a polarization dependence of the spectral weight accumulating in the front. While the region up to $100\,\mathrm{cm}^{-1}$ seems to be dominated in RR by the broad, but harshly sharpening peak number (2), leading to an in- and a proceeding decrease upon cooling, a different behavior is found in RL. Here, a broad but distinct hump, with its maximum at around $50\,\mathrm{cm}^{-1}$ rises continually towards lowest temperatures.

Up to this point, all presented measurements in this chapter were performed with yellow laser light at $\lambda = 577\,\mathrm{nm}$. Influences on the spectra by changing the wavelength of the excitation laser in the form of resonance effects were investigated with wavelengths of 514 and $476\,\mathrm{nm}$, illustrated in Fig. 4.2.4 with RR on the left and RL on the right.
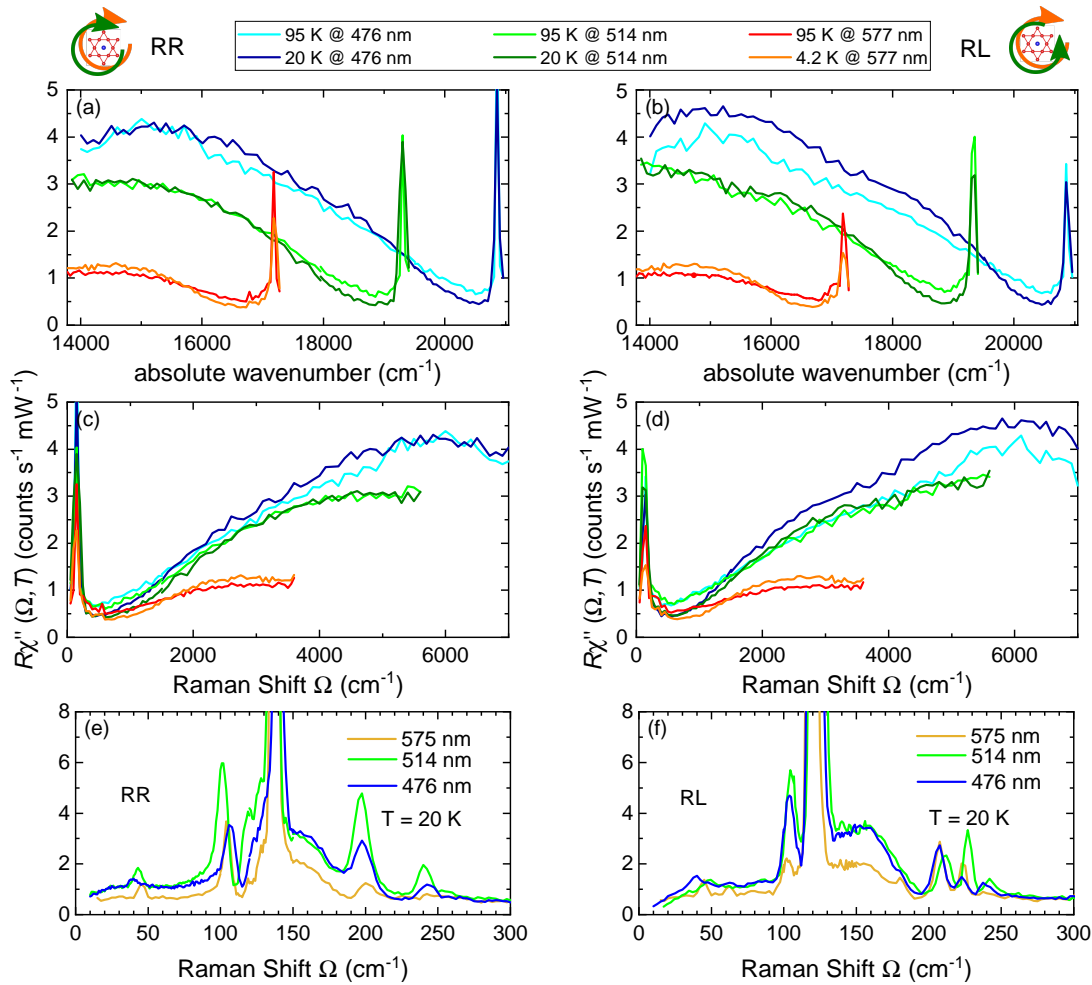
Figure 4.2.4.: Results of Raman measurements for blue ($476\,\mathrm{nm}$), green ($514\,\mathrm{nm}$), and yellow ($577\,\mathrm{nm}$) excitation laser wavelength to detect potential resonance effects. RR on the left, RL on the right column, high transferred energy spectra are displayed for the top in absolute wavenumbers and middle row as the Raman shift, low energies at the bottom row at $20\,\mathrm{K}$. The shift in spectral weight for temperatures above and below T_{CDW} can be observed in all wavelengths. No signatures of strong resonance effects are detected in the new peaks at low temperatures, hence resonance as an explanation for the manifestation thereof is excluded.

Panels (a) to (d) depict the behavior towards high wavenumbers for $T > T_{\mathrm{CDW}}$ and $T <$

T_{CDW}, with their absolute values in the top row and their corresponding Raman shift in the middle row. At the bottom, (e) and (f) take a look at the new peaks in the charge density wave phase for all three laser lines.

The long spectra can be performed to higher Ω when measuring with shorter wavelengths, by subsequently visualizing the three laserlines in absolute wavenumbers we find the broad dominant peak to overlap at similar values at around $15000\ \mathrm{cm}^{-1}$. This peak is thus most likely explained by luminescence. By comparing all four panels, we find that all laserlines in both polarization combinations observe a redistribution from small transferred energies toward higher ones. The crossing point between high and low-temperature spectra is also very similar in all cases, a luminescence nature of this behavior seems therefore unlikely. The change for the two different temperatures seems to be stronger in RL, especially in the blue laser light, but a clear statement should not be made as small deviations when entering the spectrometer might be enough to cause these changes in intensity.

When inspecting the low Raman shift region at $20\,\mathrm{K}$, the newly arising peaks can be reproduced for all laser energies with only small deviations in intensity and position, strong resonance effects as an origin of these peaks can therefore be excluded as an explanation. The general intensity of the peaks is most pronounced in the green laser, whereas yellow and blue have similar intensities. In contrast, the shoulder of the two big peaks in both polarizations exhibits some small dependence on the excitation wavelength having a slightly higher or similar intensity in the blue laserline compared to the green one. We also observe some small unclear shifts in the position of the small new peaks when comparing their differences between each laserline. While the positional change is coherent between yellow and green, some peaks are shifted in the blue to higher and some to lower wavenumbers. An issue with the spectrometer at low transferred energies seems to be the best explanation for these findings.

4.2.2. Strong coupling in the CDW phase of CsV$_3$Sb$_5$

In this section, the presented results are discussed to reveal the interrelation of the electronic system and lattice in the superconducting Kagome metal CsV$_3$Sb$_5$. First, several techniques to fully characterize the sample and measurement parameters are introduced, regarding the assignment of the distinct Raman symmetries, the laser power-dependent spot temperature, and influences due to surface degradation. Following this, the electronic continuum for high and low energies is discussed, before the lattice properties observed with Raman spectroscopy are analyzed. The lattice investigation is extended to an unconventional response and its connection to the electronic properties of the commensurate charge density wave order in CsV$_3$Sb$_5$.

Symmetry analysis above and below the CDW transition temperature

Several experiments point towards the existence of time-reversal symmetry breaking in the charge ordering phase, as described in section 2.4. The conclusion from these observations lies in a putative chiral character of the CDW phase. This chirality might lead to collective excitations being projected by A_{2g} symmetry [115], clean symmetries to identify

these potential excitations are therefore needed. The individual Raman symmetries are disentangled and analyzed in the following. Since one set of polarizations maps a linear combination of two symmetries, one can extract the individual symmetries A_{1g}, A_{2g}, $E_{g\,(1)}$, and $E_{g\,(2)}$, by measuring all six polarization configurations in CsV_3Sb_5. This method was used for three temperatures, well above, slightly below, and far below T_{CDW}, with the results presented in Fig. 4.2.5. In general, this allows the clean assignment of the two strong modes observed in the complete temperature range to the A_{1g}-symmetry for the peak at 137 cm^{-1} and to E_g at 119 cm^{-1}. Upon cooling, the arising new peaks can be assigned completely to either the A_{1g} or one of the two E_g-symmetries. The E_g symmetries are degenerate and cannot be distinguished, but we can conclude that no contribution of the A_{2g} symmetry is detectable and is in the following neglected. The chiral character of the charge order in CsV_3Sb_5 cannot be confirmed with polarization-resolved Raman spectroscopy.

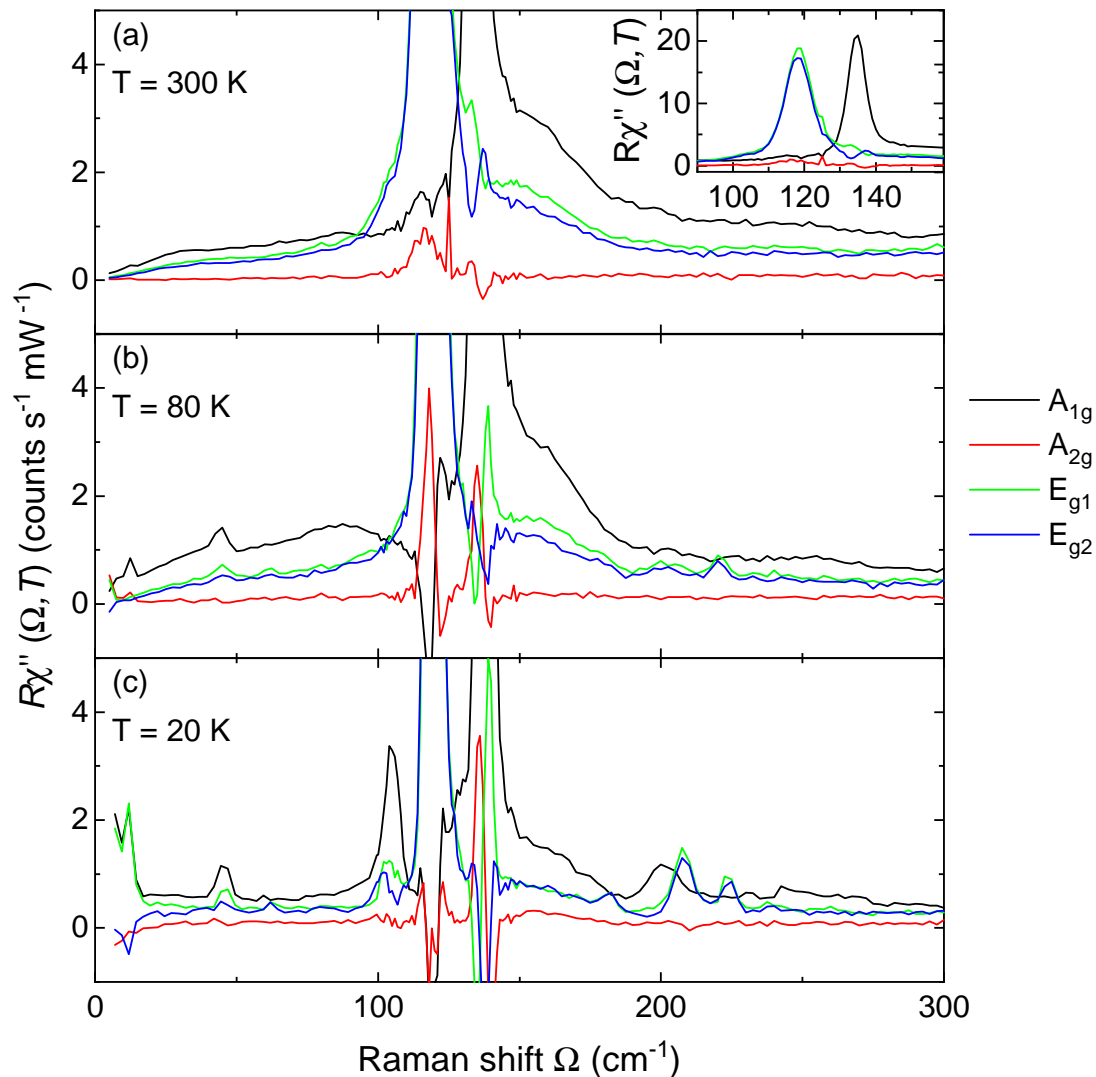**Figure 4.2.5.: Symmetry analysis of CsV_3Sb_5 for 300, 80, and 20 K.** The contributions in A_{1g} can be clearly separated, while the two E_g symmetries are degenerate. No response in the A_{2g} was observed, therefore it can be neglected.

Spot temperature

In the case of sharp ordering transition temperatures, it is clear that to reliably understand the T-dependence and correctly correlate experimentally observed changes to potential phase transitions, good knowledge of the temperature at the probed spot is essential. Two distinct calibration methods were employed to detect the localized laser heating, presented in the following:

For one, at finite temperatures we can take advantage of the Stokes and anti-Stokes transition with their ratio of intensity, given by [89]:

$$\frac{I_{AT}}{I_{ST}} = \left(\frac{\omega_i + \Omega}{\omega_i - \Omega}\right) exp\left(-\frac{\hbar\Omega}{k_B T}\right), \tag{4.6}$$

where I_{AS} and I_{ST} are the intensity of anti-Stokes and Stokes Raman spectra, respectively. $\hbar\Omega$ is the energy transferred to the system. By plotting this ratio and fitting the resulting shape with this equation, one can extract the actual probing temperature. For that, several anti-Stokes and Stokes spectra were measured at four holder temperatures (T_{Holder}) and $4\,\text{mW}$ absorbed laser power, displayed in Fig. 4.2.6 (a). The resulting temperature differences of spot and holder are plotted in panel (b) and subsequently fitted with a linear approximation, given by:

$$T_{Spot} - T_{Holder} = 5 - 0.01 T_{Holder} \text{ [K]}, \tag{4.7}$$
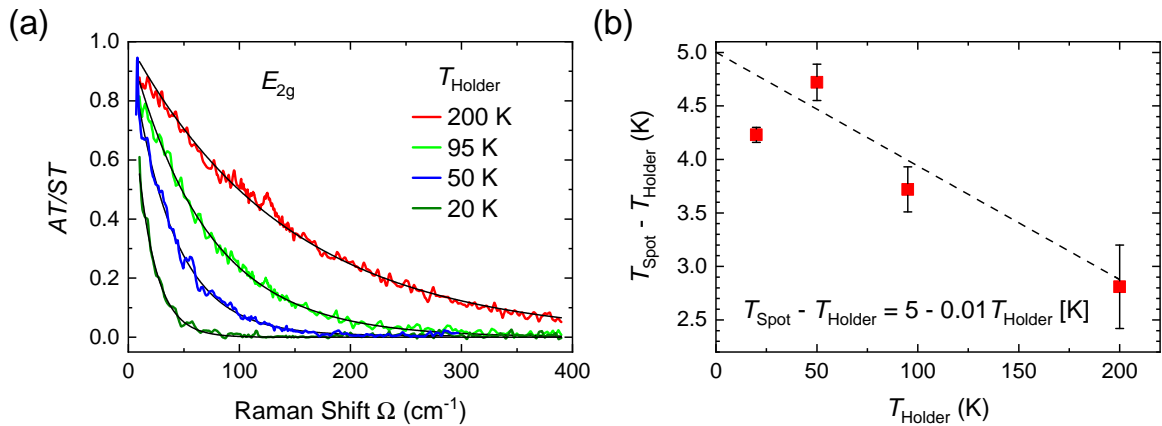
Figure 4.2.6.: **Stokes/anti-Stokes method to determine the temperature in the spot region.** The ratio of the anti-Stokes and Stokes intensity is presented in panel (a), leading via Eq. 4.6 to the resulting differences of spot and holder temperatures in panel (b).

The second approach utilized one of the very quickly arising peaks upon breaching the T_{CDW} at $45\,\text{cm}^{-1}$. By measuring the existence of the peak for different holder temperatures and varying the laser power, while assuming the charge density ordering taking place at $94\,\text{K}$, the laser power could be connected to a specific increase in temperature. The measurements are depicted in Fig. 4.2.7. The laser heating was found to be at approximately $2\,\text{K/mW}$ with this method, which is slightly higher by approximately $0.5\,\text{K/mW}$ than obtained from the Stokes/anti-Stokes approach. But since the region around the CDW is of

the utmost importance in this thesis, we use the $2\,\mathrm{K/mW}$ result in the proceeding sections as it is connected to the transition more closely. All following measurements are marked with the new calibrated spot temperature.
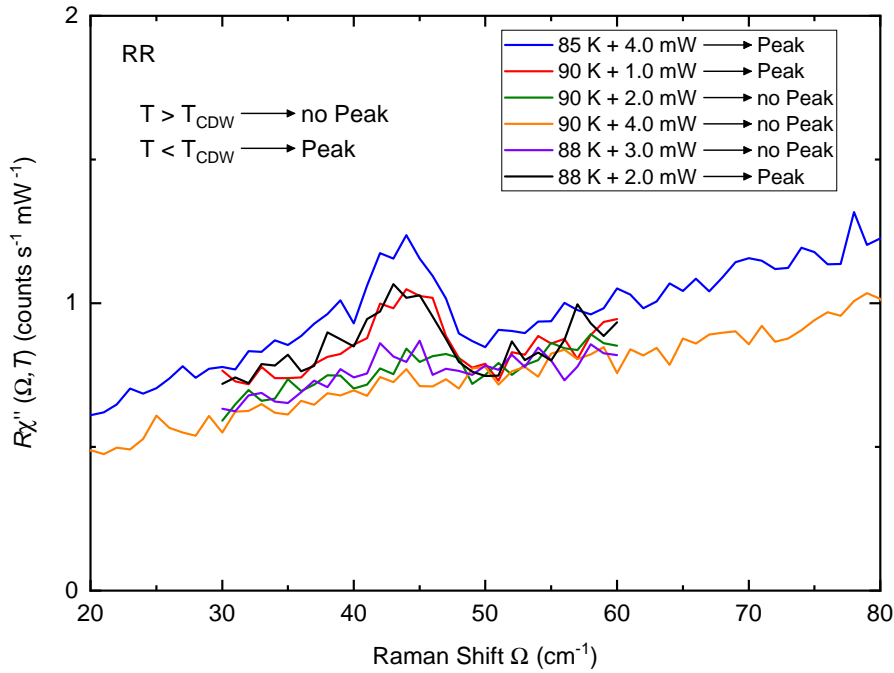
Figure 4.2.7.: Spot-temperature determination via a sharply arising new peak around the T_{CDW}. For a known transition temperature, the variation of T_{Holder} and the laser power enables the deduction of the additional heating per mW.

Consequences of surface degradation in air

A broad hump/shoulder was observed in both A_{1g} and E_g symmetry at approximately $120 - 150 \ \mathrm{cm}^{-1}$ for all temperatures. This response was observed similarly by Liu *et al.* [116] and also reported by Wulferding *et al.* [117] with anomalous temperature dependence. Measurements were performed on the same sample right after cleaving and after keeping it at ambient conditions for at least a month. The results are presented in Fig. 4.2.8 for $300\,\mathrm{K}$ in RR polarization or A_{1g} symmetry. While the intensity of the phonon mode 1_{RR} stays almost constant with slight increases from the general background, the shoulder massively grows in size. To confirm, two different laser spot positions were used, with similar results. While a clear microscopic origin cannot be given, this strong change indicates surface degradation as the leading cause of the detected shoulder.

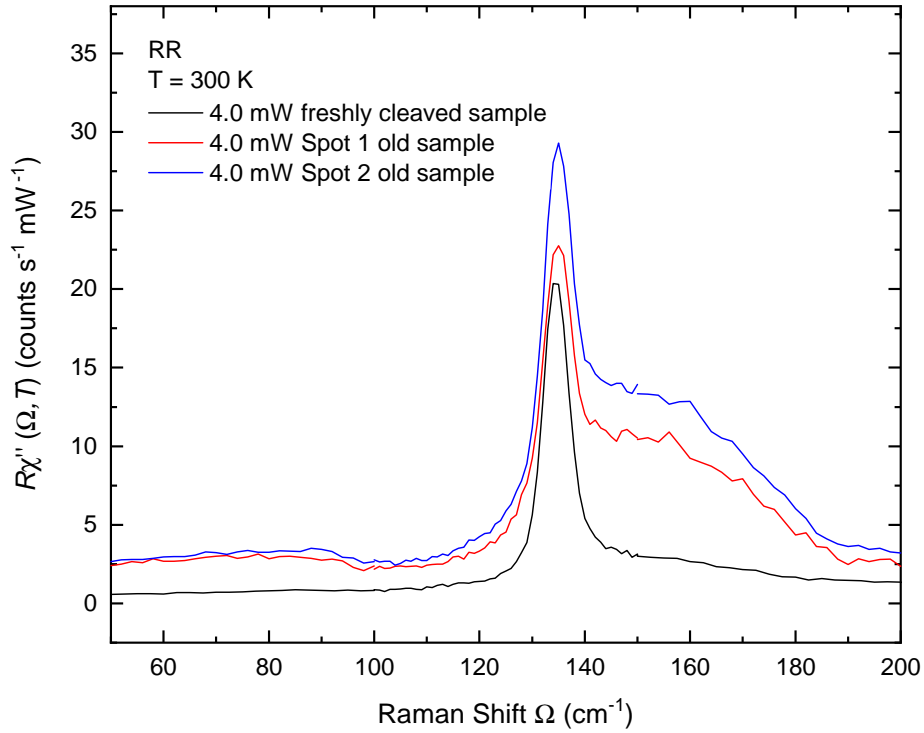**Figure 4.2.8.: Raman spectra comparing a freshly cleaved and aged sample.** By storing a crystal at ambient conditions, the shoulder observed in both circular polarization configurations rises tremendously, making the surface degradation the most likely explanation for its origin.

Gap-like behavior at high energies

The high energy spectra presented in Fig. 4.2.1 revealed no strong changes in the region of high temperatures, but rather only around and below T_{CDW}. We, therefore, focus our considerations on this temperature region with Figure 4.2.10 depicting the assigned A_{1g} and E_g response in panels (b) and (d). The described spectral weight losses at low Raman shifts, moved as additional intensity towards higher energies for low temperatures, lead to a crossing point at approximately 1500 cm^{-1}, slightly higher in A_{1g}. This behavior in the electronic Raman susceptibility is a clear signature of an energy gap (compare to 3.1.4). Due to the proximity of the starting point of the intensity shift to the charge order transition, we conclude that these observations are the manifestation of the opening of a CDW-gap with an energy of $2\Delta = 185$ meV. While this is a similarly sized gap as observed in optical conductivity measurements by Zhou et $al.$ [81], it is in contrast to findings by STS [32, 69] and ARPES [34, 33] measurements indicating a gap of ≈ 20 meV at the M-points. The observations of gap openings at the Fermi surface are well expected, so are no signs of gaps at the Γ-point in these ARPES measurements, yet in contrast to that, we clearly find the just described A_{1g} gap. By expanding the A_{1g} Raman vertices to its second order, we find this symmetry to potentially also project regions at the Brillouin zone edge. Why

the resulting intensity and its shift would remain similar in the first order E_g projection is unclear in this scenario. A different explanation revolves around the commensurate nature of the charge density wave in this material and the contribution of the electronic structure of the kagome lattice to the charge ordering. In earlier performed theoretical studies on an ideal kagome lattice, unconventional superconductivity and a chiral density wave have been predicted [118, 119]. For filling fractions corresponding to the VHs at $n = 5/12$ and $3/12$, these singularities at the Fermi surface, located at the M-point, are perfectly nested with a vector $\mathbf{Q} = (\pi, 0)$. This leads to a 2×2 charge order, consistent with the case of the V-atoms in CsV_3Sb_5. A schematic explanation of the described BZ and its vectors is presented in Fig. 4.2.9.
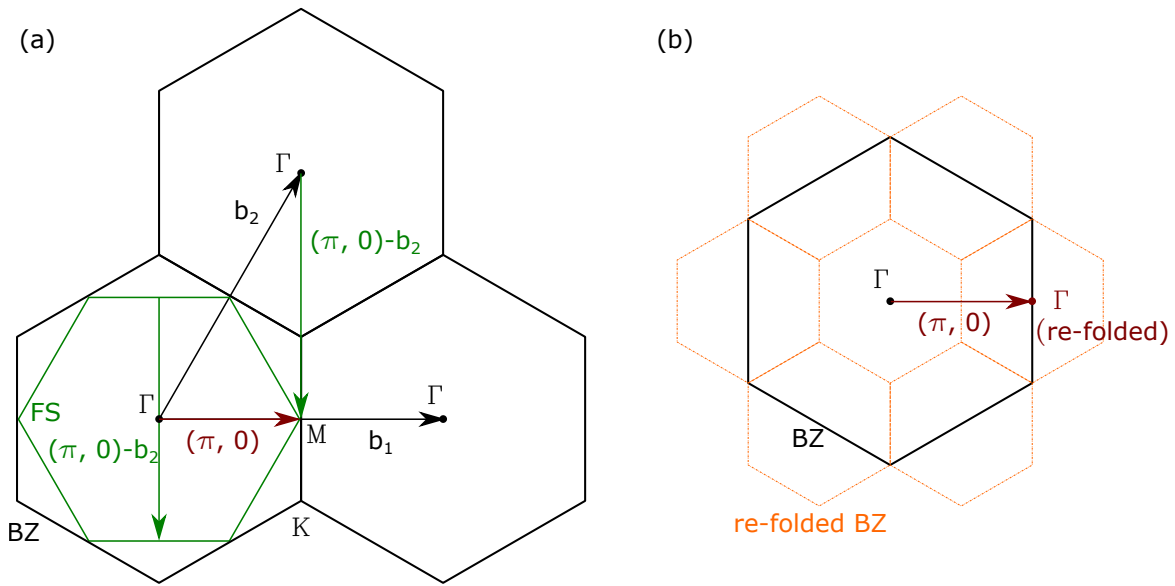

Figure 4.2.9.: Fermi surface nesting leading to a 2×2 charge order and an accompanying re-folding of the BZ in a generic kagome lattice. The nesting wave vector (green arrow) connecting the Fermi surface between the M-points is equivalent to the $\Gamma-M$ point vector $(\pi, 0)$ (dark red). Due to this nesting instability, the unit cell is doubled and the BZ is refolded, resulting in the new orange, dotted BZ. Adopted from [71].

The extension of the unit cell in real space by the lattice distortion leads to a halving of the BZ in the commensurate case relevant here (panel (b)). This leads to a backfolding of the M-point to the center of the BZ, thus it becomes projected in the A_{1g} symmetry. The backfolding was already observed experimentally by ARPES [120] for KV_3Sb_5. Yet the signatures thereof were only small in intensity and accompanied by only a small change in the local DOS. Hence, a clear reason for the similar intensity behavior for both symmetries in our Raman measurements is also not present in this explanation approach. Potentially we simply observe a gap over a wider region in momentum space. The clear gap localization manifested in ARPES around the VHs was consequently not confirmed beyond doubt in our measurements. This discrepancy between the single-particle to the two-particle picture in Raman is complemented by the magnitudes of the gaps being more than four times larger in the Raman case. As ARPES and STM are very surface-sensitive experimental approaches, whereas Raman measures much further into the bulk, the energy discrepancy

might stem from the special configuration at the outermost layer of the topological kagome metal. Near-field Raman studies on these compounds comparing the observed energy gap for far-field and near-field contributions in addition to theoretical calculations for further explanations of the polarization dependence would be desirable. But apart from these uncertainties, the here observed gap is energetically well beyond the weak coupling limit of the mean-field theory with $2\Delta/k_B T_{\text{CDW}} \sim 21 - 23$ instead of the expected value of 3.52. As the influence of the Fermi surface for the charge ordering is reduced for increased coupling strength, a simple nesting picture at the Fermi surface might not be appropriate for explaining the origin of this charge order.

Figure 4.2.10.: T-**dependent behavior of the CDW-energy gap in** A_{1g} **and** E_g **symmetry.** Panels (b) and (d) focus on the separation of the energy regions around the crossing point of the spectra. The area differences in the colored regions are plotted in (a) and (c) with colors matching their area origin. Some small deviations of the expected behavior are observed in A_{1g}, further discussed in the text.

The crossing point of the spectra in both symmetries exhibits no shift, it rather behaves as an isosbestic point, which is not in line with the temperature-dependent behavior observed by optical conductivity measurements [81], where the crossover takes place at smaller energies when approaching T_{CDW}. Yet, a non-trivial temperature dependence is found in the spectral weight shift from low to high energies. These findings are visualized as the area difference from spectra above T_{CDW} in panels (a) and (c) of Fig. 4.2.10. The areas are marked in the color of their corresponding data points, with the crossing point separating the two integrated regions. E_g exhibits expected behavior, with a continuous shift of spectral weight from low to high transferred energies, yielding its highest slope close to T_{CDW}.

The situation in A_{1g} develops more complex, as the spectral weight starts by decreasing in both regions upon cooling with its minimum at ≈ 70 K. Below this temperature, the spectra below 1600 cm^{-1} stay constant, while the high energetic portion increases much more rapidly. Since the temperature resolution is not very high and the ability to pinpoint said minimum in spectral weight for A_{1g} symmetry is therefore reduced, one needs to be cautious with far-reaching conclusions. Yet, the here extracted temperature of minimal intensity overlaps well with a region of strong anomalies [121, 77] connected to a change in the charge density wave superstructure at approximately $60 - 70$ K [79, 76]. This second transition leads to modulation along the c-axis from a $2 \times 2 \times 4$ to a $2 \times 2 \times 2$ structure upon cooling. While the statistical support of the temperature dependence discussed is not too high, the potential of a secondary phase transition influencing the electronic energy gap of the CDW phase should be kept in mind for later.

Fluctuation response

The temperature behavior slightly above the transition temperature exhibits a distinctively different nature in the weak or strong coupling limit. In the first case, the increased electronic excitations across the gap due to thermal disorder lead to the complete disappearance of the ordered phase above T_{CDW}. The strong coupling picture revolves around the chemical interaction and the lattice entropy, which leads to the breaking of the long-range ordering above T_{CDW}, but still allows short-range distortions in a fluctuation picture. This can lead to the smearing of the energy gap temperature and an increase of carrier scattering above the transition. While the smearing of the energy gap is hard to experimentally observe with Raman, the increase of low energy scattering rate in a fluctuation regime can be resolved with Raman in the form of a build-up of spectral weight at low wavenumbers towards T_{CDW} [95] (e.g. Fig. 3.1.4). The region above the phase transition and slightly below was inspected in the relevant Raman shift, the results can be seen in Fig. 4.2.11 in A_{1g} and E_g symmetry. No strong deviations of the electronic Raman response are observed in either region of the Brillouin zone. These findings do not support, but also do not prohibit the attribution of the origin of the charge order to a specific regime of coupling strength.
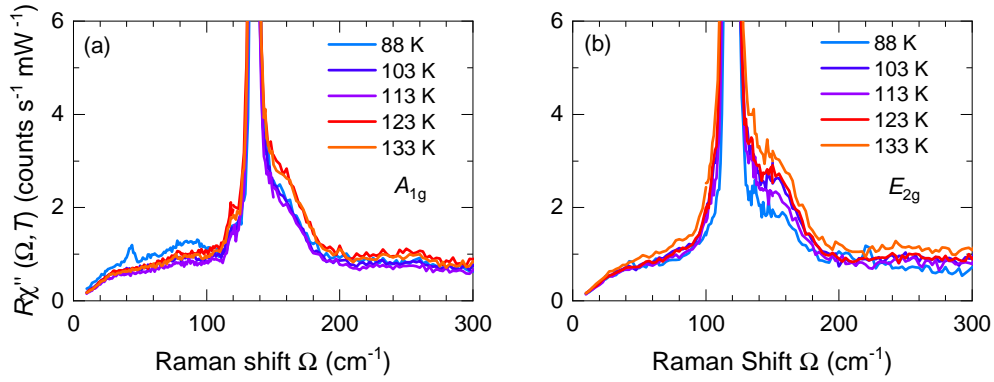
Figure 4.2.11.: Electronic Raman response at low wavenumbers above T_{CDW} in both symmetries. No signatures of fluctuations in the form of a broad increase of spectral weight at small energies were observed.

Since no fluctuations were observed above T_{CDW}, the temperatures as close to the superconducting transition were inspected similarly. A close-up of the taken spectra is displayed in Fig. 4.2.12 for A_{1g} (a) and E_g (b). The response in A_{1g} follows an expected increase in the starting slope upon cooling, overlapped with the rise and a following sharpening of a broad peak, discussed later. The E_g projects a way more drastic increase, displaying an actual hump-like rise of spectral weight at the lowest temperatures. As a simple approximation to inspect the changes in the Raman susceptibility, the spectra were integrated for the marked spaces. The results are illustrated in panel (c). As described for E_g, we observe a strong increase towards the lowest temperatures similar to either a Drude response or fluctuations of the superconducting phase. Electronic excitations like fluctuations should in principle freeze out towards low temperatures, leaving rather sharp peaks as observed in $FeSe_xS_{1-x}$ [110], the there obtained T-dependence is only partially fulfilled here. A Drude response seems therefore more reasonable in the here studied compound. In A_{1g}, the area first increases towards $60\,K$ before dropping fast to the lowest T. We can either argue that the drop is the overlap of the CDW gap and the rising and later sharpening of an unconventionally behaving mode. This can only be partially true as the change of the energy gap at low temperatures was observed to stay almost constant below $60\,K$ and as we see by a later analysis, the mode starts rising above $80\ cm^{-1}$, too far away from the start to have this much influence. Another way of looking at it revolves once more around the second CDW transition, which seemingly is connected to the A_{1g} symmetry. The secondary ordering transition is arguably not as pronounced and confined to a small temperature region, but might rather take place over a broader range. An accompanying fluctuation response around this ordering temperature potentially explains this behavior and polarization dependence.
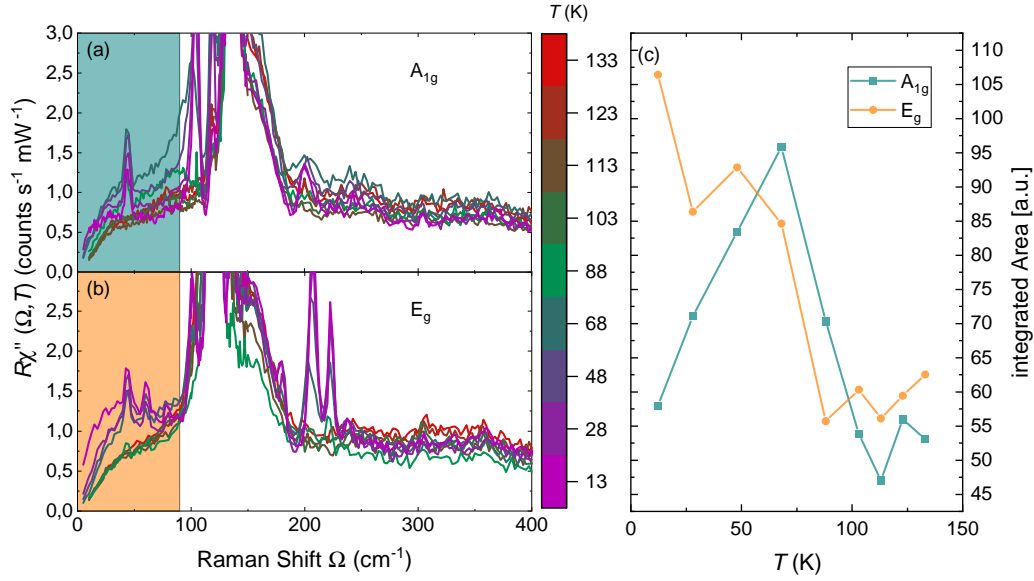
Figure 4.2.12.: Low energy response for temperatures down to below $10\,\mathrm{K}$ **in** A_{1g} **(panel(a)) and** E_g **(panel (b)).** Different electronic response behavior is observed in the two symmetries, for clearer visualization, the spectra are integrated within the marked areas and plotted in panel (c). E_g depicts presumably a Drude response, whereas an unconventional T-dependence is found in A_{1g}, discussed further in the text.

Interrelation of lattice and electronic system

The eigenfrequencies of vibrational modes in CsV_3Sb_5 give insights into the temperature dependence of the lattice and its potential interaction with the changes in the electronic system. The two modes observed in A_{1g} and E_g over the whole temperature range were identified as phonons and due to their symmetric shape subsequently fitted using a Voigt function, described earlier as a convolution of a Lorentzian and a Gaussian yielding Eq. 3.26. The phonons and their extracted energy position and linewidth are plotted in Fig. 4.2.13 for A_{1g} on the left side and E_g on the right. The sole peaks for three temperatures are in the upper row, the wavenumbers in the middle, and the linewidth at the bottom.
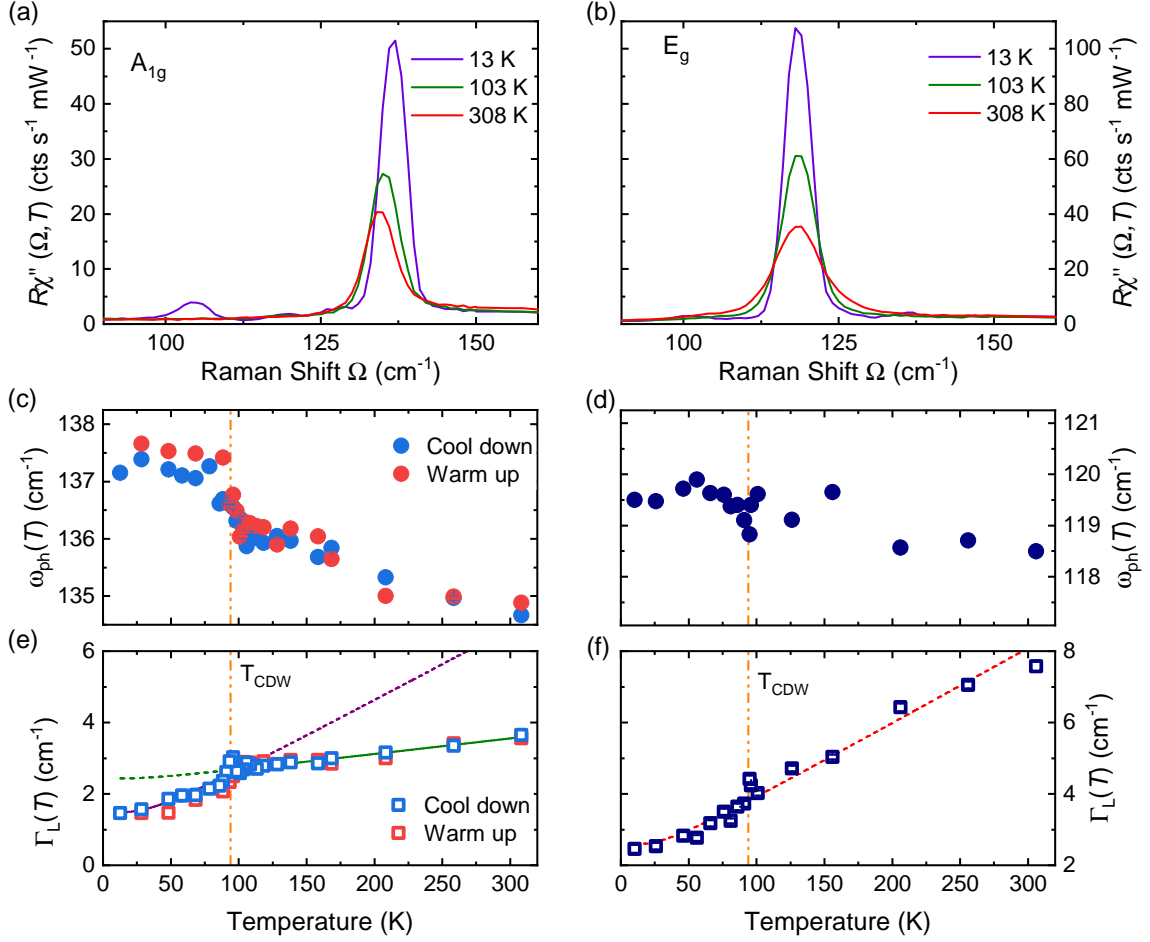
Figure 4.2.13.: Analysis of the dominant phononic modes in A_{1g} (left) and E_g (right) symmetry. (a) and (b) depict the dominant peaks in the Raman spectra of three temperatures. (c) and (d) illustrate the temperature dependences of the phonon energies, (e) and (f) those of the linewidths as derived via Lorentzian fits. T_{CDW} is marked with an orange dashed line for all extracted phonon characteristics. The smooth lines in (e) and (f) are the result of the anharmonic model described in section 4.1.2.

The charge ordering transition is indicated with an orange dashed line. The resulting energy values at their lowest temperatures are in good accordance with density functional theory (DFT) calculations and also similar to already published data by Liu et $al.$ [116] and Wu et $al.$ [79] with our results agreeing better with the latter. The resulting T-dependence of the sharpening linewidth was fitted in accordance to the earlier described anharmonic decay model with Eq. 4.1, which enables the extraction of the phonon-phonon coupling parameter $\lambda_{ph\text{-}ph,i}$. Unfortunately, no thermal expansion data was available until now, therefore a quantitative description of the energy position cannot be given here.

Fitting parameters are displayed in Tab. 4.2.1. The E_g phonon shows only small deviations to the expected temperature dependence in the linewidth and very few total changes in the energy. A lot more pronounced are anomalies in A_{1g} symmetry, for both extracted fit parameters. As the order of the charge density transition is still under debate, a consecutive cool-down and warm-up run was performed in this more responsive symmetry, trying to reveal potential hysteresis in its behavior. Generally, the phonon position displays a con-

Phonon	$A_{1g}(1_{RR})$	$E_g(2_{RL})$
$\omega_i(0)\ [\mathrm{cm}^{-1}]$	137.15 ± 0.02	119.50 ± 0.03
$\Gamma_{L,0}\ [\mathrm{cm}^{-1}]$	1.46 ± 0.06	3.10 ± 0.11
$\lambda_{\text{ph-ph},i}$	$0.68 \, ; \, T < T_{\text{CDW}}$ $0.09 \, ; \, T > T_{\text{CDW}}$	0.25 ± 0.04

Table 4.2.1.: Phonon-Phonon-Coupling parameters from the temperature dependence of the linewidths displayed in Fig. 4.2.13. To account for the variation in coupling strength in A_{1g} symmetry, we used a fit for the region below and above T_{CDW} separately.

ventional increase towards higher energies upon cooling, up close to T_{CDW}. The energy then rapidly increases, before it reaches a saturation level after around $80\,\mathrm{K}$. The linewidth displays clear anomalous behavior as well, changing their sharpening speed tremendously around the charge ordering transition. While the freezing of anharmonic decay channels takes place very slowly for high temperatures, this rate drastically increases around T_{CDW}, visualized by two different fits above and below this temperature in panel (e) with violet and green lines, respectively. The fitted curves track the data well in their corresponding T-range, which leads to two different $\lambda_{\text{ph-ph}}$-values of 0.68 for $T < T_{\text{CDW}}$ and a much smaller value of 0.09 for $T > T_{\text{CDW}}$, giving away the much stronger anharmonicity of the charge order phase. A second change of the A_{1g} phonon mode at $\approx 70\,\mathrm{K}$, which should be especially pronounced in its linewidth, was described by Wu *et al.* [79], but is not observed in this data and cannot be confirmed as the two fits can describe the data very well. Furthermore, we could not resolve any remarkable hysteresis, pointing either toward a second-order or a only weakly coupled first-order transition.

Interestingly, both characteristic parameters of the A_{1g} phonon mode reveal a precursor-like behavior. The phonon energy starts deviating dependent on the warm-up or cool-down run at around 100 to $110\,\mathrm{K}$ from the continuous high-temperature behavior, while the linewidth displays a small hump-like deviation slightly above the charge density wave transition. Since this anomalous behavior is more pronounced in the phonon energy compared to the magnitude of linewidth deviations above T_{CDW} and the phonon energy is strongly connected to the crystal lattice and its structural changes as described in the previous chapter 4.1.2, we can reach the conclusion that the charge order is predecessed by a structural change most likely on only short distances. For a commensurate charge density wave in a strong coupling limit, the ordering in the electronic density is usually interlocked with the minima of the shortened chemical bonds or clusters in the crystal lattice. In that sense, the precursor effect especially visible in the phonon energy points towards a more structurally driven system in line with a strong electron-phonon coupling picture.

As soon as the charge density wave develops, the crystal lattice is distorted into an inverse Star-of-David structure according to DFT calculations [52] and the commensurate CDW re-folds the phonon bandstructure. The result of the folded phonon bands leads to the development of several new Raman active zone folded phonon modes, changing especially the low energy region of the spectra. The measurements in both symmetries for varying temperatures are depicted in Fig. 4.2.14 with a focus on the low-intensity regime. Panel

(a) and (b) depict exemplary distinctive features arising at the lowest temperatures compared to slightly above T_{CDW}. Four new peaks are found in A_{1g} symmetry and seven in E_g symmetry, all peaks marked with an asterisk or orange diamonds. The highest wavenumber peak in E_g (240 cm^{-1}) as well as in A_{1g} (243 cm^{-1}) are only barely if at all visible at 577 cm^{-1} excitation laser, but is more pronounced for green and blue (Fig. 4.2.4) and was therefore also identified as a phonon rather than noise. It was nevertheless excluded from the following analysis due to the very weak response. The temperature dependence is visualized in panels (c) and (d) by consecutively offsetting spectra by 1.55 cts/(s mW) for temperatures as indicated. The last spectra above the CDW phase are plotted in black, several peaks become visible right at the next temperature, whereas others need lower temperatures to develop a significant contribution to the spectra.
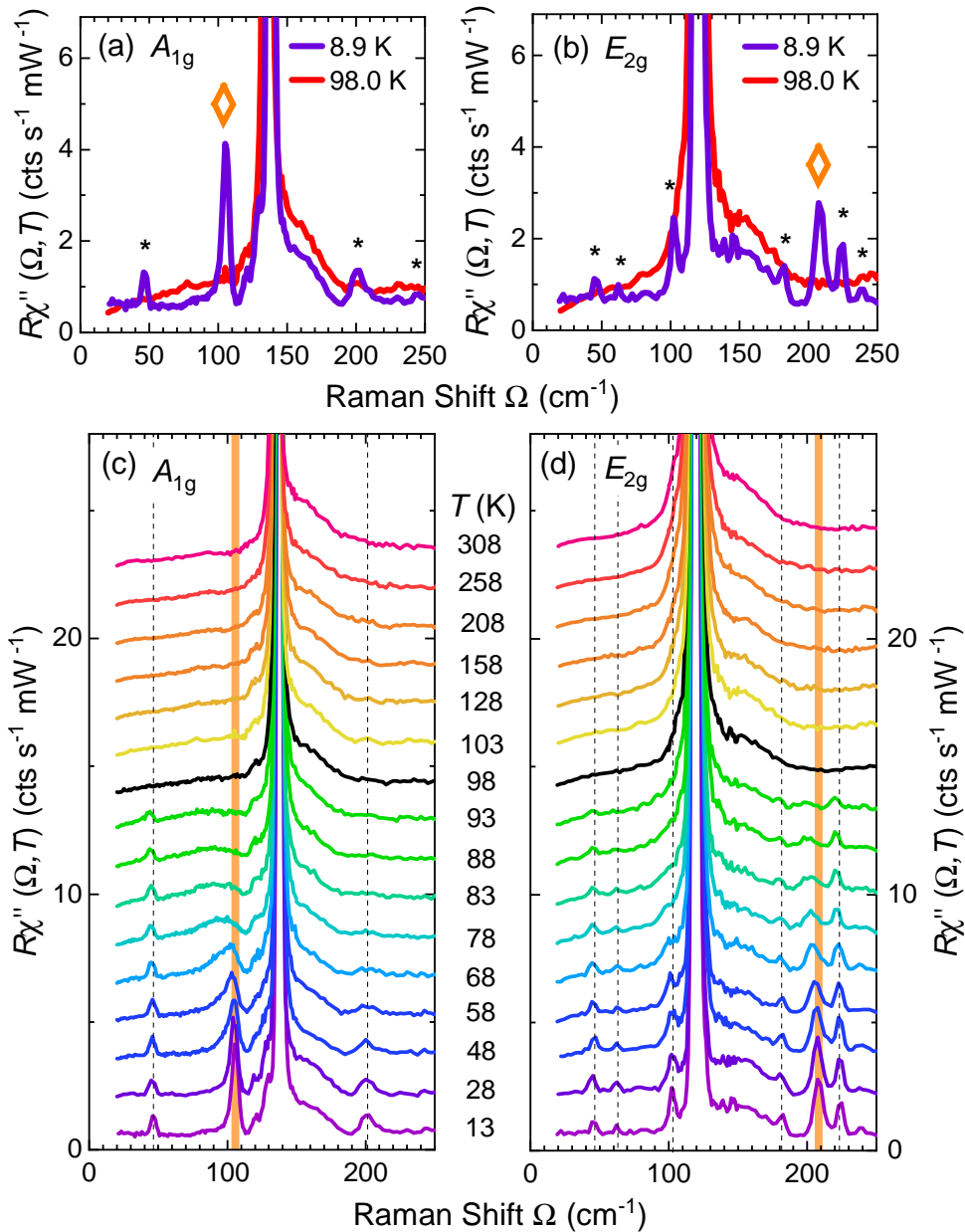
Figure 4.2.14.: Emergence of new Raman active phononic modes in both symmetries below T_{CDW}**.** Panel (a) and (b) display the final difference between well below and slightly above the charger order transition with new for now as zone-folded phonons (ZF-phonons) identified peaks marked with an asterisk or orange diamonds. (c) and (d) give the T-dependent development with consecutively offset spectra with temperatures as indicated. Black curves correspond to the temperatures directly above T_{CDW} as the starting point of the rising peaks.

It can be already observed visually that not all peaks behave similarly or as expected for a phonon in this energy and temperature range below 95 K. Two modes, one in A_{1g} and one in E_g, which are marked with orange asterisks or lines, exhibit way stronger hardening and sharpening than the others. Usually due to a lack of thermal energy lattice vibrations freeze in at specific energies and linewidths in these temperature regions below 100 K. To investigate further, we carried out a very similar analysis as for the two phonons observable

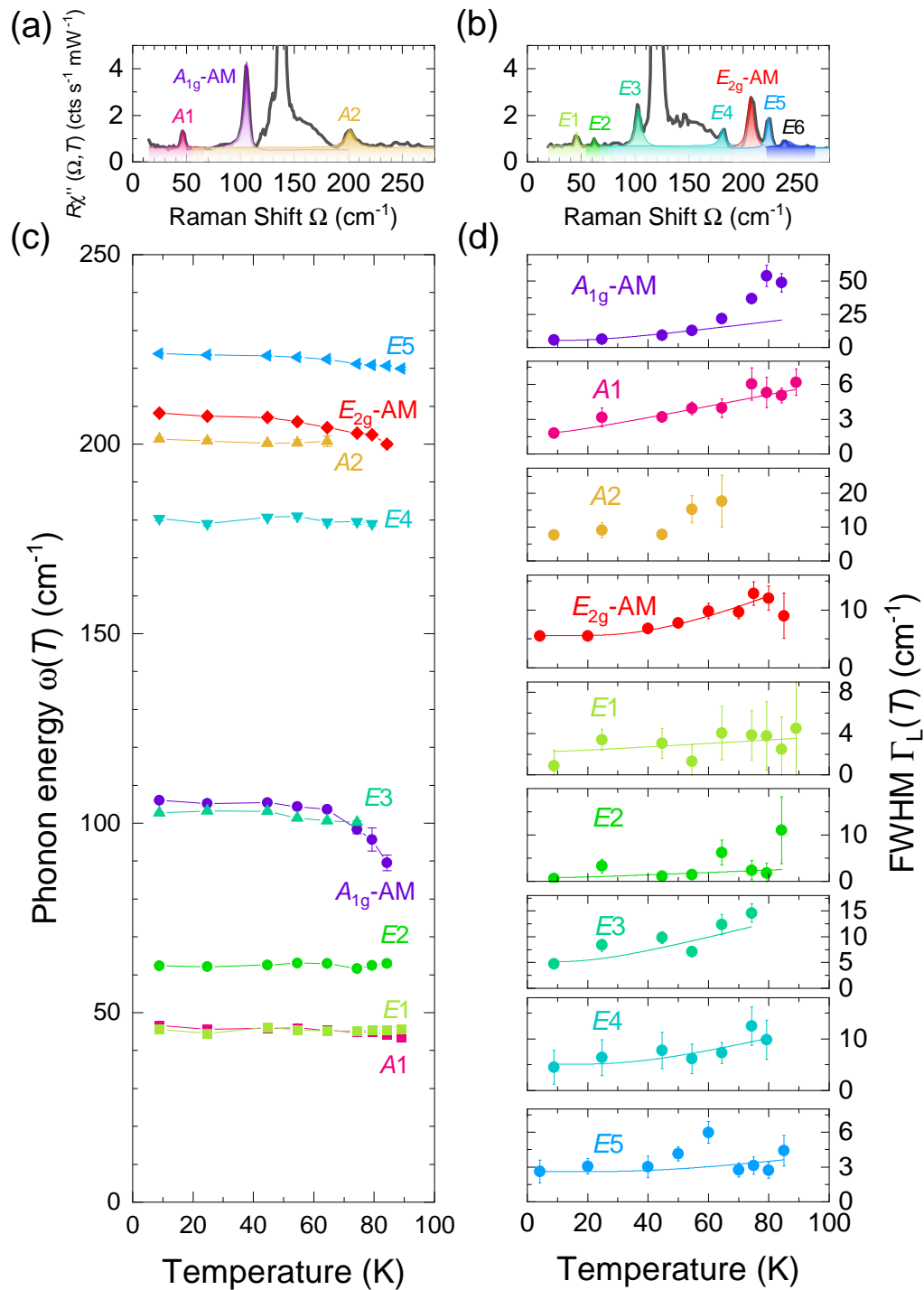in the whole temperature range, presented in 4.2.15.

Figure 4.2.15.: *T*-resolved phonon energies and linewidths of presumably zone-folded phonons. (a) and (b) name the individual peaks marked with their different fits in a specific color for the A_{1g} and E_g spectra at the lowest temperatures. Panels (c) and (d) give an overview of all the phonon energies and linewidths against temperature. The linewidths are fitted by employing Eq. 4.1, the only exception is the A2-mode, since the intensity is too weak and the noise too high to extract reasonable parameters.

From the Voigt functions we obtained the phonon energy and linewidths, the latter was fitted using an anharmonic decay model, which allows the extraction of the phonon-phonon coupling parameter $\lambda_{\text{ph-ph},i}$. The results are plotted in Fig. 4.2.15, $\lambda_{\text{ph-ph},i}$ of each mode is displayed in Tab. 4.2.2. As an exception, the A2 mode shows a too weak intensity for temperatures above $50\,\text{K}$ to allow a sensible evaluation and a subsequent fit for its coupling strength. Nevertheless, we arguably can find all of these peaks clearly, most pronounced with $514\,\text{nm}$ excitation laser up to at least $88\,\text{K}$. The observation by Wu *et al.* [79] regarding the emergence of several ZF-phonons at T_{CDW} and others at the presumable second charge ordering transition $T* = 70\,\text{K}$ or their anomalous behavior around this temperature cannot be reproduced with our data. The correctness of their description via a Landau free-energy model cannot be testified by this work.

Phonon	$A_{1g}(AM)$	$A_{1g}(1)$	$A_{1g}(2)$
$\omega_i(0)$ [cm^{-1}]	105	46	202
$\Gamma_{\text{L},0}$ [cm^{-1}]	5.3	1, 8	7.5
$\lambda_{\text{ph-ph},i}$	2.13 ± 0.43	0.44 ± 0.08	$--$
Phonon	$E_{2g}(AM)$	$E_{2g}(1)$	$E_{2g}(2)$
$\omega_i(0)$ [cm^{-1}]	208	43	60
$\Gamma_{\text{L},0}$ [cm^{-1}]	5.6	2.3	0.8
$\lambda_{\text{ph-ph},i}$	3.39 ± 0.39	0.37 ± 0.2	0.72 ± 1.31
Phonon	$E_{2g}(3)$	$E_{2g}(4)$	$E_{2g}(5)$
$\omega_i(0)$ [cm^{-1}]	101	180	224
$\Gamma_{\text{L},0}$ [cm^{-1}]	5.2	9.1	3.5
$\lambda_{\text{ph-ph},i}$	1.09 ± 0.58	0.95 ± 0.76	1.11 ± 0.74

Table 4.2.2.: Phonon energy, linewidth and phonon-phonon coupling $\lambda_{\text{ph-ph},i}$ of the newly arising peaks below T_{CDW}. The position and shape were extracted via a Voigt fit and the linewidth was fitted making use of Eq. 3.26. Two modes behave differently than expected, yielding a very high $\lambda_{\text{ph-ph}}$, they are placed at the front and marked with (AM).

The observed ZF-phonons exhibit usual behavior in their hardening, yielding maximal shifts in energy of around $2-4$ cm^{-1} for most of them. When inspecting the phonon energy equation (Eq. 4.4), one finds the lattice contraction upon cooling to be a material-dependent factor, which is adjusted by the Grüneisen parameter γ_i. As the lattice contraction slows down drastically below approximately $100\,\text{K}$, only small changes in the phonon energy are expected. Similarly, the anharmonic decay channels need defects and thermal energy to be available, thus they freeze out at low energies. Two of the peaks, one in A_{1g} (105 cm^{-1}) and one in E_g (208 cm^{-1}), exhibit strong deviations at these low temperatures when compared to the other curves regarding their energy, linewidth, and subsequent phonon-phonon coupling. As they do not behave as a phononic mode, a different origin in a CDW phase might stem from the collective oscillation of the amplitude of the order parameter, a so-called amplitude mode (AM). Their behavior is discussed in the next section. On a side note, similar findings regarding these peaks in CsV_3Sb_5 by Wu *et al.* [79] and their emergence below T_{CDW} were described as all being amplitude modes. We do not agree with this approach, as several other CDW system were found to have distinctive differences in the behavior of ZF-phonons and their AMs and consequently a vastly different physical explanation. This

is also applicable here, since we find similarly strong deviations in the trends for the here observed excited modes.

Amplitude mode of the charge density

Apart from the emergence of ZF-phonons, as they become Raman active due to the structural distortion of the lattice, and an energy gap, the charge density condensate also interacts with electromagnetic radiation and can therefore be found in Raman spectra. Thus, we can also study the collective excitations of electrons in the form of an oscillation of the electron density $\rho(r)$. From the introduced modulation of the electronic density in Eq. 2.1, we can think of two different properties of the electron collective to be excited, either the phase or the amplitude of the charge modulation. An example of a linear chain of atoms in connection with a charge order in the limit $q = 0$ is displayed in Fig. 4.2.16. A phason describes the displacement of the electron density, leading to a change of the dipole moment, thus pulling the atom pairs with them (panel (a)). These modes are therefore observable in infrared spectroscopy. The amplitudon or AM corresponds to an oscillation in the amplitude of the electron density (panel (b)), which leads to an optical wave in the 1D-chain of atoms. This form of oscillation is Raman active and gives a fingerprint of the T-dependence and interaction strength of the CDW condensate.

(a)   phason   (b)   amplitudon

Figure 4.2.16.: Schematic explanation of the two vibrational modes in a linear chain of atoms interlaced with a charge density wave. The depicted phason changes the dipole moment and is consequently infrared active, whereas the amplitudon describes a Raman active oscillation. The latter can be used to investigate the properties of the electron collective via Raman spectroscopy. Picture adapted from [67].

In contrast to the energy of phononic modes, the excitation energy of amplitude modes depends on the localized density of the charge order. Coming from low temperatures, the lack of thermal energy leaves a very clear peak, similar in energy to a phonon. Upon warming up, the peak broadens and moves to lower energies faster, than is the case for lattice vibrations, especially in the temperature range below $100\,\text{K}$. In a weak-coupling limit, the resonance frequency of the AM can be described with the mean-field theory, yielding $\omega_{\text{AM}} \propto (1 - T/T_{\text{CDW}})^\beta$. So, in an ideal scenario, a clear broadening and shift in energy to zero wavenumbers of the peak would be a characteristic signature for an AM. In CsV_3Sb_5, we find two peaks that do not fit the expected phononic behavior and were therefore identified as AM. The energy and linewidth of the A_{1g} mode at $105\,\text{cm}^{-1}$ and the E_g mode at $208\,\text{cm}^{-1}$ are plotted on a T_{CDW}-scale in Fig. 4.2.17, with data from two different samples to indicate the clear overlap. Both exhibit very strong energy shifts and phonon-phonon-coupling parameter values $\lambda_{\text{ph-ph},i}$, especially in A_{1g} symmetry. Here, the anharmonic fit model fails to describe the linewidth above $60\,\text{K}$, whereas the fit seems to be acceptable in

E_g for all of its existence. Regarding the hardening of the excitation, the mean-field approximation cannot reproduce the behavior of the peak centers when approaching T_{CDW}.
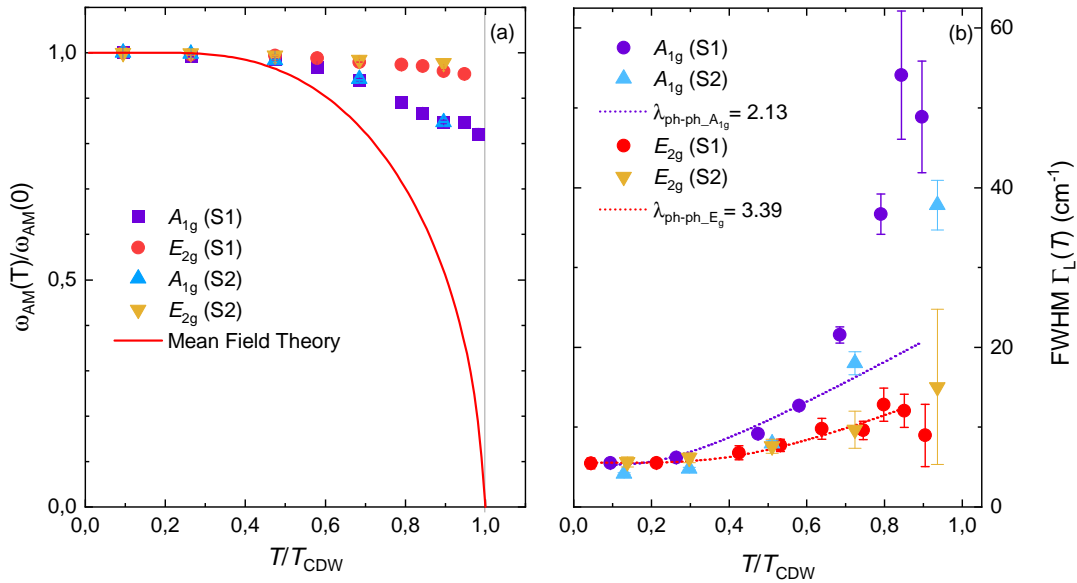

Figure 4.2.17.: Normalized peak position and connected linewidths of the A_{1g} and E_g AM plotted against T_{CDW}. The data was obtained from two different samples to make sure, not only the sample quality determines these observations. The resonance frequency cannot be reasonably described by a mean-field approximation, similar to the inability of the anharmonic decay model to describe the A_{1g} linewidth. A discussion of the meaning of these findings is given in the text.

Most likely, we can understand this fact through two potential explanations. For one, the mean-field theory is not valid for a first order phase transition, which is presumably found in this material by heat capacity measurements. Or secondly, defects or foreign atoms in the crystal can lead to strong localization of the electronic density around these specific points, which does not allow the slow shift to zero wavenumbers. Here, the electrons would be bonded too strongly for the small additional thermal fluctuations to allow these strong shifting effects. An example would be given by measurements on different crystals belonging to the tritellurides, performed by Hans Eiter [67]. Here, discrepancies between mean-field theory and data were observed for temperatures close to their charge ordering transition in a magnitude connected to their crystallinity. Very clean crystals could resolve the AM down to only a few wavenumbers. But this explanation has a weak point, as the AM of the tritelluride samples is tracked with slight adjustments by the mean-field basically until the peak vanishes, whereas we obtained the peak position very close to the phase transition without it being matched with the mean-field fit. A second example regarding the T-dependence of the AM was observed in the CDW phase of $2H$-TaS$_2$ by Grasset *et al*. [122]. They observed two amplitude modes in E_g^2 and A_{1g}, following the mean-field approximation very closely for varying temperature and pressure down to either less than half of its final energy in the pressure case or to around 75% in the case of varying T. The magnitude of Raman shift is therefore comparable to our scenario, yet the mean-field ap-

proximation is only invalid for the here observed AM in CsV_3Sb_5. Hence, we conclude the observations to be a result of a first order phase transition.

Another interesting aspect revolves around the shape changes of the A_{1g} AM. Upon closer visual inspection the peak seems unconventional and cannot be described by a simple Voigt shape. In Fig. 4.2.18, three different fit approaches were tested.

First, an already successfully utilized Voigt function. Secondly, as described by Wu *et al.* [79] coming from a Landau free energy model, it is argued that each A_{1g} mode is a doublet of two close modes, therefore a fit with a double Voigt function was taken. And finally a Fano-function convoluted with a Gaussian was used. This allows the description of asymmetric peaks, usually applied when the vibrational mode interacts with an electronic continuum. In all three cases, the Gaussian was fixed to account for the constant width of the spectrometer entrance slit.

Panel (a) of Fig. 4.2.18 displays the experimental data at $68\,\mathrm{K}$ with the three different fits. Purely visually viewed with the fitting functions as a guide to the eye, we for one cannot see any hump-like structure pointing towards two peaks, nor can we see a simple symmetric shape of a Lorentzian. This is also reproduced by the R^2-values against temperature in panel (b), revealing the Fano shape describing the observed peak shapes best, followed quite closely by the two Voigt functions. For clarification, the respective residua are compared between the Fano and Lorentzian in (c) and between Fano and double-Lorentzian in (d). As expected after the R^2 comparison, the Fano shape yields over the complete temperature range the smallest deviations to the data. From there, panels (e), (f), and (g) plot the peak energy and linewidth of the extracted data for the Fano, single Lorentzian, and double Lorentzian, respectively. The approximate peak position and corresponding linewidth for the single peak fits reveal comparable T-dependencies, tracking the visually guessed position well. In contrast, the two peak fit allows no distinction of the peak position and linewidth behavior, as the fit is heavily over-parameterized. How the earlier discussed group obtained reasonable peak and linewidth changes with these overfitted functions [79], is unknown to us. Likely a single Lorentzian was used for these characteristic properties and a two-peak fit for a cleaner description of the peak shape. We conclude this fitting procedure with the statement, that the A_{1g} AM behaves according to a single peak picture and is best described by a Fano function convoluted with a Gaussian. This is qualitatively given via its visually asymmetric shape, as well as quantitatively due to its better statistical validity.
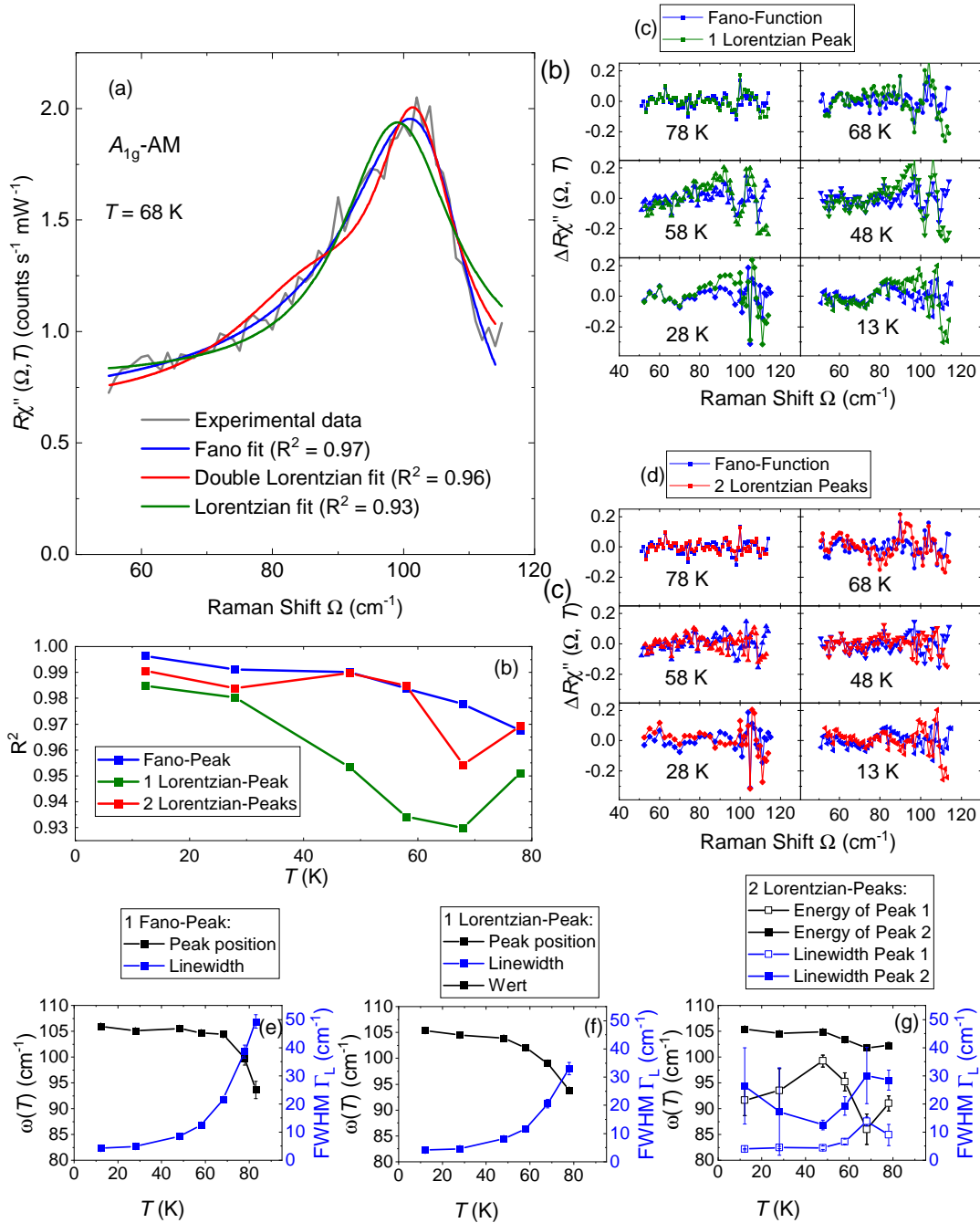
Figure 4.2.18.: Fitting results of the A_{1g} **AM, comparing different fit functions.** (a) Data at $68\,\mathrm{K}$ in grey fitted with a Fano-Gaussian convolution (blue), a Lorentzian (green), and a double-Lorentzian (red) with visually and statistically the best fit by the Fano function. (b) R^2- values of the different fit functions for all temperatures. (c) and (d) display a comparison of the residua for each individual temperature between Fano and Lorentzian or Fano and two Lorentzian, respectively. Panels (e)-(g) plot the peak positions and linewidths, with sensible trends for the two single peak functions, whereas the two Lorentzian shows over-fitted characteristics and gives no clear, physically realistic T-dependence. Thus, we conclude the Fano shape to be the best descriptor of the A_{1g} AM.

The Fano resonance is usually a consequence of strong interactions, mostly in the form of high electron-phonon coupling. To our knowledge, this is the first observation of an

asymmetric AM, hinting toward strong electron-AM interactions. By using a Fano shape according to Eq. 3.27, one receives a value for the asymmetry as $1/|q|$, which is plotted for both samples next to data of one sample of which it was extracted in Fig. 4.2.19. We observe a non-monotonic behavior in both samples, exhibiting a maximum asymmetry at around $68\,\mathrm{K}$.
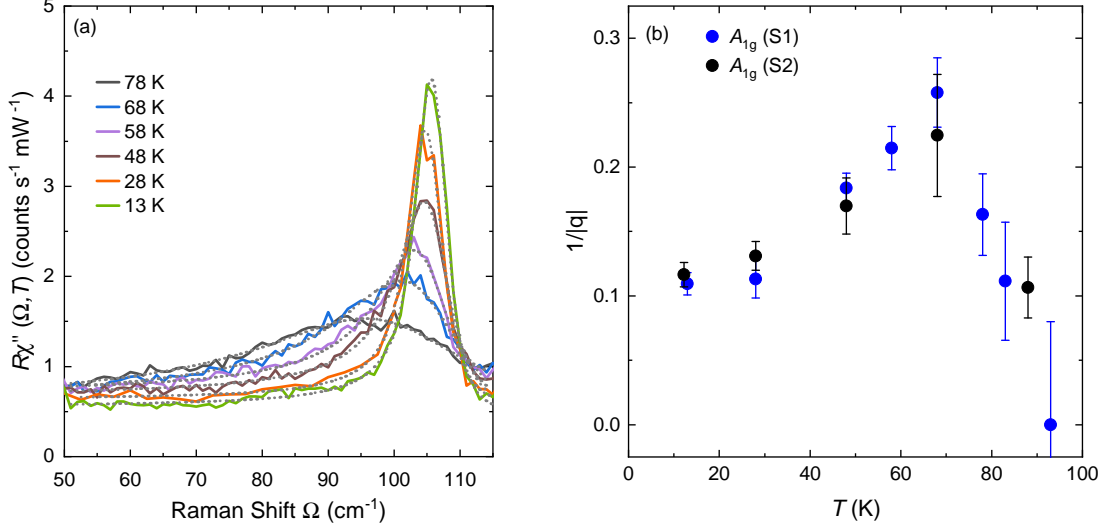

Figure 4.2.19.: Asymmetric shape of the A_{1g} AM, pointing towards a strong coupling interaction with this specific collective mode. (a) Close-up of the Raman data in the A_{1g} region at temperatures as indicated with the fits in grey dotted lines. (b) The resulting asymmetry factor $1/|q|$ behavior is non-monotonic with a maximum at approximately $68\,\mathrm{K}$.

Two questions about the existence of this asymmetry remain. Why does this mode show such a strong electron-AM interaction at all and where is its non-monotonic behavior coming from? Regarding the latter, the electron-AM interaction is presumably to a great extent dependent on the available DOS. From the earlier discussed T-dependence of the energy gap in A_{1g}, we cannot find a clear solution. Here, the spectral weight difference seems practically constant upon warming up, before rather sharply increasing at around $70\,\mathrm{K}$. This behavior was attributed to a region of strong anomalies, connected to a change in the CDW-superstructure along the c-axis [76]. In this temperature region, we would expect our measurements to be already in the gapped domain, where a potential interaction from the DOS should be smallest. While this is the case for the energy region of 200 to $1600\;\mathrm{cm}^{-1}$, we found a different behavior in the low energy regime below $100\;\mathrm{cm}^{-1}$ in Fig. 4.2.12. We observed a first increase in spectral weight upon cooling towards a maximum at approximately $68\,\mathrm{K}$, before this weight collapsed on the course towards the lowest temperatures. While this is partially explained already by the sharpening of the AM in A_{1g}, the general maximum in small energy electronic excitations in this region is still clearly visible. Such a high response is presumably connected to either a high DOS in this energy region or potentially to fluctuations of the order parameter of the c-axis modulation of the CDW phase. The AM as a collective mode of the electronic density could couple to both of these

electronic phenomena, leading to the observed non-monotonic $1/|q|$ against T behavior. The question as to why this mode exhibit this interaction in the first place is presumably a fingerprint of the strong coupling regime of the CDW phase in CsV_3Sb_5, analogous to a strong electron-phonon coupling picture in other systems having Fano-shaped peaks [107].

The anomalous nature indicating a strong coupling picture around this A_{1g} AM is therefore twofold: for one, the inability to describe the linewidth with a simple anharmonic decay model, and for another the strong AM interaction with the electronic continuum presumably at low energies. Combined with the observation of a vastly too high energy gap of $2\Delta/k_B T_{\mathrm{CDW}} \sim 21 - 23$ and a polarization dependence of the latter which maps large zones of the Fermi surface instead of only the nesting points, we conclude that these Raman results support a strong coupling picture of the CDW phase in CsV_3Sb_5.

5. TERS - Raman studies beyond the diffraction limit

The second part of this thesis addresses the development and implementation of a LT-UHV-TERS system. With such a functional low-temperature system enabling locally confined Raman measurements, several paths for subsequent research on surfaces, bulk defects and thin films are possible. For example, even though most high-T_c superconductors are considered rather homogeneous, BSCCO displayed inhomogeneities of the superconducting gap on nanometer scales in STM experiments [123]. Additionally, the superconducting properties of various cuprates have been found to be greatly influenced by defects, grain boundaries and strain influences [124], as well as being easily tune-able upon reducing layer numbers down to monolayers [125]. Since conventional Raman scattering already lead to great insights to the nature of these unconventional superconductors, the extraction of localized spectroscopic fingerprints has the obvious potential in understanding the mechanism of high-T_c superconductivity and guiding future application paths. Similarly of interest are topological insulators with their characteristic metallic surface states [126, 127]. Another option for a material choice lies in the earlier investigated kagome superconductor CsV_3Sb_5 (c. chapter 4.2). One of the issues is displayed in Fig. 5.0.1. The conventional Raman measurements probe big volumes in bulk materials and one obtained result is the large energy gap in the charge-ordered phase, as displayed in panel (a). As already stated, this points towards a strongly coupled system, which seems to be in contrast to the Fermi surface nesting picture drawn by STM and ARPES with their much smaller energy gaps. These differences might arise from the latter two measurement techniques studying a one-particle, whereas Raman observes a two-particle picture. The newly developed setup allows the investigation of both sides at the same position, in addition to surface-sensitive Raman measurements, which could give a conclusion about surface-related issues in this matter.

The task for this thesis was to prepare the way towards these potential study objects. Most existing TERS systems are based on either refractive objective lenses with long-working distances [48, 128], as they have excellent imaging properties or an on-axis parabolic mirror for minimal spot size and optimal focusing [129]. As one of the main innovations, the here developed setup is centered around an off-axis parabolic mirror with a high numerical aperture of 0.85. This optical configuration yields minimal spot sizes, low elastic stray light, and access to all polarization combinations, thus being well suited for the application on studies of the charge, spin, and lattice dynamics in correlated materials. Ag-based tips were utilized due to their favorable optical properties at visible wavelengths and higher potential field enhancement [130]. Unfortunately, tips made from this metal are prone to
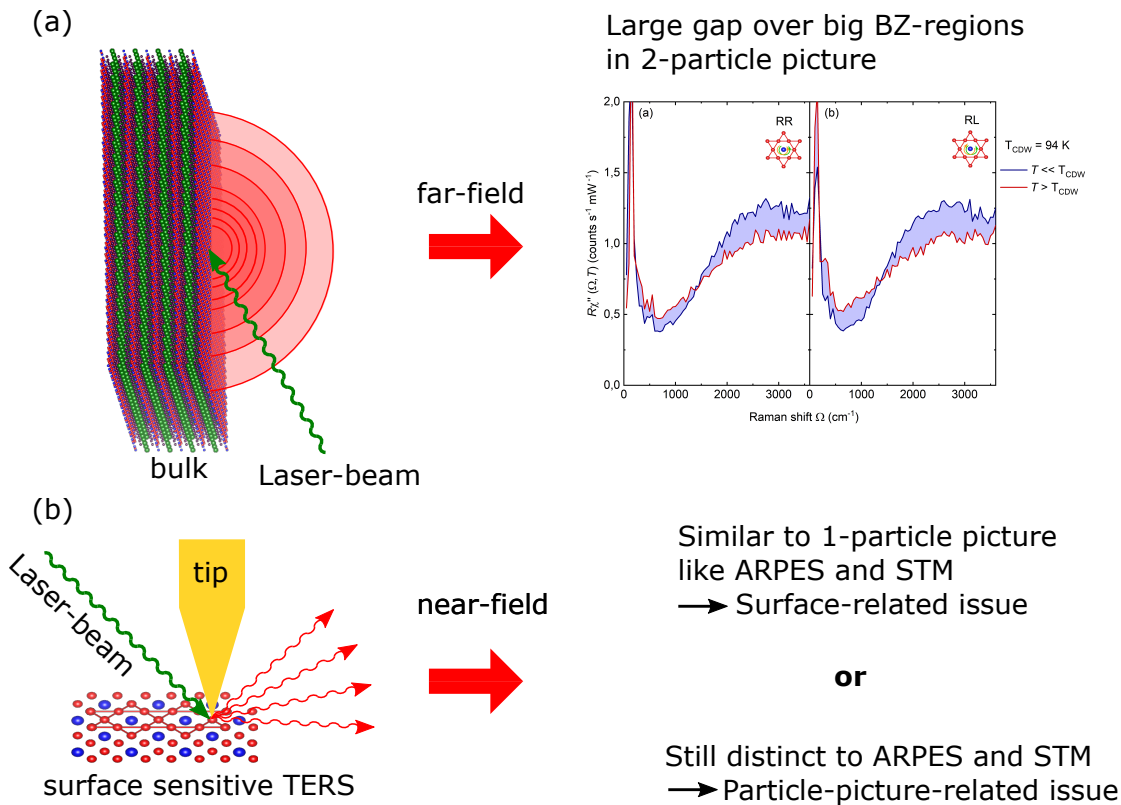
Figure 5.0.1.: Potential usage of a low temperature TERS system on CsV_3Sb_5 to investigate discrepancies brought up by different measurement techniques.

strong surface contamination, reducing their potential to zero in the course of hours [131]. A key innovation was consequently an in-situ transfer- and cleaning system. The resulting setup was proceedingly verified to exhibit strong tip enhancement beyond the diffraction limit at the lowest temperatures while maintaining access to selection rules. This was done on single-walled carbon nanotubes (SWNT) dispersed on a thin gold-film to make use of the "gap-mode" [132] and resulting higher potential enhancement factors. Unfortunately, studies on the proposed compounds like high T_c-superconductors, topological insulators, or CsV_3Sb_5 could not be realized yet due to time limitations.

5.1. Motivation and basic ideas

A theoretical overview of the fundamental properties of optics, its resolution limits, and methods to overcome the latter is given in the following pages. A more detailed description can be found in Ref. [133].

5.1.1. Angular spectrum representation

In the following section, the angular spectrum representation is introduced as a powerful mathematical tool, enabling the description of optical fields in homogeneous media. Under this representation, one understands the series expansion of plane and evanescent

waves with variable amplitudes and directions. As an example, one looks at the scattering problem drawn in Fig. 5.1.1.
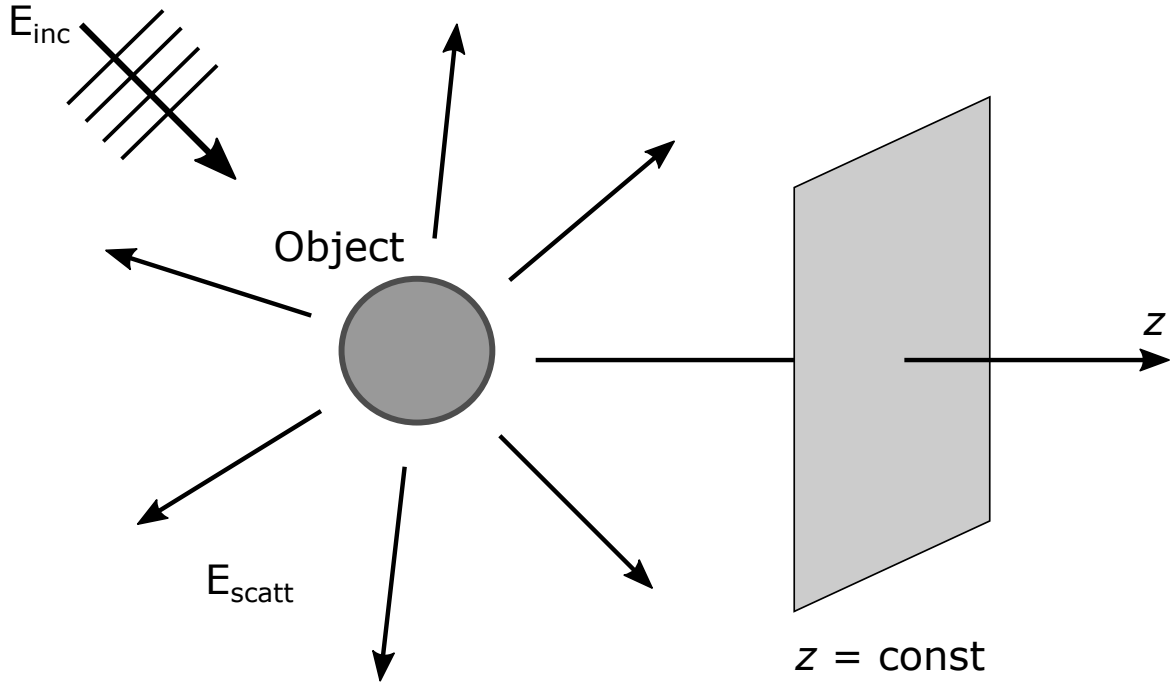

Figure 5.1.1.: Schematic for the angular spectrum representation. An incoming oscillating electric field gets isotropically scattered by an object, the resulting fields are evaluated at a plane perpendicular to an arbitrarily chosen axis z. The object is assumed to be at $z = 0$.

As a starting point, $\mathbf{E}(\mathbf{r})$ shall be the electric field at point $\mathbf{r} = (x, y, z)$ and $\mathbf{E} = \mathbf{E}_{inc} + \mathbf{E}_{scatt}$. We then define an arbitrary axis $\mathbf{z}$ and evaluate $\mathbf{E}$ in a plane $z = const$ being perpendicular to $\mathbf{z}$. In this plane, we can now evaluate the two-dimensional Fourier transformation of the electric field:

$$\hat{\mathbf{E}}(k_x, k_y; z) = \frac{1}{4\pi^2} \iint\limits_{-\infty}^{+\infty} \mathbf{E}(x, y, z) e^{-i[k_x x + k_y y]} \mathrm{dxdy}, \tag{5.1}$$

with k_x, k_y being the spatial frequencies or reciprocal coordinates corresponding to the Cartesian transverse coordinates x, y. The inverse Fourier transform is written as:

$$\mathbf{E}(x, y, z) = \iint\limits_{-\infty}^{+\infty} \hat{\mathbf{E}}(k_x, k_y; z) e^{i[k_x x + k_y y]} \mathrm{d}k_x \mathrm{d}k_y. \tag{5.2}$$

In the case of a time-harmonic optical field $\mathbf{E}$ with angular frequency ω in an homogeneous and isotropic medium, $\mathbf{E}$ has to fulfill the wave equation

$$(\Delta^2 + k^2)\mathbf{E}(\mathbf{r}) = 0, \tag{5.3}$$

with $k = \frac{2\pi n}{\lambda}$ and the refractive index $n = \sqrt{\mu \varepsilon}$, as well as the wavelength of the light λ. When we insert the Fourier representation of $\mathbf{E}(\mathbf{r})$ from Eq. 5.2 into the wave equation and

define

$$k_z \equiv \sqrt{k^2 - k_x^2 - k_y^2} \quad \text{with} \quad \text{Im}\{k_z\} \geq 0 \tag{5.4}$$

we can find, that the Fourier spectrum $\hat{\mathbf{E}}$ travels along the z-axis:

$$\hat{\mathbf{E}}(k_x, k_y; z) = \hat{\mathbf{E}}(k_x, k_y; 0) \mathrm{e}^{\pm i k_z z}. \tag{5.5}$$

The $+$ sign represents a wave propagating into the half-space $z > 0$ whereas for $z < 0$ we obtain a $-$ sign. From this equation, we can learn that we find the Fourier spectrum of $\mathbf{E}$ at any arbitrary image plane by multiplying $\hat{\mathbf{E}}$ in the object plane at $z = 0$ by the factor $\exp(\pm i k_z z)$, which is called the *propagator* in reciprocal space. By using Eq. 5.2 and 5.5, we get for arbitrary z the *angular spectrum representation*:

$$\mathbf{E}(x, y, z) = \iint\limits_{-\infty}^{+\infty} \hat{\mathbf{E}}(k_x, k_y; 0) \mathrm{e}^{i[k_x x + k_y y \pm k_z z]} \mathrm{d}k_x \mathrm{d}k_y. \tag{5.6}$$

Two scenarios can be distinguished from this equation:

$k_x^2 + k_y^2 \leq k^2$**:** for low spatial frequencies, k_z is real and the factor $\exp(i|k_z|z)$ becomes an oscillatory function. The wave propagates along the k-direction in the form of a *plane wave*.

$k_x^2 + k_y^2 > k^2$**:** for high spatial frequencies k_z is imaginary, leading to an exponentially decaying function for $\exp(-|k_z|z)$, corresponding to an *evanescent wave*.

Thus, indeed we find the angular spectrum to be a superposition of evanescent and plane waves. The latter are oscillating functions traveling infinitely in all directions, transporting information as the "far-field" to the detector of optical experiments. The possible bandwidth lies between $(k_x^2 + k_y^2) = 0$ for propagation along the z-direction with no transverse oscillation and $(k_x^2 + k_y^2) = k^2$ for a direction perpendicular to the z-axis with highest spatial oscillation frequency in the transverse plane. On the other hand, even higher oscillation frequencies are governed by evanescent waves, decaying on shorter distances along the z-axis for higher spatial frequencies. This leads to practical limitations to the extent of the bandwidth towards high frequencies.

5.1.2. The diffraction limit of light

The evanescent waves just discussed become negligible for any optical configuration, where the object and its image are further apart than λ. This leads to a hard boundary of the optical resolution, as only the far-field component in the form of plane waves can transport information further. The resolution limits of the far-field are going to be presented in the next section.

To calculate the diffraction limit of the far-field, we first look at the point spread function as a measure of the resolving power of the optical system. This function allows the description of the broadening of a single radiating point source as a direct consequence of spatial

filtering. When the wave propagates away from the source further than the wavelength, not all components in addition to the decaying evanescent waves can be collected, leading to a reduction of the spatial bandwidth. This reduction prohibits a full reconstruction of the original point source, leading to a finite spot size. In most optical regimes at the sub-wavelength regime, particles scatter as an electric dipole as the smallest electromagnetic unit. In its most general form, we can write the electric field at the point $\mathbf{r}$ by utilizing the dyadic Green function $\bar{\mathbf{G}}(\mathbf{r}, \mathbf{r}_0)$ as:

$$\mathbf{E}(\mathbf{r}) = \frac{\omega^2}{\varepsilon_0 c^2} \bar{\mathbf{G}}(\mathbf{r}, \mathbf{r}_0)\mathbf{p}, \tag{5.7}$$

with the dipole located at $\mathbf{r}_0$ and a dipole moment $\mathbf{p}$. By assuming the distance of the dipole and the objective lens to be much further than the wavelength λ, we can neglect contributions of the evanescent waves. Then the Green function allows the description of the mapping of an electric dipole from its source to its image. The result depends on two characteristics of the primary objective lens in the optical system, for one the numerical aperture NA:

$$\mathrm{NA} = n \sin \theta_{max} \tag{5.8}$$

using θ_{max} as the maximum angle, under which light can enter the objective. For another the (transverse) magnification M is relevant, given by:

$$M = \frac{n \cdot f'}{n' \cdot f}. \tag{5.9}$$

n, n', f, f' are the refractive indices and the focal lengths on the object and image side, respectively. We use these definitions to describe the quantity $|\mathbf{E}|^2$ in the form of the point spread function for a dipole oriented along the x-axis as it is the relevant quantity for the optical system:

$$\lim_{\theta_{max} \ll \pi/2} |\mathbf{E}(x, y, z = 0)|^2 = \frac{\pi^4}{\varepsilon_0^2 nn'} \frac{p_x^2}{\lambda^6} \frac{NA^4}{M^2} \left[2\frac{J_1(2\pi\tilde{\rho})}{2\pi\tilde{\rho}} \right]^2, \qquad \tilde{\rho} = \frac{\mathrm{NA}\rho}{m\lambda}. \tag{5.10}$$

Here, ε_0 is the dielectric constant, p_x is the dipole moment along the x-axis, J_1 is the first order Bessel function and ρ is the distance of the center of the dipole. The term in the brackets is the well-known Airy function. One can define the Airy disk radius as the width of the point spread function Δx at which the point spread function becomes zero:

$$\Delta x = 0.6098 \frac{M\lambda}{\mathrm{NA}} \tag{5.11}$$

The resulting disk is proportional to the wavelength and the magnification and inversely proportional to the numerical aperture of the optical system. On the basis of this result one may determine the minimal distance of two point sources separated by $\Delta r_{||} = \sqrt{\Delta x^2 + \Delta y^2}$ in the object plane below which they cannot be distinguished in the image plane. The setup for the following discussion is illustrated in Fig. 5.1.2.
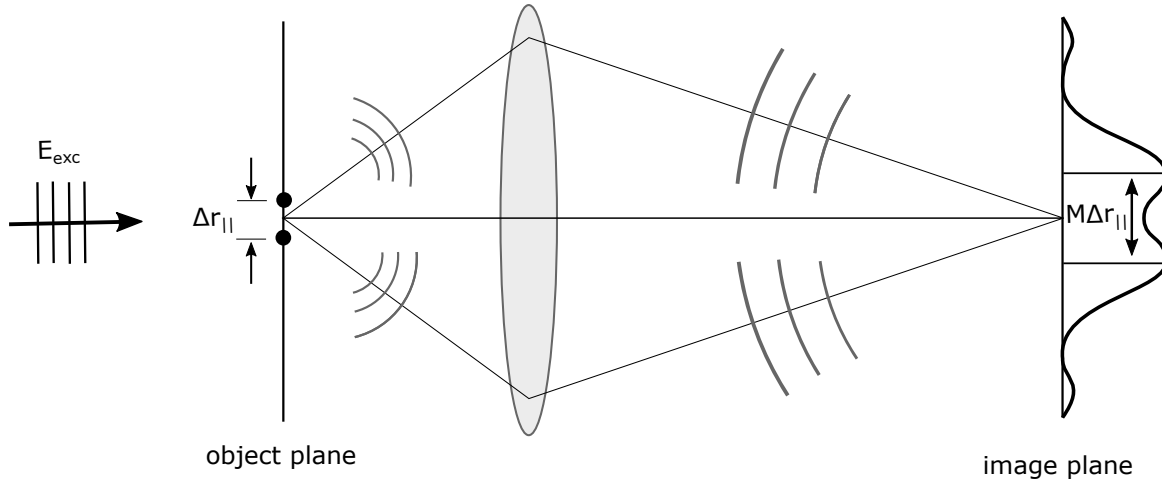
Figure 5.1.2.: Schematic explanation of the diffraction limit. Two points separated by $\Delta r_{||}$ in the object plane act as scattering centers for an incoming light beam, where the resulting waves are collected with an optical system having a numerical aperture NA. The distance of the maximal intensity of the collected light at the focus point in the image plane is dependent on the magnification M of the optical system. The resolution limit gives the minimal distance of $\Delta r_{||}$ at which the two point sources can be distinguished.

The two point emitters are mapped in an overlapping fashion into the image plane. The boundary of indistinguishability can be defined as the separation of the two maxima of the respective point spread functions by the width of one of them: the narrower the point spread function the better the resolution. The resolving power also depends on the collected bandwidth of spatial frequencies $\Delta k_{||} = \sqrt{\Delta k_x^2 + \Delta k_y^2}$ in the optical system. Similar to the quantum mechanical uncertainty principle, we get

$$\Delta k_{||} \Delta r_{||} \geq 1. \tag{5.12}$$

The upper bound of $\Delta k_{||}$ is given as $k = (\omega/c)n = (2\pi/\lambda)n$ in the far-field optics, leading to an optimal resolution by accounting for the complete spectrum of $\Delta k_{||} = [-k, ..., k]$:

$$\text{Min}\left[\Delta r_{||}\right] = \frac{\lambda}{4\pi n}. \tag{5.13}$$

In an actual experiment, one cannot sample through the entire spectral range of $\Delta k_{||}$, therefore the upper limit will be defined by the numerical aperture of the system, leading to:

$$\text{Min}\left[\Delta r_{||}\right] = \frac{\lambda}{4\pi \text{NA}}. \tag{5.14}$$

Similarly, the formulation by Abbe considers the point spread function of Eq. 5.10 for two dipoles with an axis perpendicular to the optical axis. The distance of the two dipoles $\Delta r_{||}$ is mapped onto the distance $M\Delta r_{||}$ in the image plane. In order to distinguish these, Abbe states that the maximum of one point spread function needs to coincide with the first minimum of the second point spread function. This distance is given by the Airy disk radius discussed earlier and we find for the minimum distance $\text{Min}\left[M\Delta r_{||}\right]$ the well-

known Abbe diffraction limit [134]:

$$\text{Min}\left[\Delta r_{||}\right] = 0.6098\frac{\lambda}{\text{NA}} \tag{5.15}$$

Rayleigh formulated the resolution limit quite similarly, deriving it from calculations regarding a grating spectrometer and not microscopy.

There are several pathways of how to reach resolutions smaller than the given limit, by either prior knowledge of some characteristics or enhancing the numerical aperture by for example 4Pi microscopy [135], but these techniques are still limited by diffraction. In order to truly overcome these limits, one needs to exploit the potential of the evanescent waves disregarded so far.

5.1.3. Evanescent waves and surface plasmons

Evanescent waves never occur in homogeneous matter with constant refractive indices, they emerge only when light interacts with inhomogeneities of interfaces. An example would be a metal-dielectric interface, consisting of two materials differing in their refractive indices. By utilizing evanescent waves and their properties, the diffraction limit can be overcome. We will now discuss, how the information of the near-field can be transmitted using the far-field, before turning to the plasmon properties of a metal generating evanescent waves.
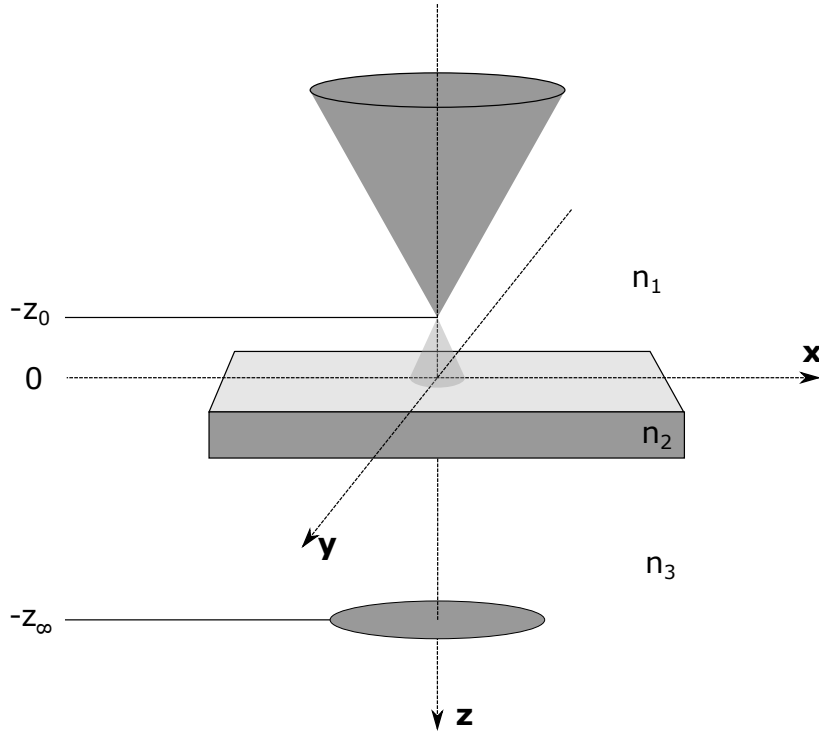
Figure 5.1.3.: Access of evanescent waves via the confinement of a source field at $-z_0$. The sample and the source field are in the vicinity of each other with $z_0 \ll \lambda$, enabling the detection and mapping of high spatial frequencies at the detection plane at $z_\infty \gg \lambda$.

We consider a sample plane at $z = 0$, the source plane at $z = -z_0$, and the detection plane at $z = z_\infty$ as depicted in Fig. 5.1.3. The source is an optical probe used in near-field microscopy, e.g. a very thin tip, generating evanescent waves in its vicinity. The distance z_0 between the sample and the optical probe is in the subwavelength regime. Here, the sample plane acts as an infinitely thin boundary between two media with different refractive indices n_1 and n_2. From the earlier discussed angular spectrum representation, we can write for the source field arriving at the sample before any interaction takes place:

$$\mathbf{E}_{\text{source}}(x, y; 0) = \iint\limits_{-\infty}^{+\infty} \hat{\mathbf{E}}_{\text{source}}(k_x, k_y; -z_0) e^{i\left[k_x x + k_y y \pm k_{z_1} z_0\right]} \mathrm{d}k_x \mathrm{d}k_y. \tag{5.16}$$

From here, we assume the thin sample to be represented by a transmission function $T(x, y)$ in real space, which we convolute with $\mathbf{E}_{source}$ in Fourier space:

$$\hat{\mathbf{E}}_{\text{sample}}(\kappa_x, \kappa_y; 0) = \iint\limits_{-\infty}^{+\infty} \hat{\mathbf{T}}(\kappa_x - k_x, \kappa_y - k_y) \hat{\mathbf{E}}_{\text{source}}(k_x, k_y; -z_0) e^{ik_{z_1} z_0} \mathrm{d}k_x \mathrm{d}k_y, \tag{5.17}$$

with $\hat{\mathbf{T}}((k'_x, k'_y)$ being the Fourier transformed transmission function and $k'_i = \kappa_i - k_i \in \{x, y\}$. The sample field is now supposed to travel to the detector plane, located in the far-field at $z = -z_\infty$.

$$\mathbf{E}_{\text{detector}}(x, y; z_\infty) = \int\!\!\!\int\limits_{-\infty}^{+\infty} \hat{\mathbf{E}}_{\text{sample}}(\kappa_x, \kappa_y; 0) e^{i[\kappa_x x + \kappa_y y]} e^{i\kappa_z z_\infty} \mathrm{d}k_x \mathrm{d}k_y. \tag{5.18}$$

Since $z_\infty \gg \lambda$, the propagator $\exp[i\kappa_z z_\infty]\}$ allows only plane-wave components at the detector. By using the transverse wavenumber $\kappa_\| = \sqrt{\kappa_x^2 + \kappa_y^2}$, these waves fulfill

$$|\kappa_\|| \leq k_3 = \frac{\omega}{c} n_3 \tag{5.19}$$

and when accounting for the finite collection by a lens with numerical aperture NA:

$$|\kappa_\|| \leq k_3 \text{NA}. \tag{5.20}$$

We find $\boldsymbol{\kappa}_\| = \mathbf{k}'_\| \pm \mathbf{k}_\|$, as the transverse wavevectors of the sample $\mathbf{k}'_\|$ is shifted by the spatial frequencies of the source field $\mathbf{k}_\|$, which is a manifestation of the convolution we performed of $\hat{\mathbf{T}}$ and $\hat{\mathbf{E}}_{\text{source}}$. This leads to the following form:

$$\left|\mathbf{k}'_{\|,\text{max}} \pm \mathbf{k}_{\|,\text{max}}\right| = \frac{2\pi \text{NA}}{\lambda}. \tag{5.21}$$

In the case of a confined source with lateral dimensions L, for example in the form of an aperture or tip diameter, the highest spatial frequencies can be estimated to be $\mathbf{k}_{\|,max} \approx \pi/L$ and therefore:

$$\mathbf{k}'_{\|,\text{max}} \approx \left|\frac{\pi}{L} \mp \frac{2\pi \text{NA}}{\lambda}\right| \tag{5.22}$$

Thus, the limit of resolving the sample has a strong dependence on the magnitude of L and λ: for $L \gg \lambda$ we obtain the normal diffraction limit, while for $L \ll \lambda$ the highest detectable spatial frequencies are defined by the confinement given by L. We can conclude that the use of a highly confined source field leads to high spatial frequencies becoming accessible in the far-field, hence the resolution becomes better for higher confinement.

Coming from the near- and far-field interaction, the next question arises with regard to the generation of evanescent waves utilizing a metallic tip. The interaction of light with a metal is by and large described by the Drude model of conduction electrons, predicting the oscillation of charges with a phase difference of $180°$ relative to the electric driving field. The excitation of such surface and volume charge-density oscillations following the interaction of electric fields oscillating at optical frequencies with the metal's free-electron gas are called plasmons. Plasmons are used for various detection systems, the larger field is coined plasmonics [136, 137]. Here, especially the oscillations close to the surface (their quantized quasi-particles are called surface plasmon polaritons, SPP) are of importance, since these quasi-particles give rise to strongly enhanced optical near-fields at metal-dielectric interfaces. Furthermore, the SPPs are bound locally to the surface and do not radiate at planar interfaces. Yet, for specific spatially confined geometries, the properties of SPP can be altered in the near-field as they are scattered at local structures smaller than their wavelength.

This enables the local radiation of these oscillations, which gives an increased interaction potential of the electric field oscillation with its surrounding. This allows the investigation of e.g. inelastically scattered light processes on the spatial scales of the confinement with strongly enhanced scattering probabilities. The high confinement and strong potential enhancement have proven useful in numerous Raman techniques, most pronounced in surface-enhanced Raman spectroscopy (SERS) [138, 139, 140] and tip-enhanced Raman spectroscopy (TERS) [141, 142, 47, 143, 144]. A detailed description of the SPPs and their properties, as derived from the Drude-Sommerfeld model and including interband transitions, are described in detail in Ref. [133]. Here, only the propagation of SPPs along and in close proximity to the interface are presented briefly.

If the plasmon propagates along the metal-dielectric interface of a metal having the complex $\varepsilon_1 = \varepsilon_1' + i\varepsilon_1''$ and a dielectric having ε_2, the wave propagation can be described with the complex parallel wavenumber:

$$k_x = k_x' + ik_x''. \tag{5.23}$$

The real part determines the wavelength of the SPP and the imaginary part the damping of the charge-density oscillation. One obtains:

$$k_x' \approx \sqrt{\frac{\varepsilon_1'\varepsilon_2}{\varepsilon_1' + \varepsilon_2}} \frac{\omega}{c} \quad \text{and} \tag{5.24}$$

$$k_x'' \approx \sqrt{\frac{\varepsilon_1'\varepsilon_2}{\varepsilon_1' + \varepsilon_2}} \frac{\varepsilon_1''\varepsilon_2}{2\varepsilon_1'(\varepsilon_1' + \varepsilon_2)} \frac{\omega}{c}. \tag{5.25}$$

The wavelength of an SPP can then be given as:

$$\lambda_{\text{SPP}} = \frac{2\pi}{k_x'} \approx \sqrt{\frac{\varepsilon_1' + \varepsilon_2}{\varepsilon_1'\varepsilon_2}} \lambda. \tag{5.26}$$

λ is the wavelength in vacuum and if we assume $\varepsilon_2 = -\delta\varepsilon_1'$ with $\delta < 1$, we find the plasmon wavelength to be always shorter than the wavelength in the transparent medium. Ohmic losses lead to an exponential decay of the oscillations along the interface. For the propagation length, we use k_x'' to receive the $1/e$ decay length of the electric field intensity as $1/2k_x''$. By using $\lambda = 532\,\text{nm}$, $\varepsilon_2 = 1$, and the dielectric functions for silver ($\varepsilon_1 = -18.2 + 0.5i$) and gold ($\varepsilon_1 = -11.6 + 1.2i$), the decay length lies at approximately 50 and $8\,\mu\text{m}$, respectively.

The exponential decay length of the electric field of an SPP perpendicular to the metal interface can be found to be:

$$k_{1,z} = \frac{\omega}{c} \sqrt{\frac{\varepsilon_1'^2}{\varepsilon_1' + \varepsilon_2}} \left[1 + i\frac{\varepsilon_1''^2}{2\varepsilon_1'}\right] \quad \text{and} \tag{5.27}$$

$$k_{2,z} = \frac{\omega}{c} \sqrt{\frac{\varepsilon_2^2}{\varepsilon_1' + \varepsilon_2}} \left[1 - i\frac{\varepsilon_1''^2}{2(\varepsilon_1' + \varepsilon_2)}\right], \tag{5.28}$$

for a metallic and dielectric medium, respectively. By choosing the same values as for the propagation along the interface, one obtains the $1/e$ decay length to be $1/k_{1,z} = 19\,\text{nm}$ (metal) and $k_{2,z} = 354\,\text{nm}$ (dielectricum) for silver and $1/k_{1,z} = 24\,\text{nm}$ (metal) and $k_{2,z} = 276\,\text{nm}$ (dielectricum) for gold. The decay into the metal is therefore much shorter than into the dielectric. This decay into air has been experimentally verified by scanning tunneling optical microscopy [145]. With these characteristic length scales, one gets a first insight into the dimensions for which SPP physics can become relevant.

5.1.4. Scanning near-field optical microscopy

Scanning near-field optical microscopy (SNOM) is a technique capable to break the diffraction limit by utilizing evanescent waves. In addition to its high resolution, it proves advantageous also due to its non-invasive nature and the possibility to adapt the optics in order to investigate different properties e.g. chemical structure, local stress, or polarization dependence. The first idea for such a device was proposed by Edward Hutchinson Synge in 1928 based on a thin metal film with a small aperture [146] but was not applicable until Ash and Nicholls succeeded in 1972 by using microwave radiation ($\lambda \approx 3\,\text{cm}$) on an aluminum test grid. By using an aperture of $1.5\,\text{mm}$, they established a resolution of around $\lambda/60$ [147]. These aperture-based SNOMs are more popular, yet they have, among others, several issues concerning artifacts, contrast, sensitivity, and interference. Most apertures are based on a fiber tip which is metal-coated (mostly aluminum) on the sides and metal-free at the tip apex. The latter setup quenches the leakage of the sample field from the side [148].

For this thesis, the aperture-less SNOM technique proved more suitable due to its potentially higher intensities and the possibility of in-situ tip transfer. In this configuration, the aperture is replaced by a thin and sharp metallic tip, which is brought to distances much smaller than the wavelength of the exciting light. The incident radiation excites evanescent waves at the tip, which interact with the sample, leading to an enhancement of the Raman scattering in a spatial domain equivalent to the tip apex. The alignment of the polarization along the tip axis yields the largest confinement and therefore the highest increase of spatial frequencies [149]. In Fig. 5.1.4 a schematic of a tip-based SNOM is depicted. The tip is kept at a constant height above the sample via a feedback loop and scanned across the surface, revealing its topography. The interacting evanescent waves in the confined region are investigated at each point via the far-field detector, enabling the acquisition the optical response in a spatially resolved manner connected to the surface topography. The metallic tips can be much sharper than the commonly used apertures, allowing a much higher resolution. These key components are commonly manufactured via electrochemical etching, due to a high reproducibility and good aspect ratio. A description of the used approach for gold and silver tips is presented in 5.2.1. In contrast to these advantages of the tip-based SNOM, there are also several challenges, the most pronounced regards the high background signal in the far-field generated by the metallic tip [150]. Therefore, careful extraction of the near-field signal becomes necessary, especially in a bulk or thin-film material.
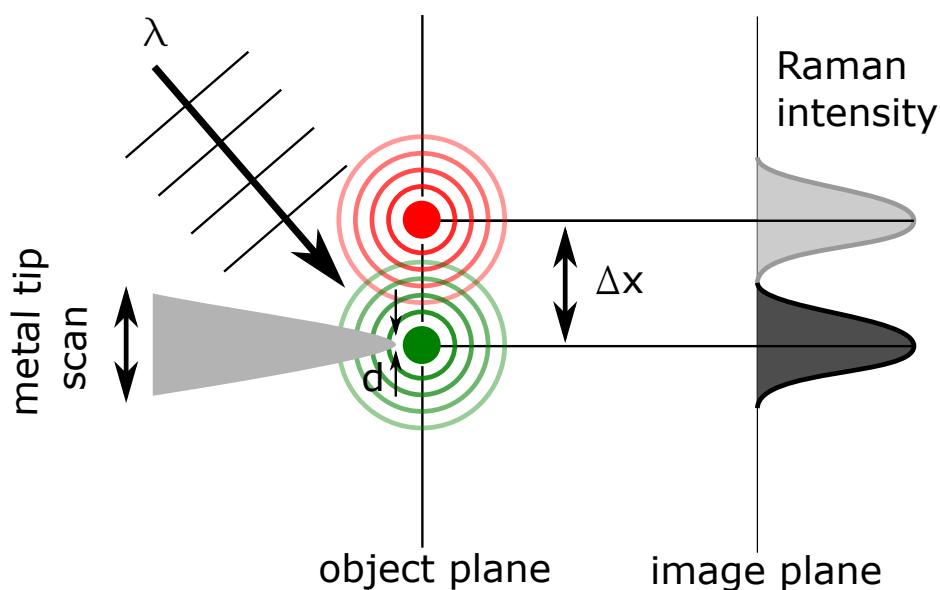
Figure 5.1.4.: Apertureless SNOM utilizing a sharp metallic tip as confinement source. The near-field increases the Raman response, if the tip apex is in close vicinity to one of the two point emitters. By Scanning the tip and mapping the scattered intensity as a function of the tip position, a spatially resolved image of the object plane can be generated, whose resolution power is not limited by diffraction, but by the radius of the tip apex.

5.1.5. Introduction to STM-TERS

In linear optical spectroscopies, the response is proportional to the magnitude of the exciting and, in the case of Raman spectroscopy, also of the scattered electric field. For practical purposes only an evanescent field can be used where no energy is transferred. This limitation favors near-field techniques such as SERS and TERS. While they are similar in their enhancement nature, SERS allows the investigation of even single molecules but is limited to (rough) substrates made of noble metals, such as gold, silver, and copper [151]. It is also strongly dependent on the interaction of substrate and absorbed molecules. This hinders the general use for a larger variety of samples. This limitation can be circumvented by exploiting the near-field of a metallic tip. This leads to TERS, a combination of scanning probe microscopy (SPM) and Raman spectroscopy, allowing, for instance, chemical imaging with high spatial resolution. As the method of locally enhancing the scattering probability strongly depends on the vicinity of a metallic tip, the SPM method of choice should include a highly accurate distance control between the tip and sample. While several SPM techniques are functional, scanning tunneling microscopy (STM) offers the potential of an in-situ tip-exchange, which is a pre-requisite of optimal tip enhancement using silver tips. A brief description of the operating principle of a STM is illustrated in Fig. 5.1.5. An ideally atomically sharp tip is approached to a distance of a few Åof a sample just before mechanical contact. By applying a bias voltage, a tunneling current sets in depending exponentially on the tip-sample distance. While two different modes of STM operation are possible, the constant-current and constant-height mode, here only the first mode was used in order to protect the tip from crashing. The separation of tip and sample is carefully controlled by a feedback loop in this mode, adjusting the height of the tip with a piezo motor to keep the

tunneling current constant. By scanning the tip across the sample surface with two additional piezoelectric positioners, one can map the sample topography by tracking the height position z of the tip. This allows the highly precise investigation of the topography of the surfaces. STS can be used at a fixed position recording the tunneling current as a function of the bias voltage V. The derivative dI/dV is proportional to the density of electronic states (DOS) [152].
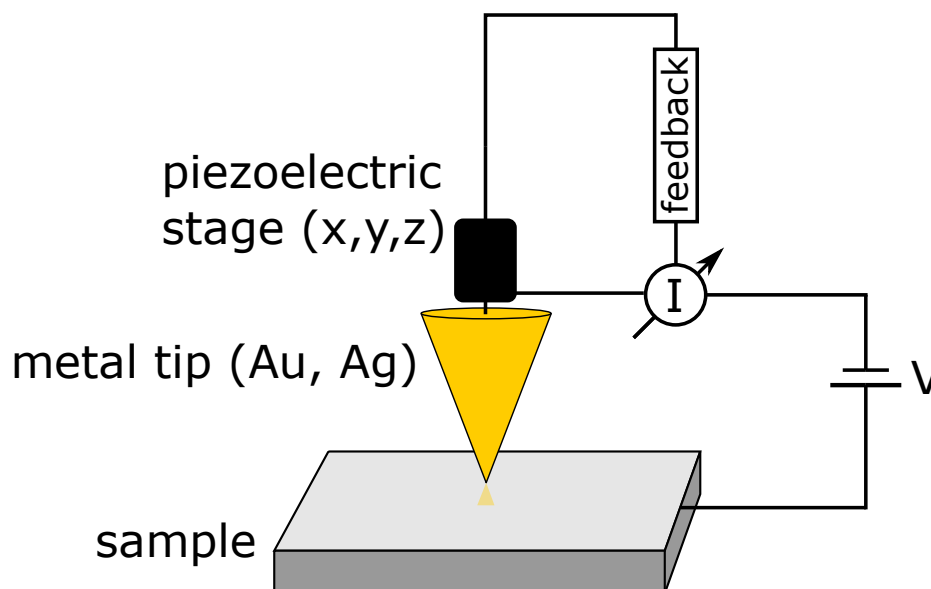

Figure 5.1.5.: Operating principle of scanning tunneling microscopy. A metallic tip is brought into close proximity of a (conducting) sample. By applying a bias voltage a tunneling current depending exponentially on the distance is induced and can be recorded. A feedback loop and a piezoelectric stage keep the current constant by adjusting the position z of the tip. If the tip is scanned in $x - y$ direction while z is adjusted the topography of the surface can be mapped out. A topographic image can be obtained by plotting the height of the z-piezo against the tip position. Alternatively, z is kept constant and the current is recorded, yet this method puts the tip into more risk of damage by touching the surface.

From the STM imaging technique, we can obtain the topography of the sample and identify regions of interest, but can also control the tip-sample distance to govern the near-field excitations. Various effects may contribute to the desired enhancement:

lighting rod effect   An electrostatic phenomenon where the electric charges in a conductor with a specific geometrical shape have boundaries leading to field-line crowding and to spatial confinement of the charge density. If a very thin metal tip is illuminated by laser light polarized along the tip axis, the free electrons are electromagnetically excited by inducing surface charges. The sharp geometrical singularity of the tip apex leads to a strong localization in this region, thus a highly enhanced oscillating electric field arises, enhancing the Raman scattering. This phenomenon is purely geometrical and shows no dependence on frequency [153].

surface plasmon scattering   A collective excitation of unbound electrons (SPPs) can be generated, if the frequency of the excitation laser light matches the plasmon resonance frequency of the tip material. Thus, the excitation thereof is wavelength de-

pendent, explaining the different enhancement factor maxima of silver (blue-green light) and gold (yellow-red light) [154]. Adjusting the laser light to the plasmon frequency of the tip material is crucial for a functioning TERS system.

chemical enhancement If the tip is in direct contact with the sample, the excitation of the tip via the laser light can induce a charge transfer between the molecular sample and the tip. The overlapping of orbitals generate new energy states triggering resonance effects and thus leading to a stronger signal. The enhancement from this process is smaller than for the previously described effects and is happening on much shorter distances [155].

depolarization effect The excitation through the metallic tip partially depolarizes the inelastically scattered light. Thus, the TERS signal does not show the same polarization dependence as conventional far-field Raman spectroscopy. This phenomenon can be taken advantage of to increase the contrast, by using a polarizer to remove the far-field scattered portion of the response, leaving only the near-field scattered light behind [156].

These different excitations of the local tip-substrate cavity can produce a large optical enhancement of up to two orders of magnitude in relation to the excitation amplitude of the incoming light. This is a manifestation of the quadratic scaling of the near-field intensity for incoming and scattered light [157]. Choosing the optimal conditions to achieve the highest potential near-field enhancements is of great importance for the here developed TERS system. Various different groups have performed calculations and experimental studies on the different variables influencing the efficiency of tip-substrate systems, most importantly here the electric field polarization[149], the tip geometry[158], and the tip-substrate interaction[159]. The charge-density distribution at the apex of a metallic tip for different incoming light polarizations is depicted in Fig. 5.1.6. Standing waves are formed by the surface charges interacting with the oscillating field, whose wavelength is smaller than the exciting light. The standing waves are in line with the incoming polarization, leading to a strong anisotropy in the extent of charge re-orientation at the tip-apex. For a polarization perpendicular to the tip axis (x-direction in Fig. 5.1.6 on the left side) and a wavevector of the light along the tip, the charges separate to diametrically opposed points, hence the tip apex remains electrically neutral. Conversely, a wavevector perpendicular and polarization along the tip apex induces surface charge oscillations which are rotationally symmetric and have their highest amplitude locally at the tip apex. This strong oscillation along the tip apex yields the highest contribution to the near-field and therefore to the enhancement of the Raman scattering rate. It is noteworthy, that Yang $et\ al.$ calculated the incoming wavevector angle dependence of the tip enhancement for a side illumination geometry and found it at an angle of $40-60°$ [157]. This was explained by the proximity to the surface and the resulting interference of incident and reflected enhancement field, which decreased the field intensity at the substrate.
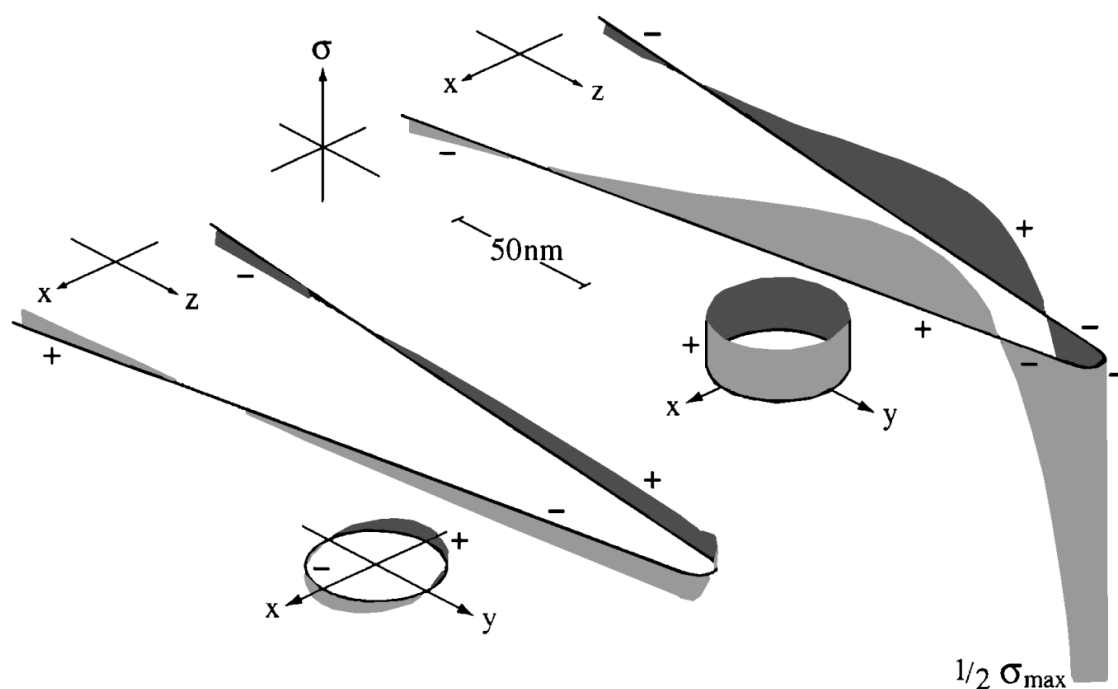
Figure 5.1.6.: Charge density distribution for different polarizations of the excitation light. (a) Splitting of the charges in the case of light with a wavevector along the tip axis z and electric field in x direction. (b) The light propagates in the x-direction with its electric field vector oriented along the z-axis. The surface charge wave has a node at the tip apex in the first scenario, whereas in the second one, a large accumulation of charges takes place at the foremost part of the tip. This leads to very high potential enhancement. Diagram taken from [149].

The induced standing waves are strongly confined by the geometry of the tip apex, thus the influences of the shape were calculated and studied several times, for tetrahedral tips in cantilever-based atomic force microscopy [160], as well as etched wire tips for STM [161]. The most pronounced dependence lies in the radius of the tip apex, illustrated in Fig. 5.1.7, calculated via the finite difference time domain method (FDTD) [158]. In the figure, the enhancement is depicted against the excitation wavelength with different curves for varying tip radii from 10 to 100 nm. For short wavelengths one reveals a peak visible for all tip geometries at approximately 350 nm, stemming from the resonant-induced plasmon excitations. The SPP-dominant region is replaced for higher wavelengths by the lightning rod effect in the form of a broad shoulder. Since this mechanism has a clear geometric nature, the resulting enhancement increases drastically for decreased tip apex sizes. To some extent in contrast to these calculations, a group around Yang *et al.* [157] also calculated the dependence of the tip radius on the field enhancement, with the result of only small dependencies on the radius for its range of 10 to 75 nm and only a sharp increase due to the lightning rod effect at radii below ten nanometer. Differences in their assumed illumination setup potentially explain these distinct results.
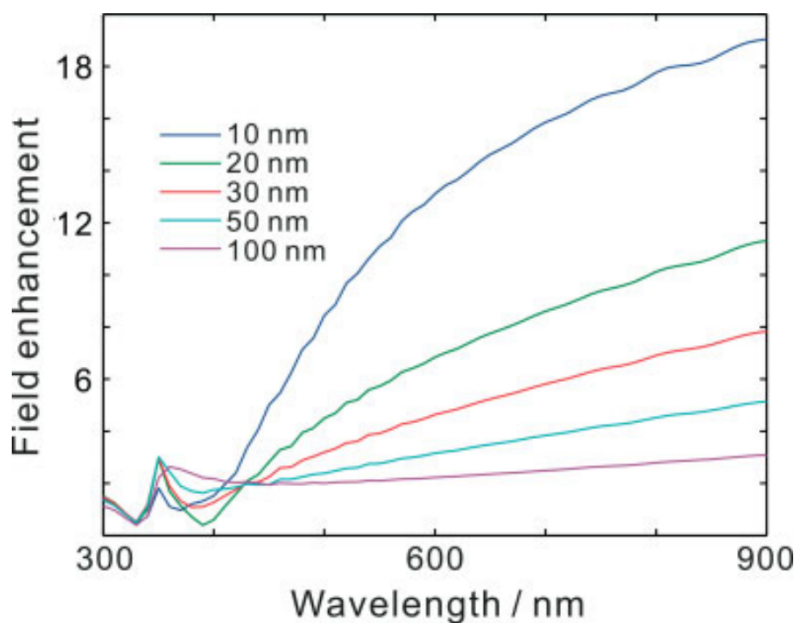
Figure 5.1.7.: Numerical simulation of wavelength-dependent field enhancement for vary-ing tip radii. Different radii are depicted as different colored lines. The peak at low wavelengths stems from plasmon excitation, whereas the broad shoulder at higher wavelengths is a manifestation of field line crowding. Figure taken from [158].

For the work here, the last important parameter of the tip enhancement lies in the interaction between the metallic tip and the substrate. Yang Zhi Lin *et al.* calculated the influence on a Ag-tip with and without a metallic substrate (Au) (Fig. 5.1.8 [159]). The effect is described by the so-called plasmon gap, emerging in the confined space between the metallic tip and substrate. It becomes clear, that the additional substrate drastically increases the enhancement field, defined as the ratio of the maximum local field and the incoming field amplitude, from a field enhancement value of 16 to 242. The effect is coined plasmon gap, emerging between two metallic surfaces close to each other. Since the Raman intensity is approximately proportional to the fourth power of the field enhancement, the final Raman signal can be additionally enhanced by around five orders of magnitude in the vicinity of a metallic substrate.
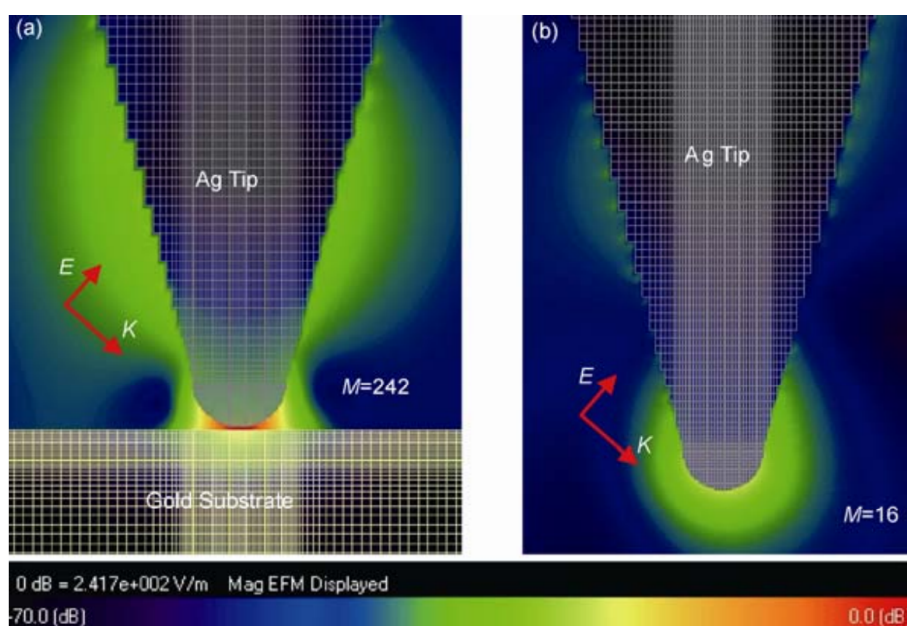
Figure 5.1.8.: Finite difference time domain (FDTD) calculation of the electric field distribution. (a) Field distribution of a silver tip with 25 nm tip radius 2 nm above a gold substrate. (b) The same Ag-tip in vacuum. The maximum field enhancement is 242 or only 16 for the tip over a gold substrate or in isolation, respectively. Taken from [159].

In accordance with these parameters regarding the tip geometry, the tip position, and the best-suited optical configuration, an experimental TERS system was designed, optimized, and set up. The finished setup is described in the next section.

5.2. Experimental setup

This section describes details of the re-designed customized low-temperature UHV-TERS system and its key components. The materials optimal for tips and their ex-situ preparation are discussed first, before moving to the augmentation of the chambers, then the sample transfer including the storage, and thereafter the in-situ preparation of the tips and samples. Proceedingly, the new optical path is described with the adjusted alignment procedure of the optical components. The section is completed by an introduction to the investigated single-wall carbon nanotubes and their physical properties with details regarding their STM and Raman scattering behavior.

5.2.1. Materials and preparation of the tip

A successfully operating STM-based TERS system is crucially dependent on the STM tip, enabling local excitations of plasmonic vibrations at the tip. Material, size, shape, and orientation have been found to strongly affect the potential enhancement factor at the tip apex. The reproducible manufacturing and cleaning of highly enhancing tips remains one of the bottlenecks of TERS. Gold or silver tips are fabricated and used frequently, due to their high free electron density, the appropriate dielectric constants, and the corresponding resonant

SPP response at visible wavelengths. Gold is more widely in use, as the reproducible production of very sharp, conical tips allows easier access to small structures [162]. Yet, their optical properties are inferior to silver, due to high absorption losses stemming from interband transition at wavelengths smaller than $600\,nm$. Their resonance is confined in the red visible region of light. Silver offers the potential of larger enhancement factors and optimal performance at a much broader range than gold down to short wavelengths [130]. To obtain the highest enhancement factors, the excitation of plasmons in the tip should happen at resonance conditions, making green the optimal laser light for silver tips. On the other hand, silver shows much lower chemical stability, corroding under ambient or aqueous conditions over the course of only hours, due to reactions with different sulfides, sulfates and oxides [131]. The fabrication of sharp Ag-tips tends also to be more difficult and sophisticated in comparison to Au. During this work, both types of tips were fabricated and used, with gold mostly for STM scanning and characterization in the beginning and silver for later tip-enhanced measurements. Their individual recipes are presented next.

The tips were prepared via electrochemical etching with pulsed currents. A similar setup was used regardless of the tip material, schematically depicted in Fig. 5.2.1 (a). The voltage pulses are provided by two function generators, allowing the generation of equidistant square pulses with adjustable voltage amplitudes, offset voltages, and pulse lengths and separations. The described pulses were applied to the electric circuit, which consists of a ring cathode and the metal wire supposed to be etched. The ring cathode was built out of platinum for the gold tips or gold for the silver tips. The procedure for gold tips was optimized by Nitin Chelwani and Gabriele Rager (née Eckleder), while for the silver tips, Gabriele Rager and Pablo Cova Fariña developed the recipe.
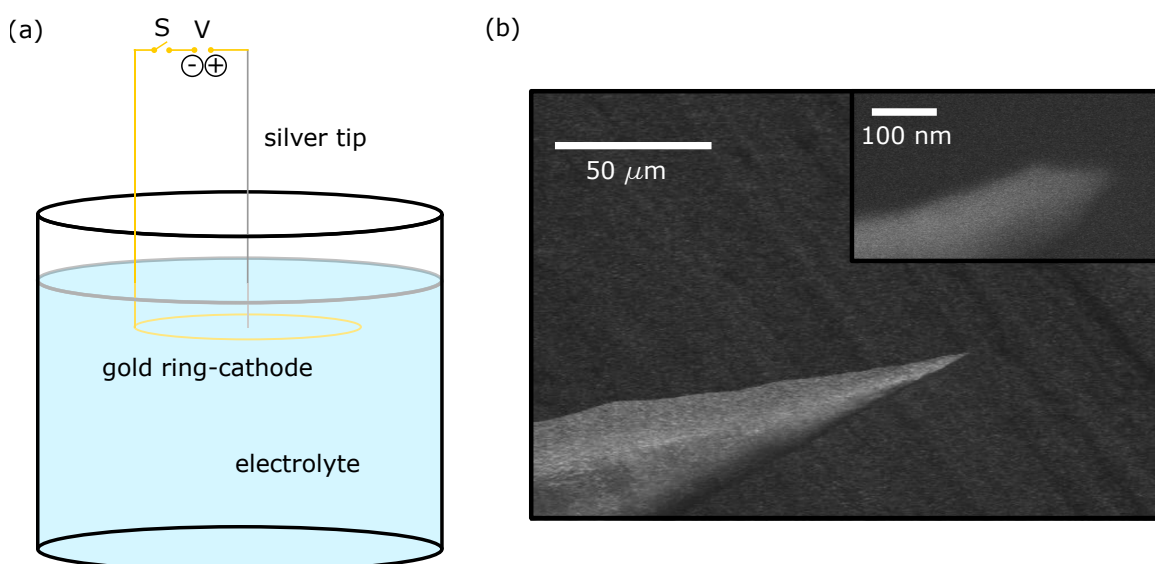

Figure 5.2.1.: Tip fabrication schematic and an exemplary silver tip. (a) depicts the electrical circuit for the etching of silver tips. Here, the ring cathode is made of gold. (b) displays an example of a silver tip with a tip apex diameter of around $20\,nm$. The tip was fabricated by Pablo Cova Fariña and the picture was taken with a scanning electron microscope. The gold ring cathode shown in panel (a) was exchanged for one made of platinum when gold tips were fabricated.

For the gold tips, the $100\,\mu$m thick wires were first cleaned by rinsing with acetone, before they underwent a 6 hours annealing process at $800\,°$C, in order to achieve a single crystalline tip apex after etching [163] yielding higher potential enhancement factors. These highly ordered metallic wires were subsequently submerged by around $5\,$mm and then etched in 37% fuming hydrochloric acid (HCl). The chosen voltage pulses had an AC voltage of $8\,$V and a DC offset voltage of $0.4\,$V, combined with a duration of $30\,\mu$s and a separation of $300\,\mu$s. The current leads to an etching reaction at the electrolyte surface, reducing the wire diameter locally until the submerged portion drops off, leaving a very thin tip. With this procedure, tips with an apex diameter well below $50\,$nm could be manufactured in a highly reproducible fashion. The gold tips were extensively used for several characterization measurements of the setup, due to their easier and more reproducible fabrication. Yet their lower potential enhancement factors especially at higher laser energies as well as their Raman luminescence limit their suitability for our TERS setup. Therefore, the focus was shifted to silver tips having a potentially higher enhancement, especially in the green wavelength range. A thorough discussion of the procedure and its development can be found in [164], while only a brief outline is given in the following.
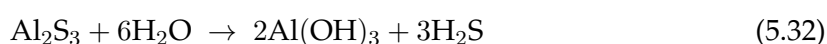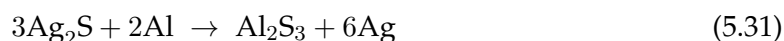
Only a few publications have targeted the development of a reproducible silver tip etching process, achieving stable and sharp tips. Three main electrolytes have been in use for STM measurements, namely, citric acid [165], ammonia [166] and perchloric acid [167]. The preparation of Ag-tips for TERS was developed by Lloyd *et al.* [168] and was taken and optimized for the available fabrication setup. Following Lloyd, a mixture of 2M nitric acid and ethanol was used as an electrolyte, leading to the following chemical reaction, when the Ag-wire is lowered in the solution:

$$3\mathrm{Ag} + 4\mathrm{NO_3H} \;\rightarrow\; 3(\mathrm{Ag^+\,[NO_3]^-}) + 2\mathrm{H_2O} + \mathrm{NO} \tag{5.29}$$
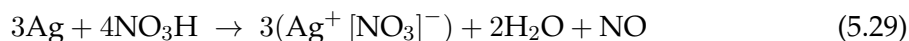
The cleaning process was optimized for Ag, because even though silver is a noble metal, it oxidizes rapidly with hydrogen sulfide in air [169], reducing the reproducibility of this etching process:

$$2\mathrm{Ag} + \mathrm{H_2S} \;\rightarrow\; \mathrm{Ag_2S} + \mathrm{H_2} \tag{5.30}$$

To counteract this chemical reaction to its most pronounced corrosion product $\mathrm{Ag_2S}$ an aluminum foil was used for the sulfur reduction. In this approach, the silver wire was covered in the foil and placed in $\approx 70\,°$C hot distilled water with around $5\,$g of NaCl as the catalyst of the reaction, resulting in the following processes:

$$3\mathrm{Ag_2S} + 2\mathrm{Al} \;\rightarrow\; \mathrm{Al_2S_3} + 6\mathrm{Ag} \tag{5.31}$$

$$\mathrm{Al_2S_3} + 6\mathrm{H_2O} \;\rightarrow\; 2\mathrm{Al(OH)_3} + 3\mathrm{H_2S} \tag{5.32}$$

This cleaning procedure of the Ag-wires leads to a much higher reproducibility of the tip fabrication.

As a next step, the tip shape and sharpness were optimized. The apex radius of the

manufactured tips in the moment of drop-off can be estimated as [170]:

$$r = R\sqrt{(\rho_{Ag} - \rho_e)L/\sigma}. \tag{5.33}$$

Here, R and L are radius and length of the dropping part of the wire, σ is the tensile strength of the wire, and ρ_{Ag} and ρ_e are the densities of the wire and the electrolyte, respectively. Since the etching reaction takes place at the surface of the electrolyte, one can quickly conclude from this approximation, that the penetration depth and the thickness of the wire crucially influence the resulting tip diameters. Thus, a certain amount of electrolyte was extracted from the etchant volume, before a $50\,\mu$m thick Ag-wire (99.99%) approached the surface without touching it. By knowing the exact dimensions of the beaker and the extracted volume, the penetration depth can be closely estimated. Empirically, the best tips were etched when submerged for approximately 0.6 mm.

In the last step, the voltage pulses were optimized, leading to the best results at an AC voltage of 5.0 V and a DC offset of 1.5 V, allowing the fabrication of tips with apex diameters below 50 nm in the best cases.

5.2.2. Augmentation of the existing setup

While the tip fabrication using Ag could be optimized, the corrosion problem persisted. The potential TERS enhancement factors of silver tips decrease to $1/e$ from its value right after fabrication within less than three hours [171] and practically vanish in the course of two days [172]. According to Chelwani *et al.* and our own experience this degradation could not successfully be dealt with using the TERS chamber alone because of the long time scales given by the characterization and mounting of the tips [173].

For attacking this central problem, the existing setup had to be re-designed and upgraded to enable in-situ cleaning and preparing as well as storing the tips and samples in UHV conditions and at low temperatures. The necessary augmentation included the TERS chamber itself and required the installation of both an additional preparation chamber and a load lock. All new parts had to be designed and constructed from scratch.

The general schematic setup is displayed in Fig. 5.2.2 and identifies the three chambers and the transfer arm. Each of the chambers may be pumped and used separately as guaranteed by UHV gate valves between the chambers. An actual picture of the laboratory can be found in Fig. 5.2.3. The changes to the setup design required also a reconstruction of the optical path as indicated by a turquoise ellipse in the figure. For vibration-sensitive measurements like STM and TERS a sufficiently stable setup is required having an optimal suppression of vibrations of all kind. Thus, the whole setup was mounted on an optical table, which itself is supported by four vibration isolators (Newport, S-2000 stabilizer), suppressing vibrations from the building in a broad bandwidth of frequencies.

TERS chamber

For the low-temperature measurements, the customized optical and STM stage is part of a ^{4}He, cryogenically pumped UHV cryostat (Janis Research, CNDT series). To reduce heat-

ing by radiation and stabilize the temperature, a custom-built radiation shield was designed and cooled with liquid nitrogen. To reduce the vibrations stemming from the boiling of said nitrogen, the N_2-tank was pumped down to around $10\,\text{mbar}$ with an additional scroll pump. The resulting solidification of the nitrogen stops the bubbling and therefore the vibrations. For keeping the nitrogen solid, the pump was on during the entire measurement. With the vibrations from the pump isolated efficiently, no traces of noise were found in the STM signal any further.

To allow in-situ transfer between the different chambers, a wobble stick, a rotatable storage platform, and a small window at the back of the cryostat have been implemented. The underlying mechanism will be discussed later. For an easier tip approach and sample/tip transfer a $45°$-tilted window is combined with a camera and an adjustable monitor, giving a clear picture of the two piezo towers, storing the tip and sample in the center of the cryostat. Two windows in the front part of the cryostat are available for the spectroscopy part of the optical path and the illumination of the sample. The main chamber is pumped with a turbo pump (HiPace 300, Pfeiffer Vacuum), which itself is pre-pumped by a dry Scroll pump (HiScroll 12, Pfeiffer Vacuum). After several baking cycles, a base pressure of $8 \times 10^{-9}\,\text{mbar}$ could be achieved before filling in the cryo-liquids, leading to a final minimal pressure of $1.4 \times 10^{-11}\,\text{mbar}$ after cooling. During extended measurement cycles, the pressure was kept below $1.5 \times 10^{-10}\,\text{mbar}$ at all times. If needed in the future, the bottom part of the main chamber has a port for the installation of an additional ion pump. The possible temperature range after the augmentation was observed to be $16 \leq T \leq 320\,\text{K}$, but T was kept constant at approximately $20\,\text{K}$ for the measurements.
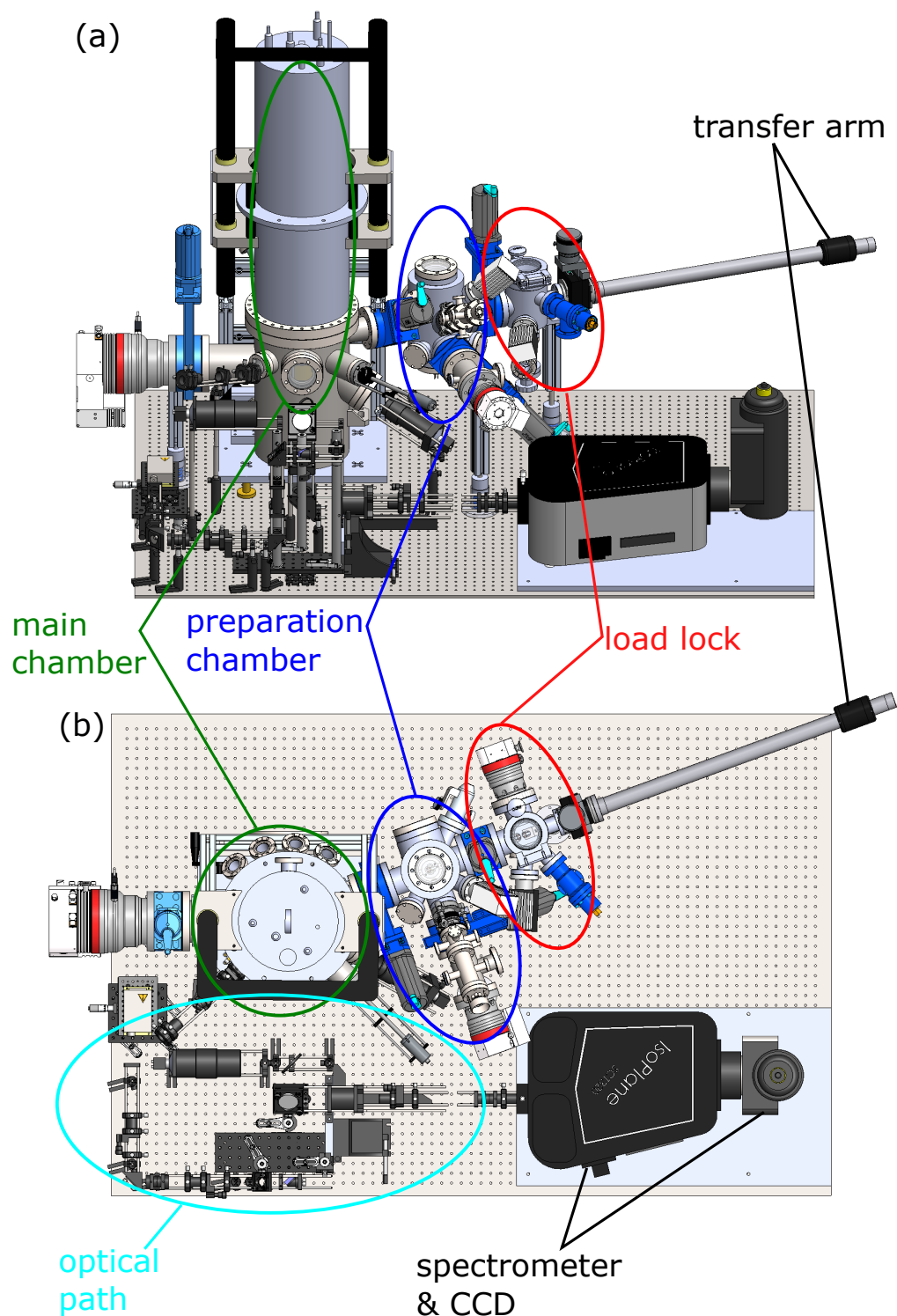
Figure 5.2.2.: Schematic drawing of the new setup from two different perspectives. The main chamber was re-designed (green), while an in-situ sample and tip preparation chamber (blue) and a load-lock (red) were planned and custom-built. To account for the innovation, the optical path had to be adjusted (turquoise).

Preparation chamber and load lock

The preparation chamber is equipped with a custom-built radiative heating stage and an adjustable ion gun using argon. Additionally, a conductive heater for local tip heating was installed, but not yet tested. The cleaning procedures can be observed via two windows on the top and the back of the setup. The preparation chamber is pumped with a turbo pump stage (HiCube 80 Eco series, Pfeiffer Vacuum), reaching a base pressure of $\approx 3x10^{-8}$ mbar after baking.

The load lock is the smallest chamber for fast pump down. It is equipped with a turbo pump (HiCube 80, Pfeiffer Vacuum) and a scroll fore-pump. After several hours of a slow and careful baking procedure, so as to not damage the easy-access gate and its viton O-ring, a pressure of around 5×10^{-8} mbar is reached. A small storage table allows one to deliver three different tip or sample holders simultaneously for reducing the pump time. The load lock can be vented by clean nitrogen gas. A magnetic transfer arm (MDS linear transfer arm $40 - 600$, VAB Scanwell) is mounted directly to the load-lock chamber. The vertical position of the arm may be adjusted to the required positions in the preparation and the TERS chamber by a z table.

Since these long additional chambers, transfer arms, and flanges are susceptible to vibrations, they were stabilized with self-made spring-structures, effectively damping these noise factors.
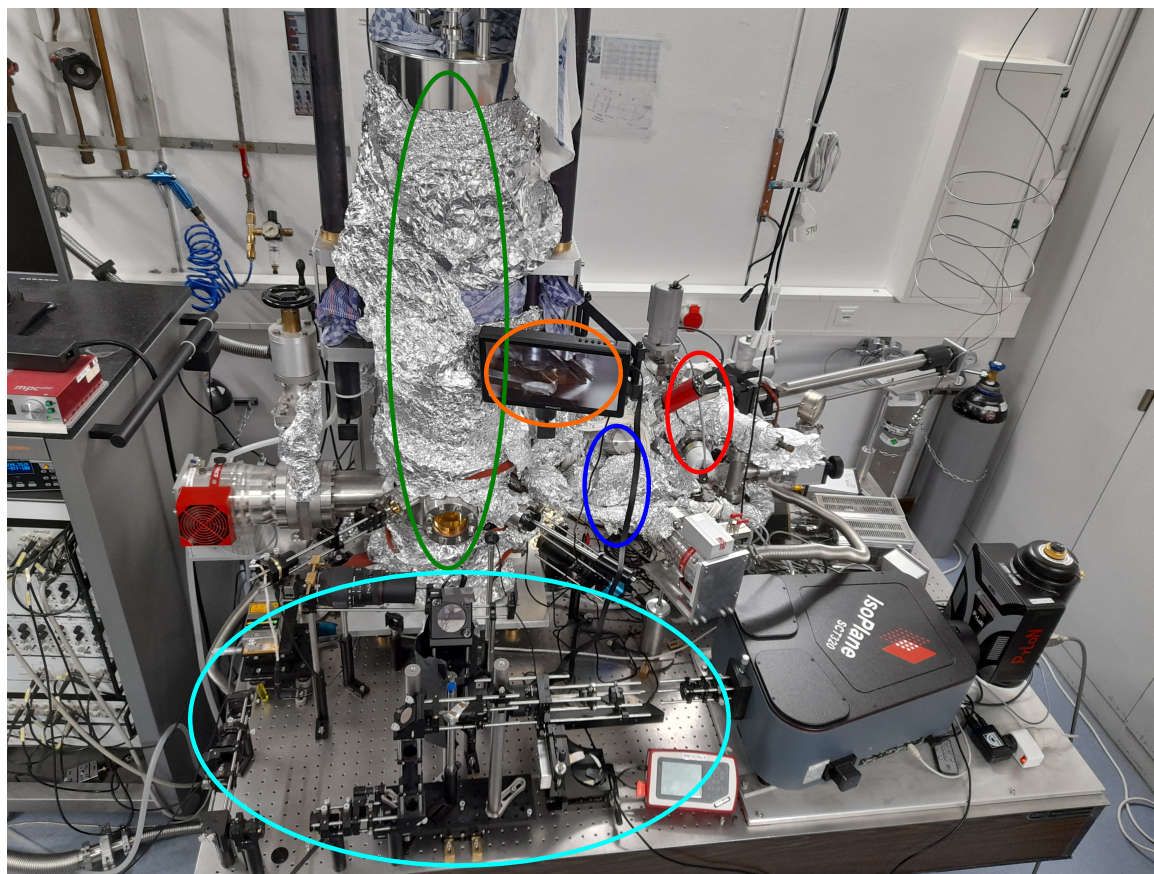
Figure 5.2.3.: Picture of the actual laboratory after the modifications. The perspective and the colors are chosen to be comparable to Fig. 5.2.2. The cryostat is in the center (green), the new chambers (blue and red) on the right side. On the monitor in the middle (orange circle) one can see a close-up of a silver tip and a thin-film gold sample (c. Fig. 5.2.10). The optical equipment (turquoise) is in the front, the spectrometer is on the right, and the electric control units are placed in the rack on the left.

Fig. 5.2.3 shows a photo of the laboratory from a similar perspective as Fig. 5.2.2. The individual parts are encircled using the same color scheme. The small monitor marked with orange. The observation system proved extremely useful for tip/sample transfer and the initial rough approach of the tip. Furthermore, it was also intended to be used for fine-adjusting the tip during the planned conductive heating procedure. As an example, one can see a close-up of a silver tip over a thin-film gold sample with a distance of approximately 200 μm. The actual TERS-cryostat and its new additional chambers are covered with aluminum foil and heating for baking. The rack on the left hand side houses the electric control unit of the STM, as well as the measurement units for temperature, pressures, laser power, and helium level. The STM unit can be remotely accessed and controlled via the software "Daisy". The remaining control units may be read out and controlled remotely by a home-made LabVIEW interface.

Sample transfer and storage

The transfer system for the samples and tips had to be designed and adjusted to an already existing setup. A schematic drawing is shown in Fig. 5.2.4. The transfer starts in a closed

and pumped state at the load-lock (3). In every stage, the transfer can be observed through several windows (W2-W6), and the chambers can be separated by two valves (V1 and V2). The transfer holders (see Fig. 5.2.5 (b) and (c)) are universally suited for tips and samples and are lifted from a small home-built aluminum table by a fork attached to the transfer arm. Once lifted, it can be moved to the preparation chamber (2) and placed on the heating platform (displayed in the bottom inset). From there, it can be transferred to the main chamber (1). The STM stage to which samples and tips may be attached is illustrated in the left upper inset (encircled). The circular storage carousel (purple) has sixteen potential sites, but for now, only eight are available. It may be rotated by tipping it with the wobble stick. Due to its connection to the radiation shield, it pre-cools the samples. To allow the transfer, the main radiation shield of the cryostat has an opening, which can be fully or partially closed with an additional semi-circular radiation shield. The semi-circle is mounted on the storage platform and enhances the holding time at low temperatures. The storage-carousel may be tightened at several positions to reduce vibrations.
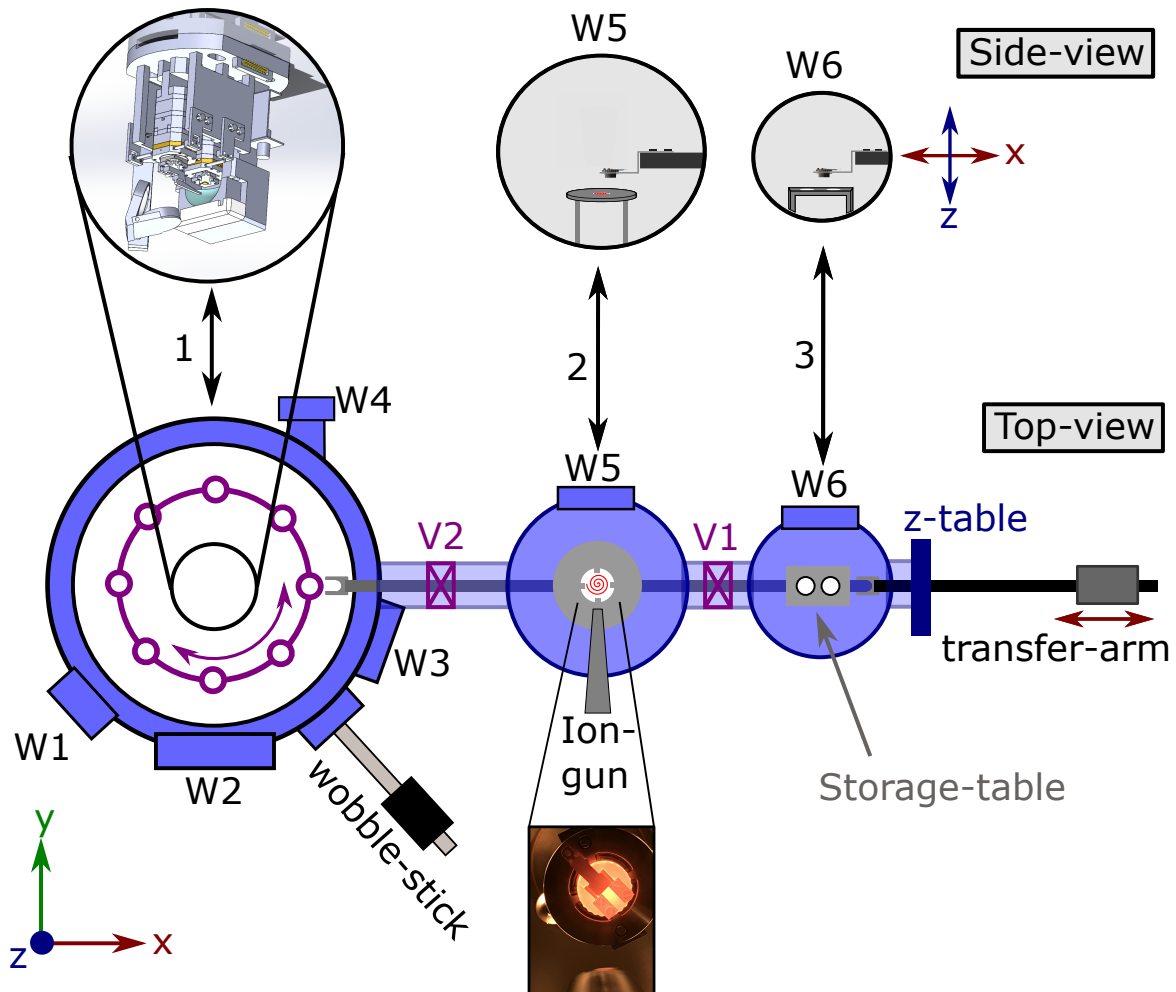
Figure 5.2.4.: Schematic view of the transfer system. Samples and tips are transferred centrally through the three numbered chambers. From left: (1) TERS chamber, (2) preparation chamber with a heated sample (see inset below), and (3) load lock chamber and transfer arm. The upper row presents the TERS head including the parabolic mirror (encircled inset on the left) and two side views along the y-axis of (middle) the heatable sample stage with the fork and (right) the storage table with the transfer fork. The sample transfer between the chambers is facilitated by the magnetically coupled transfer arm and a z-axis manipulator to adjust the height. The samples and tips are then stored on a pre-cooled storage carousel with eight sites in the TERS chamber (purple). From here, they are picked up with the wobble-stick and attached to the piezo towers. The chambers can be separated by valves (V1, V2). Several windows (W2-W6) allow visual control while operating the setup. W1 and W2 are used for sample illumination and Raman measurements, respectively.

Once the transfer holders are placed on one of the storage sites of the carousel, they can be attached and thermally connected to the radiation shield with a screw driven by the wobble stick. The tip/sample holder can be grabbed with the wobble stick and transferred into re-designed spring-loaded click holders on the piezo towers of the STM unit in the center of the cryostat. This "heart" of the setup is schematically shown in Fig. 5.2.5 (a). In (b) and (c) the assembled transfer holders are shown with a sample and a tip holder, respectively, which may be rotated. The tip/sample holders are secured by a spring made of stainless steel or tantalum (for heating) on the transfer holder, illustrated in orange.

This design enables the automatic attach and detachment of sample and tip holder while guaranteeing reasonably good thermal contact when clicked in. The sample (yellow in blue) is attached with glue for use below 320 K. For heating the sample in the preparation chamber a tantalum spring presses the sample on the holder. The tip holder illustrated in panel (c) can be adjusted for its angle and length, to account for slightly different tip lengths and directions.
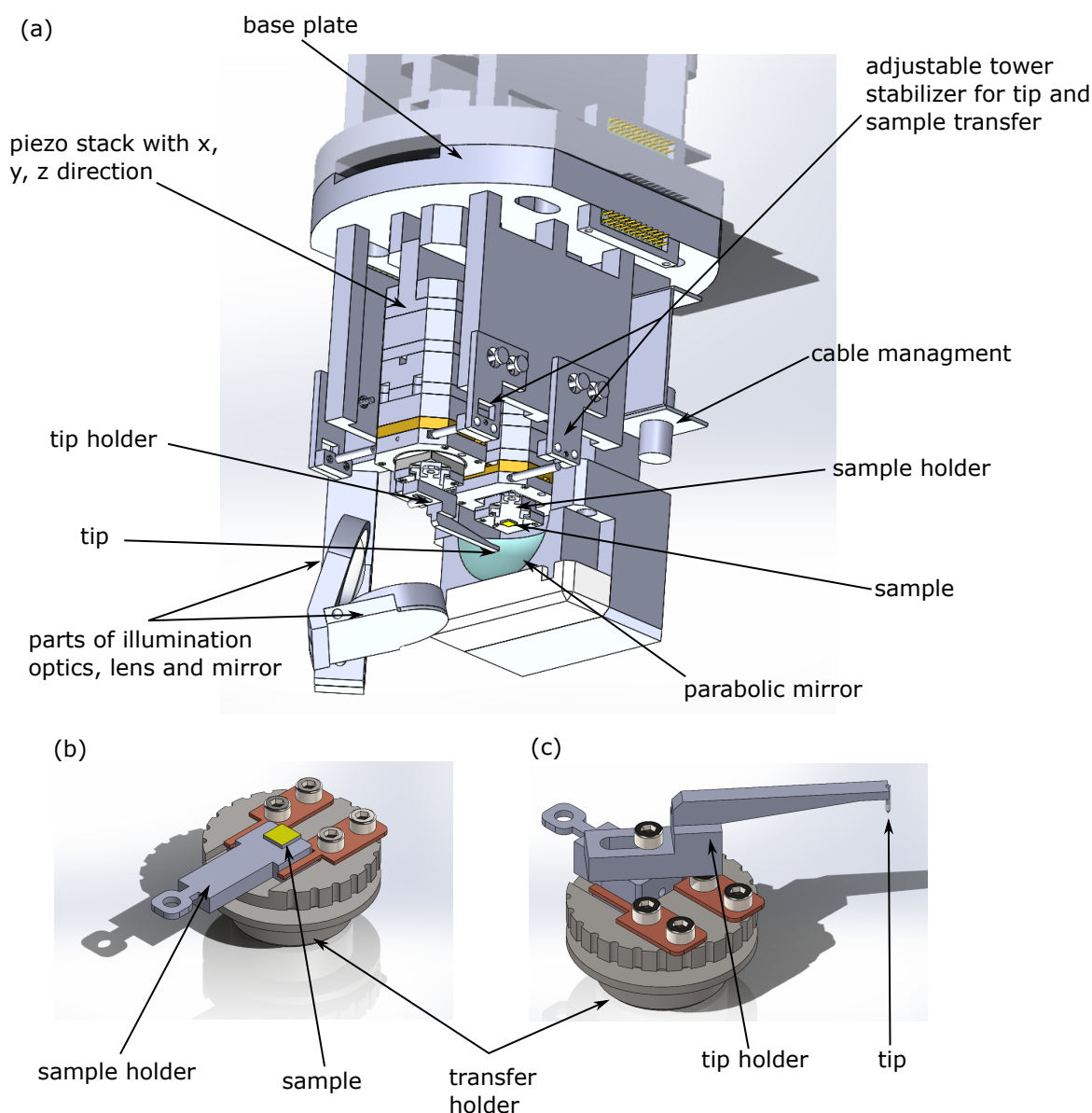

Figure 5.2.5.: Microscope unit and transfer holders assembled with sample or tip holder. (a) Two towers consisting of several stacked piezo motors, the parabolic mirror as the last optical component in front of the sample, and a lens and mirror of the Köhler illumination system. Upgrades were made to allow in-situ transfer and attachment of sample and tip without damaging the stacked piezo motors. Panel (b) and (c) depict the assembled transfer holders in a sample or tip configuration, respectively. The springs for fixing the sample or tip holder are shown in orange.

The microscope unit consists of two towers each having three piezo motors that allow controlled movement and scanning of tip and sample in three dimensions. In addition, there are temperature sensors, heaters. This design is vulnerable to strong tilting of the

towers under force application, for the transfer and sample attachment such deformations had to be minimized. The connection of the STM to the optical path is made with an off-axis parabolic mirror, that covers a solid angle of π. The last optical components of the Köhler illumination (lens and mirror) are also directly attached to the STM unit and may be adjusted in-situ after cool-down.

In-situ preparation of samples and tips using the new chambers

There are several ways described in the literature, to clean degraded tips and prepare them for the highest resolutions in a STM or TERS setting. A clean and smooth metallic surface is the starting point for most approaches. Thus, gold and silver bulk samples were chosen and built into the UHV setup. By heating these samples to high temperatures between 500 and $800\,°\text{C}$, their surface equilibrates to an atomically flat topography. Residues such as dirt and atomic imperfections can be removed by bombardment with nonreactive ions like Argon as illustrated in Fig. 5.2.6. The ion gun is operated with 99.99% pure Ar at an adjustable pressure of approximately $5 \times 10^{-5}\,\text{mbar}$. A radiative design for heating the sample was chosen to avoid mechanical contact between the heating coils and the transfer holders. The heating stage consists of a tungsten coil which is powered by a $10\,\text{A}$ current source. The maximal current was set at $5.6\,\text{A}$, to ensure the integrity of the tungsten wire. The energy transfer to the sample was maximized by drilling a hole into the transfer holder, as depicted in Fig. 5.2.6 (c). Both cleaning procedures were repeated several times, each taking between 15 and 30 minutes.
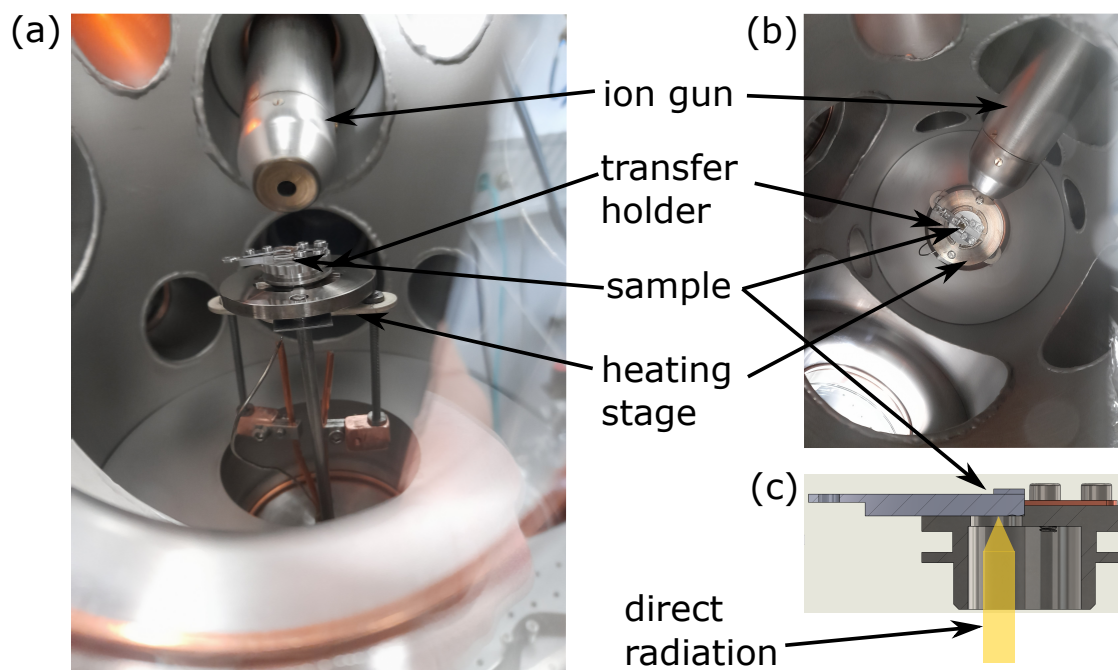
Figure 5.2.6.: Interior of the preparation chamber. (a) and (b) show the transfer holder with a gold sample from two different perspectives on top of the heating platform with the ion gun pointing at the sample surface. (c) cross sectional view of the transfer holder. The direct radiation comes very close to the sample through the hollow center of the holder.

After the bulk sample was cleaned, a selected tip was approached into tunneling mode. By either very fast scanning of the sample surface or small voltage pulses, dirt particles get off the tip and clean gold or silver atoms accumulate at the tip apex. Alternatively, the repeated controlled indentation of the tip into the sample allows the rearrangement of the atomic configuration at the apex of the tip [174]. All three methods have been used successfully. Yet, the most pronounced and reproducible results were observed when using a field emission procedure. Here, the tip and the sample were brought into close proximity and a high voltage was applied. When the tip got close, a high tunneling current was measured, effectively either leading to an electron bombardment or the emission of electrons from the tip. In both cases, heating by high currents at the tip apex takes place, which removes oxidized material and even sharpens the tip by a decapitation process [175, 176]. In our setup, a voltage of around $72\,\text{V}$ was set over a series resistor of $R = 1\,\text{M}\Omega$, while the tip was approached until a current of a at most slightly below $1\,\mu\text{A}$ was reached. The current increases slowly indicating the tip to elongate. When the tip reaches the metallic surface the current spikes. Upon immediate retraction of the tip, some parts of the tip apex were ripped off, similar to the drop-off during the electrochemical etching. The resulting rip-off structure turns out to be much smaller than the etched tip. Additional voltage pulses further improved the resolution and stability of the STM measurements. Most of the following measurements were performed on thin-film gold samples, which were also used for this field emission procedure.

Additionally, samples were cleaved in-situ, effectively giving clean surfaces. The approach was successfully utilized for a CsV_3Sb_5 and a Bi-2212 sample.

Optical path

A schematic drawing of the optical setup is shown in Fig. 5.2.7. A solid state laser emitting at $532\,nm$ (Coherent sapphire SF 532) was used for all proceeding measurements, but could have been easily exchanged to a $660\,nm$ laser (Laser Quantum, Ignis-FS 660). The laser is mounted on a platform, adjustable in height and perpendicular to the optical path. The laser beam is spatially filtered and expanded to a diameter of $6\,mm$ by the first pinhole system (L1, $f = 10$ mm; PH1, $d = 30$ μm; L2, $f = 60$ mm). The resulting divergence of the beam lies at $2 \times 10^{-4}\,rad$. This beam diameter is a result of Zemax simulations, aiming at minimizing the spot size on the sample and therefore the area contributing to the far-field [173]. Subsequently, the polarization direction and the laser power of the light are selected by the combination of a $\lambda/2$ waveplate and a polarizer (P1). The beam is spatially filtered again by a pinhole system (L3, $f = 50$ mm; PH2, $d = 30$ μm; L4, $f = 60$ mm), before being directed to the optical flat (B. Halle Nachfl., Berlin). The latter is a rectangular cuboid manufactured of fused silica with a silver coating on the back surface, splitting the beam into three beams with the highest intensity in the middle at $90\,\%$ and $4\,\%$ on the side beams. The silica cuboid is polished to a flatness of $\lambda/20$ over the entire length of $40\,mm$, leading to the three beams being parallel within $6 \times 10^{-7}\,rad$. In accordance with a proposal of Chen *et al.* [177] and Lee *et al.* [178], this facilitates the alignment of the laser beam parallel to the optical axis of the parabolic mirror. The optical flat is mounted on a height-adjustable platform, enabling the compensation of the temperature-induced length variation in the cryostat without changing the beam direction. It also allows the simple change of the position of the incoming beam on the parabolic mirror, while keeping the aligned beam parallel to the optical axis. The laser beam then passes the first semi-transparent mirror (SM1) and the front window of the cryostat (W2), before being collected by the parabolic mirror and focused onto the sample. The inelastically scattered light is emitted in all directions from the approximately point-like focus. The paraboloid collects approximately one half of this light and reflects it in a parallel fashion toward the semi-transparent mirror (SM1). From SM1 the beam is focused by an objective lens (O1, Canon, $f = 85$ mm). The light is parallelized again by a confocal lens (L5, $f = 40$ mm) to a beam having a diameter of $12\,mm$. Before the desired polarization state is selected (P2), the elastic component is blocked by an edge filter (F1, Iridian 532nm LPF). The polarized photons are now rotated into the most efficient direction of the spectrometer by a $\lambda/2$ waveplate. Finally, the inelastically scattered light is focused (L6, $f = 50$ mm) onto the entrance slit of the spectrometer (Isoplane SCT320, Princeton Instruments) and detected by a CCD (Pylon-400BRX, Princeton Instruments).

Two independent observation systems provide images of sample and tip with different resolution for controlled transfer, tip approach and optical alignment. Through window W3 camera C2 equipped with a Zoom lens (MVL700, ThorLabs) provides an overall image with field of view of maximally 6×10 mm. The interior of the main chamber can be

illuminated by several LED light sources. A second camera (C1) with a commercial zoom objective (Sigma Optics) uses the second semi-transparent mirror (SM2) and the paraboloid as an objective lens for microscopic observation of the sample surface, tip, and laser spot. For this reference image sample and tip are illuminated by a Köhler illumination system, which was designed and implemented earlier [179].
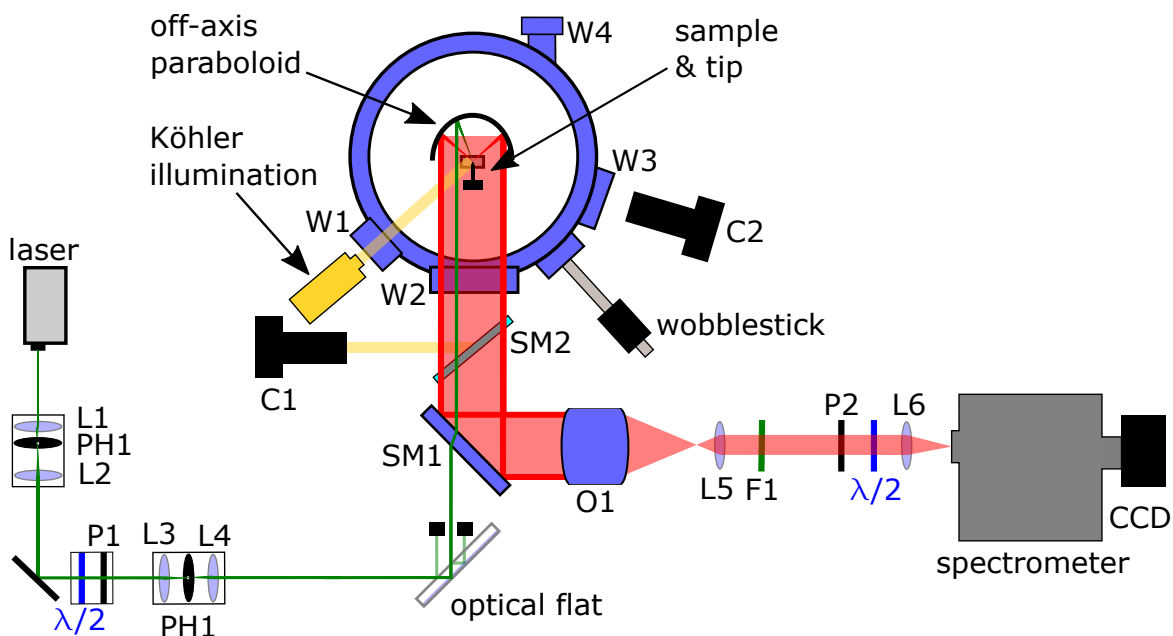

Figure 5.2.7.: Scheme of the optical setup. The laser beam is spatially filtered and expanded to a diameter of 6 mm. The waveplate ($\lambda/2$) and the polarizer (P1) allow the adjustment of power and polarization of the incoming photons. The beam is aligned parallel to the optical axis of the parabolic mirror using the optical flat and focused by the paraboloid onto the sample. Inelastically scattered, red-shifted light is collected and reflected towards the spectrometer. Photons having the selected polarization and energy reach the CCD. The Köhler illumination system guaranties the best contrast for observation (C1 and C2).

As opposed to a conventional objective the parabolic mirror along with the off-axis conditions allows to get rid of a major fraction of the stray light and minimizes the focal spot size, consequently improving the contrast between near- and far-field. It also acts as an microscope objective lens, simplifying the tip approach and the positioning of the tip into the laser spot. Furthermore, the mirror can be cooled down with the cryostat and also baked, making it compatible with UHV conditions. Here, we used one half of a paraboloid with a solid angle of $\Omega = \pi$ and a numerical aperture of NA≈ 0.87. Its diameter and focal length are 30 and 8 mm, respectively. The optical configuration was set in a way, that the sample surface is parallel to the optical axis, as illustrated in Fig. 5.2.8. This configuration keeps the polarization leakage below 7%. The leakage of a conventional glass system is better but one has to deal with directly reflected laser light and very limited space. For alignment, two differently oriented {100}-silicon samples were mounted in the cryostat. One was tilted by around 30° towards the optical axis and another one was glued parallel to the optical axisas shown in Fig. 5.2.8 (a) and (b). As the inelastically scattered light is very weak in intensity and cannot be observed directly, the tilted sample (Fig. 5.2.8(a)) is used as

a mirror to reflect the laser light into the collection optics. Using this additional beam, the semi-transparent mirror SM1, the objective lens O1 and lenses L5 and L6 can be aligned. For the easiest alignment of these components, the beams of the incoming and reflected light were aligned to coincide.
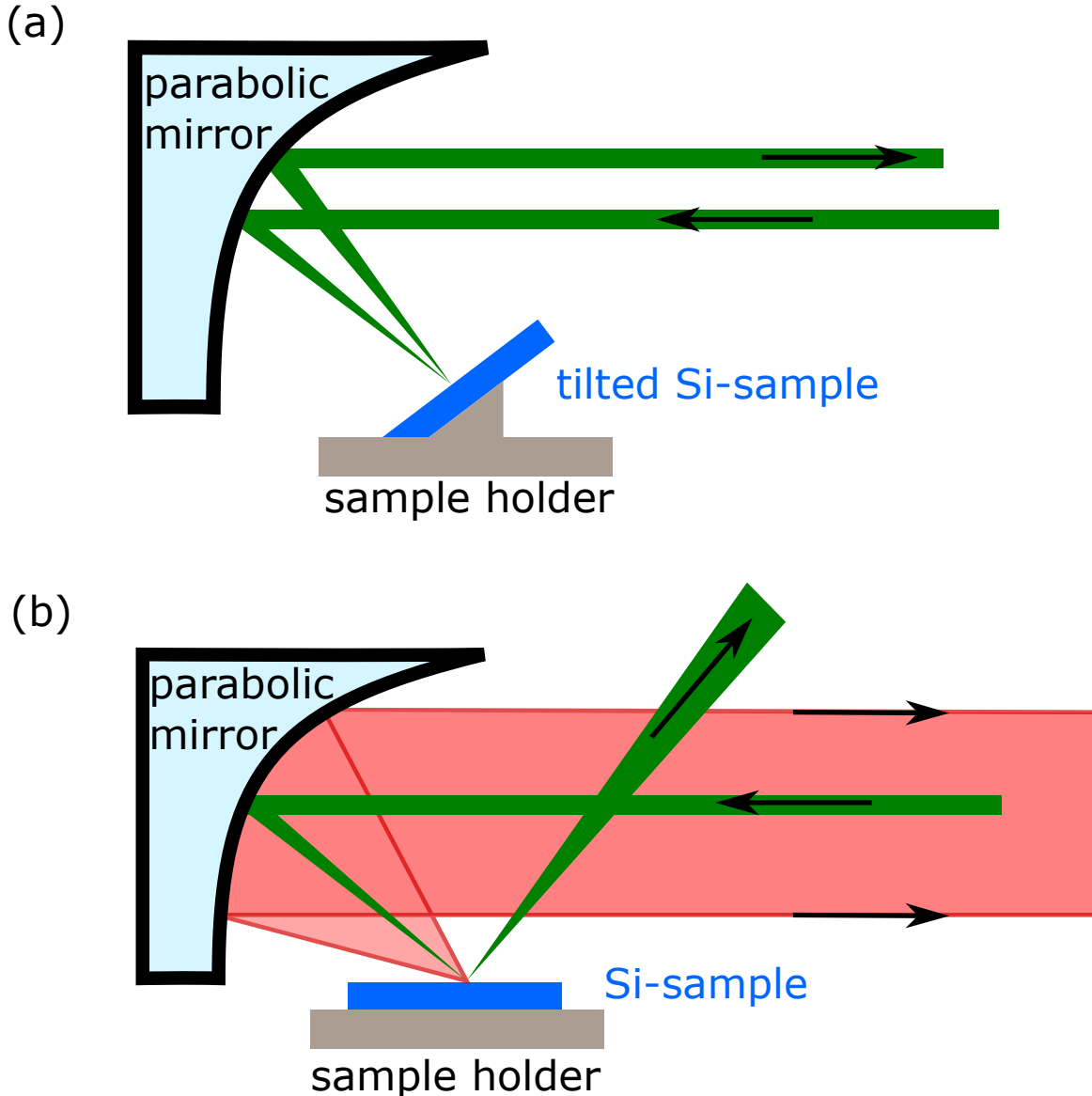

Figure 5.2.8.: Alignment configurations with two different {001}**-Si samples.** (a) The optical components after the parabolic mirror are aligned with a direct reflection of the laser beam, by using a tilted Si-sample as a mirror. (b) The measurement configuration removes most of the stray light and enables the later discussed alignment of the beam onto the optical axis.

After this coarse alignment, the sample parallel to the optical axis was moved into the focus (5.2.8(b)). Now, while the direct beam is reflected away from the optical path, the inelastic portion of the scattered light is collected by the parabolic mirror and reflected along the already aligned optical path towards the spectrometer.

The main challenge is a minimal laser spot for confining the scattering volume of the far field. To this end, the incoming beam must be perfectly parallel to the optical axis of the

parabola and should have minimal divergence. While the divergence can be controlled relatively easily, the alignment along the optical axis requires special measures [177]. A schematic of the optical flat and the parallel light on the parabolic mirror can be found in Fig. 5.2.9.
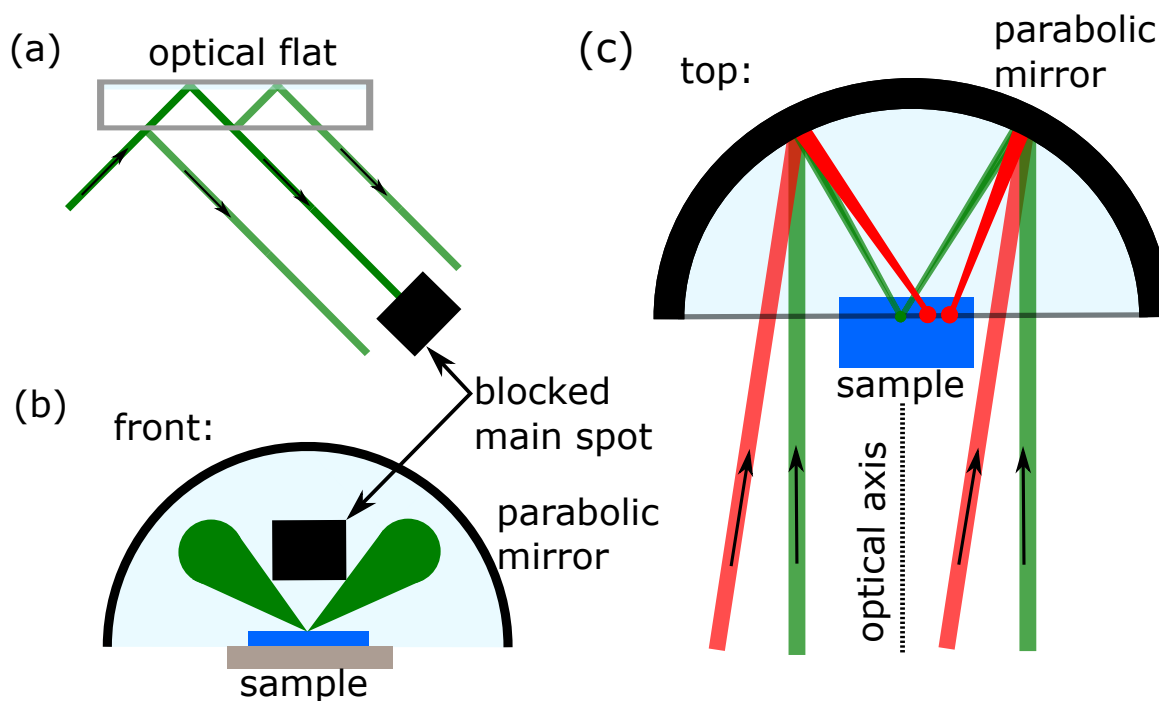

Figure 5.2.9.: Alignment procedure of the incoming laser beam. An optical flat (a quartz cuboid with a silver coating at the back) splits the beam into three strictly parallel beams and directs them toward the parabolic mirror. Panels (b) and (c) picture the beams on the parabolic mirror from the front and the top, respectively. The two side beams only overlap in the focus point, if they are exactly parallel to the optical axis (shown as a dotted line).

For aligning the optical path onto the optical axis of the parabolic mirror, the center beam of the optical flat is blocked. The two side beams are then directed towards the parabolic mirror, hitting the two quadrants as drawn in Fig. 5.2.9 (b). The two parallel beams intersect only if they are also parallel to the optical axis of the parabolic mirror. An example of a perfectly aligned (green) and a misaligned (red) set of beams is depicted in panel (c). As long as the beams are not parallel to the optical axis or the sample is not in the focus of the parabolic mirror two separate spots appear on the Si. The optical flat may be tilted over two axes for aligning the beams parallel to the optical axis of the paraboloid. The optical flat is shifted along the direction of the incoming beam, thus determining the position of the exciting laser on the paraboloid without changing its direction. The focus on the sample is found by changing the height of the sample tower. By iteratively tilting and shifting the optical flat, while adjusting the height of the sample, the two spots can be brought to overlap in the focal point in a controlled and reproducible fashion.

After focusing, the two alignment beams were blocked and the central high-intensity beam was used for excitation. The Si-phonon at 520 cm^{-1} was used for fine tuning the

optical elements in the Raman arm of the optics. The resulting small spot sizes of the main beam observed with both camera systems are pictured in Fig. 5.2.10 and 5.2.11 on the right side for C2 and C1, respectively. On the respective left sides, a silver tip in roughly approached but not yet tunneling mode is depicted.

The tip and its shadow can be seen very clearly and sharply, allowing a coarse approach down to approximately single μm, estimated from the tip thickness. The final spot size is approximated to be $5\,\mu$m. The ellipticity of the spot in Fig. 5.2.11(b) results from geometrical aberrations.
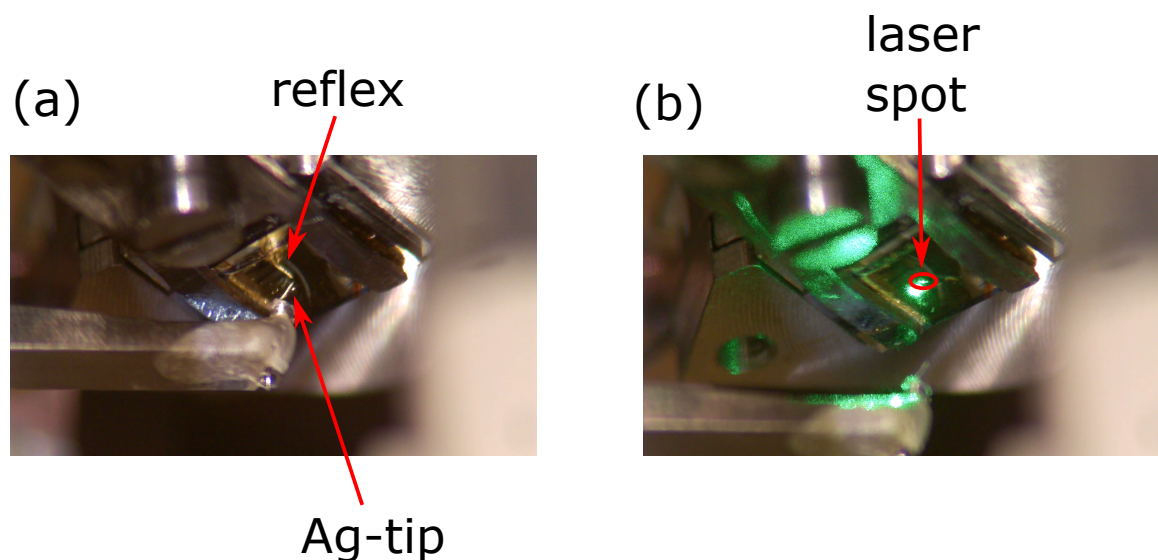

Figure 5.2.10.: Perspective of Camera 2 on the tip and laser spot. (a) silver tip attached to its holder and the reflex of the tip on the gold surface. (b) laser spot as a small green dot. The additional brighter reflex comes from the window. Here, the tip is further away from the sample, for clearer visibility of the spot. Both illustrations depict the case of a thin gold film sample with carbon nanotubes.
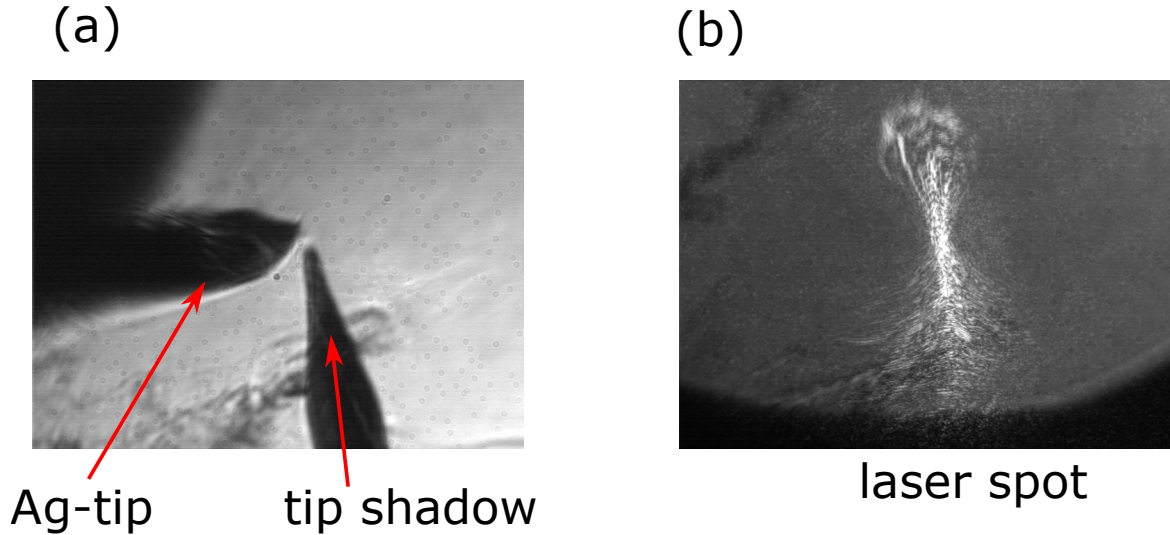
(a)

Ag-tip   tip shadow

(b)

laser spot

Figure 5.2.11.: Images of Camera 1 of tip and laser spot. (a) Ag-tip and shadow coming from the left and bottom, respectively. The sample-tip distance in this illustration is much closer than in the depiction of Fig. 5.2.11. (b) main laser spot of the optical flat driven into the focus. Both images were acquired on a gold film sample with carbon nanotubes.

5.2.3. Single wall carbon nanotubes

To benchmark the augmentation, single-walled carbon nanotubes (SWNT) were investigated as targets for STM, Raman, and TERS. A short introduction to their geometry, basic features, and Raman excitations is given in the following.

SWNTs have been investigated intensively using Raman spectroscopy. The 1D character leads to van Hove singularities in the density of states, inducing various resonance effects [180]. The nanometer-resolved excitation response of SWNT provides an easy and detailed characterization tool for the vibrational and geometrical properties of individual nanotubes. A schematic of how the structure can be imagined and defined is given in Fig. 5.2.12. These tubes consist of a single layer of graphene being rolled up in a seamless fashion to a long cylinder of several microns [181]. Along the circumference one finds usually between 10 and 40 carbon atoms. Each nanotube can be described with the chiral vector $\mathbf{C}_H$

$$\mathbf{C}_h = n\mathbf{a}_1 + m\mathbf{a}_2 \equiv (n, m), \tag{5.34}$$

as the number of unit vectors $n\mathbf{a}_1$ and $m\mathbf{a}_2$ of the honeycomb lattice of the graphene layer. A usual convention is the brief notation of (n, m) for the chiral vector $\mathbf{C}_H$. The tube diameter can be written in terms of the integers (n, m):

$$d_t = C_h/\pi = \frac{\sqrt{3(m^2 + mn + n^2)}}{\pi} a_{CC}, \tag{5.35}$$

with C_h being the length of the chiral vector $\mathbf{C}_h$ and a_{CC} the nearest-neighbor C-C distance in graphite ($= 1.421$ Å). The angle between $\mathbf{a}_1$ (horizontal vector in Fig. 5.2.12(b)) and

downwards to $\mathbf{C}_h$ is defined as the chiral angle θ [182], which can be expressed as:

$$\theta = \tan^{-1}\left(\sqrt{3}m/(m+2n)\right). \tag{5.36}$$
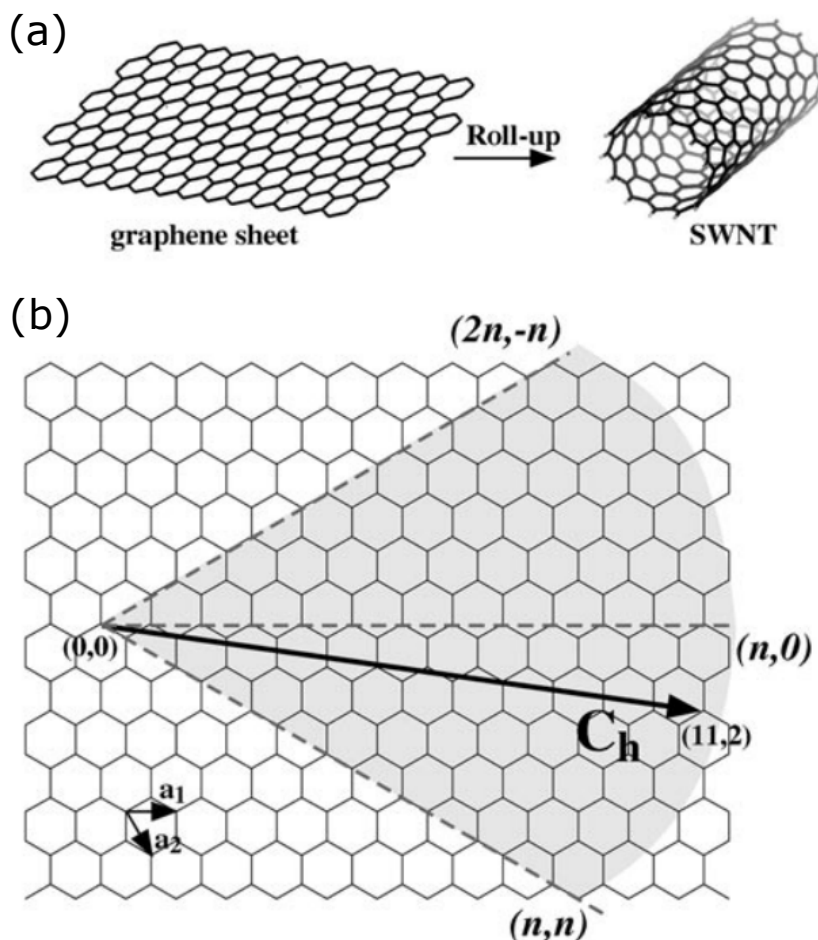

Figure 5.2.12.: Representation of single-walled carbon nanotubes. (a) Graphene sheet being rolled up into a seamless tube. (b) Illustration describing the distinct possibilities of building a nanotube from a 2D graphene sheet. a_1 and a_2 are the lattice vectors, $C_h = na_1 + ma_2$ is the roll-up vector with quantized indices. In the shaded region, the possible combinations of n and m are unique. Schematic taken from [183].

The SWNT can therefore be fully defined either by the chiral indices (n, m) or equivalently by the combination of tube diameter d_t and chiral angle θ. An angle of $\theta = 0°$ along $\mathbf{a}_1$ is called "zigzag" with $(n, 0)$ or $(0, m)$, whereas $\theta = 30°$ corresponds to the name "armchair" and $n = m$. The angle can be varied to be $0° = \theta = 30°$, one speaks of chiral nanotubes in these cases.

The electronic structure is going to be discussed from the viewpoint of a tight binding model. One starts with a 2D layer of graphene and introduces the periodic boundaries of

the cylinder structure of SWNT. The two-dimensional energy dispersion of graphite was calculated by Saito *et al.* [184], giving the energy eigenvalues when only considering the valence π and conduction π^* bands of graphite:

$$E_{g2D}^{\pm}(\mathbf{k}) = \frac{\epsilon_{2p} \pm \gamma_0 \omega(\mathbf{k})}{1 \mp s\omega(\mathbf{k})}, \tag{5.37}$$

with the C-C transfer energy $\gamma_0 > 0$, E^+ and E^- denoting the energies for the π^* and π bands, respectively, and s is the overlap of the electronic wave function on adjacent sites. $\omega(\mathbf{k})$ is given by

$$\omega(\mathbf{k}) = \sqrt{|f(\mathbf{k}|^2)} = \sqrt{1 + 4\cos\left(\frac{\sqrt{3}k_x a}{2}\right)\cos\left(\frac{k_y a}{2}\right) + 4\cos^2\left(\frac{k_y a}{2}\right)}. \tag{5.38}$$

The electronic energy dispersion is plotted in Fig. 5.2.13 (a) with the parameters $\gamma_0 = 3.013$ eV, $s = 0.129$ and $\epsilon_{2p} = 0$ in accordance with experimental data [185]. The inset depicts the energy dispersion along three high symmetry points (Γ, M, and K), revealing the crossing of the conduction π^* and valence π band at the K-points in the hexagonal Brillouin zone. Thus, due to this degeneracy, graphene has no gap and shows metallic behavior in its single-layer structure.
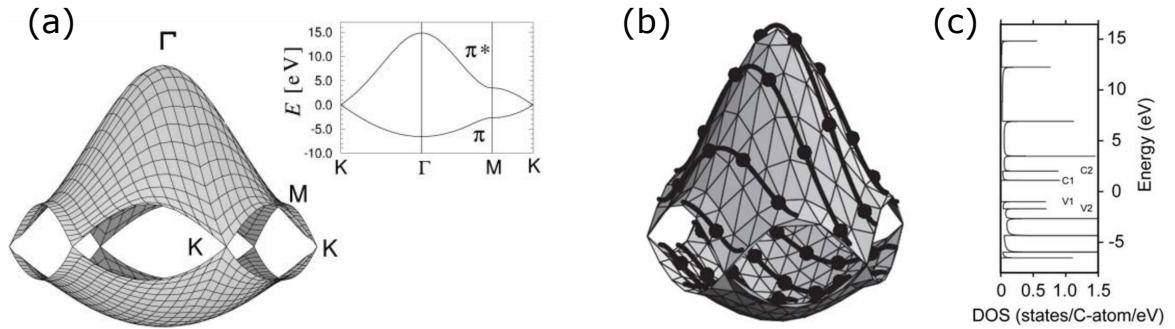

Figure 5.2.13.: Tight binding calculations of 2D-graphene (a) and a (4,2) nanotube (b). The inset in panel (a) visualizes the energy dispersion between the high symmetry points Γ, M, and K. The valence band π and the conduction band π^* are degenerate at the K-points at the Fermi energy. The geometric boundaries of a SWNT lead to only a distinct set of k-states dependent on the diameter and the chirality of the tube. The resulting cutting lines in the calculated 2D-graphene energy dispersion are depicted for a (4,2) nanotube with the thick lines in panel (b). (c) The energy dispersion of the cutting lines can then be transformed into the electronic density of states with V1, V2, C1, and C2 denoting the contributions of the two highest valence bands and lowest conduction bands. The images were taken from [186].

When rolling up the 2D layer, additional periodic boundary conditions arise from the circumferential direction. Hence, only a certain set of k states from the just described electronic energy dispersion are allowed. This set is determined by the diameter and the chirality of the tube structure and can therefore be completely described by the indices (n, m). An example of the resulting cutting lines for a specific SWNT, namely (4,2), is given in Fig. 5.2.13 (b) as thick black lines. If the cutting lines cross the K-point, the nanotube will also behave metallic, while this is not the case in the shown example, the SWNT (4,2) there-

fore has a band gap in the electronic structure and subsequently a semiconducting nature. Note, that in both the metallic and the semiconducting state, the states close to the Fermi energy are all in the vicinity of the K-point. Hence, most of their transport and other properties are strongly dependent on the actual shape of the energy dispersion as well as on the closest cutting line to the K-point. This enables a general categorization via the equation $(2n + m) \bmod 3$. If the sum is divisible by 3, the SWNT are metallic e.g. passes through the K-point, while for a rest of 1 or 2, we find semiconducting nanotubes S1 or S2, respectively [187]. Finally, one can conclude that the electronic properties of single SWNT are entirely determined by their corresponding geometrical structure [188, 189].

The cutting lines in the energy dispersion lead to an altered band diagram of the SWNT compared to a simple graphene sheet, which can be simplified to the electronic DOS, depicted for the (4,2) nanotube in Fig. 5.2.13 (c). The highest DOS stems from VHs, which are localized at the closest position of the cutting lines to the K-point. Optical transitions mainly take place between the highest DOS singularity of the individual valence and conduction bands. The corresponding energies between the bands is conventionally denoted as E_{ii}, with i standing for the order of the valence or conduction bands taking part in the transition. The energy difference can be inversely connected to the diameter for the metallic and semiconducting case by [190, 191]:

$$E_{11}^M(d_t) = 6a_{C-C}\,\gamma_0/d_t, \quad \text{and} \quad E_{11}^S(d_t) = 2a_{C-C}\,\gamma_0/d_t. \tag{5.39}$$

By attributing a number i to the order of a valence or conduction band symmetrically distributed with respect to the Fermi energy, the optical transitions E_{ii} take place for $\delta i = 0$ for parallel or $\delta i = \pm 1$ for perpendicular polarization of the electric field with the nanotube axis as a reference [192]. The latter configuration is strongly suppressed by a depolarization effect, thus only the parallel configuration is relevant [193]. In Fig. 5.2.14 the energy separation of the highest DOS in the energy bands against the nanotube diameter d_t for all (n, m) is plotted, a so-called Kataura plot [194]. Semiconducting nanotubes are depicted as black points, while metallic as red circles. The used values are matched for experimental results and the most commonly used laser energy during this work ($532\,\text{nm}$ or $2.33\,\text{eV}$) is marked as a green line. This plot is of great importance for resonant Raman spectroscopy, allowing the determination of the most common diameter d_t in a given SWNT bundle. For that matter, specific transitions are resonantly enhanced, if the exciting laser energy and the transition are closely matched. Resonant Raman spectroscopy, therefore, employs as many different laser lines as possible to characterize the sample fully.
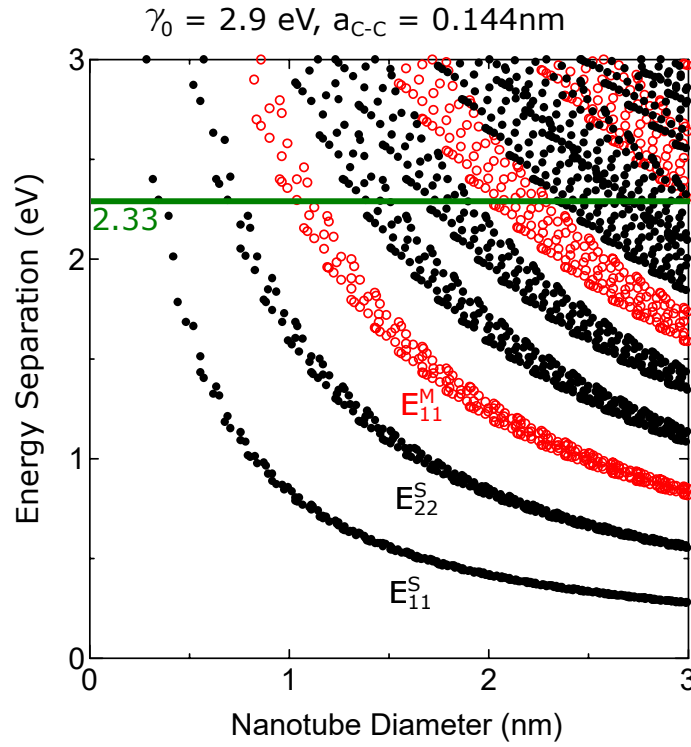
$$\gamma_0 = 2.9 \text{ eV}, \, a_{\text{C-C}} = 0.144 \text{nm}$$

Figure 5.2.14.: Kataura plot of the radial breathing mode (RBM). The energy difference of the singularities in the DOS against the nanotube diameter d_t in accordance with equation 5.39. Metallic and semiconducting nanotubes are depicted as red circles and black points, respectively. The green line marks the energy of the employed laser during this work. Plot adopted from [195].

Several different Raman processes allow the thorough characterization with respect to the physical properties and the material quality of the investigated SWNTs, which will be described in the following. The Raman processes can be categorized by their numbers of emitted phonons (one-phonon, two-phonon, and multiple-phonon scattering process) and by the order of a Raman process with respect to the number of scattering sequences. The typical bands in Raman spectra are described from low to high transferred energy:

Radial breathing mode (RBM): This first-order Raman process describes the increase and decrease of the tube diameter similar to a "breathing" motion. Their frequency is found in the range of $100 - 250$ cm^{-1} and has been connected empirically to the tube diameter numerous times. As an example Bachilo *et al.* have found the following expression [196]:

$$\nu_{\text{RBM}} = \frac{A_1}{d_t} + A_2, \quad (5.40)$$

with the Raman frequency of the RBM of a SWNT ν_{RBM} as an experimental result, $A_1 = 223.5$ cm^{-1} nm, and $A_2 = 12.5$ cm^{-1} as numerical values. The resulting diameter can then be connected with Eq. 5.35 to obtain the characteristic indices (n, m) of the individual SWNT.

D-band: A first-order disorder- or defect-induced scattering process has been well studied in sp^2-hybridized carbon materials like graphene located at the K-point of the BZ and was identified to be a resonance process of a phonon and an electronic transi-

tion between linearly dispersive valence and conduction band [197]. Its excitation is therefore dependent on the laser energy and is observed at 1350 cm^{-1} for a green laser at 532 nm [198]. Furthermore, it involves the scattering of a vacancy or impurity of the carbon lattice and is not observable in clean SWNT.

G-band (G$^+$ and G$^-$): The G-band in graphene is the signature of the vibration of two dissimilar carbon atoms in the honeycomb lattice with an energy of 1582 cm^{-1}. In the case of a rolled-up nanotube, the curvature of the tube and the accompanying folding of the Brillouin zone complicates the lineshape of the Raman response [199]. The vibration of the hybridized carbon atoms can either take place along the tube axis (G$^+$, higher energies $\approx$ 1591 cm^{-1}) showing no dependence on the tube diameter or tangential to the circumferential direction of the tube (G$^-$, lower energy) with a strong dependence on d_t^{-2}. This is quickly understood as the curvature lowers the C-C force constant more profoundly for smaller diameters, subsequently decreasing the excitation frequency as well. Additionally, the decrease differs in magnitude dependent on the metallic or semiconducting nature of the SWNT. This has been related empirically by Joria *et al.* [200] to

$$\omega_{G^-} = 1591 \text{ cm}^{-1} - C/d_t^2, \tag{5.41}$$

with $C_M = 79.5$ cm^{-1} ·nm^2 for metallic and $C_S = 47.7$ cm^{-1} ·nm^2 for semiconducting SWNT, respectively. The lineshape is also dependent on the electronic properties as both excitation peaks yield a symmetric lineshape for semiconducting nanotubes, whereas only G$^+$ is symmetric in the metallic system. ω_{G^-} has an asymmetric lineshape, described with a Breit-Wigner-Fano peak, which takes a coupling to an electronic continuum into account [201]. This difference in lineshape allows an easy characterization of the electronic properties. The intensity ratio of the D- and G$^+$-band have been described as a characterization method for the number of impurity particles and defects in the SWNT sidewalls [202].

M-band: Overtone of an out-of-plane TO-phonon mode located at 1755 cm^{-1} [203].

G'-band: The second overtone of the D-band, thus similarly dependent on the excitation light, but located at approximately 2700 cm^{-1} for the here used laser energy. Since this process is also present in defect-free carbon nanotubes, the ratio $I_D/I_{G'}$ is commonly utilized to assess the quality of the manufactured SWNT [204].

The SWNTs used during this work were suspended in H_2O. The solution was stirred for five minutes in the ultrasonic bath, to guarantee the homogeneous distribution of nanotubes. A state-of-the-art UHV-sputtering setup was used to freshly manufacture thin films with either 100 nm gold or silver on top of a Si-substrate. Between one and three drops of SWNT-solution were put on one side of the sample to ensure a high enough density of nanotubes in a specific region and a clean metallic surface in another. The sample was dried for a few minutes under a constant flow of highly clean nitrogen before the remains of the solution were removed by dipping the sample in clean water. After drying the sample again, it was moved into an atomic force microscope (AFM) under ambient conditions

and the SWNT distribution was checked, as well as the approximate surface quality of the metallic surface after this procedure. If both characteristics were sufficient, the sample was transferred into the UHV system. Two exemplary AFM images are presented in Fig. C.1.1. Note, that this dropping method leads to a high density of bundled nanotubes along one direction, making it hard to distinguish between them with our topographic measurements [183].

5.3. Results

In this section, the previously described upgraded setup is characterized regarding its performance in STM and Raman measurements, before the obtained experimental results regarding TERS are presented and discussed.

5.3.1. Characterization of the equipment

First, for reducing the vibrational noise the room itself and the equipment were isolated and left alone for several minutes before starting the measurements remotely. A resulting STM image of a clean surface of bulk-Au is displayed in Fig. 5.3.1(a). The height of an atomic monolayer in Au(111) is $235\,\text{pm}$ [205] and is used for an estimate of the noise and a first z-calibration of the STM head at room-temperature (c. Fig. 5.3.1(b)). For another issue, the piezo motors have to be re-calibrated after cool-down. Highly ordered pyrolytic graphite (HOPG) is broadly used for atomic-scale calibration of scanning techniques in all three dimensions. It is a bulk crystal made out of several layers of graphene, stacked in an ordered fashion. The interaction in one layer is far stronger than between its van-der-Waals coupled layers. HOPG has a smooth surface and can be cleaved easily. The distance of two layers is well defined to be $0.3354\,\text{nm}$. Two calibrated topographic test images are shown in Fig. 5.3.1, panel (c) depicts a measurement at room temperature and panel (d) at $20\,\text{K}$. The tunneling current was set at $1\,\text{nA}$ for both, and the speed of the tip was set at 100 and $250\,\text{nm/s}$ for high and low temperatures, respectively. Note that the measurements in panel (a) and (c) used a gold tip, in contrast to the silver tip of panel (d). The much higher signal-to-noise level at low temperatures can at least partially be explained by this fact, as the silver tips tended to take longer before obtaining clear topographic images. Another option would be the higher used scanning speed at low temperatures to allow more measurements at the cooled-down state. From here on, all proceeding STM measurements were performed using a Ag-tip.
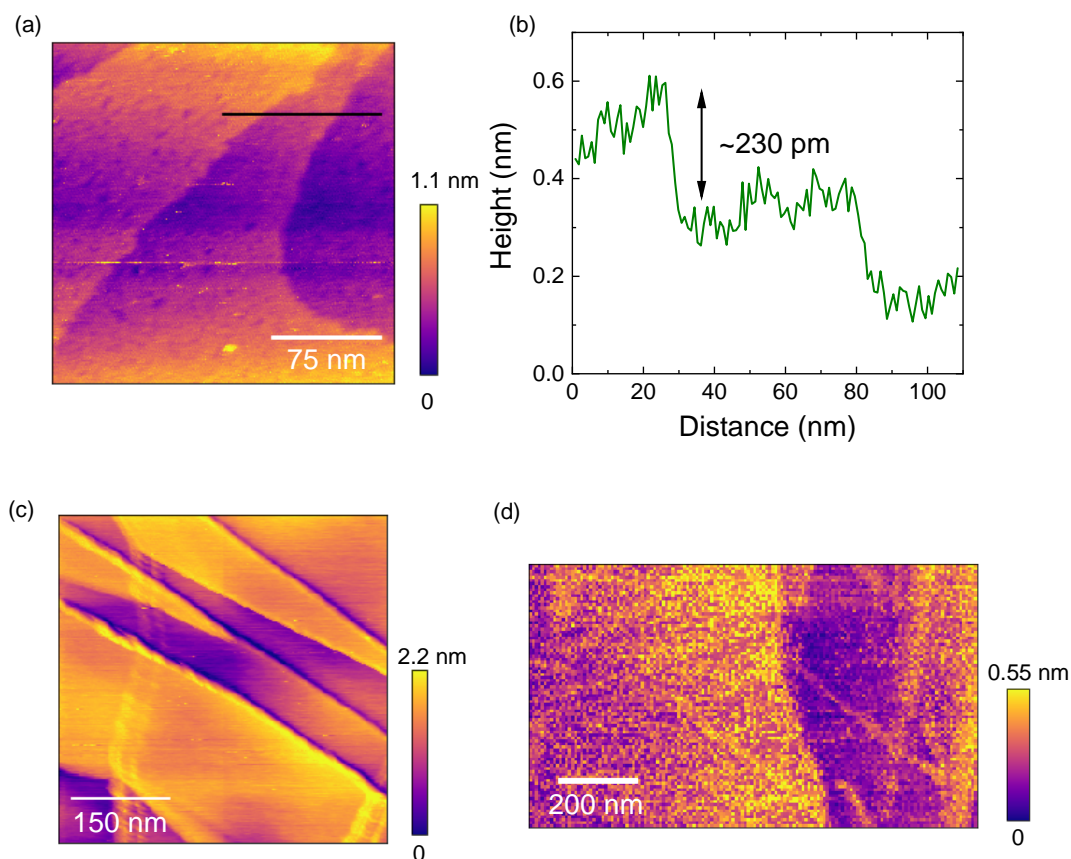
(a)

(b)

(c)

(d)

Figure 5.3.1.: Topographic image of Gold (upper row) and HOPG (lower row) at room-temperature and at $20\,K$ **for calibration.** Panel (a) presents the surface of a clean Au-sample at room-temperature measured witha Au-tip. Along the black line, the step sizes are measured and visualized in panel (b). This allows the first z-direction calibration of the STM head. (c) Several steps are visible in HOPG with a height of approximately $0.34\,nm$ as expected. The topographic images on HOPG were performed with a Ag-tip. (d) Calibration measurement to account for "freezing" of the piezo-motor. While a much higher noise level was observed during the calibration measurements, a significantly clear edge in the center was obtained, enabling the re-calibration of the z-direction.

In both images of HOPG, a flat surface with clear edges is visible. The edge of the low-temperature measurement in the center was observed to have a clear enough structure in the z-direction to adjust for the smaller movements by the piezo motor after the cool-down. Unfortunately, the observed noise level does not allow the calibration in the x- and y-direction, since one would need to observe the distance between single carbon atoms. Yet, for the purpose of height calibration, the illustrated images are sufficient and we proceeded with measurements on different samples.

As described earlier, SWNTs were used for the characterization of STM, Raman, and TERS. Several drops of liquid containing SWNT were placed on $100\,nm$ thin gold films on a silicon substrate. A topographic image was obtained (Fig. 5.3.2) for a tunneling current of $1\,nA$ and a scanning speed of $250\,nm/s$. The step size between two measured heights was set at approximately $10\,nm$, but the directional distance was not calibrated at low temperatures. Several bundles of SWNT are visible in the form of long tubes with varying thicknesses of around $1\,nm$ in accordance with the literature [206, 207]. Underneath the

nanotubes individual islands of the evaporated gold can be resolved. With the used scanning parameters only nanotube bundles are resolved. Since these bundles are by far smaller than the diffraction limit, we proceed with the characterization of our Raman setup.
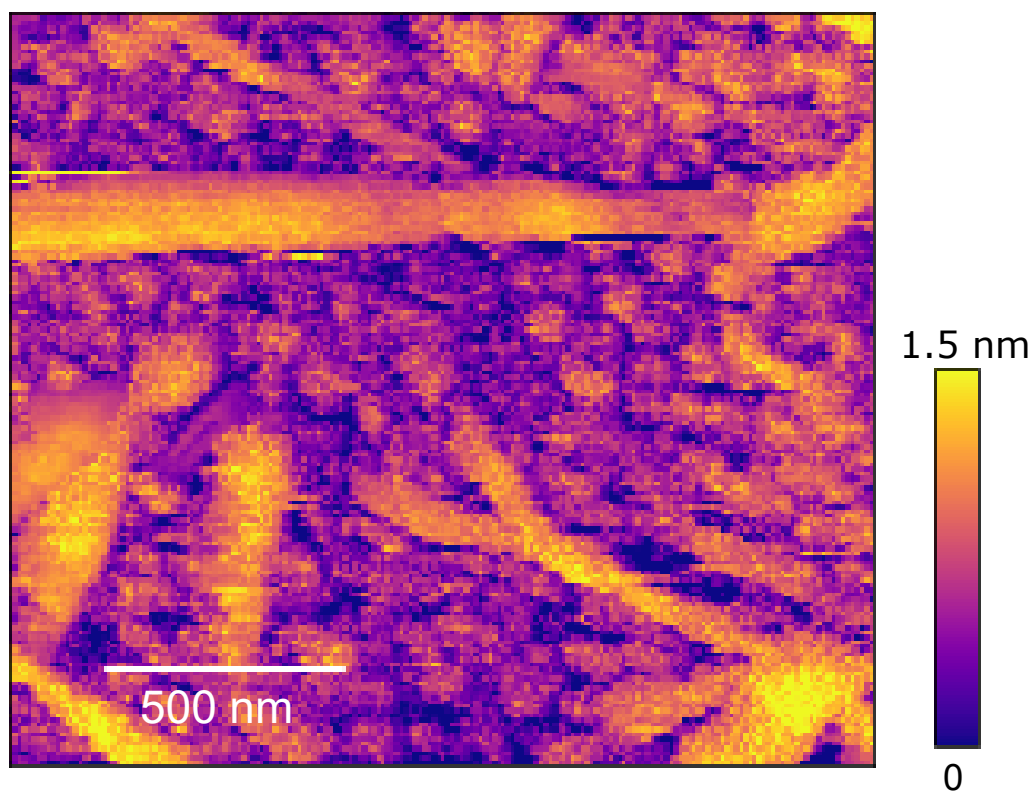

Figure 5.3.2.: Topographic image of SWNT on thin gold film at 20 **K.** Several aligned bundles of nanotubes can be resolved on top of the evaporated gold islands.

For calibrating the sensitivity of the Raman setup {100} silicon samples were used. The polarization was selected to be in the XY configuration for a measurement between 338 to 1028 cm^{-1} with a step size of approximately 0.5 cm^{-1}. The laser power and the dwell time per exposure were set at 1 mW and 1 s, respectively. The resulting silicon phonon is depicted in Fig. 5.3.3 in the range of 350 to 700 cm^{-1}. The observed Raman response saturates at ≈ 2500 cts/(s mW), a value that was used as a benchmark to quantify the alignment quality after each cool-down.
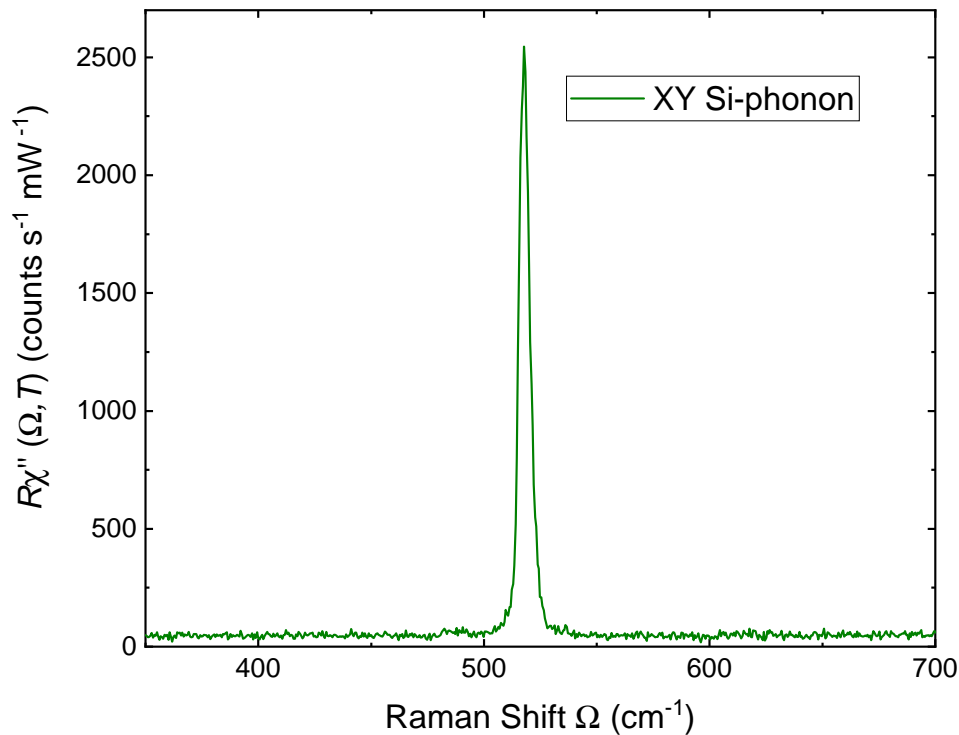
Figure 5.3.3.: Raman response of the Silicon phonon in XY polarization. After the approx-
imate alignment of the optical path for the scattered light, the countrate of the
silicon phonon is used for a fine adjustment. This procedure results in a maxi-
mum of 2500 counts per second and mW laser power before entering the cryostat
and a small background signal. For the following measurements, this countrate
was used as a reference for good alignment.

5.3.2. Tip enhancement in single wall carbon nanotubes

In the following section, the comparison of far- and near-field Raman results of SWNTs
dispersed on a thin gold film sample on a silicon substrate. All measurements were per-
formed at $20\,K$ using a silver tip. The successful deposition of SWNT onto a specific part of
the sample was verified by ambient atomic force microscopy measurements, as shown in
Sec. C.1. The remaining pristine Au region of the sample was occasionally used as a spot
for re-preparing the tip.
For the measurements the following preparation protocol was used:

1. Silver tips were prepared and cleaned in-situ on bulk Au or Ag.

2. The tip quality was verified by topography measurements as shown in Fig. 5.3.4.

3. Thereafter, the bulk sample was replaced by the gold thin film with SWNTs in a small
   region.

4. The sample was properly aligned using Raman measurements.

5. The tip was moved into the laser spot.

6. STM measurements enabled the localization of a clearly visible SWNT.

7. If the quality was found to be insufficient, the tip was re-prepared on a clean part of the gold thin film using the field emission approach, before restarting from step 4.

8. The tip was moved on top of the SWNT.

9. The influence of the retracted tip alone on the Raman spectra was analyzed.

10. The tip was approached to the sample.

11. The measurements were started by remote control.

The topographic image was measured with a constant tunneling current of $1\,nA$ (step 2, Fig. 5.3.4). Several SWNT-like structures are visible. The resolved nanotubes vary substantially in size possibly due to clustering of the individual tubes. The resolution is insufficient for a detailed analysis. Fig. 5.3.5 shows the comparison of Raman spectra obtained with the tip approached ($1\,nA$ tunneling current) and retracted at the white spot indicated in Fig. 5.3.4. The measurements focus on the G^-- and G^+-band transitions. Spectra in XY and YX configurations (with respect to the sample axis) are shown in Fig. 5.3.5 (a) and (b), respectively. Here, the incoming light with X-polarization in the sample plane also has contributions parallel to the tip axis, whereas the Y-polarization has mainly contributions perpendicular to the tip.
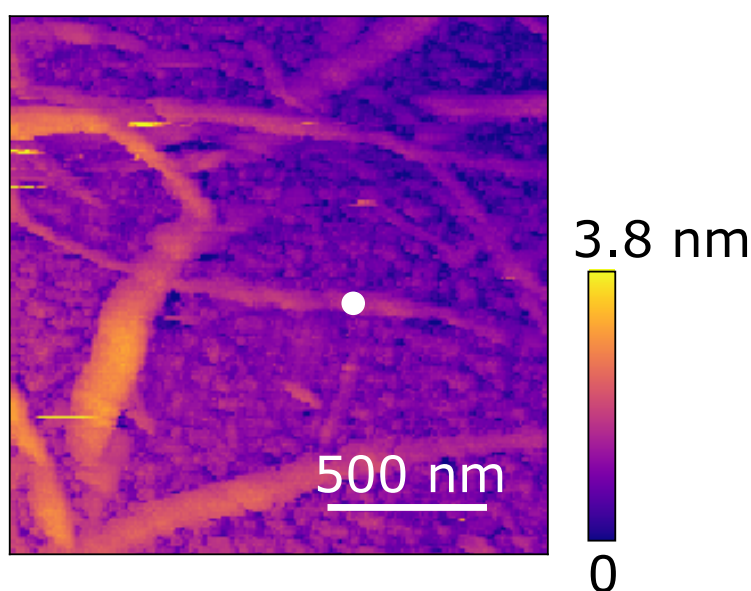

Figure 5.3.4.: Topography of the laser spot region preceding the Raman measurements in Fig. 5.3.5. The image was recorded with a constant tunneling current of $1\,nA$. The depth profile is color-coded as indicated on the right. The Raman spectra were measured on top of the horizontal SWMT bundle at the position of the white spot.

The Raman measurements were performed in the range from 1293 to $1877, 8$ cm^{-1} with a binning of 1, resulting in a step size of 0.5 cm^{-1}. Since the laser power outside the cryostat was only 0.25 mW, the absorbed power and the resulting local heating are neglected for now. The measurements were repeated several times to increase the statistical significance. The results shown in Fig. 5.3.5 and 5.3.6 were obtained consecutively, without changing the tip position and only slightly readjusting the optical path after changing the polarizations. With the tip retracted, the background signal is almost twice as strong for YX configuration. Also the G$^-$- (≈ 1569.7 cm^{-1}) and the G$^+$-band (≈ 1593.8 cm^{-1}) have higher spectral weights as determined by fits using Lorentz functions.
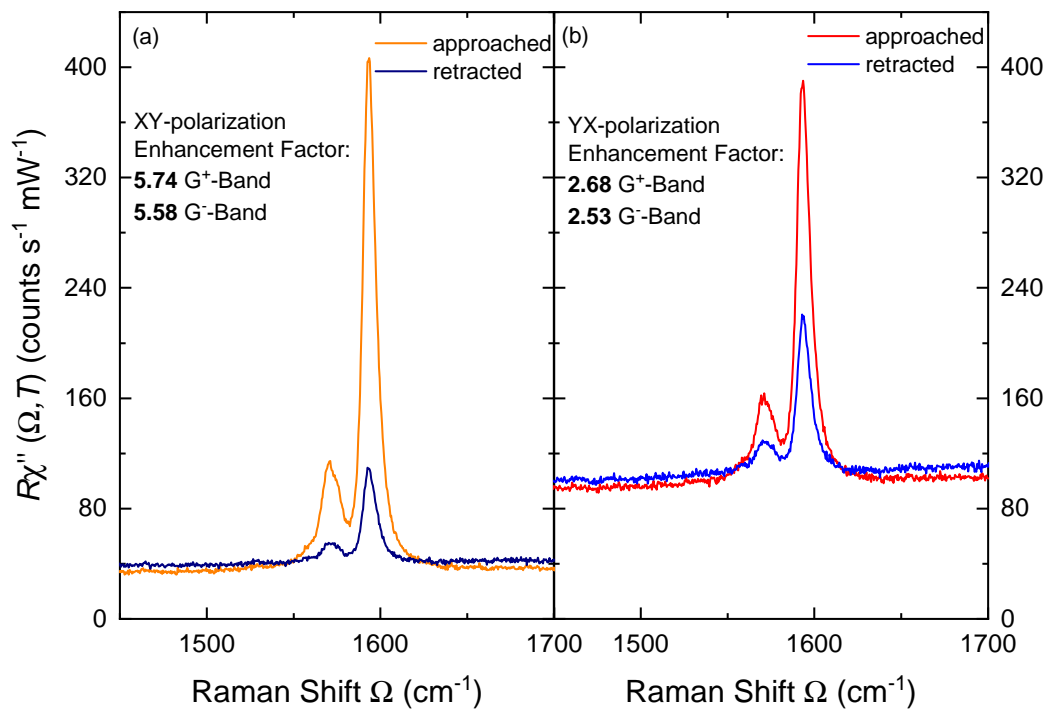

Figure 5.3.5.: Raman signal for retracted and approached (tunneling mode) Ag-tip. Panels (a) and (b) depict the XY- and YX-polarization on the sample surface, respectively. The enhancement factors of the G$^-$- and G$^+$-band are bigger by a factor of approximately two for XY than for YX configuration. The background response is higher in the YX configuration but gets slightly diminished when the tip is approached, potentially due to some blocking of the laser spot.

With the tip approached background and phonons change distinctly. For both polarization combinations, the background stays almost constant with only a slight reduction, most likely as a result of the tip blocking some portion of the laser spot and thus the far-field contribution. In contrast to this observation, the Raman response of the G$^-$- and G$^+$-band transition becomes significantly stronger in both polarizations. Interestingly, the measured increase is bigger by a factor of approximately two in XY- than in YX-polarization. For a quantitative analysis, the peaks were fitted with two Lorentzian peaks and a simple background, giving a relation of the two peaks and their intensities, defined here as the enhancement factor EF:

$$EF = \frac{I_{\text{approached}}}{I_{\text{retracted}}} = \frac{I_{\text{total}}}{I_{\text{far}}} \qquad (5.42)$$

The resulting values for EF can be found in Tab. 5.3.1. Note, that this is the actual intensity magnification, rather than a comparison of the near and far field contributions [208]. In the latter case, one would get the Raman enhancement factor g as:

$$g = c * \frac{V_{\text{far}}}{V_{\text{near}}} = \left(\frac{I_{\text{total}}}{I_{\text{far}}} - 1 \right) \frac{V_{\text{far}}}{V_{\text{near}}}, \qquad (5.43)$$

with c being the contrast and V_{far} over V_{near} the fraction of the contributing scattering volumes. In our case here, the actual number of participating nanotubes in the far field compared to only one nanotube right at the tip gives the ratio of the scattering volumes. The ratio may be estimated via the spot diameter and the area fraction covered by nanotubes. The minimal spot diameter can be calculated to be

$$\text{d} = 1.27 \cdot \lambda \cdot M^2 \cdot \frac{f}{D} \approx 900 \, \text{nm} \qquad (5.44)$$

with M^2 being assumed to be 1 for a perfect Gaussian spot and $f = 8 \, \text{mm}$, the beam diameter $D = 6 \, \text{mm}$, and $\lambda = 532 \, \text{nm}$. It is unrealistic that a spot diameter of approximately $1 \, \mu\text{m}$ can be achieved. The microscopic image (Fig. 5.2.11) rather suggests $D_f \approx 5 \, \mu\text{m}$. The topographic image (Fig. 5.3.4) revealed several bundles in this area with estimates of $40 - 120$ SWNTs per bundle in the literature [209]. Instead of this vague estimate, a more robust approximation of the participating nanotubes can be given via the covered area in the topographic images. On the basis of these considerations we retrieve a coverage in the range of approximately $C \approx 0.3 - 0.8$. We proceed with an average of $C = 0.5$. We now can re-adjust the equation of g with respect to the participating areas instead of the volumes:

$$g = \left(\frac{I_{\text{total}}}{I_{\text{far}}} - 1 \right) \frac{C \cdot A_{\text{far}}}{A_{\text{near}}} = \left(\frac{I_{\text{total}}}{I_{\text{far}}} - 1 \right) \frac{C \cdot (D_f)^2}{(2r_{\text{near}})^2}. \qquad (5.45)$$

Here, the near-field contributions are estimated to be stemming from the area in the vicinity of the tip, having an approximately circular shape with a radius in the range of $r_{\text{near}} \approx 1 - 10 \, \text{nm}$. The lower given limit is an approximation from TERS mapping resolutions observed by Liao *et al.* [41], whereas the upper limit is given by an approximate radius of the tips in the SEM pictures. The resulting values of g are listed in Tab. 5.3.1.

Furthermore, we can estimate the size of the tip-enhanced nanotube with the empirical relation of tube diameter and G^--band frequency presented in Eq. 5.41 [200]. We adjust the empirical value for the G^+-peak to 1593.8 cm^{-1} and assume a semiconducting nanotube, since no clear asymmetry and a rather small linewidth of ≈ 9 cm^{-1}, attributed to semiconducting nanotubes [210], is observed for the G^--band. This leads to a diameter of $d_t = 1.41 \, \text{nm}$, agreeing fairly well with the STM extracted SWNT height. These values of d_t correspond to an assigned semiconducting nanotube for the transition E_{33}^S from the Kataura plot and potentially assigned indices of $(14, 6)$.

Measurements were also performed in the range 72 to 791 cm^{-1} with a wavenumber

distance of approximately $0.5\,\text{cm}^{-1}$, using a laser power of $0.25\,\text{mW}$. Here, the goal was to observe changes in the RBM in the two different crossed polarization configurations depending on the Ag-tip position. This is of particular interest, since the breathing mode is a clear fingerprint of a fully intact SWNT, allowing the most accurate approximation of the tube diameter. The spectra are illustrated in Fig. 5.3.6 with the RBM clearly visible at $170\,\text{cm}^{-1}$. By using Eq. 5.40, one can extract a reasonable value for the tube diameter $d_t \approx 1.42\,\text{nm}$, in very good agreement to the extracted value from the G^+ and G^--peaks. This similarity can be interpreted as a signature of the same SWNT being enhanced by the vicinity of the metallic tip, but one has to be cautious with this statement as the diameter extracted using only the far-field spectra with a retracted tip shows just slight variations by maximally $10\,\text{cm}^{-1}$ for the G-band approach and visually no change for the RBM mode. As the far-field in principle visualizes an average of the SWNT in the spot region, the typical diameter very well might be at $\approx 1.4\,\text{nm}$.

Similar to the measurements for higher transferred energies, the background is around double in the YX configuration and it decreases slightly when approaching the tip for both polarization configurations.
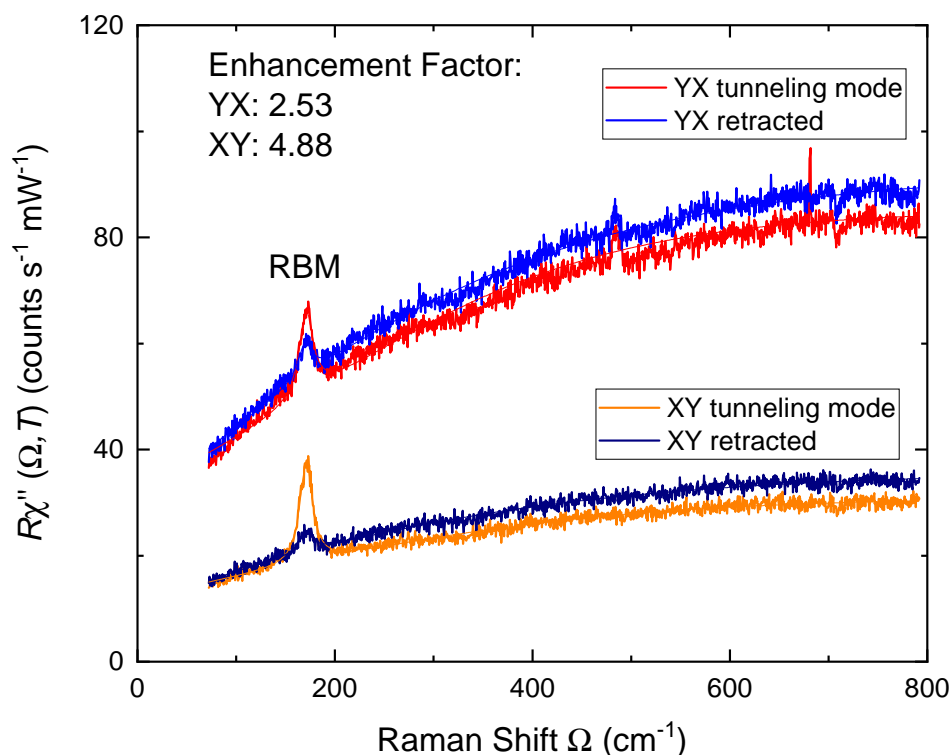

Figure 5.3.6.: Raman signal for retracted and tunneling mode of the Ag-tip. Panels (a) and (b) depict the XY- and YX-polarization on the sample surface, respectively. Similar to the results of the G^-- and G^+-band, the enhancement of the RBM at $175\,\text{cm}^{-1}$ is bigger in the XY case and the background gets diminished. In order to extract the enhancement factor, the spectra were fitted with Eq. 5.46, leading to the peak area ratios of 2.37 (YX) and 4.76 (XY).

The peaks and the electronic continuum were fitted using the following phenomenological approximation:

$$R\chi''(\Omega) = R\chi''(0) + B1 \cdot \tanh(B2 \cdot \Omega + B3) + \frac{2A}{\pi} \cdot \frac{\Gamma}{4(\Omega - \Omega_0)^2 + \Gamma^2} \tag{5.46}$$

$B1$, $B2$ and $B3$ are fitting constants for the background response, A stands for the area of the peak and Γ and Ω_0 are the FWHM and the peak position of the radial breathing mode. The resulting enhancement factor EF and g-values can be found in Tab. 5.3.1.

As a final general enhancement feature, we investigated the defect or impurity-induced D-band transition as well as the M-band. Raman spectra were taken using XY-polarization from 1341 to 1878 cm^{-1} with a binning of 5, resulting in a point distance of 2.5 cm^{-1}. The measurements were performed at a different time and spot as previously and the tip subject to several cleaning procedures up to this point. In Fig. 5.3.7 the virtually invisible D- and M-band are enhanced strong enough to detect them easily upon approaching the tip at 1385 and 1750 cm^{-1}, respectively.
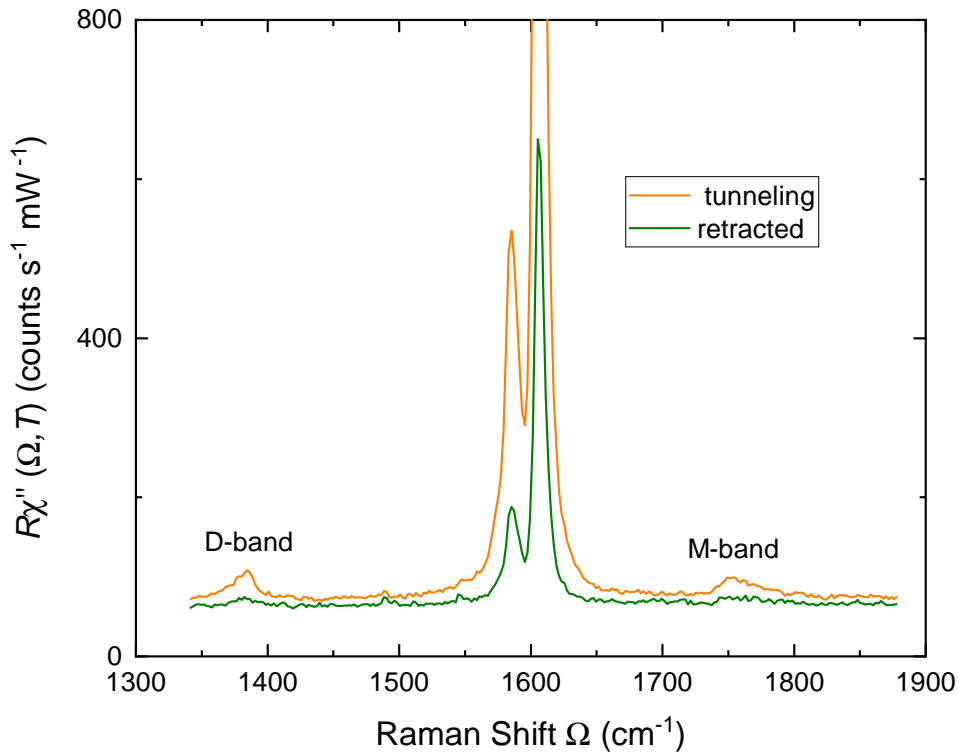

Figure 5.3.7.: Raman spectra including the D- and M-band enhancement. Both excitations yield much lower intensities than the G-band peaks in the center. For the retracted tip, the peaks marked as D- and M-band are next to invisible and only become detectable upon tip approach.

While the M-band is not of particular interest, the D-band enables local characterization. Fig. 5.3.8 (b) and 5.3.12 show that for some tip positions the D band is not even observ-

able with enhancement. Apparently the defect concentration varies along the tubes. The quantitative enhancement of the characteristic vibration modes are collected in Tab. 5.3.1:

Table 5.3.1.: Enhancement factors EF of the nanotube excitations. Calculated intensity magnification of XY and YX polarization from the data illustrated in Fig. 5.3.5 and 5.3.6 by using Eq. 5.42 for EF and Eq. 5.45 for g.

	RBM		G$^+$-band		G$^-$-band	
	EF	g	EF	g	EF	g
XY	4.88	$1.94 \times 10^{5-7}$	5.58	$2.29 \times 10^{5-7}$	5.74	$2.37 \times 10^{5-7}$
YX	2.53	$7.65 \times 10^{4-6}$	2.53	$7.65 \times 10^{4-6}$	2.68	$8.40 \times 10^{4-6}$

The enhancement factors for g of the G$^+$-band have been described in the literature previously, with values mainly settling between 10^4 to 10^6 [211, 212, 213], but can also reach up to 10^8 as published by Liao *et al.* [41]. The here presented enhancement factors on the order of 10^{5-7} are consequently above usual observations but are not reaching the final limits of potential signal enhancements.

Distance dependence

A different set of measurements was performed as a function of the tip-sample distance from $100\,$nm to the tunneling mode. In the first step, Raman measurements were obtained in a XY polarization configuration for a Raman shift of 1293 to $1877, 8$ cm^{-1} and a binning of 1, resulting in a point separation of 0.5 cm^{-1}. This allows the extraction of the G$^-$- and G$^+$-band enhancement as a function of distance, which is depicted in Fig. 5.3.8. The left column takes a look at the actual Raman measurements, whereas the right side gives the enhancement as described by Eq. 5.42. Panel (a) illustrates the taken spectra with a consecutive offset of $20\,$cts/(s mW), whereas panel (b) enables an easier discussion of the two end stages of the tip showing only the raw data of the measurement with closest and farthest tip distance. In contrast to the measurements shown in the previous section, the background is independent of the tip approach. This seems to be most likely explained by the tip position on the laser spot, leading to a blockage of only very little of the participating far field. Apart from that, a clear increase in the intensity of the G$^-$- and G$^+$-band is observable. These transitions were analyzed and compared in panels (c) and (d), respectively, by fitting the peaks of the panel (a) again with a linear background and two Lorentzian functions. The changes are statistically more robust for the G$^+$-band, as its general transition probability is higher from the beginning, giving a clearer fit whereas the starting point of the G$^-$-band is very hard to distinguish from the background. Nevertheless, upon approaching one finds a region for both peaks where no clear changes to the intensity are observable, before the increase sets in at around $50\,$nm. The G$^+$-band excitation shows a clear signature of tip enhancement, which is easily extractable. The Raman signal in the region of high tip-sample distances behaves very stably with only small deviations as expected for the usual noise of inelastic light scattering independent of the tip movement. Once the tip comes closer than $50\,$nm, the EF becomes noisier and increases rapidly, be-

fore saturating for the lowest distances at around $EF = 3.3$. The enhancement seems to be stable if the set tunneling current is varied from 0.5 to $4\,\text{nA}$. By fitting the data of panel (d) with an exponentially decaying function, we find the distance for a decrease to $1/e$ at $32\,\text{nm}$, close to other findings in the literature [214]. Due to the high signal-to-noise ratio of the G^--band, one needs to be cautious with the extracted enhancement factors for these transitions, yet the general shape of its distance dependence is arguably reliable as it shows similar characteristics as the G^+-band.
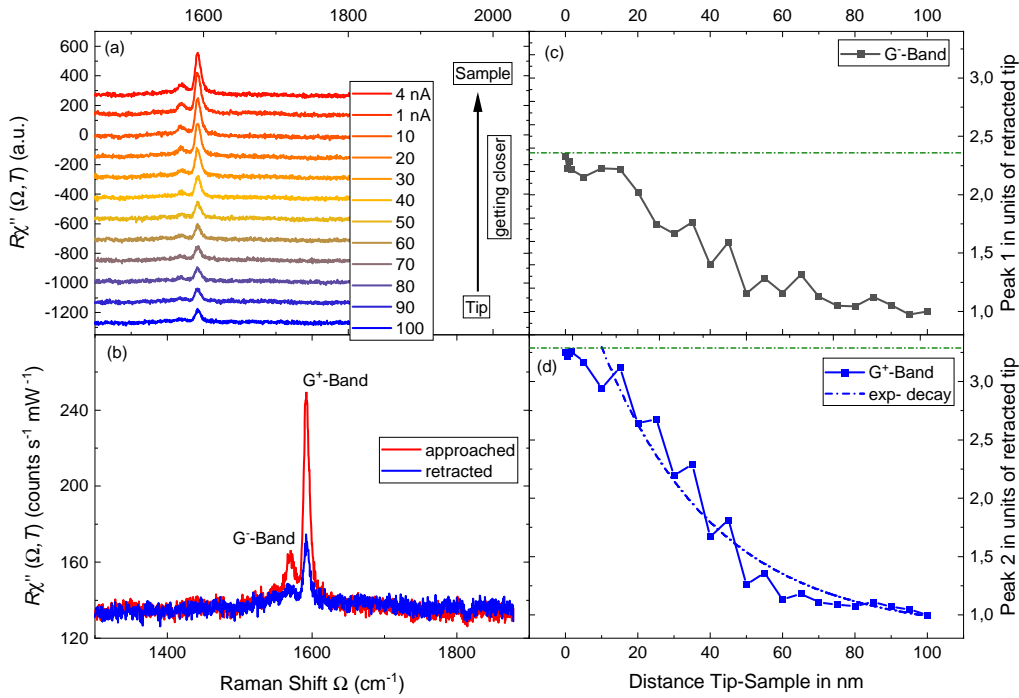

Figure 5.3.8.: Distance dependent measurement of the G^-- and G^+-band excitation enhancement with XY-polarizations. Panel (a) depicts the influences of the approaching tip, the measurements are offset in a consecutive fashion by $70\,\text{cts}/(\text{s mW})$. The retracted mode and the tunneling mode are compared in panel (b), illustrating a constant background and clearly enhanced transition peaks. The G^-- and G^+-band peaks were fitted as a function of the tip-sample distances in panels (c) and (d), respectively. The G^+-distance dependence is fitted using an exponentially decaying function.

In the next step, the influence of the tip approach on the RBM excitation probability was investigated. For that matter, the spectrometer was adjusted to observe Raman shifts from 193 to $839\,\text{cm}^{-1}$. Since the transition has a much smaller cross-section, the binning was set at 10 corresponding to a resolution of approximately $5\,\text{cm}^{-1}$. The tip was approached from $95\,\text{nm}$ until a tunneling current of $4\,\text{nA}$ was reached. The results are illustrated in Fig. 5.3.9 (a) with a consecutive offset of $20\,\text{cts}/(\text{s mW})$. Visually the investigated peak cannot be observed when the tip is far away from the sample. Thus, the previous discussion of the EF does not make sense, since the starting intensity of the far field is zero. Instead, a simple comparison in the form of the intensity difference to the far field background is

plotted in panel (b) with a color scale in accordance with the tip-sample distance of the raw data. The extracted intensity difference of the RBM can be studied in panel (c). The two latter panels clearly visualize the intensity increase upon approaching, yet the form of the curve looks more linear in comparison to what was observed in Fig. 5.3.8 and no clear starting point of the enhancement can be obtained, most likely due to suppression by the noise level.
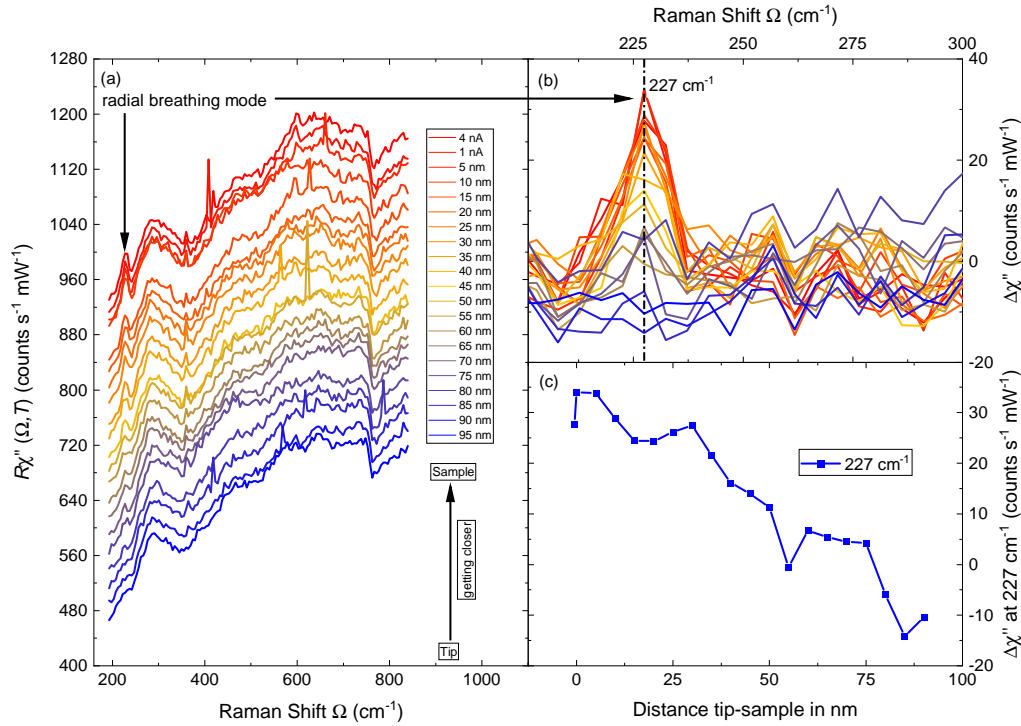

Figure 5.3.9.: Spectral weight of the radial breathing mode as a function of the tip distance. Panel (a) depicts the evolution of the Raman active breathing mode at around $227\,\mathrm{cm}^{-1}$ upon tip approach in steps of $5\,\mathrm{nm}$. The rising intensity is compared to the far field background by subtracting the latter, depicted in (b) and (c).

One has to note, that the Raman shift of the RBM in this set of measurements differs from the earlier observed frequency and is found at $227\,\mathrm{cm}^{-1}$. By using equation 5.40 we find a SWNT with a tube diameter $d_t = 1.04\,\mathrm{nm}$, again comparable with general findings in the literature [196, 215]. By using the Kataura plot from Fig. 5.2.14, this mode putatively stems from a metallic transition, namely the $\mathrm{E}_{11}^{\mathrm{M}}$ with several equally likely indices $(10, 5)$, $(9, 6)$, and $(8, 7)$.

To conclude the distance relation to the tip enhancement, the background of the low and high energy response was inspected. Therefore, Raman spectra were taken in a range from 131 to $2161\,\mathrm{cm}^{-1}$ in the form of 5 different overlapping measurements. The binning was set to 5, the step-size was, therefore, $\approx 2.5\,\mathrm{cm}^{-1}$. The low energy measurements as well as the broader region are presented in Fig. 5.3.10 (a) and (b), respectively. The measurements of the latter panel were multiplied by factors smaller than 10% to match in intensity with their neighboring spectra.
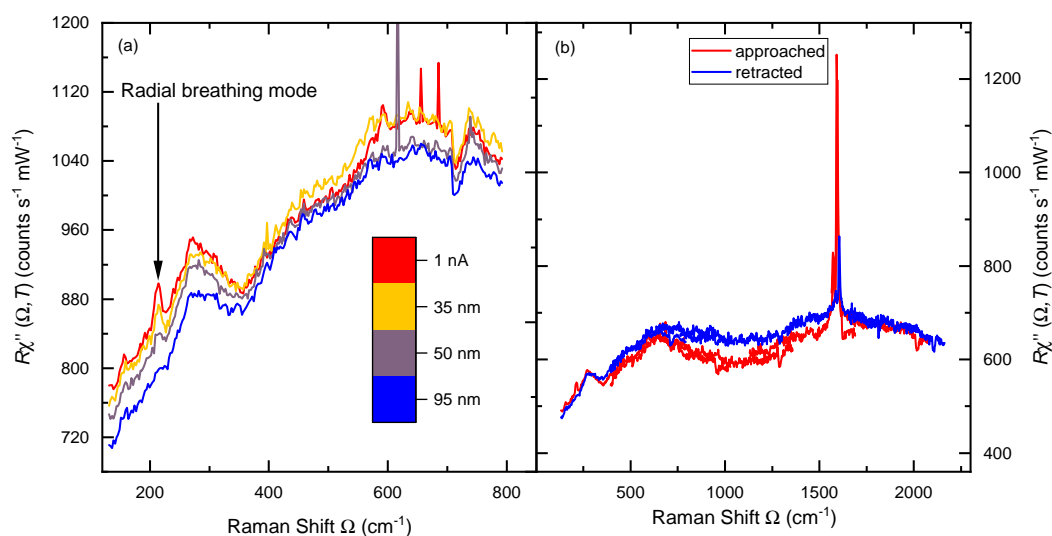
Figure 5.3.10.: Distance dependence of the background shape. Panel (a) focuses on the RBM, these results are then connected to the large Raman shifts in panel (b). No strong deviations upon tip approach are observed.

The low energy measurements reveal again the increase of the RBM intensity upon tip approach. Two additional characteristics in the spectra should be discussed furthermore. On the one hand, a small peak at around 160 cm^{-1} is observed without any visible sign of dependence on the tip position, thus we assign it to the far field. Thus, this might be a manifestation of SWNT differing in diameter and only the specific RBM of the SWNT beneath the tip is enhanced. The corresponding diameter sits at 1.52 nm and can be connected to the E_{33}^S transition. The second issue revolves around the broad hump with a peak at around 275 cm^{-1}. The peak or shoulder visually sharpens, when approaching the tip, but still keeps a broad shape compared to the other RBM peaks even to the lowest tip-sample distances. While the energy of this broad peak is still reasonable for a SWNT, its shape is unconventional. Since this peak shape was not observed for other already discussed measurements, some additional defects in the spot region or rather several double-walled nanotubes (DWNT) were probed locally during this set of measurements. These kinds of nanotubes show a different set of more complicated breathing modes leading to several broader peaks in the region of 250 to 300 cm^{-1} due to their increased diameter, quite comparable to the here observed Raman response [216]. As this peak sharpens, presumably one of these DWNT is localized in the vicinity of the tip.

The high energy spectra illustrated in Fig. 5.3.10 (b) give the dependence of the background to the tip approach. While some spectral weight in the region of around 1100 cm^{-1} is lost as the tip is close to the sample, the general intensity distribution remains the same.

To sum up the distance-dependent measurements, tip enhancement in our system was found to have a $1/e$ decay length of 32 nm and an onset point at approximately 50 nm tip-sample distance, extracted from the behavior of the G$^+$-, G$^-$-band, and RBM of SWNT. The influences on the electronic background were kept small during these measurements,

which is an ideal setup to proceed with spatially resolved TERS experiments.

Lateral dependence

The spatial resolution of our system is presented in Fig. 5.3.11, which will be discussed in the following. A STM topographic image is shown in panel (a) with several visible clusters of nanotubes. The region of interest was set around a horizontal, but thinner cluster. A step-by-step rastering of this region was then performed by using a custom-made MATLAB program, which was used to get a TERS topographic image. For the individual Raman measurements $9\,$s integration time, a Raman shift of 1293 to $1877,8$ cm^{-1}, and a binning of 1 was set. The polarization was adjusted to be XY. Since the G$^+$-band shows high enhancement and the biggest intensity, it was used to track the measured response and potential spatially dependent changes. The results are shown in Fig. 5.3.11(b), while the measured background can be found in panel (c). The points of Raman measurements marked in white and the STM picture are overlapped in Fig. 5.3.11 (d) and the region of highest intensity are marked in greenish. The background shows no signs of a dependence on the tip position on the sample, while the G$^+$-response repeats distinct features of the STM picture. Most pronounced is the response in the center right on top of a horizontal nanotube structure. The region in the right upper corner, where the STM image shows only the grown gold islands leads to the smallest observed Raman response, while some additional clusters of nanotubes on the left side lead to some additional increase in panel (b). It is worth mentioning, that the stronger response is most pronounced for the horizontal clusters of SWNT. Since the G$^+$-band is a vibration of the misaligned carbon atoms along the axis of the tube, some polarization dependence of its excitation in relation to its orientation would explain this result, but this dependence would be expected as a result of the normal incoming light polarization contributing mainly to the far-field. The enhancement itself would be expected to be radially homogeneous with respect to the tip axis as calculated theoretically [217]. Apart from the depolarization effect taking place at the tip apex, this selective enhancement can be understood in our system, as our tip also has some slight angle, likely leading to this additional anisotropy.

To understand the spatial resolution a line perpendicular to the investigated nanotube cluster was used to illustrate the edges obtained by STM and TERS in Fig. 5.3.11(e) and (f). The clear increase in height with a FWHM$\approx 115\,$nm observed by STM can be compared to the TERS image, revealing the edge clearly in a range of at least $70\,$nm. Due to time limitations a higher resolved TERS image could not be obtained, yet most importantly this resolution is already well below the diffraction limit.
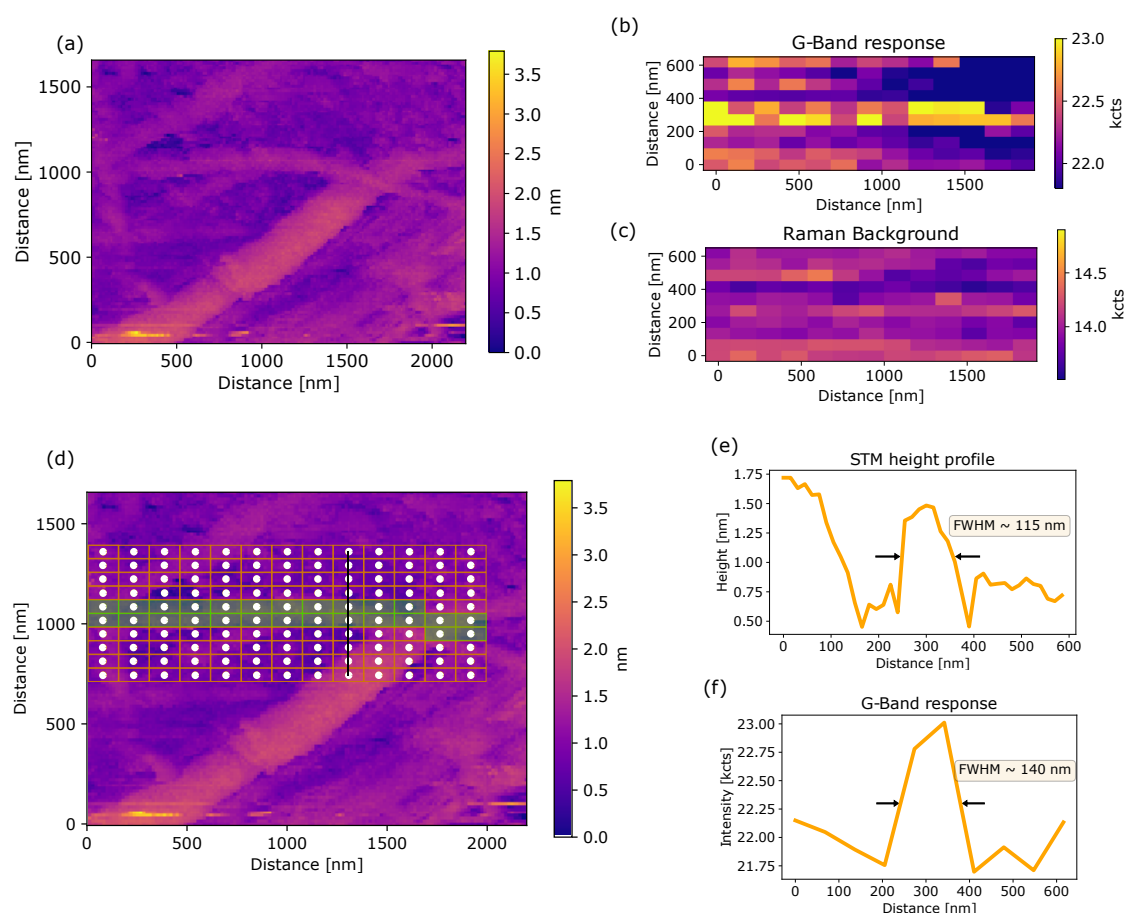
Figure 5.3.11.: Comparison of topography and near-field Raman measurements. (a) topography of the SWNT on top of the gold film, (b) and (c) illustrate the spatially resolved G^+-band response and the Raman background, respectively. Due to time reasons, the step size of the near field measurements is much larger than for the STM scan, nevertheless several features are visible with the most pronounced response at a horizontal cluster of SWNT in the middle. Topography and point-by-point Raman response are superposed in panel (d), with the high Raman response region being highlighted in green right on top of a mostly detached SWNT. The white points mark the tip positions of each taken Raman spectra. A black line in panel (d) represents the line from bottom to top which is plotted as the height and G^+-response profile in (e) and (f), respectively. The edge of the nanotube in the center has been localized with the Raman approach with a resolution of 70 nm.

Polarization dependence

A final characterization of our setup regarded the polarization dependence of the tip enhancement, hinted already by the experiments with XY and YX polarization configuration in Fig. 5.3.5 and 5.3.6. A schematic of the incoming light polarization can be found on top of Fig. 5.3.12. The nomenclature here uses the X and Y polarization as the projection of a and b in the sample plane. We find only the a-configuration to have a contribution along the tip axis, hence this incoming polarization should yield the highest enhancement of the Raman signal. To check this, the optical path was aligned to be as perpendicular to the tip axis as possible ($\Theta \approx 90°$), leading to the cleanest contributions along or perpendicular

to the tip with X- and Y-polarization on the sample, respectively. Raman measurements were then performed from 1341 to 1877 cm^{-1} and a point distance of ≈ 2.5 cm^{-1} in the four X- and Y- combinations for the retracted and tunneling mode. The resulting spectra were normalized so that the G^{+}-band peak in the retracted tip configuration is one and the background starts at zero. The results are presented in Fig. 5.3.12.
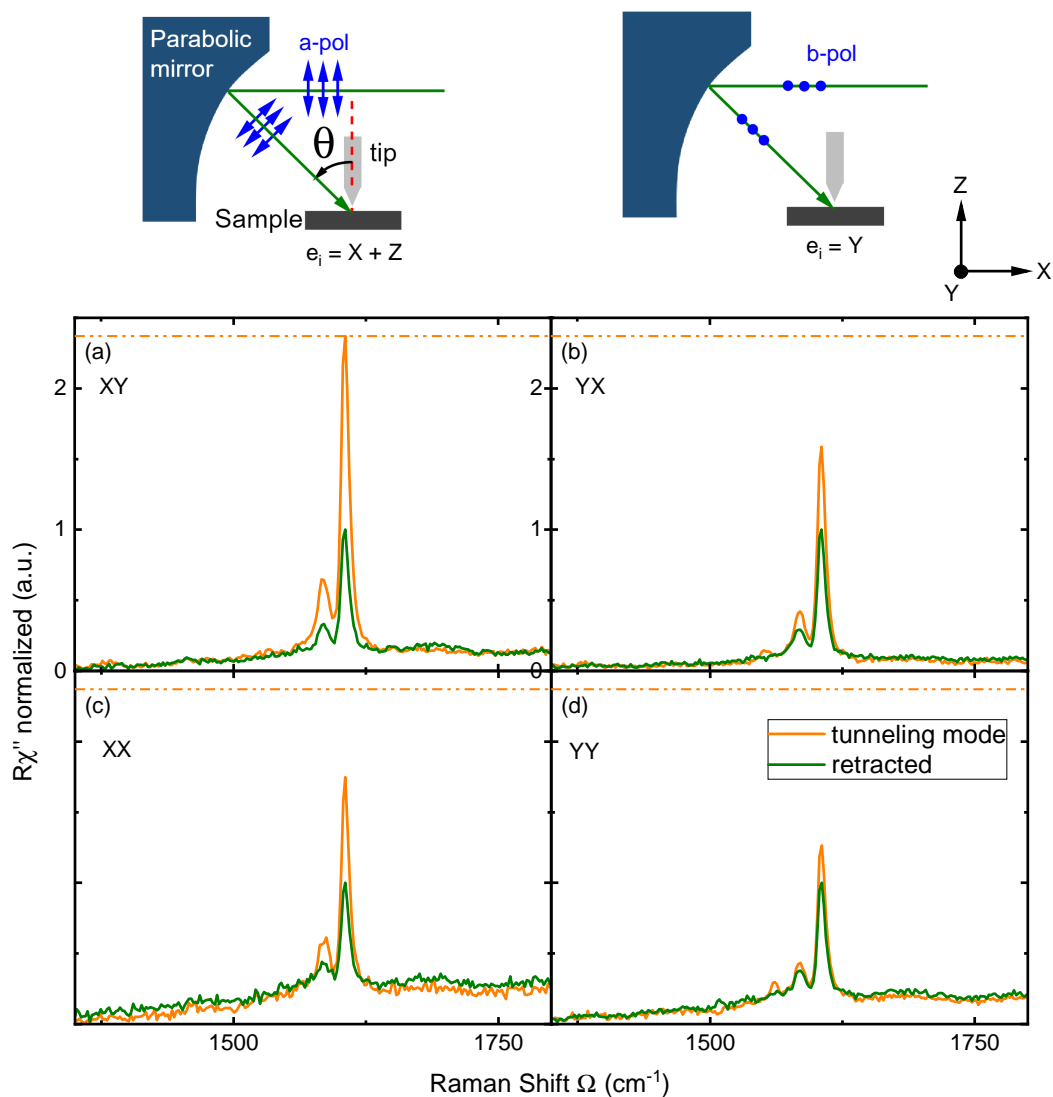

Figure 5.3.12.: Enhancement factors depending on the used polarizations. Raman excitations get especially enhanced when the incoming polarization has a contribution along the tip-axis. All spectra are normalized at their maximum intensity in retracted mode. Schematic adopted from [218].

The observed EF are listed in Tab. 5.3.2.

The highest enhancement factors according to eq. 5.42 are obtained for incoming X-polarization, which can be seen in the left panels of Fig. 5.3.12. Furthermore, the crossed polarization configurations lead to higher Raman intensities and also larger EF, compared to their corresponding parallel configuration. This behavior allows the distinction of the far and near field by only changing the polarization outside of the cryostat, at least in a

Table 5.3.2.: Enhancement factors EF for different sets of polarization. The incoming polarization is marked with an "i", the scattered one with an "s". The EF were calculated using Eq. 5.42 on the data of Fig. 5.3.12

EF	Y_s	X_s
X_i	2.37	1.74
Y_i	1.26	1.59

material in which XY and YX map the same Raman symmetries. In such a scenario, the tip is kept at its position, while the processes (enhanced and not) can be studied and compared very specifically. Thin film fourfold crystals like the iron-based superconductors would be a potential candidate, for example, a monolayer of FeSe may be interesting because of its enhanced superconducting transition temperature [219].

Another option of comparing the far- and near-field while not changing the tip or polarization utilizes the height-adjustable platform of the optical flat. This allows the precise variation of the polar angle Θ of the incoming light with respect to the tip axis. Consequently, one would observe an increase or decrease of the c-axis contribution in the bulk sample for x-polarization, as well as a corresponding variation of the field enhancement at the tip apex without changing tip position or polarization.

6. Summary

The thesis describes experimental Raman scattering work and the augmentation of equipment. In the first part, results of light scattering experiments on Fe_3Sn_2 and CsV_3Sb_5 are presented and analyzed. In both materials, the active ions occupy a kagome lattice. The related electronic band structure entails numerous unconventional properties such as Dirac and Weyl nodes, density waves, superconductivity and ferromagnetism. The question as to the expected dichotomy between bulk and surface comparable to that in topological insulators revived the idea of experimental methods enabling depth profiling. Tip enhanced Raman scattering (TERS) is one of the possibilities affording a window into this direction. Thus, the second part describes in some detail the augmentation of the existing TERS equipment which includes a new UHV chamber for preparation and a load lock. The chambers were designed, fabricated, attached, and successfully tested. Tip enhancement was demonstrated at $20\,K$ using single-wall carbon nanotubes (SWNTs).

In the high T_C kagome ferromagnet Fe_3Sn_2 the interaction of lattice dynamics with the electronic and magnetic properties were studied. The experimental results were compared with DFT calculations. The energies of all phonons were predicted with a precision of better than 5% except for one line. All phonons harden and sharpen upon cooling. The linewidths and positions can be described in terms of an anharmonic model and the lattice expansion enabling the mode-specific extraction of the phonon-phonon coupling parameter $\lambda_{\text{ph-ph,i}}$ and the Grüneisen parameter γ_i, respectively. All phonons follow the expected trend yielding small values of $\gamma_i \lesssim 0.5$. Only the lowest-energy A_{1g} mode exhibits an anomaly close to $100\,K$ where the spins reorient from perpendicular to parallel to the kagome plane. The coupling parameter $\lambda_{\text{ph-ph}}$ of this mode increases significantly below $100\,K$, and the energy exhibits an anomaly between 150 and $80\,K$. Using thermodynamic variables the macroscopic Grüneisen parameter γ_m is determined in addition to the mode-specific ones. The comparison of γ_m and γ_i suggests that the low-energy A_{1g} mode being characterized by Sn vibrations perpendicular to the kagome planes couples stronger to the spins than the other modes. It is argued that the specific eigenvector of this mode enhances the coupling and that the phonon may contribute to the spin reorientation.

As a second compound, CsV_3Sb_5 with the V atoms occupying sites of a kagome structure, was investigated for its potentially unconventional charge-ordering and superconducting properties. Here, the Raman study focused on the interplay of the lattice with the electronic system. To this end, spectra as a function of symmetry and temperature were measured and compared to DFT-calculations. At selected temperatures all four symmetries were individually extracted. No indications of anti-symmetric A_{2g} excitations could be detected arguing against a chiral charge density wave (CDW). At high energies a gap-like re-distribution of spectral weight is observed upon entering the CDW state below $95\,K$.

The extracted energies are similar in the two relevant symmetries and approximately four times larger than those observed by either ARPES or STM. The large energy gap favors a strong coupling picture. For substantiating this hypothesis the phonons were analyzed. Two phononic modes having A_{1g} and E_g symmetry are observable in the complete temperature range. The A_{1g} phonon exhibits a discontinuity of the energy and of the coupling strength at the transition temperature T_{CDW} including a precursor effect above T_{CDW}. In the CDW phase new lines pop up because of zone folding. Two of the additional lines are identified as amplitude modes of the CDW order parameter owing to their strong variation with temperature. Yet, they appear at finite energy close to T_{CDW}, while not following the mean-field theory predictions, confirming a first-order phase transition. The shape of the A_{1g} AM is asymmetric and is best described by a Fano function. The extracted asymmetry factor $1/|q|$ has a maximum at around 70 K well below T_{CDW} close to the appearance of a putative additional c-axis modulation in the charge order. The asymmetric line shape is interpreted in terms of strong coupling between the electron density oscillations of the AM and the electronic continuum. The large gap, the discontinuities of the A_{1g} phonon as well as the AMs and the Fano-line shape of the A_{1g} AM favor a strong-coupling rather than a weak coupling scenario.

Driven by the quest for visualizing bulk versus surface properties in correlated systems, the application of TERS acquired increasing interest also in condensed matter studies. Crucial bottlenecks are clean metallic tips, ideally made of silver, and the surfaces of the samples. Thus, the existing TERS setup was augmented to allow the in-situ transfer, preparation, and cleaning of tips and samples using novel procedures like field emission or heating. For preparation and cleaning an additional chamber was designed and attached to the existing setup. It has an ion gun and a heating platform and is UHV compatible. Tips and samples are picked up in the load-lock chamber by a transfer arm and transported to either the preparation or the TERS chamber. The optical observation of transfer, sample and tip alignment was re-designed and implemented. The off-axis parabolic mirror in the TERS chamber serves as high-speed collection and observation optics. In spite of the metallic coating of the paraboloid the Raman selection rules remain effective by and large. The system was benchmarked using SWNTs dispersed on a gold film. The scanning tunneling microscope (STM) resolves various bundles of SWNTs. Tip enhancement was demonstrated at 20 K on one of the bundles displaying signal contrasts of near- and far-field between 4 and 5 in spite of the high density of SWNTs in the far-field focus. Major advances result from the excellent vacuum conditions of approximately 5×10^{-11} mbar and the in-situ preparation of Ag tips which are virtually free of luminescence in the visible range of the spectrum. Although solids could not yet be studied for the lack of time it was possible to perform TERS measurements with enhancement factors in the range of $10^5 - 10^7$ at 20 K under UHV conditions in the augmented system.

A. Fe$_3$Sn$_2$

A.1. Quantitative analysis of the phonons in of Fe$_3$Sn$_2$

The Raman spectra taken for Fe$_3$Sn$_2$ in A_{1g} and E_g were fitted according to section 3.2.2 with a Voigt function for all temperatures. The background was observed to be virtually constant and was subtracted. Exemplary, the fits are presented for the two symmetries at 4.2 K, verifying the good agreement of fit and data.
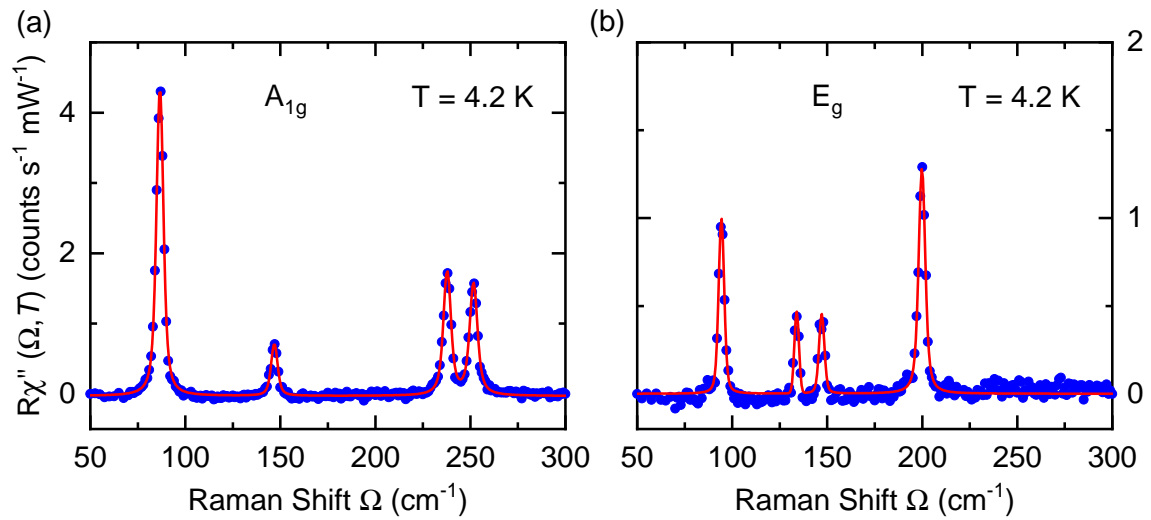

Figure A.1.1.: Fitting results at 4.2 **K using a Voigt function for the phonon lines in** A_{1g} **(a) and** E_g **(b).** A constant background was subtracted before the fitting procedure, to account for the electronic continuum.

B. CsV$_3$Sb$_5$

B.1. Resonance effects in CsV$_3$Sb$_5$ at 88 K

Three different laserlines were used in order of investigating potential resonance effects at low transferred energies. Fig. B.1.1 depicts the resulting spectra close below T_{CDW} in RR and RL polarization. While the general shape remains similar, especially the green laser at $\omega_i = 532$ nm displays stronger intensities for the different peaks, identified as either phonons or as an amplitude mode. The background signals remain rather similar, as we have seen already for high Raman shifts in Fig. 4.2.1. All the peaks observed at lowest temperatures can also be found for different laser lines close to T_{CDW}. This experimental finding is not in line with claims made by Wu et $al.$ connecting the later arising peaks to the emergence of a secondary charge ordered phase [79].
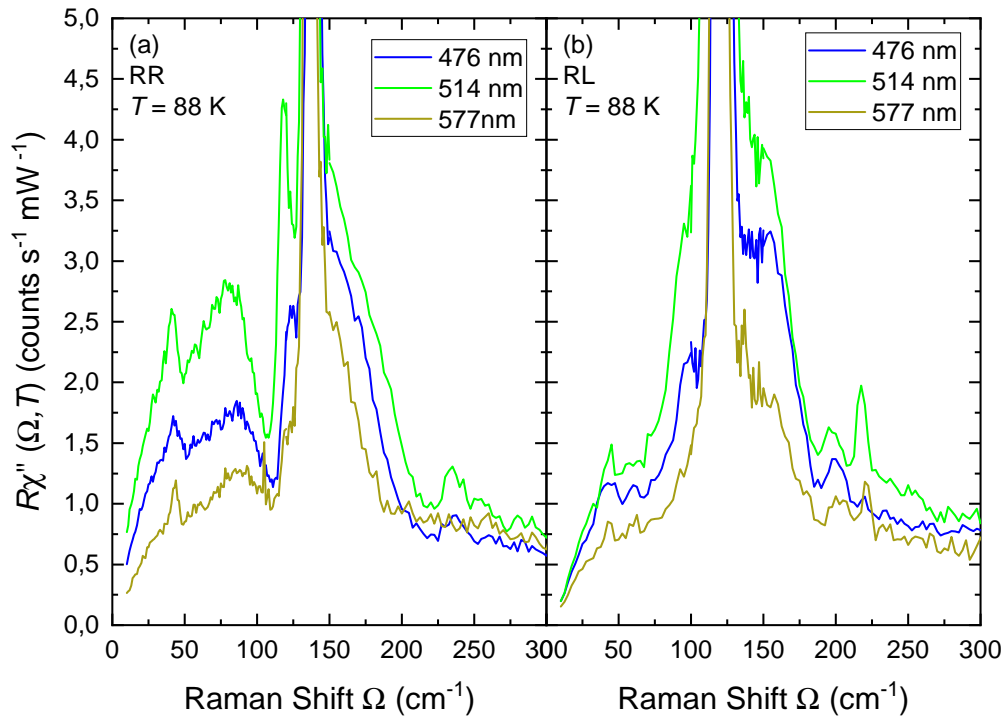

Figure B.1.1.: Raman spectra for different laserlines in CsV$_3$Sb$_5$ with circularly polarized light at 80 K plus laser heating. RR is illustrated in (a) and RL in (b), the ZF-phonons and AM vary a lot in intensity for the different excitation wavelengths.

C. TERS

C.1. Atomic force microscopy data

Atomic force microscopy (AFM) measurements at ambient conditions were used for clarification of the successful deposition of carbon SWNT on the substrate surface and sufficiently clear surfaces of solvent residues. Two exemplary images of a 100 nm thick evaporated gold film on silicon as substrate with a broad region of interest are presented in Fig. C.1.1. SWNT clusters are visible clearly with somewhat differing density.
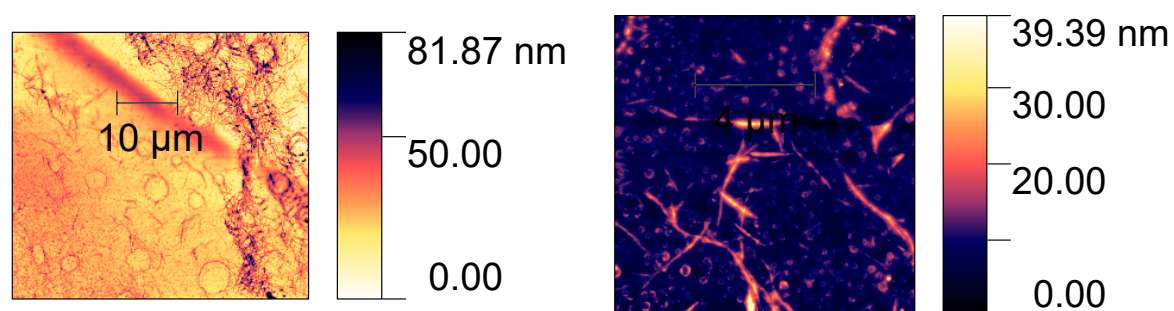

Figure C.1.1.: AFM pictures of SWNT on a Au-thin film.

Bibliography

[1] J. RICHTER, J. SCHULENBURG, AND A. HONECKER (2004) pp. 85–153.

[2] U. YU, *Ising antiferromagnet on the Archimedean lattices*, Physical Review E **91**, 062121 (2015).

[3] J. MARTINEZ, *Archimedean lattices*, Algebra Universalis **3**, 247 (1973).

[4] D. J. J. FARNELL, O. GÖTZE, J. RICHTER, R. F. BISHOP, AND P. H. Y. LI, *Quantum $s = \frac{1}{2}$ antiferromagnets on Archimedean lattices: The route from semiclassical magnetic order to nonmagnetic quantum states*, Physical Review B **89**, 184407 (2014).

[5] A. A. ABRIKOSOV, *Nobel Lecture: Type-II superconductors and the vortex lattice*, Reviews of Modern Physics **76**, 975 (2004).

[6] B. PARTOENS AND F. M. PEETERS, *From graphene to graphite: Electronic structure around the K point*, Physical Review B **74**, 075404 (2006).

[7] I. SYOZI, *Statistics of Kagome Lattice*, Progress of Theoretical Physics **6**, 306 (1951).

[8] C. PENG, Y. JIANG, D. SHENG, AND H. JIANG, *Doping Quantum Spin Liquids on the Kagome Lattice*, Advanced Quantum Technologies **4**, 2000126 (2021).

[9] T. NEUPERT, M. M. DENNER, J.-X. YIN, R. THOMALE, AND M. Z. HASAN, *Charge order and superconductivity in kagome materials*, Nature Physics **18**, 137 (2022).

[10] A. MIELKE, *Ferromagnetism in the Hubbard model and Hund's rule*, Physics Letters A **174**, 443 (1993).

[11] F. POLLMANN, P. FULDE, AND K. SHTENGEL, *Kinetic Ferromagnetism on a Kagome Lattice*, Physical Review Letters **100**, 136404 (2008).

[12] I. I. MAZIN, H. O. JESCHKE, F. LECHERMANN, H. LEE, M. FINK, R. THOMALE, AND R. VALENTÍ, *Theoretical prediction of a strongly correlated Dirac metal*, Nature Communications **5**, 4261 (2014).

[13] S.-Q. SHEN (2017) pp. 207–229.

[14] E. LIU, Y. SUN, N. KUMAR, L. MUECHLER, A. SUN, L. JIAO, S.-Y. YANG, D. LIU, A. LIANG, Q. XU, J. KRODER, V. SÜSS, H. BORRMANN, C. SHEKHAR, Z. WANG, C. XI, W. WANG, W. SCHNELLE, S. WIRTH, Y. CHEN, S. T. B. GOENNENWEIN, AND C. FELSER, *Giant anomalous Hall effect in a ferromagnetic kagome-lattice semimetal*, Nature Physics **14**, 1125 (2018).

[15] D. Chen, C. Le, C. Fu, H. Lin, W. Schnelle, Y. Sun, and C. Felser, *Large anomalous Hall effect in the kagome ferromagnet LiMn6Sn6*, Physical Review B **103**, 144410 (2021).

[16] G. Xu, B. Lian, and S.-C. Zhang, *Intrinsic Quantum Anomalous Hall Effect in the Kagome Lattice Cs2LiMn3F12*, Physical Review Letters **115**, 186802 (2015).

[17] B. R. Ortiz, L. C. Gomes, J. R. Morey, M. Winiarski, M. Bordelon, J. S. Mangum, I. W. H. Oswald, J. A. Rodriguez-Rivera, J. R. Neilson, S. D. Wilson, E. Ertekin, T. M. McQueen, and E. S. Toberer, *New kagome prototype materials: discovery of* KV_3Sb_5, RbV_3Sb_5 *, and* CsV_3Sb_5, Physical Review Materials **3**, 094407 (2019).

[18] X. Gui and R. J. Cava, *LaIr$_3$Ga$_2$: A Superconductor Based on a Kagome Lattice of Ir*, Chemistry of Materials **34**, 2824 (2022).

[19] Q. Wang, S. Sun, X. Zhang, F. Pang, and H. Lei, *Anomalous Hall effect in a ferromagnetic Fe$_3$Sn$_2$ single crystal with a geometrically frustrated Fe bilayer kagome lattice*, Physical Review B **94**, 075135 (2016).

[20] L. Ye, M. Kang, J. Liu, F. von Cube, C. R. Wicker, T. Suzuki, C. Jozwiak, A. Bostwick, E. Rotenberg, D. C. Bell, L. Fu, R. Comin, and J. G. Checkelsky, *Massive Dirac fermions in a ferromagnetic kagome metal*, Nature **555**, 638 (2018).

[21] H. Li, B. Ding, J. Chen, Z. Li, Z. Hou, E. Liu, H. Zhang, X. Xi, G. Wu, and W. Wang, *Large topological Hall effect in a geometrically frustrated kagome magnet Fe$_3$Sn$_2$*, Applied Physics Letters **114**, 192408 (2019).

[22] A. Mielke, *Ferromagnetic ground states for the Hubbard model on line graphs*, Journal of Physics A: Mathematical and General **24**, L73 (1991).

[23] Z. Lin, J.-H. Choi, Q. Zhang, W. Qin, S. Yi, P. Wang, L. Li, Y. Wang, H. Zhang, Z. Sun, L. Wei, S. Zhang, T. Guo, Q. Lu, J.-H. Cho, C. Zeng, and Z. Zhang, *Flatbands and Emergent Ferromagnetic Ordering in Fe$_3$Sn$_2$ Kagome Lattices*, Physical Review Letters **121**, 096401 (2018).

[24] N. Kumar, Y. Soh, Y. Wang, and Y. Xiong, *Magnetotransport as a diagnostic of spin reorientation: Kagome ferromagnet as a case study*, Physical Review B **100**, 214420 (2019).

[25] A. Biswas, O. Iakutkina, Q. Wang, H. C. Lei, M. Dressel, and E. Uykur, *Spin-Reorientation-Induced Band Gap in Fe$_3$Sn$_2$: Optical Signatures of Weyl Nodes*, Physical Review Letters **125**, 076403 (2020).

[26] Y. Hu, X. Wu, B. R. Ortiz, X. Han, N. C. Plumb, S. D. Wilson, A. P. Schnyder, and M. Shi, *Coexistence of Tri-Hexagonal and Star-of-David Pattern in the Charge Density Wave of the Kagome Superconductor AV$_3$Sb$_5$*, (2022), arXiv:2201.06477 .

[27] J. Zhao, W. Wu, Y. Wang, and S. A. Yang, *Electronic correlations in the normal state of the kagome superconductor* KV_3Sb_5, Physical Review B **103**, L241117 (2021).

[28] B. R. ORTIZ, S. M. TEICHER, Y. HU, J. L. ZUO, P. M. SARTE, E. C. SCHUELLER, A. M. ABEYKOON, M. J. KROGSTAD, S. ROSENKRANZ, R. OSBORN, R. SESHADRI, L. BALENTS, J. HE, AND S. D. WILSON, CsV_3Sb_5: *A Z2 Topological Kagome Metal with a Superconducting Ground State*, Physical Review Letters **125**, 1 (2020), arXiv:arXiv:2011.06745v1 .

[29] B. R. ORTIZ, S. M. TEICHER, L. KAUTZSCH, P. M. SARTE, N. RATCLIFF, J. HARTER, J. P. RUFF, R. SESHADRI, AND S. D. WILSON, *Fermi Surface Mapping and the Nature of Charge-Density-Wave Order in the Kagome Superconductor* CsV_3Sb_5, Physical Review X **11**, 41030 (2021), arXiv:2104.07230 .

[30] H. LI, H. ZHAO, B. ORTIZ, Y. OEY, Z. WANG, S. D. WILSON, AND I. ZELJKOVIC, *Emergence of unidirectional coherent quasiparticles from high-temperature rotational symmetry broken phase of AV3Sb5 kagome superconductors*, (2022), arXiv:2203.15057 .

[31] M. H. CHRISTENSEN, T. BIROL, B. M. ANDERSEN, AND R. M. FERNANDES, *Theory of the charge density wave in AV_3Sb_5 kagome metals*, Physical Review B **104**, 214513 (2021).

[32] H. ZHAO, H. LI, B. R. ORTIZ, S. M. L. TEICHER, T. PARK, M. YE, Z. WANG, L. BALENTS, S. D. WILSON, AND I. ZELJKOVIC, *Cascade of correlated electron states in the kagome superconductor* CsV_3Sb_5, Nature **599**, 216 (2021).

[33] R. LOU, A. FEDOROV, Q. YIN, A. KUIBAROV, Z. TU, C. GONG, E. F. SCHWIER, B. BÜCHNER, H. LEI, AND S. BORISENKO, *Charge-Density-Wave-Induced Peak-Dip-Hump Structure and the Multiband Superconductivity in a Kagome Superconductor CsV_3Sb_5*, Physical Review Letters **128**, 036402 (2022).

[34] Z. WANG, S. MA, Y. ZHANG, H. YANG, Z. ZHAO, Y. OU, Y. ZHU, S. NI, Z. LU, H. CHEN, K. JIANG, L. YU, Y. ZHANG, X. DONG, J. HU, H.-J. GAO, AND Z. ZHAO, *Distinctive momentum dependent charge-density-wave gap observed in CsV_3Sb_5 superconductor with topological Kagome lattice*, (2021), arXiv:2104.05556, arXiv:2104.05556 .

[35] H. LI, G. FABBRIS, A. H. SAID, J. P. SUN, Y.-X. JIANG, J.-X. YIN, Y.-Y. PAI, S. YOON, A. R. LUPINI, C. S. NELSON, Q. W. YIN, C. S. GONG, Z. J. TU, H. C. LEI, J.-G. CHENG, M. Z. HASAN, Z. WANG, B. YAN, R. THOMALE, H. N. LEE, AND H. MIAO, *Discovery of conjoined charge density waves in the kagome superconductor CsV_3Sb_5*, Nature Communications **13**, 6348 (2022).

[36] H. CHEN, H. YANG, B. HU, Z. ZHAO, J. YUAN, Y. XING, G. QIAN, Z. HUANG, G. LI, Y. YE, S. MA, S. NI, H. ZHANG, Q. YIN, C. GONG, Z. TU, H. LEI, H. TAN, S. ZHOU, C. SHEN, X. DONG, B. YAN, Z. WANG, AND H.-J. GAO, *Roton pair density wave in a strong-coupling kagome superconductor*, Nature **599**, 222 (2021).

[37] F. KRETZSCHMAR, T. BÖHM, U. KARAHASANOVIĆ, B. MUSCHLER, A. BAUM, D. JOST, J. SCHMALIAN, S. CAPRARA, M. GRILLI, C. DI CASTRO, J. G. ANALYTIS, J. H. CHU, I. R. FISHER, AND R. HACKL, *Critical spin fluctuations and the origin of nematic order in $Ba(Fe_{1-x}Co_x)_2As_2$*, Nature Physics **12**, 560 (2016).

[38] T. P. DEVEREAUX, D. EINZEL, B. STADLOBER, R. HACKL, D. H. LEACH, AND J. J. NEUMEIER, *Electronic Raman scattering in high- T_c superconductors: A probe of $d_{x^2-y^2}$ pairing*, Physical Review Letters **72**, 396 (1994).

[39] S. UCHIDA AND S. SUGAI, *Infrared and Raman studies on commensurate CDW states in transition metal dichalcogenides*, Physica B+C **105**, 393 (1981).

[40] C. CHEN, N. HAYAZAWA, AND S. KAWATA, *A 1.7 nm resolution chemical analysis of carbon nanotubes by tip-enhanced Raman imaging in the ambient*, Nature Communications **5**, 3312 (2014).

[41] M. LIAO, S. JIANG, C. HU, R. ZHANG, Y. KUANG, J. ZHU, Y. ZHANG, AND Z. DONG, *Tip-Enhanced Raman Spectroscopic Imaging of Individual Carbon Nanotubes with Subnanometer Resolution*, Nano Letters **16**, 4040 (2016).

[42] N. CHIANG, X. CHEN, G. GOUBERT, D. V. CHULHAI, X. CHEN, E. A. POZZI, N. JIANG, M. C. HERSAM, T. SEIDEMAN, L. JENSEN, AND R. P. VAN DUYNE, *Conformational Contrast of Surface-Mediated Molecular Switches Yields Ångstrom-Scale Spatial Resolution in Ultrahigh Vacuum Tip-Enhanced Raman Spectroscopy*, Nano Letters **16**, 7774 (2016).

[43] N. JIANG, N. CHIANG, L. R. MADISON, E. A. POZZI, M. R. WASIELEWSKI, T. SEIDEMAN, M. A. RATNER, M. C. HERSAM, G. C. SCHATZ, AND R. P. VAN DUYNE, *Nanoscale Chemical Imaging of a Dynamic Molecular Phase Boundary with Ultrahigh Vacuum Tip-Enhanced Raman Spectroscopy*, Nano Letters **16**, 3898 (2016).

[44] E. A. POZZI, G. GOUBERT, N. CHIANG, N. JIANG, C. T. CHAPMAN, M. O. MCANALLY, A.-I. HENRY, T. SEIDEMAN, G. C. SCHATZ, M. C. HERSAM, AND R. P. V. DUYNE, *Ultrahigh-Vacuum Tip-Enhanced Raman Spectroscopy*, Chemical Reviews **117**, 4961 (2017).

[45] J. F. SCHULTZ, S. MAHAPATRA, L. LI, AND N. JIANG, *The Expanding Frontiers of Tip-Enhanced Raman Spectroscopy*, Applied Spectroscopy **74**, 1313 (2020).

[46] D. V. VORONINE, G. LU, D. ZHU, AND A. KRAYEV, *Tip-Enhanced Raman Scattering of MoS_2*, IEEE Journal of Selected Topics in Quantum Electronics **23**, 138 (2017).

[47] J. M. KLINGSPORN, N. JIANG, E. A. POZZI, M. D. SONNTAG, D. CHULHAI, T. SEIDEMAN, L. JENSEN, M. C. HERSAM, AND R. P. V. DUYNE, *Intramolecular Insight into Adsorbate–Substrate Interactions via Low-Temperature, Ultrahigh-Vacuum Tip-Enhanced Raman Spectroscopy*, Journal of the American Chemical Society **136**, 3881 (2014).

[48] S. SHENG, W. LI, J. GOU, P. CHENG, L. CHEN, AND K. WU, *Low-temperature, ultrahigh-vacuum tip-enhanced Raman spectroscopy combined with molecular beam epitaxy for in situ two-dimensional materials' studies*, Review of Scientific Instruments **89**, 053107 (2018).

[49] D. ZHANG, Z. HOU, AND W. MI, *Progress in magnetic alloys with kagome structure: materials, fabrications and physical properties*, Journal of Materials Chemistry C **10**, 7748 (2022).

[50] K. MOMMA AND F. IZUMI, *VESTA 3 for three-dimensional visualization of crystal, volumetric and morphology data*, Journal of Applied Crystallography **44**, 1272 (2011).

[51] K. S. KIM, A. L. WALTER, L. MORESCHINI, T. SEYLLER, K. HORN, E. ROTENBERG, AND A. BOSTWICK, *Coexisting massive and massless Dirac fermions in symmetry-broken bilayer graphene*, Nature Materials **12**, 887 (2013).

[52] H. TAN, Y. LIU, Z. WANG, AND B. YAN, *Charge Density Waves and Electronic Properties of Superconducting Kagome Metals*, Physical Review Letters **127**, 46401 (2021), arXiv:2103.06325 .

[53] Z. LIANG, X. HOU, F. ZHANG, W. MA, P. WU, Z. ZHANG, F. YU, J.-J. YING, K. JIANG, L. SHAN, Z. WANG, AND X.-H. CHEN, *Three-Dimensional Charge Density Wave and Surface-Dependent Vortex-Core States in a Kagome Superconductor* CsV_3Sb_5, Physical Review X **11**, 031026 (2021).

[54] F. H. YU, T. WU, Z. Y. WANG, B. LEI, W. Z. ZHUO, J. J. YING, AND X. H. CHEN, *Concurrence of anomalous Hall effect and charge density wave in a superconducting topological kagome metal*, Physical Review B **104**, L041103 (2021).

[55] Y. HU, S. M. TEICHER, B. R. ORTIZ, Y. LUO, S. PENG, L. HUAI, J. MA, N. C. PLUMB, S. D. WILSON, J. HE, AND M. SHI, *Topological surface states and flat bands in the kagome superconductor* CsV_3Sb_5, Science Bulletin **67**, 495 (2022).

[56] H. GIEFERS AND M. NICOL, *High pressure X-ray diffraction study of all Fe–Sn intermetallic compounds and one Fe–Sn solid solution*, Journal of Alloys and Compounds **422**, 132 (2006).

[57] Z.-Z. LIN AND X. CHEN, *Tunable Massive Dirac Fermions in Ferromagnetic* Fe_3Sn_2 *Kagome Lattice*, physica status solidi (RRL) – Rapid Research Letters **14**, 1900705 (2020).

[58] Z. HOU, W. REN, B. DING, G. XU, Y. WANG, B. YANG, Q. ZHANG, Y. ZHANG, E. LIU, F. XU, W. WANG, G. WU, X. ZHANG, B. SHEN, AND Z. ZHANG, *Observation of Various and Spontaneous Magnetic Skyrmionic Bubbles at Room Temperature in a Frustrated Kagome Magnet with Uniaxial Magnetic Anisotropy*, Advanced Materials **29**, 1701144 (2017).

[59] T. KIDA, L. A. FENNER, A. A. DEE, I. TERASAKI, M. HAGIWARA, AND A. S. WILLS, *The giant anomalous Hall effect in the ferromagnet* Fe_3Sn_2 *—a frustrated kagome metal*, Journal of Physics: Condensed Matter **23**, 112205 (2011).

[60] J.-X. YIN, S. S. ZHANG, H. LI, K. JIANG, G. CHANG, B. ZHANG, B. LIAN, C. XIANG, I. BELOPOLSKI, H. ZHENG, T. A. COCHRAN, S.-Y. XU, G. BIAN, K. LIU, T.-R.

CHANG, H. LIN, Z.-Y. LU, Z. WANG, S. JIA, W. WANG, AND M. Z. HASAN, *Giant and anisotropic many-body spin–orbit tunability in a strongly correlated kagome magnet*, Nature **562**, 91 (2018).

[61] G. L. CAER, B. MALAMAN, AND B. ROQUES, *Mossbauer effect study of Fe_3Sn_2*, Journal of Physics F: Metal Physics **8**, 323 (1978).

[62] B. MALAMAN, D. FRUCHART, AND G. L. CAER, *Magnetic properties of Fe_3Sn_2 . II. Neutron diffraction study (and Mossbauer effect)*, Journal of Physics F: Metal Physics **8**, 2389 (1978).

[63] L. A. FENNER, A. A. DEE, AND A. S. WILLS, *Non-collinearity and spin frustration in the itinerant kagome ferromagnet Fe_3Sn_2*, Journal of Physics: Condensed Matter **21**, 452202 (2009).

[64] K. Y. CHEN, N. N. WANG, Q. W. YIN, Y. H. GU, K. JIANG, Z. J. TU, C. S. GONG, Y. UWATOKO, J. P. SUN, H. C. LEI, J. P. HU, AND J.-G. CHENG, *Double Superconducting Dome and Triple Enhancement of T_c in the Kagome Superconductor CsV_3Sb_5 under High Pressure*, Physical Review Letters **126**, 247001 (2021).

[65] F. H. YU, D. H. MA, W. Z. ZHUO, S. Q. LIU, X. K. WEN, B. LEI, J. J. YING, AND X. H. CHEN, *Unusual competition of superconductivity and charge-density-wave state in a compressed topological kagome metal*, Nature Communications **12**, 3645 (2021).

[66] G. GRÜNER, *Density Waves in Solids* (CRC Press, 2018).

[67] D. HANS-MARTIN EMIL EITER AND R. GROSS, *Carrier and Lattice Dynamics in Systems with Charge and Spin Order*, (2014).

[68] R. E. PEIERLS, RUDOLF AND PEIERLS, *Quantum theory of solids* (Oxford University Press, 1955).

[69] Y. X. JIANG, J. X. YIN, M. M. DENNER, N. SHUMIYA, B. R. ORTIZ, G. XU, Z. GUGUCHIA, J. HE, M. S. HOSSAIN, X. LIU, J. RUFF, L. KAUTZSCH, S. S. ZHANG, G. CHANG, I. BELOPOLSKI, Q. ZHANG, T. A. COCHRAN, D. MULTER, M. LITSKEVICH, Z. J. CHENG, X. P. YANG, Z. WANG, R. THOMALE, T. NEUPERT, S. D. WILSON, AND M. Z. HASAN, *Unconventional chiral charge order in kagome superconductor KV_3Sb_5*, Nature Materials **20**, 1353 (2021).

[70] H. LI, T. T. ZHANG, T. YILMAZ, Y. Y. PAI, C. E. MARVINNEY, A. SAID, Q. W. YIN, C. S. GONG, Z. J. TU, E. VESCOVO, C. S. NELSON, R. G. MOORE, S. MURAKAMI, H. C. LEI, H. N. LEE, B. J. LAWRIE, AND H. MIAO, *Observation of Unconventional Charge Density Wave without Acoustic Phonon Anomaly in Kagome Superconductors AV_3Sb_5 (A=Rb, Cs)*, Physical Review X **11**, 1 (2021), arXiv:2103.09769 .

[71] M. KANG, S. FANG, J.-K. KIM, B. R. ORTIZ, S. H. RYU, J. KIM, J. YOO, G. SANGIOVANNI, D. DI SANTE, B.-G. PARK, C. JOZWIAK, A. BOSTWICK, E. ROTENBERG, E. KAXIRAS, S. D. WILSON, J.-H. PARK, AND R. COMIN, *Twofold van Hove singularity*

and origin of charge order in topological kagome superconductor CsV_3Sb_5, Nature Physics **18**, 301 (2022).

[72] K. NAKAYAMA, Y. LI, T. KATO, M. LIU, Z. WANG, T. TAKAHASHI, Y. YAO, AND T. SATO, *Multiple energy scales and anisotropic energy gap in the charge-density-wave phase of the kagome superconductor CsV_3Sb_5*, Physical Review B **104**, L161112 (2021).

[73] E. UYKUR, B. R. ORTIZ, S. D. WILSON, M. DRESSEL, AND A. A. TSIRLIN, *Optical detection of the density-wave instability in the kagome metal KV_3Sb_5*, npj Quantum Materials **7**, 16 (2022).

[74] C. MU, Q. YIN, Z. TU, C. GONG, H. LEI, Z. LI, AND J. LUO, *S-Wave Superconductivity in Kagome Metal CsV_3Sb_5 Revealed by 121/123 Sb NQR and 51 V NMR Measurements*, Chinese Physics Letters **38**, 077402 (2021).

[75] Q. XIAO, Y. LIN, Q. LI, W. XIA, X. ZHENG, S. ZHANG, Y. GUO, J. FENG, AND Y. PENG, *Coexistence of Multiple Stacking Charge Density Waves in Kagome Superconductor CsV_3Sb_5*, (2022), arXiv:2201.05211 .

[76] Q. STAHL, D. CHEN, T. RITSCHEL, C. SHEKHAR, E. SADROLLAHI, M. C. RAHN, O. IVASHKO, M. V. ZIMMERMANN, C. FELSER, AND J. GECK, *Temperature-driven reorganization of electronic order in CsV_3Sb_5*, Physical Review B **105**, 195136 (2022).

[77] L. YU, C. WANG, Y. ZHANG, M. SANDER, S. NI, Z. LU, S. MA, Z. WANG, Z. ZHAO, H. CHEN, K. JIANG, Y. ZHANG, H. YANG, F. ZHOU, X. DONG, S. L. JOHNSON, M. J. GRAF, J. HU, H.-J. GAO, AND Z. ZHAO, *Evidence of a hidden flux phase in the topological kagome metal CsV_3Sb_5*, (2021), arXiv:2107.10714 .

[78] Y. XIANG, Q. LI, Y. LI, W. XIE, H. YANG, Z. WANG, Y. YAO, AND H.-H. WEN, *Twofold symmetry of c-axis resistivity in topological kagome superconductor* CsV_3Sb_5 *with in-plane rotating magnetic field*, Nature Communications **12**, 6727 (2021).

[79] S. WU, B. R. ORTIZ, H. TAN, S. D. WILSON, B. YAN, T. BIROL, AND G. BLUMBERG, *Charge density wave order in kagome metal AV_3Sb_5 (A= Cs, Rb, K)*, (2022), 10.1103/PhysRevB.105.155106, arXiv:2201.05188 .

[80] S. CHO, H. MA, W. XIA, Y. YANG, Z. LIU, Z. HUANG, Z. JIANG, X. LU, J. LIU, Z. LIU, J. LI, J. WANG, Y. LIU, J. JIA, Y. GUO, J. LIU, AND D. SHEN, *Emergence of New van Hove Singularities in the Charge Density Wave State of a Topological Kagome Metal* $\mathbf{RbV_3Sb_5}$, Physical Review Letters **127**, 236401 (2021).

[81] X. ZHOU, Y. LI, X. FAN, J. HAO, Y. DAI, Z. WANG, Y. YAO, AND H.-H. WEN, *Origin of charge density wave in the kagome metal* $\mathbf{CsV_3Sb_5}$ *as revealed by optical spectroscopy*, Physical Review B **104**, L041101 (2021).

[82] E. UYKUR, B. R. ORTIZ, O. IAKUTKINA, M. WENZEL, S. D. WILSON, M. DRESSEL, AND A. A. TSIRLIN, *Low-energy optical properties of the nonmagnetic kagome metal* $\mathbf{CsV_3Sb_5}$, Physical Review B **104**, 045130 (2021).

[83] C. MIELKE, D. DAS, J.-X. YIN, H. LIU, R. GUPTA, Y.-X. JIANG, M. MEDARDE, X. WU, H. C. LEI, J. CHANG, P. DAI, Q. SI, H. MIAO, R. THOMALE, T. NEUPERT, Y. SHI, R. KHASANOV, M. Z. HASAN, H. LUETKENS, AND Z. GUGUCHIA, *Time-reversal symmetry-breaking charge order in a kagome superconductor*, Nature **602**, 245 (2022).

[84] F. DU, S. LUO, B. R. ORTIZ, Y. CHEN, W. DUAN, D. ZHANG, X. LU, S. D. WILSON, Y. SONG, AND H. YUAN, *Pressure-induced double superconducting domes and charge instability in the kagome metal* KV_3Sb_5, Physical Review B **103**, L220504 (2021).

[85] A. TSIRLIN, P. FERTEY, B. R. ORTIZ, B. KLIS, V. MERKL, M. DRESSEL, S. WILSON, AND E. UYKUR, *Role of Sb in the superconducting kagome metal* CsV_3Sb_5 *revealed by its anisotropic compression*, SciPost Physics **12**, 049 (2022).

[86] D. JOST, L. PEIS, G. HE, A. BAUM, S. GEPRÄGS, J. C. PALMSTROM, M. S. IKEDA, I. R. FISHER, T. WOLF, S. LEDERER, S. A. KIVELSON, AND R. HACKL, *Quantum critical fluctuations in an Fe-based superconductor*, Communications Physics **5**, 201 (2022).

[87] H.-S. XU, Y.-J. YAN, R. YIN, W. XIA, S. FANG, Z. CHEN, Y. LI, W. YANG, Y. GUO, AND D.-L. FENG, *Multiband Superconductivity with Sign-Preserving Order Parameter in Kagome Superconductor* CsV_3Sb_5, Physical Review Letters **127**, 187004 (2021).

[88] C. C. ZHAO, L. S. WANG, W. XIA, Q. W. YIN, J. M. NI, Y. Y. HUANG, C. P. TU, Z. C. TAO, Z. J. TU, C. S. GONG, H. C. LEI, Y. F. GUO, X. F. YANG, AND S. Y. LI, *Nodal superconductivity and superconducting domes in the topological Kagome metal CsV3Sb5*, (2021), arXiv:2102.08356, arXiv:2102.08356 .

[89] T. P. DEVEREAUX AND R. HACKL, *Inelastic light scattering from correlated electrons*, Reviews of Modern Physics **79**, 175 (2007).

[90] A. BAUM, A. MILOSAVLJEVIĆ, N. LAZAREVIĆ, M. M. RADONJIĆ, B. NIKOLIĆ, M. MITSCHEK, Z. I. MARANLOO, M. ŠĆEPANOVIĆ, M. GRUJIĆ-BROJČIN, N. STOJILOVIĆ, M. OPEL, A. WANG, C. PETROVIC, Z. V. POPOVIĆ, AND R. HACKL, *Phonon anomalies in FeS*, Physical Review B **97**, 054306 (2018).

[91] A. A. ABRIKOSOV AND L. A. FAL'KOVSKI, *Raman scattering of light in superconductors* (1961).

[92] S. DJURDJIĆ MIJIN, A. BAUM, J. BEKAERT, A. ŠOLAJIĆ, J. PEŠIĆ, Y. LIU, G. HE, M. V. MILOŠEVIĆ, C. PETROVIC, Z. V. POPOVIĆ, R. HACKL, AND N. LAZAREVIĆ, *Probing charge density wave phases and the Mott transition in T-TaS$_2$ by inelastic light scattering*, Physical Review B **103**, 245133 (2021).

[93] P. B. ALLEN, *Fermi-surface harmonics: A general method for nonspherical problems. Application to Boltzmann and Eliashberg equations*, Physical Review B **13**, 1416 (1976).

[94] S. A. WEIDINGER AND W. ZWERGER, *Higgs mode and magnon interactions in 2D quantum antiferromagnets from Raman scattering*, The European Physical Journal B **88**, 237 (2015).

[95] S. CAPRARA, C. DI CASTRO, M. GRILLI, AND D. SUPPA, *Charge-Fluctuation Contribution to the Raman Response in Superconducting Cuprates*, Physical Review Letters **95**, 117004 (2005).

[96] T. BÖHM, F. KRETZSCHMAR, A. BAUM, M. REHM, D. JOST, R. HOSSEINIAN AHANGHARNEJHAD, R. THOMALE, C. PLATT, T. A. MAIER, W. HANKE, B. MORITZ, T. P. DEVEREAUX, D. J. SCALAPINO, S. MAITI, P. J. HIRSCHFELD, P. ADELMANN, T. WOLF, H.-H. WEN, AND R. HACKL, *Microscopic origin of Cooper pairing in the iron-based superconductor $Ba_{0.6}K_{0.4}Fe_2As_2$*, npj Quantum Materials **3**, 48 (2018).

[97] M.-A. MÉASSON, Y. GALLAIS, M. CAZAYOUS, B. CLAIR, P. RODIÈRE, L. CARIO, AND A. SACUTO, *Amplitude Higgs mode in the $2H - \mathbf{NbSe_2}$ superconductor*, Physical Review B **89**, 060503 (2014).

[98] B. LORET, N. AUVRAY, Y. GALLAIS, M. CAZAYOUS, A. FORGET, D. COLSON, M.-H. JULIEN, I. PAUL, M. CIVELLI, AND A. SACUTO, *Intimate link between charge density wave, pseudogap and superconducting energy scales in cuprates*, Nature Physics **15**, 771 (2019).

[99] N. CHELWANI, A. BAUM, T. BÖHM, M. OPEL, F. VENTURINI, L. TASSINI, A. ERB, H. BERGER, L. FORRÓ, AND R. HACKL, *Magnetic excitations and amplitude fluctuations in insulating cuprates*, Physical Review B **97**, 024407 (2018).

[100] A. BAUM, H. N. RUIZ, N. LAZAREVIĆ, Y. WANG, T. BÖHM, R. HOSSEINIAN AHANGHARNEJHAD, P. ADELMANN, T. WOLF, Z. V. POPOVIĆ, B. MORITZ, T. P. DEVEREAUX, AND R. HACKL, *Frustrated spin order and stripe fluctuations in FeSe*, Communications Physics **2**, 14 (2019).

[101] Y. GALLAIS, R. M. FERNANDES, I. PAUL, L. CHAUVIÈRE, Y.-X. YANG, M.-A. MÉASSON, M. CAZAYOUS, A. SACUTO, D. COLSON, AND A. FORGET, *Observation of Incipient Charge Nematicity in $Ba(Fe_{1-x}Co_x)_2As_2$*, Physical Review Letters **111**, 267001 (2013).

[102] H. KONTANI, T. SAITO, AND S. ONARI, *Origin of orthorhombic transition, magnetic transition, and shear-modulus softening in iron pnictide superconductors: Analysis based on the orbital fluctuations theory*, Physical Review B **84**, 024528 (2011).

[103] D. JOST, *Cooper pairing and fluctuations in Fe-based superconductors*, Ph.D. thesis (2019).

[104] T. BÖHM, A. F. KEMPER, B. MORITZ, F. KRETZSCHMAR, B. MUSCHLER, H.-M. EITER, R. HACKL, T. P. DEVEREAUX, D. J. SCALAPINO, AND H.-H. WEN, *Balancing Act: Evidence for a Strong Subdominant d-Wave Pairing Channel in $Ba_{0.6}K_{0.4}Fe_2As_2$*, Physical Review X **4**, 041046 (2014).

[105] F. VENTURINI, *Raman Scattering Study of Electronic Correlations in Cuprates: Observation of an Unconventional Metal-Insulator Transition*, Ph.D. thesis, Technische Universität München (2003).

[106] N. Fluctuations and F. Kretzschmar, *Nematic Fluctuations, Fermiology and the Pairing Potential in Iron-Based Superconductors*, Ph.D. thesis, Technical University Munich (2015).

[107] U. Fano, *Effects of Configuration Interaction on Intensities and Phase Shifts*, Physical Review **124**, 1866 (1961).

[108] S. Schippers, *Analytical expression for the convolution of a Fano line profile with a gaussian*, Journal of Quantitative Spectroscopy and Radiative Transfer **219**, 33 (2018).

[109] M. Sato and Y. Ando, *Topological superconductors: a review*, Reports on Progress in Physics **80**, 076501 (2017).

[110] N. Lazarevic, A. Baum, A. Milosavljevic, L. Peis, R. Stumberger, J. Bekaert, A. Solajic, J. Pesic, A. Wang, M. Scepanovic, M. V. Milosevic, C. Petrovic, Z. V. Popovic, and R. Hackl, *Evolution of lattice, spin, and charge properties across the phase diagram of $FeSe_{1-x}S_x$*, (2022), arXiv:2202.02227 .

[111] G. He, L. Peis, R. Stumberger, L. Prodan, V. Tsurkan, N. Unglert, L. Chioncel, I. Kézsmárki, and R. Hackl, *Phonon Anomalies Associated with Spin Reorientation in the Kagome Ferromagnet Fe_3Sn_2*, Physica Status Solidi (B) Basic Research (2021), 10.1002/pssb.202100169, arXiv:2107.14623 .

[112] C. Postmus, J. R. Ferraro, and S. S. Mitra, *Pressure Dependence of Infrared Eigenfrequencies of KCl and KBr*, Physical Review **174**, 983 (1968).

[113] P. G. Klemens, *Anharmonic Decay of Optical Phonons*, Physical Review **148**, 845 (1966).

[114] M. Balkanski, R. F. Wallis, and E. Haro, *Anharmonic effects in light scattering due to optical phonons in silicon*, Physical Review B **28**, 1928 (1983).

[115] D. V. Khveshchenko and P. B. Wiegmann, *Raman scattering and anomalous current algebra in Mott insulators*, Physical Review Letters **73**, 500 (1994).

[116] G. Liu, X. Ma, K. He, Q. Li, H. Tan, Y. Liu, J. Xu, W. Tang, K. Watanabe, T. Taniguchi, L. Gao, Y. Dai, H.-H. Wen, B. Yan, and X. Xi, *Observation of anomalous amplitude modes in the kagome metal CsV_3Sb_5*, (2022), 10.1038/s41467-022-31162-1, arXiv:2201.05330 .

[117] D. Wulferding, S. Lee, Y. Choi, Q. Yin, Z. Tu, C. Gong, H. Lei, and K.-Y. Choi, *Fermi surface instabilities in electronic Raman scattering of the metallic kagome lattice CsV_3Sb_5*, , 1 (2021), arXiv:2108.11690 .

[118] M. L. Kiesel, C. Platt, and R. Thomale, *Unconventional Fermi Surface Instabilities in the Kagome Hubbard Model*, Physical Review Letters **110**, 126405 (2013).

[119] S.-L. Yu and J.-X. Li, *Chiral superconducting phase and chiral spin-density-wave phase in a Hubbard model on the kagome lattice*, Physical Review B **85**, 144402 (2012).

[120] Z. Jiang, H. Ma, W. Xia, Q. Xiao, Z. Liu, Z. Liu, Y. Yang, J. Ding, Z. Huang, J. Liu, Y. Qiao, J. Liu, Y. Peng, S. Cho, Y. Guo, J. Liu, and D. Shen, *Observation of electronic nematicity driven by three-dimensional charge density wave in kagome lattice KV_3Sb_5*, (2022), https://doi.org/10.48550/arXiv.2208.01499, arXiv:2208.01499 .

[121] C. Li, X. Wu, H. Liu, C. Polley, Q. Guo, Y. Wang, X. Han, M. Dendzik, M. H. Berntsen, B. Thiagarajan, Y. Shi, A. P. Schnyder, and O. Tjernberg, *Co-existence of two intertwined charge density waves in a kagome system*, Physical Review Research **4**, 033072 (2022).

[122] R. Grasset, Y. Gallais, A. Sacuto, M. Cazayous, S. Mañas-Valero, E. Coronado, and M.-A. Méasson, *Pressure-Induced Collapse of the Charge Density Wave and Higgs Mode Visibility in $2H - \mathbf{TaS_2}$*, Physical Review Letters **122**, 127001 (2019).

[123] K. M. Lang, V. Madhavan, J. E. Hoffman, E. W. Hudson, H. Eisaki, S. Uchida, and J. C. Davis, *Imaging the granular structure of high-Tc superconductivity in underdoped $Bi_2Sr_2CaCu_2O_{8+\delta}$*, Nature **415**, 412 (2002).

[124] J. Zhang, H. Wu, G. Zhao, L. Han, and J. Zhang, *A Review on Strain Study of Cuprate Superconductors*, Nanomaterials **12**, 3340 (2022).

[125] Y. Yu, L. Ma, P. Cai, R. Zhong, C. Ye, J. Shen, G. D. Gu, X. H. Chen, and Y. Zhang, *High-temperature superconductivity in monolayer $Bi_2Sr_2CaCu_2O_{8+\delta}$*, Nature **575**, 156 (2019).

[126] W. Ko, M. Kolmer, J. Yan, A. D. Pham, M. Fu, F. Lüpke, S. Okamoto, Z. Gai, P. Ganesh, and A.-P. Li, *Realizing gapped surface states in the magnetic topological insulator $MnBi_{2-x}Sb_xTe_4$*, Physical Review B **102**, 115402 (2020).

[127] X.-L. Qi and S.-C. Zhang, *Topological insulators and superconductors*, Reviews of Modern Physics **83**, 1057 (2011).

[128] P. Zhang, L. Chen, S. Sheng, W. Hu, H. Liu, C. Ma, Z. Liu, B. Feng, P. Cheng, Y. Zhang, L. Chen, J. Zhao, and K. Wu, *Melamine self-assembly and dehydrogenation on Ag(111) studied by tip-enhanced Raman spectroscopy*, The Journal of Chemical Physics **156**, 204301 (2022).

[129] M. Sackrow, C. Stanciu, M. A. Lieb, and A. J. Meixner, *Imaging Nanometre-Sized Hot Spots on Smooth Au Films with High-Resolution Tip-Enhanced Luminescence and Raman Near-Field Optical Microscopy*, ChemPhysChem **9**, 316 (2008).

[130] T. Schmid, L. Opilik, C. Blum, and R. Zenobi, *Nanoscale Chemical Imaging Using Tip-Enhanced Raman Spectroscopy: A Critical Review*, Angewandte Chemie International Edition **52**, 5940 (2013).

[131] T.-X. Huang, S.-C. Huang, M.-H. Li, Z.-C. Zeng, X. Wang, and B. Ren, *Tip-enhanced Raman spectroscopy: tip-related issues*, Analytical and Bioanalytical Chemistry **407**, 8177 (2015).

[132] R. WANG, Z. HE, A. V. SOKOLOV, AND D. KUROUSKI, *Gap-Mode Tip-Enhanced Raman Scattering on Au Nanoplates of Varied Thickness*, The Journal of Physical Chemistry Letters **11**, 3815 (2020).

[133] L. NOVOTNY AND B. HECHT, *Principles of Nano-Optics*, 2nd ed. (Cambridge university press, 2012).

[134] E. ABBE, *Beiträge zur Theorie des Mikroskops und des mikroskopischen Wahrnehmung*, Arch. Mikrosk. Anat. , 413 (1873).

[135] S. W. HELL, S. LINDEK, C. CREMER, AND E. H. K. STELZER, *Confocal microscopy with an increased detection aperture: type-B 4Pi confocal microscopy*, Optics Letters **19**, 222 (1994).

[136] P. JOHNS, K. YU, M. S. DEVADAS, AND G. V. HARTLAND, *Role of Resonances in the Transmission of Surface Plasmon Polaritons between Nanostructures*, ACS Nano **10**, 3375 (2016).

[137] T. ZHANG AND F. SHAN, *Development and Application of Surface Plasmon Polaritons on Optical Amplification*, Journal of Nanomaterials **2014**, 1 (2014).

[138] A. CAMPION AND P. KAMBHAMPATI, *Surface-enhanced Raman scattering*, Chemical Society Reviews **27**, 241 (1998).

[139] L. XIA, M. CHEN, X. ZHAO, Z. ZHANG, J. XIA, H. XU, AND M. SUN, *Visualized method of chemical enhancement mechanism on SERS and TERS*, Journal of Raman Spectroscopy **45**, 533 (2014).

[140] P. L. STILES, J. A. DIERINGER, N. C. SHAH, AND R. P. VAN DUYNE, *Surface-Enhanced Raman Spectroscopy*, Annual Review of Analytical Chemistry **1**, 601 (2008).

[141] Z. ZHANG, S. SHENG, R. WANG, AND M. SUN, *Tip-Enhanced Raman Spectroscopy*, Analytical Chemistry **88**, 9328 (2016).

[142] J. STEIDTNER AND B. PETTINGER, *Tip-Enhanced Raman Spectroscopy and Microscopy on Single Dye Molecules with 15 nm Resolution*, Physical Review Letters **100**, 236101 (2008).

[143] M. SUN, Z. ZHANG, H. ZHENG, AND H. XU, *In-situ plasmon-driven chemical reactions revealed by high vacuum tip-enhanced Raman spectroscopy*, Scientific Reports **2**, 647 (2012).

[144] L. LANGELÜDDECKE, P. SINGH, AND V. DECKERT, *Exploring the Nanoscale: Fifteen Years of Tip-Enhanced Raman Spectroscopy*, Applied Spectroscopy **69**, 1357 (2015).

[145] O. MARTI, H. BIELEFELDT, B. HECHT, S. HERMINGHAUS, P. LEIDERER, AND J. MLYNEK, *Near-field optical measurement of the surface plasmon field*, Optics Communications **96**, 225 (1993).

[146] E. Synge, *XXXVIII. A suggested method for extending microscopic resolution into the ultra-microscopic region*, The London, Edinburgh, and Dublin Philosophical Magazine and Journal of Science **6**, 356 (1928).

[147] E. A. Ash and G. Nicholls, *Super-resolution Aperture Scanning Microscope*, Nature **237**, 510 (1972).

[148] N. M. Arslanov and S. A. Moiseev (2004) pp. 25–34.

[149] L. Novotny, R. X. Bian, and X. S. Xie, *Theory of Nanometric Optical Tweezers*, Physical Review Letters **79**, 645 (1997).

[150] M. Schnell, A. Garcia-Etxarri, J. Alkorta, J. Aizpurua, and R. Hillenbrand, *Phase-Resolved Mapping of the Near-Field Vector and Polarization State in Nanoscale Antenna Gaps*, Nano Letters **10**, 3524 (2010).

[151] B. Sharma, R. R. Frontiera, A.-I. Henry, E. Ringe, and R. P. Van Duyne, *SERS: Materials, applications, and the future*, Materials Today **15**, 16 (2012).

[152] H. J. Zandvliet and A. van Houselt, *Scanning Tunneling Spectroscopy*, Annual Review of Analytical Chemistry **2**, 37 (2009).

[153] A. B. Zrimsek, N. Chiang, M. Mattei, S. Zaleski, M. O. McAnally, C. T. Chapman, A.-I. Henry, G. C. Schatz, and R. P. Van Duyne, *Single-Molecule Chemistry with Surface- and Tip-Enhanced Raman Spectroscopy*, Chemical Reviews **117**, 7583 (2017).

[154] M. Zhang, R. Wang, Z. Zhu, J. Wang, and Q. Tian, *Experimental research on the spectral response of tips for tip-enhanced Raman spectroscopy*, Journal of Optics **15**, 055006 (2013).

[155] J. R. Lombardi, R. L. Birke, T. Lu, and J. Xu, *Charge-transfer theory of surface enhanced Raman spectroscopy: Herzberg–Teller contributions*, The Journal of Chemical Physics **84**, 4174 (1986).

[156] P. G. Gucciardi, J. C. Valmalette, M. Lopes, R. Dèturche, M. Lamy De La Chapelle, D. Barchiesi, F. Bonaccorso, C. D'Andrea, M. Chaigneau, G. Picardi, and R. Ossikovski, *Light depolarization effects in tip enhanced Raman spectroscopy of silicon (001) and gallium arsenide (001)*, AAPP Atti della Accademia Peloritana dei Pericolanti, Classe di Scienze Fisiche, Matematiche e Naturali **89**, 10 (2011).

[157] Z. Yang, J. Aizpurua, and H. Xu, *Electromagnetic field enhancement in TERS configurations*, Journal of Raman Spectroscopy **40**, 1343 (2009).

[158] W. Zhang, X. Cui, and O. J. F. Martin, *Local field enhancement of an infinite conical metal tip illuminated by a focused beam*, Journal of Raman Spectroscopy **40**, 1338 (2009).

[159] Z. YANG, Q. LI, F. RUAN, Z. LI, B. REN, H. XU, AND Z. TIAN, *FDTD for plasmonics: Applications in enhanced Raman spectroscopy*, Chinese Science Bulletin **55**, 2635 (2010).

[160] E. J. SÁNCHEZ, L. NOVOTNY, AND X. S. XIE, *Near-Field Fluorescence Microscopy Based on Two-Photon Excitation with Metal Tips*, Physical Review Letters **82**, 4014 (1999).

[161] Y. C. MARTIN, H. F. HAMANN, AND H. K. WICKRAMASINGHE, *Strength of the electric field in apertureless near-field optical microscopy*, Journal of Applied Physics **89**, 5774 (2001).

[162] T. DECKERT-GAUDIG, A. TAGUCHI, S. KAWATA, AND V. DECKERT, *Tip-enhanced Raman spectroscopy – from early developments to recent advances*, Chemical Society Reviews **46**, 4077 (2017).

[163] D. ROY, C. M. WILLIAMS, AND K. MINGARD, *Single-crystal gold tip for tip-enhanced Raman spectroscopy*, Journal of Vacuum Science Technology B, Nanotechnology and Microelectronics: Materials, Processing, Measurement, and Phenomena **28**, 631 (2010).

[164] P. C. FARIÑA, *Tip-Enhanced Raman Spectroscopy (TERS)*, (2017).

[165] A. A. GORBUNOV, B. WOLF, AND J. EDELMANN, *The use of silver tips in scanning tunneling microscopy*, Review of Scientific Instruments **64**, 2393 (1993).

[166] K. DICKMANN, F. DEMMING, AND J. JERSCH, *New etching procedure for silver scanning tunneling microscopy tips*, Review of Scientific Instruments **67**, 845 (1996).

[167] M. IWAMI, Y. UEHARA, AND S. USHIODA, *Preparation of silver tips for scanning tunneling microscopy imaging*, Review of Scientific Instruments **69**, 4010 (1998).

[168] J. S. LLOYD, A. WILLIAMS, R. H. RICKMAN, A. MCCOWEN, AND P. R. DUNSTAN, *Reproducible electrochemical etching of silver probes with a radius of curvature of 20 nm for tip-enhanced Raman applications*, Applied Physics Letters **99**, 143108 (2011).

[169] T. E. GRAEDEL, *Corrosion Mechanisms for Silver Exposed to the Atmosphere*, Journal of The Electrochemical Society **139**, 1963 (1992).

[170] Z. YU, C. WANG, Y. DU, S. THEVUTHASAN, AND I. LYUBINETSKY, *Reproducible tip fabrication and cleaning for UHV STM*, Ultramicroscopy **108**, 873 (2008).

[171] N. KUMAR, S. J. SPENCER, D. IMBRAGUGLIO, A. M. ROSSI, A. J. WAIN, B. M. WECKHUYSEN, AND D. ROY, *Extending the plasmonic lifetime of tip-enhanced Raman spectroscopy probes*, Physical Chemistry Chemical Physics **18**, 13710 (2016).

[172] L. OPILIK, Ü. DOGAN, J. SZCZERBIŃSKI, AND R. ZENOBI, *Degradation of silver near-field optical probes and its electrochemical reversal*, Applied Physics Letters **107**, 091109 (2015).

[173] N. Chelwani, D. Hoch, D. Jost, B. Botka, J.-R. Scholz, R. Richter, M. Theodoridou, F. Kretzschmar, T. Böhm, K. Kamarás, and R. Hackl, *Off-axis parabolic mirror optics for polarized Raman spectroscopy at low temperature*, Applied Physics Letters **110**, 193504 (2017).

[174] S. Tewari, K. M. Bastiaans, M. P. Allan, and J. M. van Ruitenbeek, *Robust procedure for creating and characterizing the atomic structure of scanning tunneling microscope tips*, Beilstein Journal of Nanotechnology **8**, 2389 (2017).

[175] S. Ernst, S. Wirth, M. Rams, V. Dolocan, and F. Steglich, *Tip preparation for usage in an ultra-low temperature UHV scanning tunneling microscope*, Science and Technology of Advanced Materials **8**, 347 (2007).

[176] I. Ekvall, E. Wahlström, D. Claesson, H. Olin, and E. Olsson, *Preparation and characterization of electrochemically etched W tips for STM*, Measurement Science and Technology **10**, 11 (1999).

[177] D.-C. Chen, *Portable alignment device for an off-axis parabolic mirror optical axis adjustment*, International Journal of Precision Engineering and Manufacturing **13**, 33 (2012).

[178] Y. H. Lee, *Alignment of an off-axis parabolic mirror with two parallel He-Ne laser beams*, Optical Engineering **31**, 2287 (1992).

[179] N. Chelwani, *Scanning Microscopy and Momentum-Resolved Raman Scattering in Semiconductors and Oxides*, Ph.D. thesis, Technical University Munich (2018).

[180] G. G. Samsonidze, R. Saito, N. Kobayashi, A. Grüneis, J. Jiang, A. Jorio, S. G. Chou, G. Dresselhaus, and M. S. Dresselhaus, *Family behavior of the optical transition energies in single-wall carbon nanotubes of smaller diameters*, Applied Physics Letters **85**, 5703 (2004).

[181] P. C. Dresselhaus, Mildred S and Dresselhaus, Gene and Eklund, *Science of fullerenes and carbon nanotubes: their properties and applications* (Elsevier, 1996).

[182] M. S. Dresselhaus, G. Dresselhaus, and R. Saito, *Carbon fibers based on C_{60} and their symmetry*, Physical Review B **45**, 6234 (1992).

[183] T. W. Odom, J. L. Huang, and C. M. Lieber, *STM studies of single-walled carbon nanotubes*, Journal of Physics Condensed Matter **14** (2002), 10.1088/0953-8984/14/6/201.

[184] M. S. D. R. Saito, G. Dresselhaus, *Physical Properties of Carbon Nanotubes* (Imperial College Press, London, 1998).

[185] H. A. G. M. S. Dresselhaus, G. Dresselhaus, K. Sugihara, I. L. Spain, *Graphite Fibers and Filaments*, vol. 5, sp ed. (Springer Berlin Heidelberg, 1988).

[186] S. G. Louie, in *Carbon Nanotubes* (Springer Berlin Heidelberg, Berlin, Heidelberg) pp. 113–145.

[187] C. L. KANE AND E. J. MELE, *Electron Interactions and Scaling Relations for Optical Excitations in Carbon Nanotubes*, Physical Review Letters **93**, 197402 (2004).

[188] L. CHICO, V. H. CRESPI, L. X. BENEDICT, S. G. LOUIE, AND M. L. COHEN, *Pure Carbon Nanoscale Devices: Nanotube Heterojunctions*, Physical Review Letters **76**, 971 (1996).

[189] C. T. WHITE, D. H. ROBERTSON, AND J. W. MINTMIRE, *Helical and rotational symmetries of nanoscale graphitic tubules*, Physical Review B **47**, 5485 (1993).

[190] J. W. MINTMIRE AND C. T. WHITE, *Universal Density of States for Carbon Nanotubes*, Physical Review Letters **81**, 2506 (1998).

[191] C. T. WHITE AND T. N. TODOROV, *Carbon nanotubes as long ballistic conductors*, Nature **393**, 240 (1998).

[192] H. AJIKI AND T. ANDO, *Aharonov-Bohm effect in carbon nanotubes*, Physica B: Condensed Matter **201**, 349 (1994).

[193] H. AJIKI, *Magneto-optical spectra of carbon nanotubes: effect of Aharonov–Bohm flux on depolarization effect*, Physica B: Condensed Matter **323**, 206 (2002).

[194] H. KATAURA, Y. KUMAZAWA, Y. MANIWA, I. UMEZU, S. SUZUKI, Y. OHTSUKA, AND Y. ACHIBA, *Optical properties of single-wall carbon nanotubes*, Synthetic Metals **103**, 2555 (1999).

[195] Q. CHENG, S. DEBNATH, E. GREGAN, AND H. J. BYRNE, *Vibrational mode assignments for bundled single-wall carbon nanotubes using Raman spectroscopy at different excitation energies*, Applied Physics A **102**, 309 (2011).

[196] S. M. BACHILO, M. S. STRANO, C. KITTRELL, R. H. HAUGE, R. E. SMALLEY, AND R. B. WEISMAN, *Structure-Assigned Optical Spectra of Single-Walled Carbon Nanotubes*, Science **298**, 2361 (2002).

[197] I. PÓCSIK, M. KOÓS, AND O. BERKESI, in *Nanostructured Carbon for Advanced Applications* (Springer Netherlands, Dordrecht, 2001) pp. 169–176.

[198] R. VIDANO, D. FISCHBACH, L. WILLIS, AND T. LOEHR, *Observation of Raman band shifting with excitation wavelength for carbons and graphites*, Solid State Communications **39**, 341 (1981).

[199] A. M. RAO, P. C. EKLUND, S. BANDOW, A. THESS, AND R. E. SMALLEY, *Evidence for charge transfer in doped carbon nanotube bundles from Raman scattering*, Nature **388**, 257 (1997).

[200] A. JORIO, A. G. SOUZA FILHO, G. DRESSELHAUS, M. S. DRESSELHAUS, A. K. SWAN, M. S. ÜNLÜ, B. B. GOLDBERG, M. A. PIMENTA, J. H. HAFNER, C. M. LIEBER, AND R. SAITO, *G-band resonant Raman study of 62 isolated single-wall carbon nanotubes*, Physical Review B **65**, 155412 (2002).

[201] S. D. M. BROWN, A. JORIO, P. CORIO, M. S. DRESSELHAUS, G. DRESSELHAUS, R. SAITO, AND K. KNEIPP, *Origin of the Breit-Wigner-Fano lineshape of the tangential G -band feature of metallic carbon nanotubes*, Physical Review B **63**, 155414 (2001).

[202] A. I. LÓPEZ-LORENTE, B. M. SIMONET, AND M. VALCÁRCEL, *Raman spectroscopic characterization of single walled carbon nanotubes: influence of the sample aggregation state*, The Analyst **139**, 290 (2014).

[203] G. G. SAMSONIDZE, R. SAITO, A. JORIO, A. G. S. FILHO, A. GRÜNEIS, M. A. PIMENTA, G. DRESSELHAUS, AND M. S. DRESSELHAUS, *Phonon Trigonal Warping Effect in Graphite and Carbon Nanotubes*, Physical Review Letters **90**, 027403 (2003).

[204] J. REICH, STEPHANIE AND THOMSEN, CHRISTIAN AND MAULTZSCH, *Carbon nanotubes: basic concepts and physical properties* (John Wiley & Sons, 2004).

[205] H. WALEN, D.-J. LIU, J. OH, H. LIM, J. W. EVANS, Y. KIM, AND P. A. THIEL, *Self-organization of S adatoms on Au(111): 3R30° rows at low coverage*, The Journal of Chemical Physics **143**, 014704 (2015).

[206] J. LEFEBVRE, R. ANTONOV, AND A. JOHNSON, *STM morphology study of ropes of single-wall carbon nanotubes*, Applied Physics A: Materials Science Processing **67**, 71 (1998).

[207] P. KIM, T. W. ODOM, J. HUANG, AND C. M. LIEBER, *STM study of single-walled carbon nanotubes*, Carbon **38**, 1741 (2000).

[208] J. STEIDTNER AND B. PETTINGER, *High-resolution microscope for tip-enhanced optical processes in ultrahigh vacuum*, Review of Scientific Instruments **78**, 103104 (2007).

[209] A. HARTSCHUH, E. J. SÁNCHEZ, X. S. XIE, AND L. NOVOTNY, *High-Resolution Near-Field Raman Microscopy of Single-Walled Carbon Nanotubes*, Physical Review Letters **90**, 095503 (2003).

[210] A. DAS AND A. K. SOOD, *Renormalization of the phonon spectrum in semiconducting single-walled carbon nanotubes studied by Raman spectroscopy*, Physical Review B **79**, 235429 (2009).

[211] A. SHIOTARI, T. KUMAGAI, AND M. WOLF, *Tip-Enhanced Raman Spectroscopy of Graphene Nanoribbons on Au(111)*, The Journal of Physical Chemistry C **118**, 11806 (2014).

[212] C. VANNIER, B.-S. YEO, J. MELANSON, AND R. ZENOBI, *Multifunctional microscope for far-field and tip-enhanced Raman spectroscopy*, Review of Scientific Instruments **77**, 023104 (2006).

[213] B. PETTINGER, P. SCHAMBACH, C. J. VILLAGÓMEZ, AND N. SCOTT, *Tip-Enhanced Raman Spectroscopy: Near-Fields Acting on a Few Molecules*, Annual Review of Physical Chemistry **63**, 379 (2012).

[214] S. S. KHARINTSEV, G. G. HOFFMANN, P. S. DOROZHKIN, G. DE WITH, AND J. LOOS, *Atomic force and shear force based tip-enhanced Raman spectroscopy and imaging*, Nanotechnology **18**, 315502 (2007).

[215] M. DRESSELHAUS, G. DRESSELHAUS, R. SAITO, AND A. JORIO, *Raman spectroscopy of carbon nanotubes*, Physics Reports **409**, 47 (2005).

[216] S. SUZUKI AND H. HIBINO, *Characterization of doped single-wall carbon nanotubes by Raman spectroscopy*, Carbon **49**, 2264 (2011).

[217] L. NOVOTNY, E. J. SÁNCHEZ, AND X. SUNNEY XIE, *Near-field optical imaging using metal tips illuminated by higher-order Hermite–Gaussian beams*, Ultramicroscopy **71**, 21 (1998).

[218] L. PEIS, G. HE, D. JOST, G. RAGER, AND R. HACKL, *Polarized tip-enhanced Raman spectroscopy at liquid He temperature in ultrahigh vacuum using an off-axis parabolic mirror*, (2022), 2212.11655v1, arXiv:2212.11655 .

[219] R. PENG, H. C. XU, S. Y. TAN, H. Y. CAO, M. XIA, X. P. SHEN, Z. C. HUANG, C. WEN, Q. SONG, T. ZHANG, B. P. XIE, X. G. GONG, AND D. L. FENG, *Tuning the band structure and superconductivity in single-layer FeSe by interface engineering*, Nature Communications **5**, 5044 (2014).

List of publications

1. **L. Peis***, G. He*, D. Jost, G. Rager, and R. Hackl. *Polarized tip-enhanced Raman spectroscopy at liquid He temperature in ultrahigh vacuum using an off-axis parabolic mirror*,
Rev. Sci. Instrum. 94, 063701 (2023)

2. N. Lazarevic, A. Baum, A. Milosavljevic, **L. Peis**, R. Stumberger, J. Bekaert, A. Solajic, J. Pesic, A. Wang, M. Scepanovic, M. Milosevic, C. Petrovic, Z. Popovic, R. Hackl. *Evolution of lattice, spin, and charge properties across the phase diagram of $FeSe_{1-x}S_x$*,
Phys. Rev. B 106, 094510 (2022)

3. D. Jost, **L. Peis**, G. He, A. Baum, S. Geprägs, J. Palmstrom, M. Ikeda, I. Fisher, T. Wolf, S. Lederer, and R. Hackl. *Quantum critical fluctuations in an Fe-based superconductor*,
Nat Commun Phys 5, 201 (2022)

4. G. He*, **L. Peis***, R. Stumberger, L. Prodan, V. Tsurkan, N. Unglert, L. Chioncel, I. Kézsmárki, and R. Hackl. *Phonon anomalies associated with spin reorientation in the Kagome ferromagnet Fe_3Sn_2*,
physica status solidi (b) 259, no. 5 (2021): 2100169

5. L. Kreuzer, T. Widmann, N. Hohn, K. Wang, L. Bießmann, **L. Peis**, J. Moulin, V. Hildebrand, A. Laschewsky, C. Papadakis, and P. Müller-Buschbaum. *Swelling and Exchange Behavior of Poly(sulfobetaine)-Based Block Copolymer Thin Films.*,
Macromolecules (2019)

---

*contributed equally

Acknowledgment

During my time working on this PhD thesis at the Walther-Meißner-Institute and the Leibniz Institute for Solid State and Materials Research, I had an amazing time with lots of nice and helpful colleagues and friends. I'd like to express my gratitude towards several people for their contributions to the presented work.

Prof. Dr. Rudi Hackl for being a very caring supervisor, ready to help at any minute. Thank you for the good times, the best experiences while moving laboratory equipment, and many opportunities to visit remarkable people abroad.

Prof. Dr. Bernd Büchner For being my mentor during the last years and providing a great working atmosphere at the IFW.

Prof. Dr. Rudolf Groß for the opportunity to perform interesting measurements and to work in a good atmosphere at the Walther-Meißner-Institute.

Prof. Dr. Thomas Devereaux for your kind hospitality during our visits in Stanford with awesome music and superb steaks. Looking forward to more enlightening discussions.

Dr. Ge He for the best introduction to the act of building cryogenic setups. Why this is so much fun is actually beyond me.

Dr. Daniel Jost I still owe you so much, great times behind and ahead with you quasi-steroid taking punk. Best (Fat-)man in the world, that's not just a coffee mug text, you are the real deal!

Dr. Andreas Baum for your incredible perseverance and stamina, combined with your knowledge and dedication. Always ready to answer questions, even after leaving the WMI.

Ramona "Ramonsresponse" Stumberger For being the best master student I ever had. Late nighters and trying not to lose ones nerves are still deeply rooted in my heart. Thank you for all that fun stuff.

Gabriele Rager and Pablo Cova Fariña for developing the Ag tip fabrication method and providing several of the tips.

Manuel Müller for awesome coffee and lunch breaks! And also fabricating several Ag films for me, whenever I needed some. This made my life so much easier! I salute you, dear Meme-God!

Florian Fesquet for being the lovable french weirdo, love hanging out with you!

Dr. Stephan Geprägs for growing the best gold and other thin films, that one could ask for. Always a pleasure working with you.

All students and colleagues at the WMI for the pleasant time, good atmosphere, and lots of fun after working hours.

Lilian Prodan, Vladimir Tsurkan, and Christoph Meingast for kindly providing measurements beyond Raman spectroscopy on the samples of interest during this thesis and the helpful discussions.

Emma Cuddy and Nico Unglert for your calculations and helpful contributions in several compounds during this work.

The WMI Workshop for bearing with my microscopic parts with the utmost patience and being always very helpful with all kinds of problems.

The Helium Hall for providing the cryogenics and assistance with related issues.

Sybilla Plöderl and Maria Botta who were of great support in keeping my lab space clean. Thank you so much for this.

Emel Dönertas for the smooth handling of all administrative tasks.

Dieter Guratzsch, Dr. Matthias Opel, and Michael Renger for keeping all the software and hardware issues at bay.

Dr. Frederic Felsen and Fabian Schlachter I am convinced that you two have listened to more of my "thoughts" and problems, than anyone else. You two are my best examples of the German education system failure, I am so glad to have you in my life.

All my friends at the Freisinger Kletterhalle For all the training hours, parties, outdoor experiences, and bullshit conversations. Beste Kletterhalle der Welt!

My parents and my brother I cannot really put my gratitude into words, everything I am today is because of you. So thanks for that, I guess ;) I love you very much!

"That's all Folks!"